Precise nanoscale characterisation of novel Heusler thermoelectrics via analytical electron microscopy

Robert William Henry Webster MPhys

Submitted in fulfilment of the requirements for the

Degree of Doctor of Philosophy

School of Physics and Astronomy

College of Science and Engineering

Unversity of Glasgow

July 2020

Abstract

Thermoelectric power generation presents an opportunity to 'scavenge' energy that would otherwise be wasted as heat. Heusler alloys, a class of materials often comprising inexpensive, non-toxic elements, are promising for practical use in a new generation of thermoelectric devices. Recently, efficient thermoelectric Heusler alloys have overcome a performance-limiting thermal conductivity through the introduction of nanostructures that scatter phonons and impede thermal transport. However, the nature and stability of nanostructures can be difficult to discern, especially the minor compositional variations that derive from inhomogeneous phase segregation.

Throughout this thesis TiNiSn, which forms the basis for some of the most promising n-type half-Heusler thermoelectrics, is studied through a unique combination of elemental and diffractive analysis in the scanning transmission electron microscope (STEM). Epitaxial thin films of TiNiSn are grown by pulsed laser deposition and FIB-prepared cross-sections of these are characterised in STEM with a focus on aberration-corrected STEM-EELS spectrum imaging and scanning precession electron diffraction (SPED), yielding precise chemical and structural quantification with nanoscale spatial resolution. The results throughout this thesis demonstrate the importance of STEM for quantitative studies of thermoelectric materials, as it can provide the analytical precision required for accurate identification of minority phases in TiNiSn specimens that would otherwise be overlooked in bulk analytical techniques.

Sensitivity to very small elemental concentrations is a cornerstone of the use of STEM-EELS for chemical characterisation. Precisions of 0.3 % were achieved through adoption and development of refined, reference-based, absolute elemental quantification protocols which were essential in overcoming difficulties with large uncertainties posed by conventional methods. The success of this approach, in part, is due to advances made in characterisation of experimental conditions including, for the first time, an automated, standard-less approach to the measurement and correction of energy dispersion non-uniformities. Dispersion correction enables reliable, absolute calibration of energy-loss in spectra to yield a precision better than 0.1 eV.

These developments in STEM-EELS were then used in three investigations of TiNiSn thin films exploring aspects of nanostructuring, phase segregation and crystallographic strain and coherency. We discovered the spontaneous formation of nanostructures during thin film growth, gaining some insight into the phase segregation mechanisms that lead to their nucleation. Novel *in situ* STEM studies of phase segregation facilitated direct observations of the thermal evolution of nanoscale phases and results enabled characterisation of diffusion rates of Ni migration between full- and half-Heusler phases, for which the activation energy was calculated as 0.3 eV. Combining SPED with advances in detector technology, STEM structural investigations highlighted an interesting strain texture associated with nanostructuring of the half-Heusler thin films. Finally, combining SPED results with STEM-EELS measurements is proposed as a route to 'correlative-STEM' analysis, which unifies nanoscale chemical and structural information for greater insights into the impact of nanostructures in thermoelectrics.

For my grandparents

Harry, Hilda and Wilma,

Who I wish were here to share this moment.

Acknowledgements

The work culminating in this thesis would not have been possible without the help and support of others, whom I would take this opportunity to thank. Dr. Donald MacLaren, for supervision and guidance. Dr. John Halpin, whose input and support has been invaluable in all aspects of my work. Dr. Sam McFadzean, Colin How & William Smith for all their help and support on the microscopes. Dr. Gary Paterson, for his help with code for processing SPED data. Prof. Alan Craven, for all the useful discussions about EELS. Michael Scott, for the enthusiasm and hard work given during his final-year project. Prof. Jan-Willem Bos and Dr. Srinivas Popuri, for provision of materials for PLD. Dr. Matthew Steer, who generously let me monopolise some time in his lab.

I would like to thank all my fellow PhD students in MCMP, without whom the last four years wouldn't have been nearly as enjoyable. I probably owe most of them a drink for their patience while I rationalised some obscure bit of EELS theory by roping them into a discussion about it. I am especially grateful to Dr. Monifa Phillips, who took the time to help show me the ropes when I first started.

I would take a moment acknowledge the Engineering and Physical Sciences Research Council, the European Microscopy Society, the Institute of Physics and the University of Glasgow, for the funding which has supported me throughout my work and enabled me to present my work at conferences in the UK and abroad.

Finally, I am endlessly grateful to all my friends and family. Special thanks go to my Mum and Dad, whose support has helped me through writing a thesis in the middle of a global pandemic. And to Ellen, for all her love, encouragement and endless patience with me, cheering me on no matter how far apart we are.

Declaration

This thesis has been written by myself and is a record of the research I have conducted in the Materials and Condensed Matter Physics (MCMP) group of the School of Physics and Astronomy at the University of Glasgow during the period 2016 - 2020 under the supervision of Dr. Donald MacLaren. The work described herein is my own, with the following notable exceptions:

- Dr. John Halpin acquired STEM-EELS data from elemental reference specimens and from the $TiNiCu_{0.1}Sn$ specimen presented in Chapter 4.
- The deposition of epitaxial vanadium thin films for work presented in Chapter 5 was carried out by undergraduate project student Michael Scott, under the supervision of myself and Dr. Donald MacLaren.
- X-ray diffraction measurements presented in Chapter 5 were acquired with the assistance of Dr. Matthew Steer.
- Dr. Donald MacLaren acquired the STEM data used in Chapter 6.
- The processing methods outlined in Section 7.1 use Python code which was developed collaboratively with Dr. Gary Paterson.

Some of the work reported in this thesis has been incorporated into the following co-authored papers:

1. **R. W. H. Webster**, J. E. Halpin, S. R. Popuri, J. W. G. Bos and D. A. MacLaren, *Spontaneous formation of nanostructures during pulsed laser deposition of epitaxial half-Heusler TiNiSn on MgO(001)*, APL Materials, **7(1)**, 2019, https://doi.org/10.1063/1.5052361.
2. J. E. Halpin, **R. W. H. Webster**, H. Gardner, M. P. Moody, P. A. J. Bagot and D. A. MacLaren, *An in situ approach for preparing atom probe tomography specimens by*

xenon plasma focused ion beam milling, Ultramicroscopy, **202**, pp121-127, 2019, https://doi.org/10.1016/j.ultramic.2019.04.005.

3. **R. W. H. Webster**, M. T. Scott , S. R. Popuri, J. W. G. Bos and D. A. MacLaren, *Epitaxial vanadium nanolayers to suppress interfacial reactions during deposition of titanium-bearing Heusler alloys on MgO(001)*, Applied Surface Science, **512**, 2020, 145649, https://doi.org/10.1016/j.apsusc.2020.145649
4. **R. W. H. Webster**, A. J. Craven, B. Schaffer, S. McFadzean, I. MacLaren and D. A. MacLaren, *Correction of EELS dispersion non-uniformities for improved chemical shift analysis*, Ultramicroscopy, **217**, 113069, 2020, https://doi.org/10.1016/j.ultramic.2020.113069
5. M. Nord, **R. W. H. Webster**, K. A. Paton, S. McVitie, D. McGrouther, I. MacLaren and G. W. Paterson, *Fast Pixelated Detectors in Scanning Transmission Electron Microscopy. Part I: Data Acquisition, Live Processing and Storage*, Microsc. Microanal., **26(4)**, pp653-666, 2020, https://doi.org/10.1017/S1431927620001713
6. G. W. Paterson, **R. W. H. Webster**, A. Ross, K. A. Paton, T. A. MacGregor, D. McGrouther, I. MacLaren and M. Nord, *Fast Pixelated Detectors in Scanning Transmission Electron Microscopy. Part II: Post-Aquisition Data Processing, Visualisation and Structural Characterisation*, Microsc. Microanal., 2020, https://doi.org/10.1017/S1431927620024307
7. C. Gilroy, K. McKay, M. Devine, **R. W. H. Webster**, N. Gadegaard, A. Karimullah, D. A. MacLaren, M. Kadodwala, *Flexoelectric active control of metamaterial chirality*, Submitted to Advanced Materials, 2020
8. A. J. Craven, **R. W. H. Webster**, B. Sala, D. A. MacLaren, S. McFadzean, B. Schaffer, I. MacLaren, *Splicing DualEELS Spectra: The effects of Spectrometer Dispersion Non-Uniformity and Stray Scattering*, In preparation, 2020
9. A. J. Craven, **R. W. H. Webster**, M. Tencé, S. McFadzean, B. Schaffer, I. MacLaren, *Stray Scattering in EELS Spectroscopy*, In preparation, 2020
10. S. J. McCartan, G. W. Paterson, **R. W. H. Webster**, T. McGregor, I. MacLaren, I. Calisir, D. A. Hall, *Using scanning precession electron diffraction to relate crystallography to chemistry in the mixed oxide electroceramic* $0.75Bi(Fe_{(1-x)}Ti^{4+}_{(x)})O_3 - 0.25BaTiO_3$, Submitted to JACERS, 2020

Contents

List of Tables

List of Figures

List of Abbreviations

3DAP	3-dimensional Atom-Probe Tomography
4DSTEM	4-dimensional Scanning Transmission Electron Microscopy
ADF	Annular Dark Field
AFM	Atomic Force Microscope
bcc	Body-Centred Cubic
BF	Bright Field
bfp	back-focal plane
CBED	Convergent Beam Electron Diffraction
CCD	Charge-Coupled Device
CHT	Circular Hough Transform
DED	Direct Electron Detector
DF	Dark Field
DFT	Density Functional Theory
DM	Digital Micrograph
EBID	Electron Beam Induced Deposition
EBSD	Electron Back-scatter Diffraction
EDS	Energy-Dispersive X-ray Spectroscopy
EELS	Electron Energy-Loss Spectroscopy
EFTEM	Energy-Filtered Transmission Electron Microscopy
ELNES	Energy-loss Near Edge Structure
EXELFS	Extended Energy-Loss Fine Structure
fcc	Face-centred Cubic
FEG	Field Emission Gun
fH	full-Heusler alloy
FIB	Focussed Ion Beam
FWHM	Full-Width, Half-Maximum
GPA	Geometric Phase Analysis
HAADF	High-Angle Annular Dark Field
HRTEM	High-Resolution Transmission Electron Microscopy
hH	half-Heusler alloy
HT	High Tension
LoG	Laplacian of Gaussian
MBE	Molecular-beam Epitaxy
MCMC	Markov-chain Monte-Carlo
MEMS	Micro-Electro-Mechanical System

mfp	Mean-Free-Path
NBED	Nano-beam Electron Diffraction
NPD	Neutron Powder Diffraction
PED	Precession Electron Diffraction
PGEC	Phonon-Glass Electron-Crystal
PLD	Pulsed Laser Deposition
PVD	Physical Vapour Deposition
RHEED	Reflection High-Energy Electron Diffraction
RMS	Root-Mean-Square
SADP	Selected Are Diffraction Pattern
SD	Sputter Deposition
SEM	Scanning Electron Microscope/Microscopy
SI	Spectrum Image
SNR	Signal-to-Noise Ratio
SPED	Scanning Precession Electron Diffraction
SSD	Single-Scattering Distribution
STEM	Scanning Transmission Electron Microscope/Microscopy
TEG	Thermoelectric Generator
TEM	Transmission Electron Microscope/Microscopy
UHV	Ultra-High Vacuum
VDF	Virtual Dark Field
VSM	Voltage Scan Module
XAFS	X-ray Absorption Fine Structure
XANES	X-ray Absorption Near-Edge Structure
XAS	X-ray Absorption Spectroscopy
XRD	X-ray Diffraction
ZLP	Zero-loss peak

The end is in the beginning and lies far ahead.

Ralph Ellison

1

Introduction

MODERN ENERGY CONSUMPTION is incredibly wasteful. In the United States of America, where the Lawrence-Livermore National Laboratory carries out some of the most detailed analysis of annual commodity use, 68% of energy consumption in 2018 was identified as 'rejected energy' [1] which serves no meaningful function in our lives. Energy that is wasted during consumption is typically lost through production of heat or sound, i.e., in conversion to either thermal or kinetic energy. As global energy consumption is anticipated to rise 25% of 2018 levels by the year 2040 [2], novel innovations in energy infrastructure are required to ensure that supply will be able to grow at a pace which meets this increase in demand. Locally [3, 4] and internationally [5, 6], energy policy is concerned with the climate crisis and investing in new sources of renewable energy to reduce carbon emissions and mitigate global heating to within 2°C above pre-industrial levels [7]. Progress towards this goal can be achieved not only with the ushering of new primary energy infrastructure; the global energy consumption landscape could be dramatically altered by novel technologies tapping into the 'rejected energy' that is a significant by-product of current processes.

Although some energy waste is thermodynamically inevitable, there is a significant portion of preventable energy loss from inefficiencies in power generation and consumption. The biggest sources of waste in the energy landscape are by far the high temperature processes involved in electricity production (34% efficient) and transportation (21% efficient) [1]. Here, as with all sectors, a considerable amount of waste takes the form of heat energy lost to the external environment. Without any significant change to the primary sources of energy, thermoelectric power generation represents a compelling green technology which could create a reduction in energy waste and CO_2 emissions [8]. The potential of thermoelectric generators (TEGs) is owed to the ability to directly convert heat into electricity. TEGs can potentially be adapted to recover energy from a diverse range of sources. Prospective applications include heat recovery from automotive/aerospace engines [9, 10] and industrial furnaces [11, 12], where waste is most significant. Thermoelectrics are also finding use ranging down to small-scale applications as sub-Watt power generators for new technologies, e.g., wireless sensing [13, 14], wearable electronics [15, 16] and the Internet of Things [17].

The viability of TEGs for widespread application such as in the cases listed above is ultimately dependent on the materials used in their manufacture. To fully realise commonplace

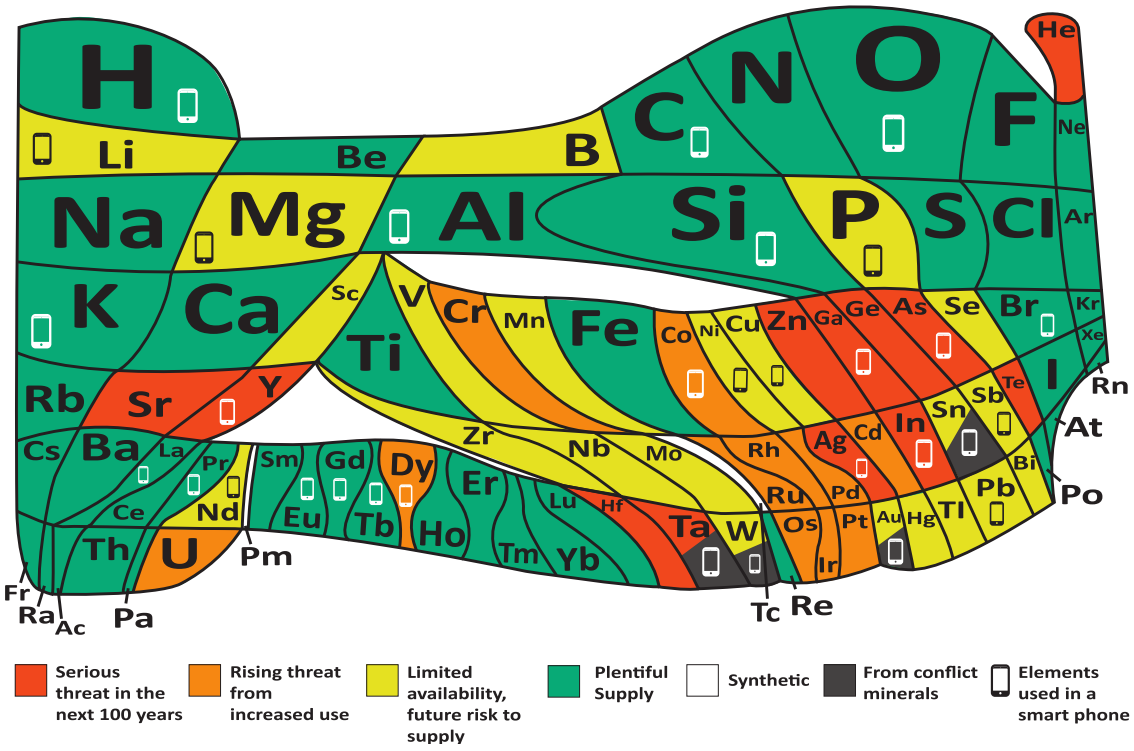

Figure 1.1: Periodic table of the elements, where the relative abundance of each element is represented by area. Colour is used to indicate threat to global supply (see legend). Reproduced from the European Chemical Society under Creative Commons license [18].

usage of TEGs, thermoelectric materials need to be derived from abundant, cheap and non-toxic elements. Currently, state of the art materials are based on heavy elements such as lead [19], bismuth [20] and tellurium [21], which have high raw material costs and pose a potential health hazard, with added concern that the supply of tellurium is under serious threat of depletion within the next century. In Figure 1.1, the scarcity of natural elements is shown in a visualisation of the periodic table produced for the 2019 UNESCO international year of the periodic table of chemical elements, where more abundant elements occupy a larger area of the table. In this table, the colouring of each element indicates the threat level to its global supply, and the elements used in the manufacture of consumer electronics – like smart-phones – are also indicated. In developing new thermoelectric materials, information resources like this provide a guide for assessing the practicality of new alloys or compounds, with a view to avoiding the use of materials already in heavy demand.

The search for superior thermoelectric materials, however, is not only underpinned by economic considerations, but must also be weighed against the optimisation of physical properties. Few materials or compounds are thermoelectrics and creating a material which is a good thermoelectric is a delicate balancing act between a material's electrical and thermal conductivities. Typically, good electrical conductivity and good thermal conductivity go hand-in-hand – such is the case for most metals [22]. For thermoelectric materials, however, it is desirable to pair good electrical conductivity with poor thermal conductivity because TEGs rely on maintaining a temperature gradient to extract an electrical current [23]; therein lies the principal challenge in developing new thermoelectric materials. Manipulating the electrical conductivity is reasonably well understood and is a regular feature of semiconductor fabrication and research [24]. Tuning the thermal conductivity, however, remains a key barrier to widespread deployment of TEGs [25] as devices can thermalise far too rapidly and therefore their efficiency is compromised after a short time in operation.

In this thesis, half-Heusler alloys are investigated as candidate thermoelectric materials. Heusler alloys are a family of intermetallic compounds typically containing three different metallic elements (though may contain more). There is a great deal of variety within this family of materials, and several of them have been flagged in the research community as rather good candidates for thermoelectric materials. We pay particular attention to the alloy TiNiSn; an n-type semiconducting compound and a promising candidate thermoelectric material due to its high power factor [26]. However, it is fundamentally limited by a thermal conductivity which, for a thermoelectric material, is relatively high [27]. In other materials,

introducing complexity into the crystal structure across several length-scales has proven an effective method to engineer lower thermal conductivities in thermoelectric materials [28] and is regarded as the best foreseeable route toward highly efficient thermoelectric devices. We are interested in how such an approach applies to half-Heusler thermoelectrics, examining how complex structures manifest in Heusler alloys and the tools required to accurately characterise them. Especially when leading toward the atomic-scale, it is important to understand how precisely we can describe materials where such small features are important to material functionality. Electron microscopes are an ideal experimental platform for an exploration of the nanoscale world, so the precision of methods available within the electron microscope for nano-characterisation are examined in detail in Chapters 3 and 4, where refinements to improve the precision of existing methods are outlined. These improvements are instrumental in the primary objectives of this thesis, which centre on developing a concrete understanding of the nature of nanoscale minority phases in half-Heusler thermoelectrics, where macro-scale bulk analytical techniques cannot adequately distinguish different features or, sometimes, ever detect them. Results of nanoscale characterisation are presented in Chapters 5, 6 and 7, where aspects of compositional variation, thermal stability and structural effects are explored with a view to understanding the formation of different types of nanostructures, their practicality for use in real-world TEGs and the implications of nanostructures present for the thermal conductivity of Heusler materials.

Throughout the rest of this chapter, the theory of thermoelectric power generation is introduced (Section 1.1), followed by a brief introduction to Heusler alloys and the implication of thermoelectric theory for half-Heusler thermoelectrics, discussing how these materials can meet the technological challenge of creating an efficient TEG (Section 1.2). The scope and context of the research within this thesis is then outlined in Section 1.3, discussing how the questions above are addressed by exploring how they apply to the fabrication of TiNiSn thin films and the analysis of both thin film and bulk materials.

1.1 The physics of thermoelectrics

Thermoelectric power generation refers to a type of solid-state device which generates power via thermoelectric effects to convert heat into electricity. The nature of these devices gives them potential applications in scavenging waste heat which, as already discussed, is a significant problem in the modern world. The heat-recovering properties of thermoelectric generators (TEGs) could improve the efficiency of existing energy production, with the possibility

to retrofit TEGs to numerous systems. To understand how these devices work - and then how to improve them - we need to understand the physics of the thermoelectric effect.

There are three manifest descriptions of the thermoelectric effect, all discovered in the 19th century and named Seebeck, Peltier and Thomson, for their discoverers. Stated briefly, the Seebeck effect is the generation of an electrical potential difference within any material when subject to a temperature gradient [29]. The Peltier effect describes how heat is either absorbed or released when a current passes through a junction between two different conductors [30]. Finally, the Thomson effect outlines how passing an electrical current through a conductor subject to a temperature gradient generates reversible heating/cooling [23]. These three effects amount to different outcomes of the same properties of the material and so are naturally inter-related. When considering power generation using thermoelectric effects, the Seebeck effect is the preferred means of describing the thermoelectric properties of the material, so will be the main focus of discussion moving forward.

1.1.1 The Seebeck effect & device design

The thermoelectric Seebeck effect manifests in all conductive materials, albeit to an extent which is hugely variable. Although Seebeck himself erroneously attributed the effect to magnetism at first [31], the eponymous effect actually describes the diffusion of charge carriers in a conducting material subjected to a thermal gradient. If we consider a conductor in one dimension with a temperature difference across its length – as illustrated in Figure 1.2 – the variance in thermal energy across the material leads to the net propagation of charge carriers towards the 'cold' end. This thermal current, and the resulting charge imbalance between the two ends, creates a potential difference, within the material. The Seebeck coefficient (sometimes referred to as the thermopower), which represents the magnitude of the thermoelectric effect in a given material, is most simply described as

$$S = \frac{dE}{dT}, \tag{1.1}$$

where dE denotes the difference in potential and dT the difference in temperature [23].

Several attempts have been made to describe the thermopower in terms of underlying material properties. Starting with the framework of Drude theory, the Peltier effect is described

in terms of thermal ($\mathbf{j}^q$) and charge ($\mathbf{j}$) current densities

$$\mathbf{j}^q = \Pi\, \mathbf{j}\ , \tag{1.2}$$

where Π is the Peltier coefficient, which is directly related to the thermopower by the Kelvin relationship between the Seebeck and Peltier effects, $S = \Pi/T$ [32]. This leads to a description of the thermopower in terms

$$S = \frac{-c_v}{3e} = \frac{k_b}{2e} \tag{1.3}$$

where c_v is the electronic heat capacity and e the electronic charge. This description, however, neglects to account for even the most basic differences in materials, including Fermi-Dirac statistics, and is found to be in error by a factor of 100 [33]. The description of the thermopower is improved somewhat by the assumptions made in the Sommerfeld free-electron model as material-specific information is incorporated into the description of the specific heat [24]. However, the most reasonable description of electronic contributions to the thermopower is found using the nearly-free electron model, such that

$$S = \frac{8\pi^2 k_b^2}{3eh^2}\, m^* T \left(\frac{\pi}{3n}\right)^{\frac{2}{3}}\ , \tag{1.4}$$

where m^* is the effective mass of the charge carriers, n is the charge carrier density; and other symbols have their usual meanings [34]. Note that this description of S omits the additional terms which arise from energy-dependent scattering effects, however this is also described by Cutler *et al.* [34]. From this expression, some of the desired features of a thermoelectric material can be inferred. First, the dependence on the effective mass (m^*) of the charge carriers indicates that a single type of charge carrier is preferable and a mix of p-type and n-type car-

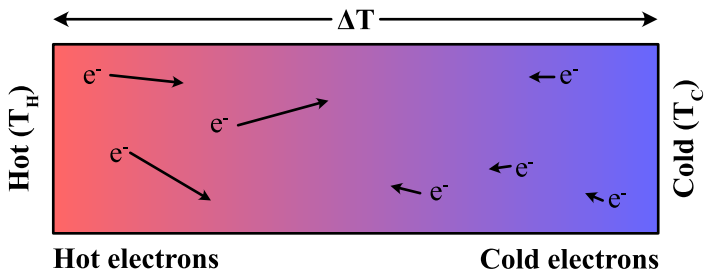

Figure 1.2: Illustration of the Seebeck thermoelectric effect in a conductive material whose faces are exposed to different temperatures. The difference in mobilities between the hot and cold electrons (or other charge carriers) results in a net drift current toward the cold side of the material.

riers effectively cancels the Seebeck voltage. Thus, semiconductors are generally preferred over metals in order to improve the thermopower. Similarly, low charge carrier concentrations (n) maximise S, pointing to low n insulators and semiconductors as ideal thermoelectric materials.

Although the dependent properties in Equation 1.4 can be easily selected to maximise the thermopower, there is a competition between optimal thermopower and the other material properties which are important to creating an effective power generator. Increasing the effective mass, while boosting the thermopower, is part of a trade-off between effective mass – defined by the second derivative of the density of states at the Fermi energy $m^* = \hbar^2 \left(d^2E/dk^2\right)^{-1}$ [24] – and the electrical conductivity of the material. The electrical conductivity is generally lower for charge carriers with large m^*, due to a reciprocal relationship with charge mobility [33]. If the electrical conductivity is low, this will limit the current which can be extracted using a thermoelectric power generator. Likewise, minimising the carrier concentration also negatively impacts the electrical conductivity [35]. Optimising the properties of a thermoelectric device therefore requires balancing of these competing properties to deliver as much electrical power as possible during operation.

The conventional device design of thermoelectric generators is intended to make use of materials that fulfil the electrical properties which give the optimal thermopower and conductivity. The premise of TEGs is based upon extracting power from a thermocouple junction, as illustrated in Figure 1.3(a). For a reasonable thermopower, as well as electrical conductiv-

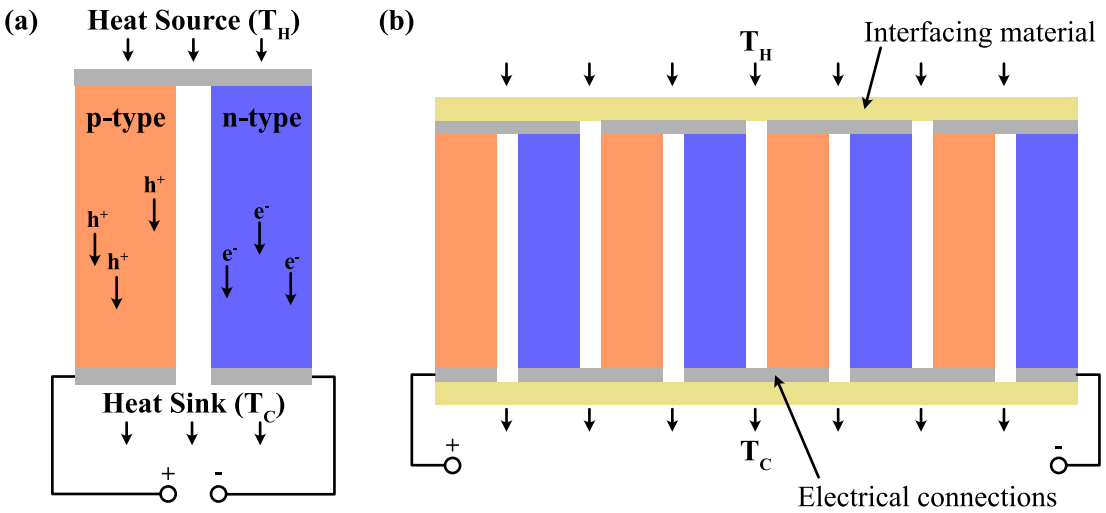

Figure 1.3: Schematic of (a) a single thermocouple junction versus (b) a thermoelectric power generator module. The thermoelectric module maximises the power extracted from the temperature difference by connecting many thermocouples together in series.

ity, semiconductors and semi-metals may possess carrier effective masses and concentrations which work well in devices [35, 36]. Materials which have a single majority charge carrier are preferred, as mixed charge carriers will both drift in the same direction and eliminate the desired potential difference. In the thermocouple, electrical connections which draw the thermoelectric current are placed on the cold side of the device, so the junction contains both *p*-type and *n*-type material to allow a continuous current to flow [23]. The *p* and *n*-type materials are connected at the hot side of the device as indicated in Fig.1.3(a). As heat transfers through the device, the cold side must act not only as the electrical contacts, but also as a heat sink to draw away heat and maintain the temperature difference between the two ends of the thermocouple. A single thermocouple junction like the one shown in Fig.1.3(a) generates a very small amount of power. To increase the power generated by a single thermoelectric generator, many thermocouple junctions are daisy-chained together in series. Connecting many junctions in series to build a module as shown in Fig.1.3(b) increases the voltage which can be extracted from the generator. Connecting the thermoelectric components in a TEG is achieved through interfacing the thermoelectric material with metallic contact electrodes. The choice of electrode material is also an important consideration when it comes to device construction, as the wrong choice of material can have a detrimental effect on the thermoelectric efficiency, either through introducing electrical resistance at the contact point or via a deleterious reaction with the thermoelectric material [37].

1.1.2 The figure of merit & thermoelectric efficiency

As alluded to in the prior section, the thermopower is not the sole factor in determining a good thermoelectric material. In addition to trade-offs between thermopower and electrical conductivity, the thermal conductivity of the material is also a significant factor in determining the efficacy of a given material in a thermoelectric generator. The combination of all these effects is described mathematically by the thermoelectric figure of merit, zT;

$$zT = \frac{\sigma S^2 T}{\kappa}\,, \tag{1.5}$$

where σ is the electrical conductivity, κ is the thermal conductivity and, as before, S is the thermopower [23]. The zT of a thermoelectric material is often used to loosely refer to its efficiency, with $zT = 1$ indicating a conversion efficiency of ~5-10 % [36]. In general terms, a thermoelectric generator is a heat engine where electrical energy (the work) is extracted

from the heat transferring between a hot and a cold body. Thus, the efficiency, η, of a TEG has a maximum theoretical limit dictated by the second law of thermodynamics. The optimal efficiency of a TEG, then, is defined by Carnot's theorem, such that

$$\eta_C = \frac{T_H - T_C}{T_H} \,, \tag{1.6}$$

where T_H and T_C are the hot side and cold side temperatures, respectively. The Carnot efficiency η_C represents the best attainable efficiency such that the efficiency of a real engine $\eta \leq \eta_C$ [38]. In the case of a thermoelectric generator, the efficiency of a real engine, η, is given by including a modifier of the Carnot efficiency

$$\eta = \frac{T_H - T_C}{T_H} \, \frac{\sqrt{1+zT}-1}{\sqrt{1+zT}+(T_C/T_H)} \,, \tag{1.7}$$

where the first part of the equation is merely Equation 1.6, and zT is the figure of merit for the temperature which is the mean value of T_C and T_H [39]. In this model for the conversion efficiency, a TEG approaches the Carnot efficiency as $zT \to \infty$. A conversion efficiency of ~10-20 % would place thermoelectric generators in parity with industrial solar cells [40, 41] and broaden the commercial viability of thermoelectrics. A more detailed examination of the relation between zT and conversion efficiency is illustrated in Figure 1.4. As mentioned above, a zT of 1 translates to efficiencies of about 5-10 % for many TEG use cases, as can be seen in the 400-600 K range in the figure. The majority of reported thermoelectric materials possess a zT which is smaller than 1 [35, 39, 42, 43]. Due to the challenge in finding materials which have $zT \geq 1$, this value has become a benchmark for thermoelectric performance within the research community.

'High-zT' thermoelectric materials – those with $zT > 1$ – do exist and include those used in current generation thermoelectric devices. Contemporary, commercial thermoelectric generators are primarily manufactured using materials based on the chalcogenides lead telluride and bismuth telluride [44, 45]. While these materials readily have peak zT values as large as ~2 [28], the use of expensive, scarce and toxic component elements restricts the commercial relevance of TEGs constructed with these materials. The realisation of efficient substitutes for these materials, which are cheaper to produce and have a lower environmental impact can be achieved by sophisticated engineering of lower-zT materials to optimise the competing properties which contribute to zT. Most of the modern approaches in research to improve thermoelectric properties involve manipulation of materials, typically via doping, in a way

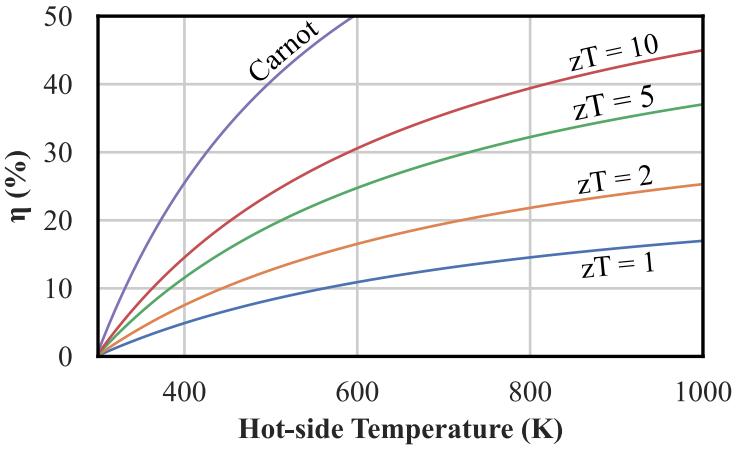

Figure 1.4: Illustration of relationship between conversion efficiency (η) and thermoelectric figure of merit (zT), as a function of the hot-side temperature (T_H). The cold-side temperature (T_C) is treated as room temperature (298 K) in these calculations. The top-most curve represents the Carnot limit.

that results in formation of nanoscale features [28, 39, 46]. Such engineering of materials to introduce complex nanoscale features has a track record of producing new high-zT materials, exploiting small-scale confinement effects which can reduce thermal conductivity through increased phonon scattering, leading to dramatic increases in a materials thermopower [47–49]. Although engineering of the electrical properties like this is successful for some thermoelectric materials, the figure of merit of other materials is instead limited by a high thermal conductivity, which introduces difficulty in preserving the temperature difference across a TEG required to extract electrical current. Modification of nanoscale structural properties can beneficially reduce the thermal conductivity [25], which is discussed next.

1.1.3 Manipulating the thermal conductivity

Creating thermoelectric materials with a high figure of merit (zT) is a balancing act that requires careful consideration of both the materials electrical and thermal properties. While it is desirable to maximise the electrical contributions to zT in Equation 1.5 ($S^2\sigma$), the thermal conductivity (κ) should be minimised. As good electrical conductivity and good thermal conductivity commonly go hand-in-hand, the desirable qualities of an efficient thermoelectric material represent a competition of material properties that must be overcome. Due to these competing properties, the ideal thermoelectric material is often described as a 'phonon-glass, electron crystal' (PGEC) [50]. Essentially, this concept means a material should allow for reasonable, coherent propagation of electrons, but conduct heat by low-energy phonons which get scattered incoherently. Actual glasses (amorphous solids) may possess the lowest

thermal conductivities of solid materials, but unfortunately typically make poor electrical conductors and hence poor thermoelectrics [51]. Material designs which decouple the thermal and electrical conductivities are therefore critical in realising better thermoelectric materials.

The thermal conductivity of any material is a combination of contributions from heat carried by charge carriers and heat carried by lattice vibrations (phonons), i.e. $\kappa = \kappa_{el} + \kappa_{lat}$. The electrical contributions, κ_{el}, are described by the Wiedemann-Franz law ($\kappa_{el} \propto \sigma T$) [33] and are impossible to completely avoid without completely eliminating charge carriers. As the electronic thermal conductivity scales directly with the electrical conductivity, this is yet another reason to prefer semiconductors before metals as thermoelectric materials. Instead, efforts to improve the thermal properties of a thermoelectric have focussed on the lattice thermal conductivity (κ_{lat}), which describes the contributions to heat conduction by phonons. In real crystalline materials, mean-free-paths for phonon interactions are hugely varied, spanning length-scales which range from the atomic scale up to several microns. This wide variety is connected to the frequency dependence of the phonon relaxation time ($\tau \sim \omega^{-2}$) which results in low-frequency phonons propagating much further than high-frequency phonons, by several orders of magnitude [52]. Due to this widely-varying behaviour, treatment of heat transport by phonons is far from trivial and solutions must disrupt phonon propagation at several lengthscales.

Common strategies to reduce the lattice thermal conductivity of thermoelectric materials rely on introducing imperfections and impurities which increase scattering rates across the whole phonon population. It is well established that phonons of different frequencies scatter from different kinds of features within a material. Higher-frequency phonons, for instance, scatter more significantly from very small, atomic-scale features such as point defects [53]. Grain boundaries scatter phonons independently of frequency [54]. However among interactions with crystal defects, grain boundaries provide the highest rate of phonon scattering at low phonon frequencies [55]. In semiconductors, this has been linked to grain size, demonstrating a significant reduction in thermal conductivity by reducing grain size from sub-mm to sub-micron scales [56]. The connection between grain boundary scattering and grain size suggests that the key factor here is the density of grain boundaries present, suggesting that smaller grains of order 10-100 nm would provide even greater benefit in such materials. Crystal dislocations have been shown to interact with phonons via the strain field which surrounds them, shifting acoustic phonon modes toward lower frequencies [57]. In the absence of other effects, this reduces the velocities of these phonon modes [33], reducing their significance in

thermal transport.

One of the main routes to creating imperfections in thermoelectric materials to provide phonon scattering is via modulation doping. Unlike conventional semiconductor doping, where the dopant atoms are uniformly distributed throughout the material [22], modulation doping involves the aggregation of dopants to form localised pockets of a second phase which is chemically distinct from the undoped main phase, as illustrated in Figure 1.5. The impact of modulation doping on phonon properties can be modelled by a layered modulation structure; i.e. the modulation occurs along one direction only. Hess demonstrated that a layered heterostructure in GaAs semiconductors increases phonon scattering at all frequencies [58]. The increase in phonon scattering rate arises from the chemical differences in the lattice, which results in different bulk phonon modes for each layer. Further, the interfaces between layers in the heterostructure themselves further contribute to phonon scattering, as these represent boundaries in the material structure. As the modulation was not found to have any major impact on the electron mobility, or electron-phonon interactions [59], approaches based on this heterostructure modulation are quite promising for thermoelectric applications.

Modulation doping as an approach to nanostructuring has been demonstrated to provide substantial benefits for thermoelectric materials. The conferred improvements are observed both in the thermal conductivity and also the figure of merit, zT [60–62]. Unlike the heterostructure modulation described above, where the formation of doped layers is deliberately and finely controlled, modulation doping in fabrication of thermoelectrics is not typically ordered, but rather occurs through the spontaneous formation of 'pockets' of a second phase, usually driven by thermodynamic processes. This more disordered modulation doping can

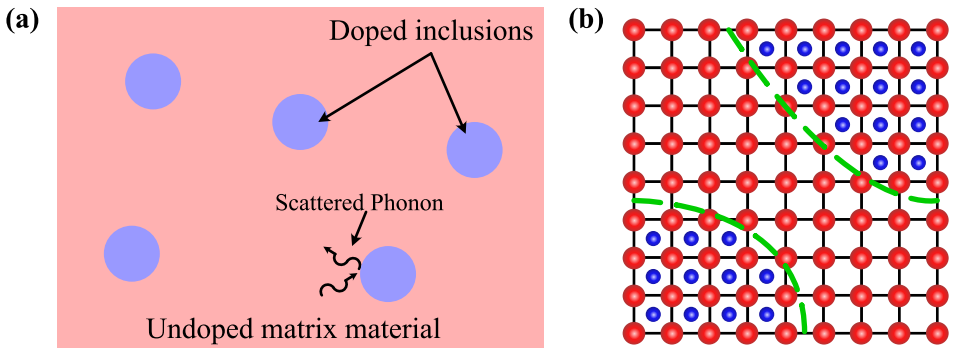

Figure 1.5: (a) Cartoon of modulation doping in a thermoelectric material, where doping only alters the composition of discrete portions of material, introducing disorder which scatters phonons. (b) Atomic-scale representation of localised chemical differences introduced by modulation doping. Adapted from [39] with permission.

result in features which cover the full range of lengthscales – sub-nanometre to microns – which are of interest in phonon interactions [28]. The challenge in designing high-zT thermoelectrics in this approach is finding combinations of chemical phases which are insoluble and so can sustain a modulated structure. One route is to intentionally grow thin films which are chemically modulated in a repeat pattern: a superlattice. There are several reported successes of improving the zT of thermoelectric materials in the superlattice approach [63–65], however layered approaches are challenging to scale to bulk quantities in an affordable manner. One set of materials where modulation doping is of special relevance are Heusler alloys. These materials, which are the subject of study in this thesis, can support incredibly complex microstructures which provide substantial boosts to their thermoelectric figure of merit [66–68]. Heusler alloys and their importance in advances in thermoelectric power generation are discussed in detail in the next section.

1.2 Half-Heusler alloys as thermoelectric materials

Heusler alloys are a family of intermetallic compounds which typically contain three metallic elements. They are a remarkably versatile set of materials which are of interest in research for a plethora of functionalities, promising for a broad range of prospective applications. Originally, Heusler alloys attracted interest for exhibiting ferromagnetism despite containing no magnetic elements [69]. Since this discovery more than a thousand members belonging to the Heusler family have been created, using elements from nearly half of the periodic table [70]. Amongst these Heusler materials, many possess useful properties such as antiferromagnetism [71, 72], half-metallicity [73, 74], superconductivity [75, 76], topological insulation [77, 78], shape memory [79, 80] and – pertinently – thermoelectricity [81–83]. These properties give scope for a range of functional applications of Heusler alloys, especially in spintronics and energy conversion. The promise of Heusler alloys for thermoelectric power generation in particular represents significant economic merit in addition to their scientific relevance. With a wide range of elements to choose from in their construction, Heuslers can be designed with plentiful, affordable components in mind; some of the more promising thermoelectric Heuslers represent a tenfold reduction of component costs compared with contemporary chalcogenide-based materials [45]. It is for this combination of economic benefit and scientific versatility that Heusler alloys occupy a prime position in thermoelectrics research.

1.2.1 Structure and properties of Heusler alloys

The first Heusler alloys to be discovered have the general chemical formula XY_2Z, where X and Y are typically transition metal elements – with X typically more electropositive than Y and Z – while Z is a metal from the main group (p-block) of the periodic table [70]. Heuslers with this XY_2Z composition are referred to throughout as full-Heusler (fH). This differentiates them from Heusler alloys which have half the quantity of element Y, i.e. with chemical formula XYZ, which are called half-Heusler (hH). Full-Heusler compounds crystallise into a cubic structure with space-group $Fm\bar{3}m$ and this is illustrated in Figure 1.6(a). This unit cell can be described as four interlocked fcc lattices; one for each of the atoms in the chemical formula. The sublattices for the X and Z atoms form an NaCl structure and these atoms have octahedral coordination, while the Y atoms sit on tetrahedral sites in between these atoms. In the half-Heusler, which has space group $F\bar{4}3m$, one of the tetrahedral Y sub-lattices are vacant, as shown in Fig.1.6(b). The introduction of vacancies on the tetrahedral sites typically leads to a contraction of the unit cell in bulk materials, such that the hH variant of a material has a marginally smaller lattice constant [84, 85]. The similarity in structure between hH and fH becomes important in enhancing thermoelectric Heuslers and is discussed later.

Although the structural differences between full- and half-Heusler are not substantive,

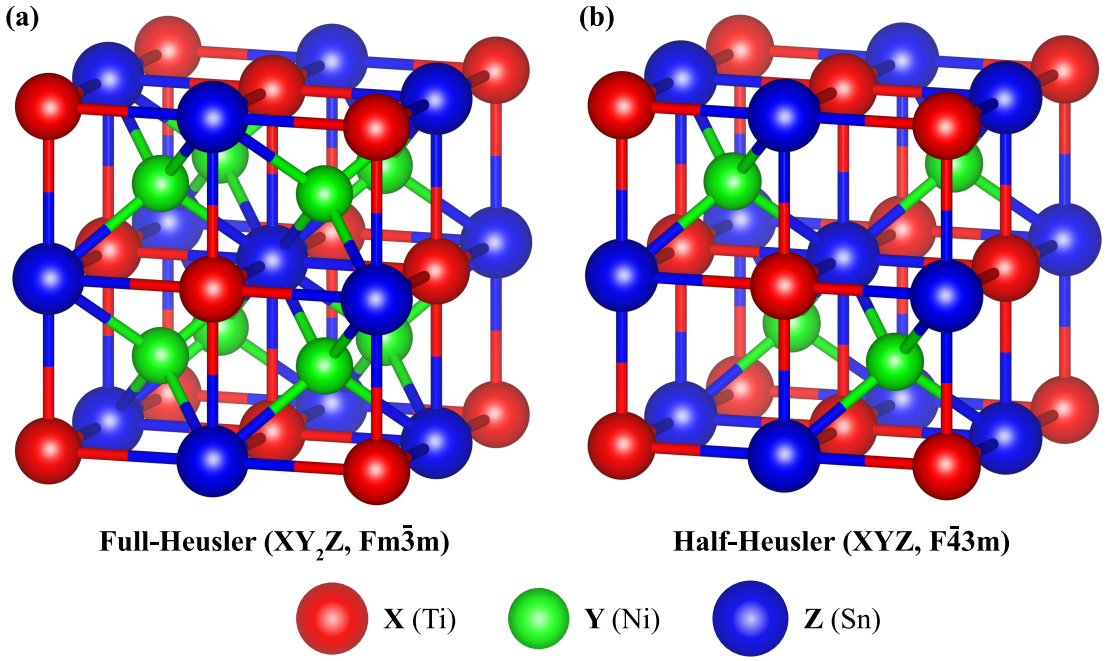

Figure 1.6: Structural models for the unit cells of (a) full-Heusler ($TiNi_2Sn$) and (b) half-Heusler alloy (TiNiSn), with space groups $Fm\bar{3}m$ and $F\bar{4}3m$, respectively. The reduction of the number of Y atoms to form the half-Heusler leaves half of the tetrahedral sites vacant.

switching from a filled to a vacant sub-lattice has a significant impact on the electrical properties of the Heuslers. As a general rule, there is a connection between the number of valence electrons per unit cell and the subsequent electrical properties of the Heusler compound [70]. The hH TiNiSn, which has 18 valence electrons, is a semiconductor material with a bandgap of ~0.5 eV, while the addition of further Ni atoms to form $TiNi_2Sn$ results in a metallic fH phase with 24 valence electrons [67, 70, 86]. TiNiSn and other 18 valence electron half-Heusler semiconductors are promising for thermoelectric applications [87]. Stoichiometric hH alloys based on *X*NiSn (*X* = Ti, Zr or Hf) typically have a thermoelectric figure of merit $zT \approx 0.5$ [88–90].

Despite the moderate baseline zT value, the 18-electron hH semiconductors have electrical properties which are very promising for thermoelectrics, with power factors ($S^2\sigma$) much greater than other candidate thermoelectrics [91, 92]. The reason that this is not reflected in the thermoelectric figure of merit lies with the thermal conductivity of the hH alloys. Compared to other thermoelectric candidate materials, the thermal conductivity of the half-Heuslers is relatively high, with typical room-temperature values around ~8 $Wm^{-1}K^{-1}$ [27]. There is significant potential to reduce the thermal conductivity of these alloys, and calculations which interpret the ideal thermal conductivity as that of an amorphous glass identify the minimum achievable thermal conductivity (κ_{min}) as approximately 0.8 $Wm^{-1}K^{-1}$ for TiNiSn [93, 94]. This indicates that there is scope to enhance the figure of merit substantially to yield $zT > 2$ via improvements in thermal conductivity. Pathways to enhancing thermoelectric Heusler alloys are discussed below.

1.2.2 Advances in thermoelectric Heusler alloys

The 'baseline' zT of ~0.5 for the half-Heusler alloys – that which is typical of single-phase specimens – is limited by the high thermal conductivity. Consequently, efforts to improve the zT of thermoelectric hH alloys have been devoted to reducing the thermal conductivity to better take advantage of the large power factor they possess. In the literature surrounding enhancement of thermoelectric hH alloys, two key approaches have been identified. The first addresses the nature of as-formed half-Heuslers, which typically form large (> 10 μm) grains [95]. As discussed earlier, grain size reduction in semiconductors is a potent approach to reducing the thermal conductivity, increasing the phonon-boundary scattering rate [56]. Beyond crystallisation in the initial melt, synthesis protocols for hH alloys can be expanded to

include further steps beyond initial synthesis, mainly by mechanical milling. These processes have been effectively used to reduce grain sizes to the order of 100s of nanometres [95]. This practically halves the thermal conductivity to ~3-4 $Wm^{-1}K^{-1}$ and forms a key component in the strategy to boost the *zT* of these materials beyond 1 [67, 96].

The flexibility of the Heusler alloys to incorporate a large variety of elements into their structure comes into the spotlight for the next route to enhancing their thermoelectric properties. Current 'in vogue' approaches involve the incorporation of additional elements into the half-Heusler structure to modify the material properties [67, 92]. Complicating the chemical make-up of the Heusler in this way can introduce manifold effects and the exact impact on the material properties is dependent on how these additions manifest in the microstructure. At a basic level, considering only the uniform distribution of the dopant, the inclusion of additional elements which provide similar electrical properties, but which have different atomic masses can be used to increase the mass-contrast within the material. In essence, this has the effect of 'flattening' the modes of the phonon dispersion, reducing the phonon phase velocities and, consequently, lowers the lattice thermal conductivity [25, 97, 98]. In practice, doping of the basic half-Heusler material can achieve a complex microstructure with benefits that can be far greater than those introduced by only increasing the mass contrast.

The success of advances in thermoelectric Heusler alloys lies almost single-handedly with the influence of chemical complexity on the material microstructure. The chemical phase space for Heusler compounds, which involves at least 3 elements, contains many secondary chemical phases in addition to the desired half-Heusler phase [99, 100]. This complexity, which increases dramatically with each further unique element, makes the fabrication of homogeneous hH materials difficult to the point of impossibility. Instead, competing atomic-scale energetics during crystal formation drive segregation of elements to form distinct regions of different chemical phases [101, 102]. This 'phase segregation' is an important source of disorder in hH alloys and the more successful enhancements of *zT* in these materials – irrespective of whether specimens contain only 3 elements, or as many as 6 – all possess these microstructural features [66, 84, 86, 103, 104]. Phase segregation can manifest in a variety of manners, across several lengthscales and some examples of the observed features are presented in Figure 1.7. The basic example of phase segregation is presented in Fig.1.7(a), which is an optical microscope image of a polished, nickel-rich TiNiSn specimen [86]. The excess Ni here is not uniformly distributed, but instead aggregates to form grains which are fH $TiNi_2Sn$ within a hH TiNiSn matrix. A similar phase segregation effect is seen in Fig.1.7(b)

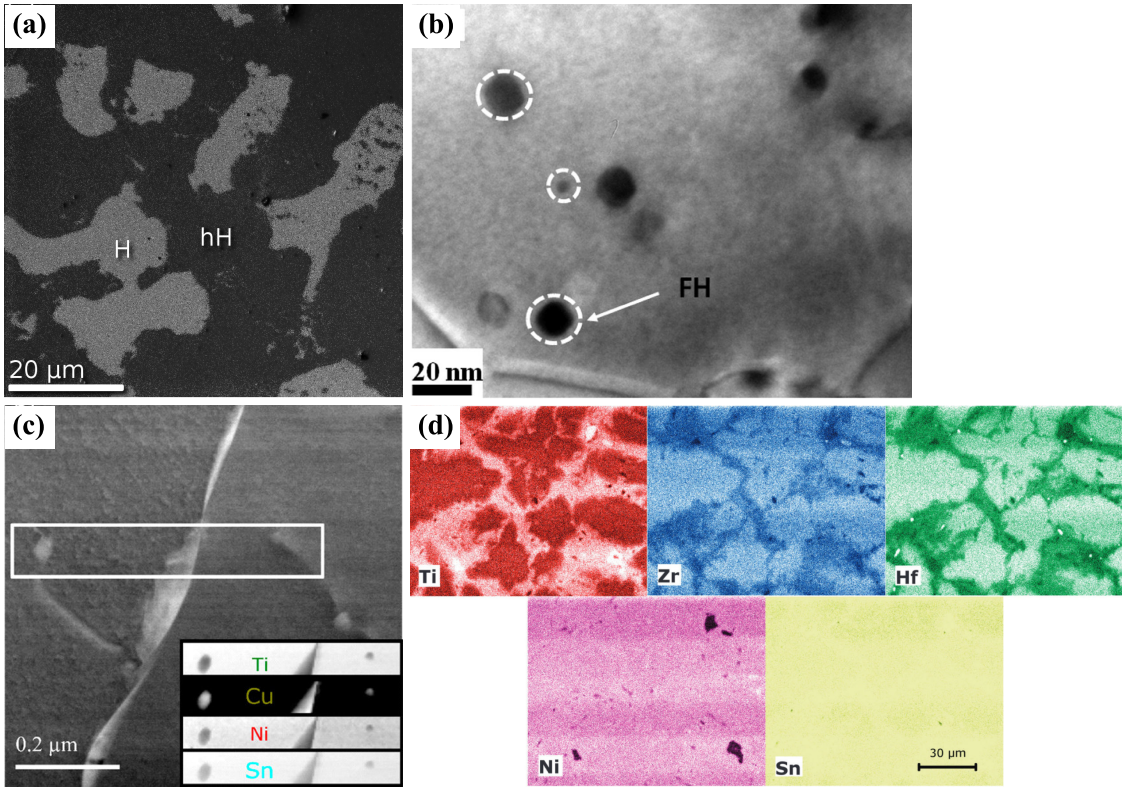

Figure 1.7: Images of examples of features which are a result of phase segregation in thermoelectric half-Heuslers. (a) Optical micrograph of a Ni-rich TiNiSn specimen. The excess Ni is segregates to form grains of a $TiNi_2Sn$ second phase. Reproduced with permission from [86]. (b) TEM image of nanoscale spherical fH inclusions with diameters of order 10 nm (circled) in half-Heusler $Zr_{0.25}Hf_{0.75}Ni_{1.4}Sn$. Reproduced with permission from [105]. (c) STEM dark field image & inset elemental maps at a grain boundary in a $TiNiCu_{0.25}Sn$ specimen. Reproduced from [104] under CC-BY license. (d) SEM-EDS elemental maps of a $Ti_{0.5}Zr_{0.25}Hf_{0.25}NiSn$ specimen segregated into different hH phases. Reproduced from [103] with permission of the PCCP owners societies.

for a $Zr_{0.25}Hf_{0.75}Ni_{1.4}Sn$ specimen, however the lengthscales involved are ~1000 times smaller [105]. In both cases, the effect of phase segregation can be understood in terms of the modulation doping framework discussed earlier, where different phases form as a result of incongruent melting and solidification at different temperatures [106]. The disorder which phase segregation introduces to the material creates atomic mass variations, nanoscale impurities and grain boundaries which act to increase scattering of phonons and reduce the lattice thermal conductivity.

The phase segregation effects observed in Figure 1.5(c-d) are of a different nature to the hH/fH segregation discussed above. Instead of straightforward hH/fH segregation, Fig.1.7(c) shows a grain boundary in a copper-doped $TiNiCu_{0.25}Sn$ specimen [104]. The effects of phase segregation in this instance are more subtle. Further to a subtle variation in the Ni concentration between grains which is challenging to discern from the figure, the copper

doping was observed to precipitate from the Heusler and form metallic Cu wetting layers at grain boundaries as well as a small number of metallic Cu nanoinclusions. In this case, the inclusion of a metallic dopant, while still increasing the disorder in the material to increase phonon scattering, also improves the electrical properties (conductivity and thermopower) of the Heusler [104]. This suggests that the wetting layers act to scatter phonons by alloy disorder, but promotes electrical conductivity between grains. Finally, a $Ti_{0.5}Zr_{0.25}Hf_{0.25}NiSn$ specimen shown in X-ray spectroscopy (EDS) elemental maps in Fig.1.7(d) segregates into grains of various hH phases [103]. These hH phases are differentiated by the *X*-site element (Ti, Zr, Hf). The alloy disorder introduced by segregation into different hH phases was shown to markedly reduce the lattice thermal conductivity. Additional doping of this material with small amounts of antimony to make an alloy containing 6 elements serves to enhance this reduction of κ_{lat} further to below 1 $Wm^{-1}K^{-1}$ at high temperatures [103]. In these many-element Heusler alloys, phase segregation like that observed in Fig.1.7(d) is found to be a natural consequence of the thermodynamic competition, which creates a 'miscibility gap' where homogenisation of the chemical content is energetically unfavourable compared to the formation of separate hH phases comprised of a subset of the available elements [102, 107]. This style of phase segregation is clearly a very promising route to introducing disorder in these materials, however the size of crystal grains is still relatively large (>10 μm) in these examples. Thermoelectric properties could potentially be enhanced further if the same chemical disorder could be reproduced on shorter lengthscales.

While the introduction of phase segregation in hH thermoelectrics was intended to influence the thermal properties of the material, benefits for the electrical properties have also been found. In the case where phase separation involves the introduction of a minority fH phase into the hH matrix, the presence of the fH inclusions can be modelled as a heterojunction, as illustrated in Figure 1.8(a). In the heterojunction, the difference in conductive properties of the full and half-Heusler – which have metallic and semiconducting properties, respectively – leads to a difference in conduction band energy in which the nanoscale fH phase provides an energy barrier to the transmission of charge carriers [105]. This barrier, which is smaller than the bandgap of the hH phase, is posited to 'filter' the charge carriers by energy. In this model, cold electrons which are closer to the conduction band minimum for the hH, have insufficient energy to pass the fH barrier and so are not permitted through the inclusion. Meanwhile, hot electrons are energetic enough that the inclusion has no effect, so continue to propagate as normal. In the context of thermoelectric devices, this can be interpreted as enhancing the current induced by a temperature gradient, as the filtering prevents cold the electrons from

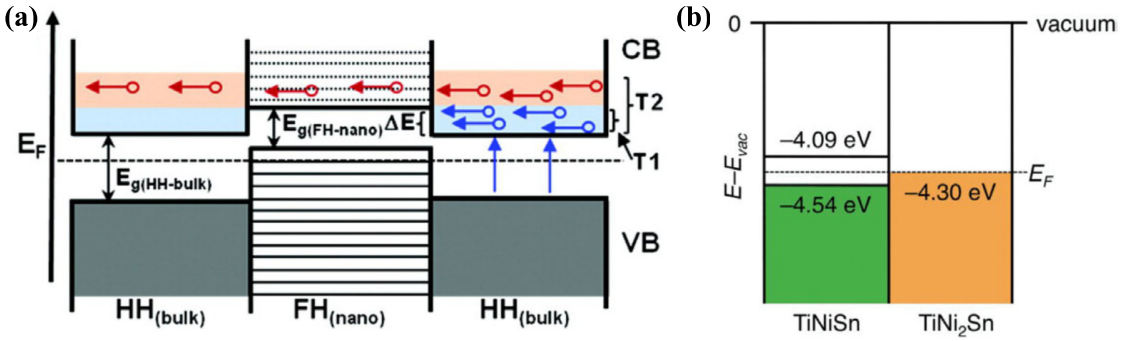

Figure 1.8: (a) Schematic band diagram of a hH/fH/hH heterojunction which illustrates the charge carrier energy filtering mechanism. Reproduced with permission from [105]. (b) Band diagram showing the energies of hH TiNiSn and fH $TiNi_2Sn$. Reproduced with permission from [86].

propagating from the cold side to the hot side.

In Fig.1.8(b), the relevant band energies for the thermoelectric hH TiNiSn and fH $TiNi_2Sn$ are illustrated, demonstrating that the Fermi energy of the metallic fH phase lies in the bandgap of the hH phase. In these materials, Douglas *et al.* propose that the improvements in electrical conductivity brought by phase separation arise not from carrier filtering, but from less energetic promotion of charge carriers from the Fermi energy of the fH to the conduction band of the hH, which involves an energy gap of 0.21 eV instead of 0.45 eV [86]. The presence of small quantities of fH therefore acts as a source of additional charge carriers, enhancing the electrical conductivity without compromising the semiconducting behaviour of the hH matrix. At present, this explanation for the enhancement of the electrical properties of Heuslers by phase segregation has greater plausibility than the energy-filtering heterojunction hypothesis. The energy-filtering properties of the heterojunction model are dependent upon the presence of a bandgap in the unoccupied density of states of the fH phase. While the small scale quantum confinement effect of the nanoinclusion could create this bandgap [49], it is not typically present in the bulk fH density of states [108]. Bandstructure calculations or experimental measurements of nanoinclusions which would be needed to confirm this hypothesis have not been found in the broader literature.

Phase segregation approaches to fabrication of thermoelectric half-Heuslers are evidently a highly successful route to enhancing both the thermal conductivity and power factor of these materials. However there is still room for further improvement. While there are some reports of nanoscale phase-segregation features [105, 109], there is a lack of reliable reproduction of such features, with phase segregation more common on lengthscales of 10's of microns,

as with the examples in Figure 1.7. One focus of ongoing research therefore concerns how to reduce feature sizes, or produce a large range of feature sizes, without compromising the phase segregation and its benefits.

1.3 Scope of research in this thesis

Throughout this thesis, the half-Heusler TiNiSn – which forms the basis for some of the most promising n-type Heusler thermoelectrics – is studied. To investigate nanostructuring in these materials, pulsed laser deposition is used to explore thin film growth of nickel-rich TiNiSn. Thin film growth provides a route to intentional engineering of nanostructures, such as nanoinclusions or superlattices, which are difficult to deliberately synthesise in bulk materials. The overarching aim is that the lessons learned from thin films and the understanding gained from interpreting how different types of features form can be fed back into the synthesis of bulk materials to produce better Heusler thermoelectrics. To achieve this, the transmission electron microscope (TEM) is the instrument of choice for characterising the thin films in this thesis, providing sub-Ångström resolution in addition to structural and chemical analytical capabilities as described in the methods (Chapter 2).

Chemical characterisation in the TEM forms the core foundation for nanoscale analysis of materials in this thesis. Building on the ability to get nanometre-resolution chemical information in the TEM using electron energy-loss spectroscopy (EELS), Chapter 3 describe the results of improvements which have been made in characterisation of the EELS spectrometer to yield better spectral energy calibrations. These developments are important for reliable energy measurements of features in the spectra and are instrumental in the progress made in producing a reliable protocol for absolute quantification of elemental concentrations, which is detailed in Chapter 4. Absolute, rather than relative, quantification allows for greater precision of results and pushes the lower threshold for detecting elemental quantities, enabling more robust interpretation of results which is critical for understanding the nature of nanometre-sized features.

The advancements made in measurement and processing of analytical data feed prominently into the rest of the thesis, starting with the growth and characterisation of TiNiSn thin films in Chapter 5. In this chapter, chemical analysis revealed that pulsed laser deposition translates the chemical microstructure of the bulk material into spontaneously formed nano-

structures in the thin films and provides insight into what nanoinclusions the Heusler can support. Chemical investigations of nanoscale phase segregation are continued in Chapter 6, where the thermal evolution of the nanostructured thin films was investigated. This chapter describes how *in situ* heating in the TEM facilitated rapid chemical analysis of thin films subjected to high temperature heat treatments and explores the thermal stability of nanostructured phases. Developing a deeper understanding of the phase stability of segregated Heusler alloys is important to their application in thermoelectric generators, where the materials will be exposed to high temperatures over long durations. Finally, in Chapter 7, a correlative approach to transmission electron microscopy is used, taking advantage of new detetector technologies, to combine the chemical analysis which has formed the bedrock of the rest of the thesis and combine this with 4-dimensional Scanning-TEM (4dSTEM) to explore nanoscale structural properties of materials. The relevance of correlative chemical and structural analysis to nanostructured Heusler thermoelectrics is perceived to lie in gaining greater understanding of nanostructures which support structural coherency, which is important in preserving the electrical properties of thermoelectrics while increasing phonon scattering. Prospects for how the work in this thesis can be continued and progressed further are outlined in Chapter 8.

Collectively, the work throughout this thesis seeks to address difficulties which arise in accurate characterisation of minority phases in thermoelectric materials using bulk analytical techniques, where minor contributions to spectra or diffraction patterns either vanish completely, or combine incoherently to form a continuum of possible states with no exact analytical solution. Through the use of transmission electron microscopy, the importance of using analytical tools which are suitable for the lengthscales involved is demonstrated and, where necessary, refinements were developed to improve the precision of data analysis protocols. The high-precision chemical analysis and nanoscale spatial resolution afforded by the TEM enabled accurate identification of minor nano-segregated phases; information which can be used to better inform the material synthesis process and potentially reveal pathways to superior thermoelectric materials. Results presented in the chapters that follow already highlight a number of unexpected minor phases, some of which cannot be observed using bulk structural analysis. Observations also raise intriguing questions over the perceived solubility limits of Ni in the Heusler structure, as well as an incommensurate relationship between off-stoichiometric Heusler compositions and corresponding lattice variations. The work here should be of broader relevance to nanostructured thermoelectrics, and some developments in techniques will be of interest for the wider electron microscopy community.

I put this out as a challenge: Is there no way to make the electron microscope more powerful?

Richard Feynman

2

Methods & Instrumentation

When Richard Feynman raised the question quoted above in his famous "Plenty of room at the bottom" lecture in 1959 [110], the transmission electron microscope (TEM) was still a fledgling technology. Today, TEMs are incredible instruments not only for high-resolution imaging of specimens, but also for providing a wealth of analytical and quantitative information through the incorporation of spectrometers and developments in electron optics and detectors. The investigations presented in this thesis have - at their core - the use of the TEM as a laboratory through which the thermoelectric materials we wish to understand may be examined right down to the atomic scale. In studies carried out at this level, precision is paramount to developing an accurate description of the material properties. Much of the work featured in later chapters builds upon the use of the TEM as an analytical tool to improve the precision and quality of results.

The TEM exploits the high spatial resolution afforded by using electrons for illumination. In addition to many imaging modalities which may give image contrast relating to, for example, crystal structure or atomic number, the TEM may also be coupled with analytical spec-

trometers to further probe the material properties via electron interactions. Electron Energy-loss Spectroscopy (EELS) and Energy-dispersive X-ray Spectroscopy (EDS) use inelastic scattering from valence and core-shells within the material to yield a breadth of chemical information including elemental composition, oxidation states of elements and other bonding information [111].

The objective of the work throughout this thesis is to take advantage of the analytical electron microscope for the study of nanoscale features in thermoelectric Heusler alloys. For this, half-Heusler thin films were fabricated by Pulsed Laser Deposition to act as model systems for the bulk materials (Section 2.1). To examine specimens in the electron microscope, they then have to be prepared to yield cross-sections that are electron-transparent which, in this work, is achieved through the use of focused ion beam sectioning (Section 2.2). The core methods employing the transmission electron microscope are discussed in Section 2.3 while other analytical tools, such as atomic force microscopy and X-ray diffraction, are covered in Section 2.4.

2.1 Thin film fabrication

The role of thin films in condensed-matter physics rose to prominence in the latter half of the 20th century, with demonstrations of new physics and exotic phenomena including, for example, high-temperature superconductivity [112], giant magneto-resistance [113], quantum cascade lasers [114] and confinement phenomena such as quantum wells, quantum dots *et-cetera* [115]. In this time, interest in thin films has lain in the challenge of synthesising, analysing and exploiting materials of increasing complexity. For example, thin film deposition can allow for higher crystallographic and/or chemical purity than bulk materials, providing a route to greater understanding of microscopic processes.

Throughout this thesis, thin films studied as part of the research were fabricated by physical vapour deposition (PVD). In PVD techniques, growth occurs in a vacuum system where a solid source material is converted to a vapour phase, that is transported to a substrate then condensed again as a thin film. PVD growth methods include molecular beam epitaxy (MBE), sputter deposition (SD) and pulsed laser deposition (PLD). Of these, sputtering and pulsed laser deposition have been used for thin film growth in this work. Although MBE has a proven track record in growth of high-quality thin films, particularly those involving Si or III-V semiconductors, the technological demands of the technique have limited the breadth of

applications of MBE in materials research. Furthermore, as MBE involves thermally evaporating material under ultra-high vacuum (UHV) [116], issues arise when attempting to deposit elements with dramatically different vapour pressures. This is often the case with Heusler alloys, which can contain elements from across the periodic table, thus needing to combine varied evaporative characteristics. Thus, PLD was selected as the growth method for Heusler alloys in this work.

Pulsed laser deposition is a technique which has been utilised to produce a plethora of materials for a broad range of applications [117]. Its' capacity for growing complex materials from a single precursor gives PLD a level of flexibility which is an advantage in preparing and studying thin films of novel materials, especially for multi-elemental materials where control of the stoichiometry is important. This motivates the use of PLD for preparing Heusler alloys in this work and the details are discussed in Section 2.1.1.

One area where pulsed laser deposition falls short is in the quality of thin films of metals. This is due to deposition of large, micron-size droplets in addition to the atomic/ionic vapour flux that is desired [118]. Thus, in instances where the intended thin film was of a simple metal, sputter deposition was used in place of PLD. The use of sputter deposition is discussed in Section 2.1.3.

2.1.1 Pulsed Laser Deposition of thin films

Pulsed Laser Deposition (PLD) – sometimes referred to as *laser-MBE* or *laser ablation deposition* in early literature [119, 120] – is a highly flexible method for thin film growth, making it a valuable research tool. This flexibility comes from the ability to fabricate thin films with complex stoichiometries; a capability that put PLD in the spotlight when Dijkkamp *et al.* demonstrated PLD growth of superconducting cuprate thin films in the 1980s [112]. Since then, many hundreds of materials have been fabricated as thin films by pulsed laser deposition methods [121]. Unlike molecular-beam epitaxy (MBE), which involves thermal evaporation of source material, PLD is capable of *non-thermal* growth. The capability to grow chemically complex thin films is a direct consequence of this, as the ablation which takes place during PLD is far less element-specific than the thermal processes of MBE. This is one of the primary motivating reasons for choosing PLD as the route for fabricating half-Heusler thin films. Additionally, PLD has been found to be capable of accessing kinetic regimes to produce morphologies that are difficult or unavailable to fabricate using other techniques [122–

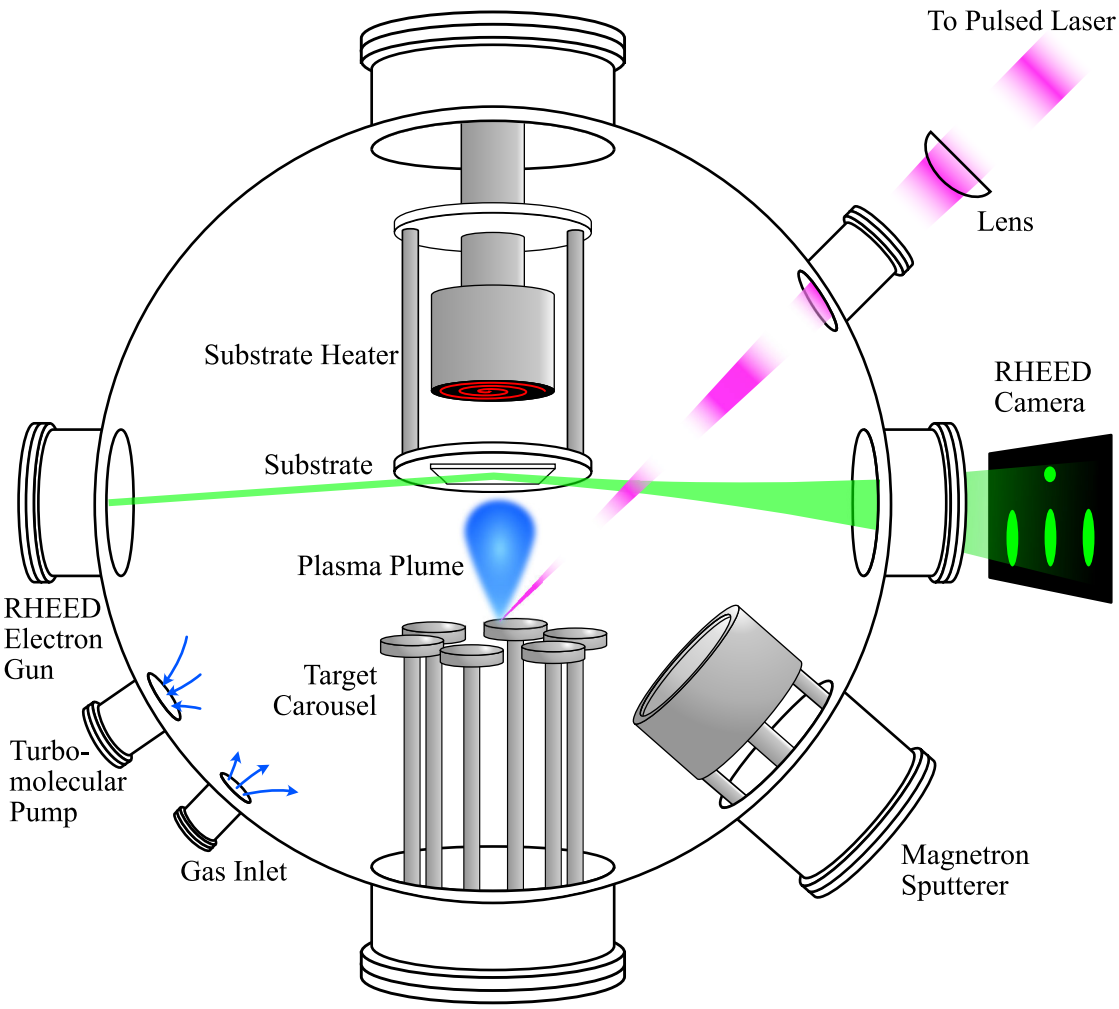

Figure 2.1: A schematic showing the interior of the pulsed laser deposition vacuum chamber. PLD targets sit on a carousel that allows them to be rastered and rotate under the focused laser. It is also possible to rotate and heat the substrate on the sample stage during depositions. RHEED apparatus in the chamber can be used to record diffraction patterns from the film surface to monitor epitaxial growth.

124]. The prospect of growth of non-equilibrium phases is also pertinent to the fabrication of Heusler alloys, which have a complicated compositional phase-space.

In operation, pulsed laser deposition involves rapidly ablating material from a bulk target by focusing a high-power laser pulse on its surface. The laser pulse typically has a duration of order 10 ns and an energy of order 100 mJ, resulting in an instantaneous power density of order 1 GW/cm^2 delivered to the surface of the target material. This high power density leads to a complex laser-matter interaction, producing several sputtering mechanisms. Photons from the pulse are either reflected or absorbed, with the absorbed photons contributing to the ablation processes. Thus, the ablating power of the laser is strongly dependent on the target material, varying with its reflectivity. The absorbed light provides enough energy to produce a range of excitations at the target surface, including surface plasmons, polaritons and free

electrons [125]. This range of excitations leads two main, vapour-producing sputtering mechanisms which are induced by the pulsed laser: *electronic* and *thermal* sputtering. In the first of these (electronic sputtering), the high energy of the laser pulse excites a significant number of electrons in the target material. In dielectrics or wide band-gap semiconductors these electrons, although excited, remain bound and relax by imparting their energy to the atoms/ions through electron-phonon interactions. Transferring energy to the lattice in this way increases the kinetic energy of the atoms by several eV, significantly increasing the vapour pressure of the material enabling a release of atoms to form a vapour plume [126]. In materials with little-to-no band-gap (i.e. metals), the relaxation time of this excitation is incredibly short, so electronic excitations have little effect on the vapour pressure. The short excitation time, however, results in highly-localised heating of material – to the point of melting – and so changes in vapour pressure are realised through thermal processes, and material can still be sputtered from the target [118, 126].

Thin film fabrication by PLD in this work was carried out in a Neocera Pioneer commercial vacuum system using a KrF excimer laser, and is illustrated in Figure 2.1. The excimer laser uses high-voltage pulses to excite a gas mixture of krypton and fluorine to form unstable KrF molecules, which release photons of wavelength 248 nm upon dissociation, thus forming the laser pulse. This process results in a pulse duration of 20 ns and each pulse typically has an energy of up to 200 mJ. Pulses can be delivered at a rate of up to 20 Hz with a driving excitation of up to 30 kV. The energy of each pulse can be adjusted, either by manipulating the potential of the excitation discharge, or by altering the size of an aperture placed on the beam-path. The fluence at the target surface, where the beam is concentrated at the focal-point of the lens, is typically 1–2 Jcm^{-2}. The vacuum of the main deposition chamber is maintained by a turbomolecular pump, which can routinely maintain a UHV pressure of 10^{-8} Torr. The adjoining loadlock and RHEED vacuum chambers are evacuated to typical pressures of 10^{-6} Torr and 10^{-9} Torr, respectively.

Pulsed laser deposition has been used for a variety of materials over the course of this work, most notably used for the fabrication of TiNiSn and $TiNi_2Sn$ thin films which are studied in Chapters 5, 6 and 7. As there are numerous factors which affect the deposition rate of PLD growth, the rate has to be calibrated for each new deposition. This has been achieved by room temperature deposition using a standard number of pulses (usually 10,000) onto a piece of silicon wafer marked with ink. An acetone bath after deposition dissolves the ink to form a trench, which allows the thickness of the deposited film to be measured via atomic force

microscopy (AFM). This is then used to assess the number of pulses required to yield the desired thickness. One of the biggest factors in limiting the deposition rate is attenuation by material deposited onto the laser window of the vacuum chamber. As this is dependent on the amount of material which has been deposited since cleaning, typical deposition rates are not included here.

2.1.2 Other sputtering mechanisms in Pulsed Laser Deposition

In addition to the generation of an atomic/ionic vapour by the laser, non-vapour material can also be ejected from the target. One of these mechanisms, hydrodynamical sputtering, is unique to pulsed laser deposition and concerns the expulsion of liquid droplets from the target. Particularly in metallic targets, it is common for the laser to induce sub-surface heating in the target that, in conjunction with the plasma formation illustrated in Figure 2.2(a), can lead to a region at the surface becoming molten, as indicated in the cartoon in Fig.2.2(b). When the target surface reaches this condition, subsequent laser pulses induce hydrodynamical sputtering in addition to the desired plasma plume. As illustrated in Fig.2.2(c), following pulses impart momentum to the surface, disturbing the molten liquid. This 'splashing' can lead to liquid material being expelled from the target (Fig.2.2(d)) which may be incident on the thin film/substrate. The aftermath of this process is illustrated in Fig.2.2(e), which shows an SEM image of hydrodynamical droplets on a TiNiSn thin film. Droplets are observed with a broad range of sizes from approximately 0.1 to 10 μm.

Droplet formation is a common issue for metallic targets due to the high absorptive power of conduction electrons in the metal. The short relaxation time of the excited conduction electrons (on the order of picoseconds) determines a slightly different sputtering mechanism than that for PLD of ceramics/polar materials [127]. Specifically, laser sputtering of metals must be facilitated by rapid and intense heating to promote thermal evaporation at the surface. Thus, the laser-induced melt which opens the path to a laser sputtering mechanism for metals is also responsible for enabling hydrodynamical sputtering and droplet formation. The number of droplets on the film is dependent on the laser fluence and the target material, but most strongly varies with the number of laser pulses the target is exposed to. Scanning the laser beam across the target surface and maximising the fluence of the laser are known to reduce the total number of droplets, though greater fluences generally produce larger droplets [118]. It has been demonstrated to be possible to prevent droplets from reaching the substrate us-

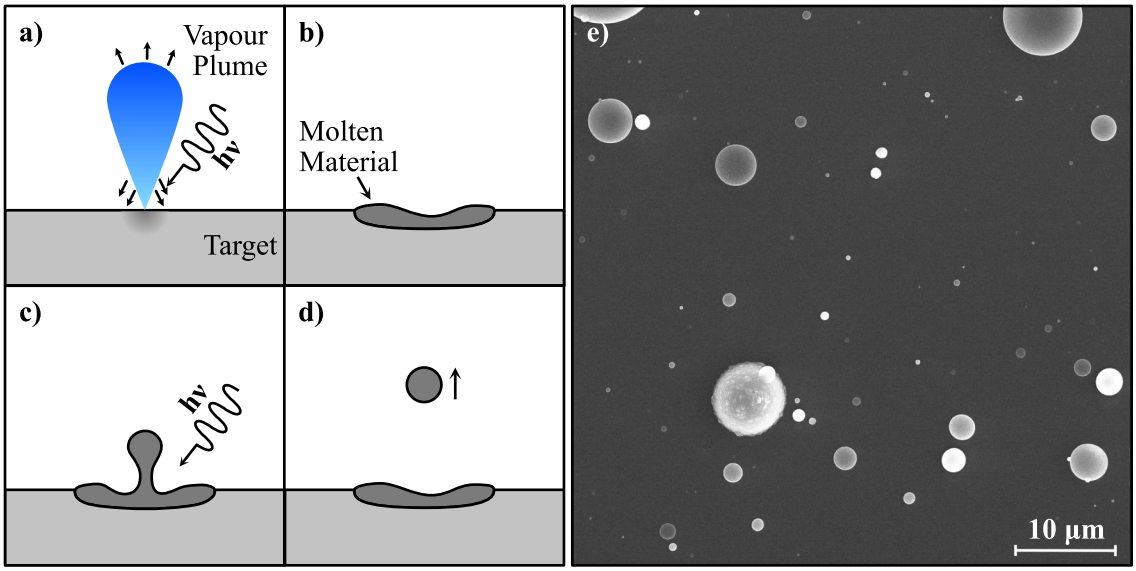

Figure 2.2: Hydrodynamical droplet formation during PLD occurs as a result of the laser inducing surface melting (b) in addition to vaporisation (a). The molten surface is splashed by subsequent pulses (c), releasing liquid material from the target surface (d). (e) An SEM image of the surface of a TiNiSn thin film shows a range of droplet sizes which have been deposited along with the thin film.

ing a mechanical filter in the path of the plume, taking advantage of the difference in time of flight of the plume and the droplets to admit the vapour and filter out the droplets [119, 128], however this technology was not available for use. Instead, to minimise the number of droplets, a maximal laser fluence was maintained in depositions and targets were rastered and rotated under the beam to distribute the exposure as greatly as possible.

Having covered the ability of the laser to produce vapours (the primary product) and liquids (hydrodynamical sputtering and droplets), another secondary effect is the fragmentation of the target under the laser to release solid particulates. This process, called *exfoliational sputtering*, arises from thermal shock induced by the laser causing stresses in the target material which can cause flaking. The propensity for exfoliational sputtering appears to be dictated by the linear thermal expansion properties of the target material, and so becomes a greater problem with high-melting-point materials [129].

2.1.3 Magnetron sputter deposition of thin films

Historically, direct current (d.c.) magnetron sputter deposition has been demonstrated to be effective for deposition of thin films of metallic species, even providing a route to fabricating interconnects for integrated circuits [130]. In this work, magnetron sputter deposition was used for the fabrication of metallic layers which are in contact with (half-) Heusler thin films.

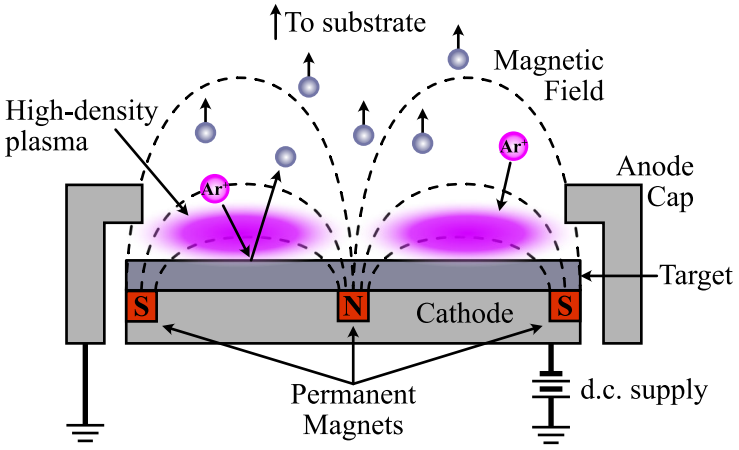

Figure 2.3: Schematic of a magnetron sputter head in side view cross-section. Ambient argon is ionised, then accelerated by the magnetic field, resulting in a magnetically-confined, high-density plasma which sputters the target surface through ion bombardment.

These include the platinum capping layers used to limit oxidation of the films after growth and, in Chapter 5, epitaxial vanadium buffer layers used to prevent interfacial reactions between TiNiSn and the MgO substrate. In these situations, magnetron sputtering is used over pulsed laser deposition not only because it is efficient, but also because it allows us to avoid the formation of hydrodynamical droplets.

D.C. magnetron sputtering exploits glow discharge physics where, above a certain threshold, a high potential difference between two electrodes separated by a gas causes electrical breakdown, ionising the gas to form a plasma maintaining an electrical current between the electrodes. In glow discharge, the charged plasma experiences acceleration toward the cathode, resulting in sputtering of the cathode material. Magnetron sputtering builds on this process by the inclusion of a permanent magnet to envelop the cathode with a magnetic field. When electrical breakdown commences, the magnetic field confines electrons close to the cathode surface, as illustrated in Figure 2.3. These electrons ionise ambient gas (typically argon) to form a high density plasma at the target surface. Ions in the plasma are accelerated toward the cathode where the ion bombardment of the surface liberates atoms from the target, which are used for deposition [131, 132].

Magnetron sputtering in the work was carried out either *in situ* in the PLD system, or in a dedicated sputter coater. For deposition in the PLD system, magnetron sputter heads from Mantis Deposition Ltd were used. For *ex situ* sputter deposition, an Emitech K575X Peltier-cooled sputter coater was used. Details of the materials deposited via magnetron sputtering and the conditions used are outlined in Table 2.1.

Material	System	Current	Argon Pressure	Deposition Rate
Vanadium	PLD Chamber	250 mA	25 mTorr	0.05 nm/s
Nickel	PLD Chamber	160 mA	10 mTorr	0.16 nm/s
Platinum	Sputter Coater	100 mA	15 mTorr	4.5 nm/s
Gold	Sputter Coater	100 mA	15 mTorr	1.3 nm/s

Table 2.1: Deposition conditions for layers fabricated by d.c. magnetron sputtering. Deposition rates are calculated by comparing deposition times with film thicknesses measured from TEM cross-sections.

2.1.4 *In situ* monitoring of thin-film deposition

For deposition of epitaxial thin films, it is desirable to have the means for instantaneous feedback about the quality of epitaxial crystalline growth. To troubleshoot the epitaxial quality of growth *in situ*, reflection high-energy electron diffraction (RHEED) was used during growth to determine the surface structure of the thin film as it forms. RHEED is a surface-sensitive diffraction technique whereby an electron beam with energy of order 10 keV is reflected from a crystalline surface at a glancing angle. Due to the low mean-free-path of electrons in solids at these energies, information contained within the RHEED patterns derives mainly from the outer-most monolayers of material. It is this surface sensitivity that makes RHEED invaluable as a diagnostic tool for epitaxial growth, leading to a rich history of its use in UHV growth methods like MBE [133, 134].

RHEED hardware is integrated into the deposition chamber for growth monitoring as illustrated in Figure 2.1. The electron gun, phosphor screen and camera are provided by k-Space Associates [135]. RHEED patterns recorded in this work use 30 keV electrons. For RHEED monitoring at elevated temperatures, the power of the substrate heating coil was kept constant to minimise deflections of the electron beam due to fluctuations in the electromagnetic field generated by the coil.

RHEED intensity-time profiles can be used to comment on the growth mode [133, 136]. Of the three main growth modes, layer-by-layer (Frank-van-der-Merwe) growth is perhaps the most easily identified using RHEED [137]. This is due to the transitions between constructive interference from complete monolayers and destructive interference from partially complete monolayers that leads to oscillations of the intensity of the RHEED pattern during growth [138]. Three-dimensional island growth (Vollmer-Weber) does not have such a clear intensity profile signature, as the increasing roughness of the surface associated with this growth mode attenuates the RHEED intensity. Island growth is instead more easily recog-

nised from a change in the overall nature of the RHEED pattern, which will comprise long streaks for a well-ordered, flat surface but will present a spotty pattern indicating transmission through islands of a rougher surface. Thus, RHEED can also give some indication of surface roughness as well as crystallinity.

2.2 Focused Ion Beam sectioning for specimen preparation

Transmission electron microscopy (TEM) depends on the illumination conferred by highly-accelerated electrons passing through a specimen. The material-dependent mean-free-path for inelastic scattering of 200 keV electrons through solids is typically around 100 nm [139]. Consequently, for high-quality imaging of materials in the TEM, where electrons must be able to pass through the sample for illumination, specimens to be examined should have a thickness that is ideally about half the mean-free-path (approximately 50 nm) or thinner. The Focused Ion Beam (FIB) microscope presents a tool for precision sectioning of bulk materials to obtain specimens which are sufficiently thin for TEM studies. FIB sectioning confers an advantage over other TEM preparation techniques as knowledge of the location of the observed feature relative to its surroundings is retained.

In this section, the methods for preparing planar cross-sectional specimens and tomography needlepoint specimens are outlined. There is also a brief introduction to some of the analytical techniques available inside the scanning electron microscope (SEM). The imaging and analytical functionality of the SEM can be used to aid extraction of specimens containing specific features or locations in the bulk material.

Two FIB-SEMs were used in this work: a FEI Nova Nano-lab – which includes a Ga^+ ion FIB – and a FEI Helios dual-beam plasma-FIB, where the FIB ion source is a xenon plasma. The methods outlined in the remainder of this section remain similar across both instruments, however only the Helios had the capability for EDS and EBSD.

2.2.1 Preparation of thin film cross-sections

To prepare electron-transparent cross-sections from PLD fabricated specimens, dual-beam scanning electron microscopes (SEMs) are an appropriate tool. The focused ion beam (FIB) in a dual beam SEM (or FIB-SEM) allows for position specific extraction and preparation of

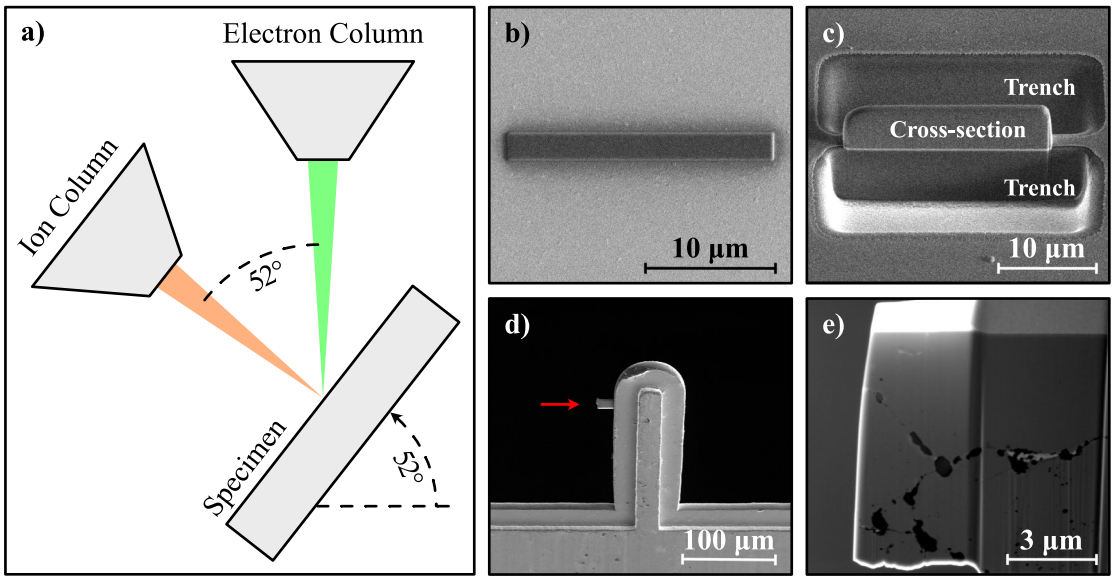

Figure 2.4: (a) Schematic of the FIB-SEM geometries for specimen preparation. (b)-(e) SEM images show stages of specimen preparation. An EBID Pt protective layer (b) is deposited prior to ion-beam deposition of Pt and (c) trench milling. The specimen is then removed from the bulk material and (d) attached to a TEM specimen holder. (e) Image of cross-section after thinning and polishing. Electron transparency causes the protective Pt layer to become very bright in the image.

planar cross-sections, using protocols which are now well established in the electron microscopy community [140–144].

In preparing material for liftout, use of the ion-beam is avoided until a protective layer of electron-beam-induced deposition (EBID) platinum has been deposited atop the area marked for liftout. This platinum pad is typically 10–20 µm long by 1–2 µm wide and ~500 nm thick, as shown in Figure 2.4(b). Once this protective layer is in place, the specimen is tilted so the surface is normal to the ion column, which is at an angle 52° from the electron column, as indicated in the geometry shown in Figure 2.4(a). At this point, automatic routines are given control of the microscope to perform trench milling either side of the protected section (Figure 2.4(c)). This automated process starts with the deposition of another protective Pt layer using ion-beam deposition, and also deposits a fiducial marker which allows the computer to use pattern recognition for spatial alignment of subsequent milling stages on the specimen. Once material has been cleared from either side of the section to form trenches, an undercut has to be made in preparation to free the section from the bulk specimen. Before the final side is cut free, the section is attached to a micro-manipulator needle using a platinum weld. Once free, the section is attached to a TEM grid then cut free from the micro-manipulator, which is then retracted. The excised section attached to the TEM grid is shown in Figure 2.4(d). Thinning of the cross-section then begins (Figure 2.4(e)), using a grazing incidence with the FIB

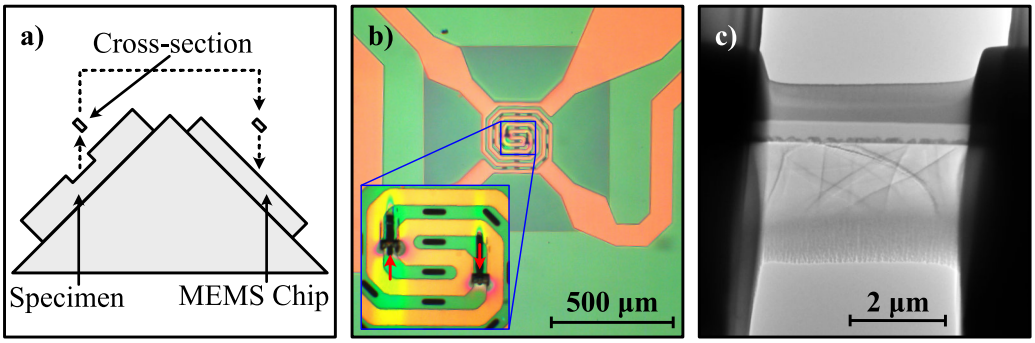

Figure 2.5: (a) Illustration of the 45° SEM holder which enables translation of the cross-section onto the heating chip. (b) Low (5x) magnification optical microscope image of the Wildfire chip membrane with 50x magnification inset, showing two cross-sections mounted over windows in the membrane. (c) TEM image of thinned cross-section over a membrane window.

at progressively lower beam voltages and currents to limit the amount of specimen damage introduced in the final thinning stages [144].

The core method for preparing cross-sectional specimens in the FIB-SEM can be adapted slightly to allow integration of the specimen into a specimen-heating chip. Preparation on these chips, which are based on micro-electro-mechanical systems (MEMS) technology, is highly desirable for performing *in situ* studies in the transmission electron microscope, such as heating or biasing of the specimen. The *Wildfire in situ* heating chips from DENSsolutions [145] were used for annealing cross-sections inside the TEM at temperatures up to 1000°C. The challenge in mounting cross-sections onto these chips is that the cross-section has to be orthogonal to the normal FIB geometry when placed on the chip. To get around this problem, both the bulk specimen and heating chip are mounted on either side of a triangular 45° SEM holder. The cross-section will therefore be tilted when lifted by the micromanipulator, and is flush with the heating chip on the other side of the holder [146], as illustrated in the schematic in Figure 2.5(a). Welding the cross-section to the chip both secures the cross-section to the chip and creates the electrical connections for heating and biasing. As with standard cross-section preparation, platinum is used for welding and here it must overlap with the electrical contacts on the chip, which are shown in the optical microscope image in Fig.2.5(b) as the copper-coloured regions snaking between the dark observation windows where samples can be placed. Once placed, the underside of the cross-section is difficult to access, so virtually all the thinning is done from the top surface, with only cursory polishing to remove the FIB-damaged surface on the underside. A TEM image in Fig.2.5(c) illustrates the part of a thinned specimen which can be viewed through the electron-transparent window.

2.2.2 Preparation of Atom-Probe Tomography specimens

For certain applications involving tomography – whether that be TEM tomography or 3-dimensional atom-probe tomography (APT) – it is preferable to prepare material into a needle-shaped specimen, instead of a flat, cross-sectional lamella. In TEM, this shape of specimen reduces variation in specimen thickness with viewing angle, while in APT, the needle shape is critical to generating the high electric field strengths required for successful operation [147].

Using the Xe plasma-FIB, several tomography needles can be prepared from single, site-specific liftout from the surface of a bulk specimen. The initial stages are similar to the typical FIB-sectioning process described previously, where first a protective layer of EBID platinum is deposted before milling commences, as indicated in Figure 2.6(a). Trench milling commences with a slight difference, in that trenches are milled at a 30° angle to the surface so that the trenches either side of the protective layer meet under the section to form a wedge shape (Figure 2.6(b)). The wedge, which is typically about 10 µm long, is lifted out using the micro-manipulator and sections of it 1–2 microns long can be lowered onto and welded to posts, as shown in Figure 2.6(c), giving perhaps 3 or 4 needles per liftout [148]. Angling

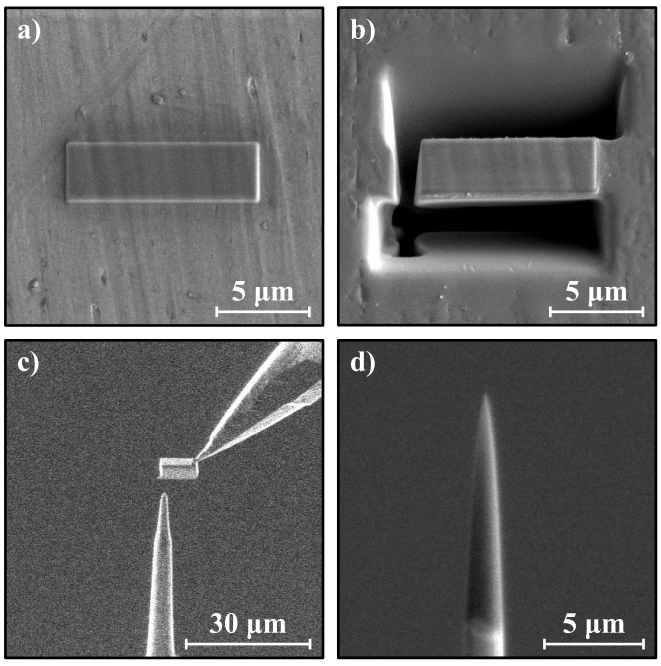

Figure 2.6: SEM images recorded at various stages of preparation of a needle specimen of nickel. (a) After initial deposition of protective Pt layer. (b) After milling 30° trenches to create wedge of material. (c) The wedge of material attached to a micro-manipulator, being lowered onto a post for mounting and shaping. (d) The final, polished needle in profile, with around 400 nm of material at the tip with a diameter smaller than 100 nm. The weld point between specimen and the post is clearly visible near the bottom of the image.

the tip toward the ion column, annular milling patterns are used to reduce the tip profile from a chunk to a fine point, until the specimen is a sufficiently sharp-tipped needle as in Figure 2.6(d). Due to the broad profile of the Xe beam, the inner diameter of the annular milling pattern is kept quite broad, with stages involving diameters of 3, 2, 1 and 0.5 μm using a beam energy of 30 kV before closing the inner diameter completely for a circular pattern to polish the needle at low energies (5 and 2 kV) [149]. Beam currents are generally kept low (< 100 pA) and are reduced further in the final stages.

2.3 The Transmission Electron Microscope

Fundamentally, the resolution of a conventional microscope operating with lenses is determined by the diffraction limit. That is, two objects are too close to each other to be considered distinct if the first diffraction minimum of one object coincides with the central maximum of the other; a rule referred to as the *Rayleigh criterion* [150]. This definition describes how the resolution of a microscope is determined by the wavelength of the illuminating radiation. Thus, for a visible light microscope operating with wavelengths of 400 - 700 nm, the resolution limit is approximately 250 nm [151]. Meanwhile, the de Broglie wavelength of an electron accelerated by 200,000 volts (a typical scenario in a modern TEM) is 2.5 pm, giving the transmission electron microscope (TEM) the potential for a hundred-thousand-fold improvement in resolution over a visible light microscope. However, there are optical aberrations introduced in the construction of the TEM which prevent us from taking full advantage of the potential resolution. Nevertheless it is now relatively commonplace to find sub-nanometre resolution limits for conventional TEM [152, 153], and sub-Ångström limits for aberration-corrected scanning TEM [154].

2.3.1 Specimen interactions in the TEM

Although the resolution limit of the TEM is undoubtedly one of its greatest strengths, the use of fast electrons for imaging specimens also confers additional advantages by introducing a plethora of possible electron-matter interactions which can also yield useful information about the specimen. A great deal of this information is carried by forward-scattered electrons, which means that the vast majority of signals of interest are contained within a very small angular range on the order of 0.1 steradians, and thus can be collected without the need for a

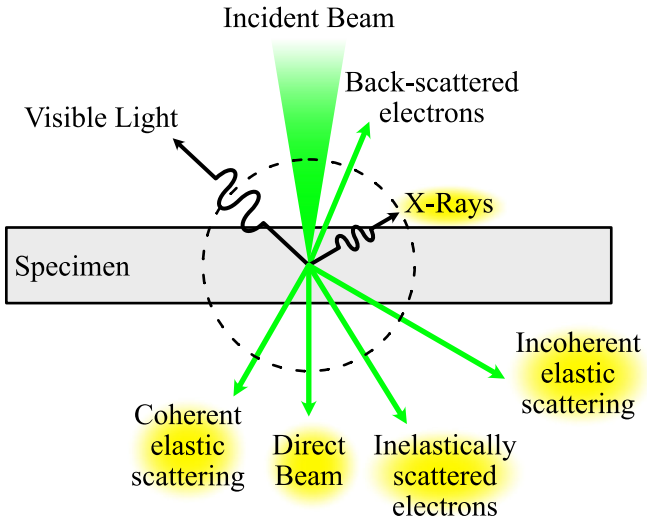

Figure 2.7: Illustration of different phenomena which are a result of high-energy electrons interacting with a specimen. Interactions with analytical applications which are used in this work are highlighted.

large field of view or collection angle. In Figure 2.7, the possible interactions (and resulting, outgoing signals) of the incident electron beam with a specimen are highlighted. These can be broadly categorised into two classes, based on whether elastic or inelastic scattering of an incident electron has occurred.

When the specimen is sufficiently thin for quality TEM imaging, elastically scattered electrons account for the majority of the available signal in the TEM. These occur as a result of electrostatic Coulomb interactions between the beam and the specimen. Coulomb interactions with the beam may involve either electrons or atomic nuclei, and the typical scattering angles vary strongly due to this. Fast electrons interacting with the electron cloud are typically scattered through a small angle no larger than a couple of degrees. The weak scattering involved at these small angles preserves the coherency of the electron beam and diffraction effects are significant. In crystalline specimens, diffraction involves scattering from atomic planes, resulting in constructive and destructive interference to form patterns which contain information about the crystal structure of a material. This is illustrated in Figure 2.8(a), which shows Bragg reflection from neighbouring atomic planes. To satisfy the Bragg condition and obtain constructive interference of the scattered electrons, the angle of incidence θ should be found so that the product $2d\sin\theta$ is an integer multiple of the radiation wavelength λ (i.e. $n\lambda = 2d\sin\theta$) [33]. For a given incident electron beam, the set of atomic planes which satisfy diffraction conditions for constructive interference is indicated by the Ewald sphere, which is illustrated in Fig.2.8(b). This shows a representation of the crystal lattice in reciprocal-space, where the Ewald sphere is used to identify crystal lattice vectors, $\mathbf{G}$, which satisfy conserva-

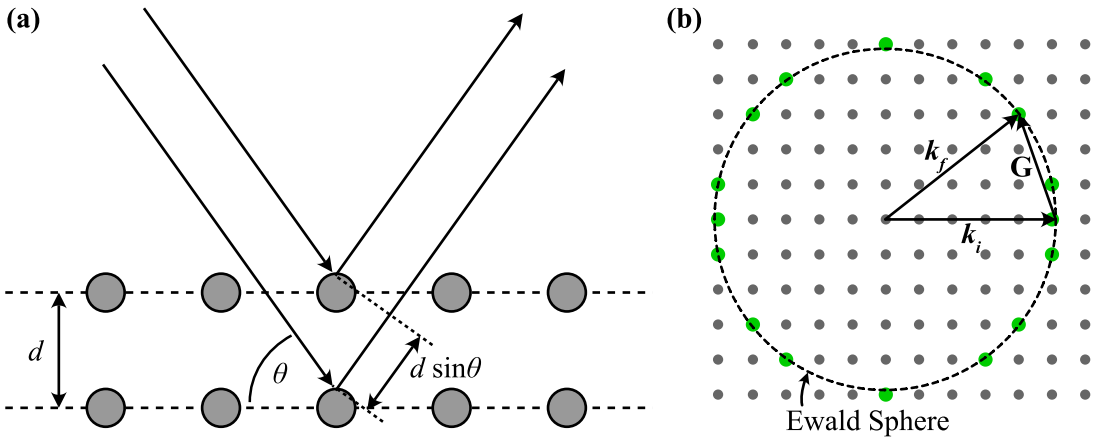

Figure 2.8: (a) Bragg reflection from planes of atoms in a crystal. The incoming radiation is deflected by 2θ and the wave striking the lower plane has a difference in path length of $2d\sin\theta$. (b) A reciprocal-space lattice with the wave-vectors of the incident and diffracted beams k_i and k_f indicated. These wave-vectors define the radius of the Ewald sphere, which illustrates the diffraction conditions which are satisfied.

tion of momentum in the Laue condition, $\mathbf{k_f} - \mathbf{k_i} = \mathbf{G}$, where $\mathbf{k_i}$ and $\mathbf{k_f}$ are the wave-vectors of the incident and diffracted beam [155]. The use of diffraction in the electron microscope is discussed further in Section 2.3.6.

Coherent scattering of electrons in diffraction is typically confined to within a few degrees of the forward, incident beam direction. At larger scattering angles, phase relations are no longer preserved and incoherent, Rutherford-type scattering dominates. This incoherent scattering can occur in any direction, including complete back-scattering by 180°. At these larger angles, the scattering rate is strongly dependent on the atomic number, Z [156]. This can be exploited to provide qualitative elemental analysis and is discussed further in Section 2.3.5.

Inelastic scattering in the TEM gives rise to much of the analytical capabilities of the instrument. Some inelastic scattering arises due to the Coulomb interaction discussed above, giving rise to braking effects on the electron beam which produce a continuous spread in electron energies, as well as producing a continuum of X-ray radiation. Other inelastic scattering events involve atomistic and quantum mechanical processes, where a portion of energy is transferred to the specimen through excitation. These excitations – which can be phonons, valence electrons or core-shell electrons – absorb a quantity of energy from the beam which is characteristic in some way of the specimen. Through these interactions the electron beam, which initially has a small energy spread, becomes polychromatic and by measuring the energies of electrons in the beam, we can gain information about the specimen material. This is the premise of electron energy-loss spectroscopy (EELS), where a spectrometer collects the

polychromatic beam and disperses it by energy to produce an energy-loss spectrum which contains features relating to the characteristic interactions of interest. EELS methods and equipment are discussed in greater detail in Section 2.3.7. The same characteristic excitations which produce the EELS spectrum also release characteristic X-ray radiation upon relaxation. These X-rays are emitted isotropically and are therefore much harder to collect with reasonable counting statistics. Recording of the X-ray spectrum in Energy-dispersive X-ray spectroscopy (EDS) can be used in quantitative chemical analysis, but is not discussed in this thesis.

In addition to the many interactions which result in useful information, it is also important to bear in mind that fast electrons are a form of ionising radiation. Consequently, the act of imaging a specimen in the TEM/STEM has the potential to be detrimental and also inflict damage upon the materials under illumination. This radiation damage can manifest in a few different ways, including reduction of the oxidation state of elements in the specimen, changes in the structure of areas exposed to the beam, charging or heating and even sputtering of material in the specimen [157, 158]. Which, if any, of these effects occur is dependent upon the material under investigation in the microscope, as well as the electron dose received by the specimen. For the thin films of materials studied in this thesis, the beam-sensitivity of MgO substrates provided clear indication of damage inflicted on specimens. Images would show clear contrast in the substrate relating to the loss of material through sputtering by the electron beam [159].

2.3.2 TEM/STEM instrumentation

The essence of the TEM can be broken down into four distinct parts: the electron gun, condenser system, objective lens, and projection system. The first of these, the electron gun, is the source of illumination in the TEM. The gun provides electrons either by thermionic emission (from a tungsten filament or LaB_6 crystal) or field emission (from a crystalline tungsten needle). For high-resolution analytical work as is done on the ARM, a cold field emission gun (FEG) provides the best source brightness and lowest spread of electron energies [160]. The cold-FEG comprises a very fine tungsten needle. Application of a voltage to an anode placed close to the tip imposes a colossal electric field (of the order of GV/m) on the needle tip, enabling electrons to tunnel from the tip into vacuum. Additional high-voltage anodes then extract the tunnelled electrons away from the tip and into the microscope column while

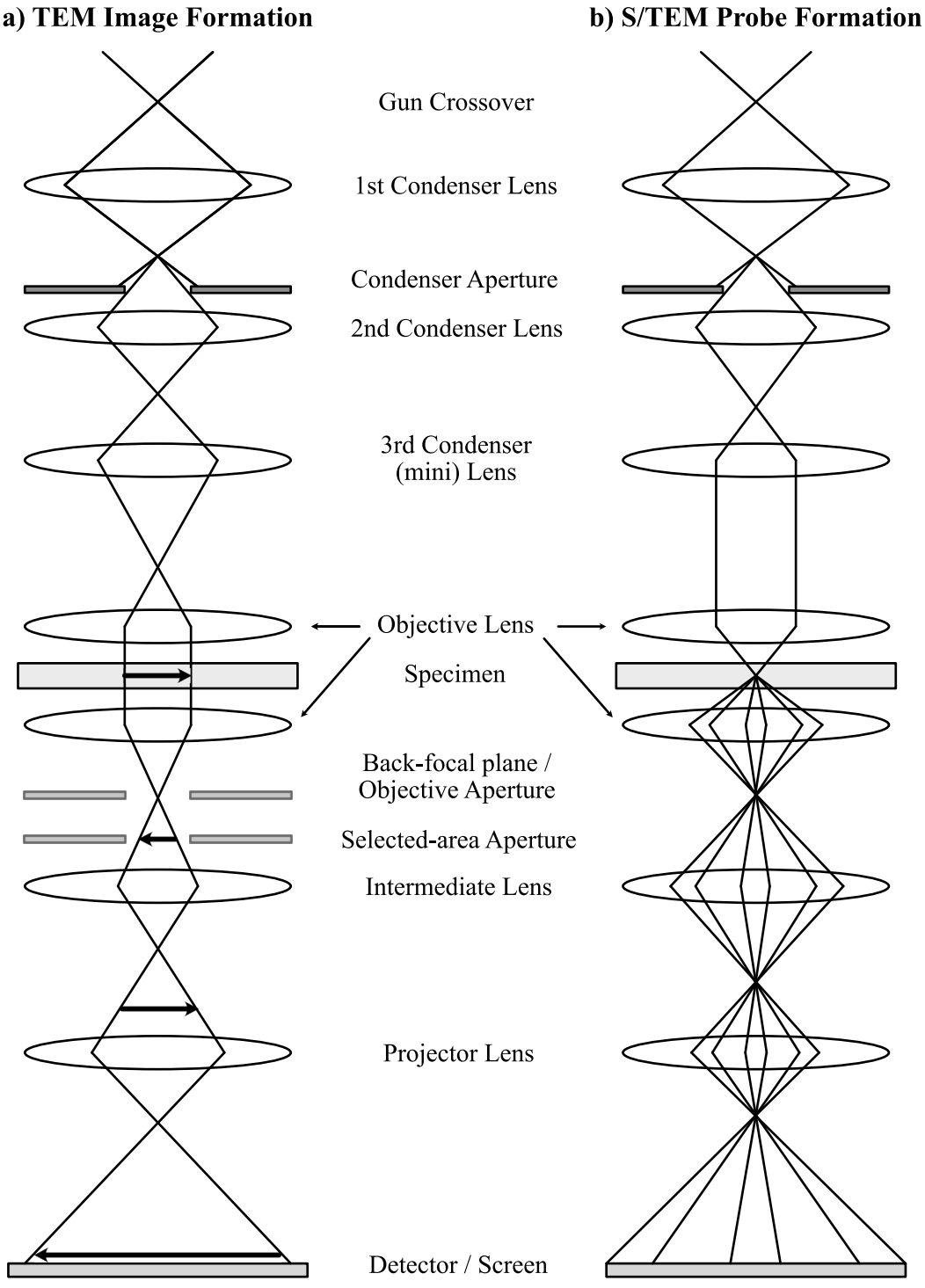

Figure 2.9: Ray diagrams of the operational modes of the transmission electron microscope. In (a), typical conditions for TEM imaging are shown, with parallel illumination at the specimen and formation of an image of the specimen by the projector system. (b) Configuration of the pre-specimen lenses to form a condensed probe at the sample, with the projector lens system magnifying the resulting diffraction pattern from the back-focal-plane onto the screen.

accelerating them to 200 keV [161]. The large voltages required for these anodes are provided by the high-tension (HT), a high-voltage power supply which is separate from the rest of the instrument. In addition to acceleration, these anodes also shape the beam to form the gun crossover, which is illustrated at the top of the ray diagrams presented in Figure 2.9.

The condenser system in most modern TEMs consists of three lenses with an aperture at the second condenser lens (C2), as shown in Figure 2.9. In sequence, the first condenser lens (C1) forms an image of the gun crossover, while C2 controls the size of the illuminated area (for imaging) or, equivalently, the convergence of the beam (for probe formation) [162]. The C3 (or mini-Condenser) lens serves to ensure that the specimen is exposed to uniform illumination by forming an image of the condenser aperture, rather than the electron source, at the specimen plane, in the same principle as Köhler illumination in light microscopy [163]. This has two main benefits, which include parallel illumination of the specimen regardless of the illumination area defined by C2 and also allows for simple switching between plane illumination for imaging, and convergent probe modes.

The next segment of the microscope is the objective lens, which surrounds the specimen. This is the main focusing lens of the microscope. The objective lens is responsible for image focus when using parallel plane illumination for conventional TEM, illustrated in Figure 2.9(a). In scanning transmission electron microscopy (STEM), the role of the objective lens is to focus the electron beam into a point-like probe – illustrated in Figure 2.9(b) – that is then used for imaging via a raster-scan of the probe across the specimen. In both TEM and STEM, the magnification and calibrations are only reproducible if specimens lie at the same height in the field of the objective lens. For this reason, a certain power of the objective lens is used as a reference, and the specimen height is adjusted to the position where this lens power provides correct focus. This reference configuration is thus commonly referred to as the *eucentric plane* or *standard focus* [162].

Finally, the remainder of the microscope after the objective lens – collectively, the projector system – is responsible for providing magnification of the image formed of the specimen. In Figure 2.9, this is illustrated as a single intermediate lens, followed by the projector lens. However, it is more common for there to be two or three intermediate lenses to provide sufficiently high magnification (typically around 0.5M× for high-resolution imaging). The projector system can be used to form an image of the specimen plane – for real-space imaging – or form a reciprocal space image by imaging the back-focal plane (bfp), where the diffrac-

tion pattern first comes into focus. Apertures shown in Fig.2.9 include an objective aperture at the bfp that can be used to admit only part of the diffraction pattern, and a selected-area aperture situated below the bfp which selects a specific real-space region of the specimen for imaging. The power settings for these lenses are commonly set by the microscope manfacturer and are not controlled individually.

Two transmission electron microscopes have been used throughout the work presented; an FEI Technai T20 TEM and a JEOL ARM200cF C_S aberration-corrected TEM/STEM. The Technai T20 uses a thermionic electron source (either W or LaB_6) and is equipped with a Gatan GIF2000 for general image recording with a CCD as well as energy-filtered imaging and energy-loss spectroscopy. The T20 is also equipped with a SIS Megaview CCD for recording of diffraction patterns. The ARM is capable of both conventional TEM and also STEM operation, using a cold-FEG electron source that is ideal for high energy resolution analytical work. It is outfitted with a spherical aberration probe corrector [164], enabling atomic-resolution STEM, and also spectrometers for energy-dispersive X-ray spectroscopy (Bruker X-Flash) and electron energy-loss spectroscopy (Gatan GIF Quantum ER) [165]. A Quantum Detectors Medipix3 hybrid-pixel electron counting detector is also fitted on the ARM for imaging via direct electron detection [166]. Both microscopes were operated with a 200 kV acceleration voltage.

2.3.3 Aberrations in the electron microscope

Electron-optical components additional to those illustrated in Figure 2.9 are used to correct aberrations introduced by the main magnetic lenses already described. There are many different types of aberrations which can be present, with higher-order aberrations having more complex symmetries [167], but it is the lowest-order aberrations which typically have the greatest effect on the beam. The three main sources of aberration which need to be considered are astigmatism, spherical aberration and chromatic aberration [168]. First, astigmatism describes the effect of non-uniformity in the magnetic fields of the lenses, which can lead to a dependence of focal length on the azimuthal angle about the optic axis. The lowest order of this effect is first-order, two-fold astigmatism, in which the profile of the beam becomes elliptical instead of circular. Stigmator lenses throughout the TEM provide compensating fields to remove the effect of astigmatism in the condenser, objective and projector systems [162].

Spherical aberration (C_S) is the stronger focusing by a lens of rays which are further from

the optic axis of the lens. This variation of effective focal length for electrons as a function of distance from the optic axis results in a point object being imaged as a disc with finite size [168]. In both TEM and STEM imaging, spherical aberration effects have a deleterious effect on image resolution, limiting the detail which can be observed. It is therefore desirable to remove the effects of C_S. For high-resolution STEM, correction of spherical aberration is necessary to achieve the sub-Ångström probe size needed for atomic-resolution imaging [169]. In the JEOL ARM200cF, a CEOS C_S aberration corrector [164] is installed in the upper column between the condenser system and objective lenses shown in Figure 2.9. The aberration corrector relies on the use of high-symmetry hexapole lenses to counteract third-order spherical aberrations introduced by the condenser and objective lenses [170]. Uncorrected, C_S aberrations have the effect of limiting the minimum probe size which can be achieved with a convergent electron beam, compromising the STEM resolution. Compensation of C_S leaves higher, fifth order aberrations (C_5) as the limiting factor for probe size, effectively improving the information limit in STEM to 0.7 Å for 200 keV electrons [171].

In practice, the aberration corrector is tuned by the user relying on an image of the electron probe for feedback. This image, referred to as the 'Ronchigram,' is essentially a convergent beam diffraction pattern and contains contrast from the specimen that can highlight the presence of defocus, astigmatism, coma, spherical aberration and other, higher-order aberrations in the probe [172]. Compared with the drift in focus and astigmatism that is commonly observed throughout microscope sessions, the long-term stability of the hexapole lenses is found to be good and so spherical aberration compensation is not tuned by the user in day-to-day operation, instead being left for more rigorous alignments of the microscope which are performed every few months. In daily use, however, the Ronchigram is still required to optimise focus/specimen height, astigmatism and coma throughout general use of the STEM.

Chromatic aberration describes the aberrations which are introduced as a result of differences in electron energies. For a lens with a given magnetic induction, electrons of lower energy are focused more strongly [168]. Initially, the electron beam is virtually monochromatic, with a very small energy spread ($\leq$ 1 eV) compared to the 200 keV energy of the beam. However, inelastic interactions with the specimen lead to a polychromatic beam propagating through the post-specimen lenses. For very thick specimens, where inelastic scattering is significant, chromatic aberrations can compromise TEM image resolution. Chromatic aberrations are not generally of concern, but some further consideration is given in the discussion of the electron energy-loss spectrometer calibrations in Chapter 3.

2.3.4 Imaging modalities in TEM

In conventional TEM, where an area of the sample is uniformly illuminated to form an image, there are many different sources of contrast, which yield different information about the specimen. Various types of contrast are best accessed by varying the configuration of the TEM, mainly through the use of apertures, to produce different types of images. For instance, amplitude contrast and diffraction contrast can be isolated using the objective aperture to select either the direct beam for bright field (BF) imaging or a diffracted beam for dark field (DF) imaging, respectively. Meanwhile phase contrast occurs whenever the image contains contributions from more than one beam, which is achieved by using either a large or no objective aperture to admit a portion of the diffraction pattern large enough to contain multiple beams.

Amplitude contrast is produced by variations of mass and/or thickness of the specimen. The root of this lies in incoherent, Rutherford scattering of the electron beam which, as mentioned earlier, is strongly dependent on atomic number [173]. Amplitude contrast is enhanced in TEM images by using an objective aperture in the back-focal-plane (bfp) – where the first reciprocal space image of the specimen is formed – to selectively admit electrons which have scattered in a specific angle. This is most typically achieved by selecting the direct beam with the objective aperture to form a BF image. In the resulting BF image, regions which have greater atomic mass or thickness scatter more of the beam to high angles and therefore appear darker in BF [174].

Diffraction contrast, unlike amplitude contrast, involves coherent electrons Bragg-scattered from atomic planes. Selecting specific diffraction contrast in the TEM is also achieved using an objective aperture in the bfp, where it is used to admit only part of the diffraction pattern for image formation. This is most straightforward for single-crystal specimens, where the diffraction pattern consists of discrete spots in a regular lattice and thus an objective aperture can be centred on a single diffraction peak to form a DF image with contrast relating to the amount of scattering from the set of atomic planes represented by the specific reflection [174]. In DF imaging, it is important to ensure that the incident beam is tilted so that the diffracted beam selected for image formation lies on the optic axis of the microscope, minimising the influence of spherical aberrations in the image.

Unlike the previous two contrast mechanisms, which are optimally imaged by using the objective aperture to select one beam, phase contrast requires multiple beams to be used in

image formation. Interference between multiple beams allows variation in intensity associated with constructive and destructive interference and everything in between depending on the difference in phase of the electrons. The phase of electrons is very sensitive to small variations in the specimen, be it thickness, orientation etc., as well as changes in the microscope focus and astigmatism [175]. It is this sensitivity that enables phase contrast to form the basis of high-resolution TEM (HRTEM) imaging, where atomic-scale lattice fringes can be visible in an image. These lattice fringes are the result of interference in the electron beam caused by the crystal structure of the specimen. Though these fringes are not themselves atoms, they provide a visual of the crystal structure that can be used to measure lattice spacings and image structural defects.

2.3.5 Imaging modalities in STEM

While TEM images are formed by plane illumination of the region to be imaged, scanning transmission electron microscope (STEM) images are formed by rastering a convergent-beam probe across the specimen, recording the transmitted beam at each position in the scan. In principle, the contrast mechanisms which exist for conventional TEM also govern STEM imaging, however different sources of contrast are not accessed through the use of apertures as discussed in the previous section. Instead, contrast in STEM imaging is dictated by the typical scattering angles associated with different contrast mechanisms and the placement of detectors to discriminatingly collect electrons scattered at specific angles. The configuration of annular detectors typically used to achieve this is illustrated in Figure 2.10. These annular detectors are typically formed of p-n diodes or scintillator-photomultipliers that record electrons which scatter into their angular range and integrate the signal to return a single value for each probe position.

Following from the discussion of scattering mechanisms in Section 2.3.1, the contrast found in STEM images from the detectors in Fig.2.10 depends on the dominant scattering mechanisms at the angles subtended by each detector. Bright field (BF) imaging in STEM uses a detector placed directly on the optic axis to collect signal from the forward-scattered direct beam with a collection angle similar to the convergence angle of the beam. As with TEM-BF imaging, the primary source of image contrast in STEM-BF is amplitude contrast, giving sensitivity to specimen thickness in addition to the atomic numbers of elements present in the specimen. TEM and STEM BF images therefore appear qualitatively very similar,

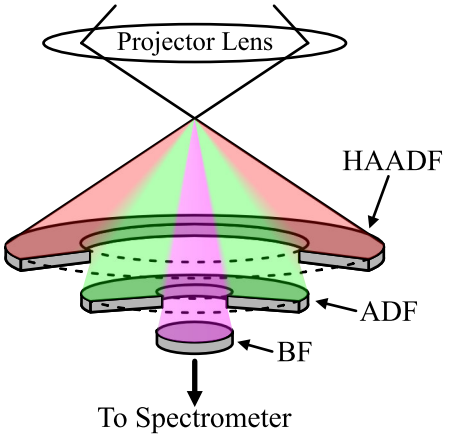

Figure 2.10: Configuration of detectors at the base of the projector system used for STEM imaging including: High-angle annular dark field (HAADF), annular dark field (ADF) and bright field (BF) detectors. The bright field detector must be retracted for use of the spectrometer for EELS.

though BF contrast in STEM is typically more pronounced [174]. Dark field (DF) imaging in STEM is then achieved through the use of annular detectors that collect electrons at larger scattering angles in a way that would be equivalent to TEM-DF imaging if the TEM beam were pivoted to trace a hollow cone during exposure. These annular dark field (ADF) images are also dominated by amplitude contrast, though some diffraction contrast may also be present. Diffraction contrast in STEM is typically present to a much lesser extent than in TEM imaging. This is due to the relatively-large convergence angles used to form the STEM probe, which limits the coherency of the incident beam [174].

The other, high-angle annular dark field (HAADF) detector, which subtends the largest scattering angles (typically $>$ 100 mrad) as illustrated in Figure 2.10, tends to lie beyond the influence of Bragg scattering and, as such, STEM-HAADF images are comprised purely of mass/thickness contrast. For HAADF images, this is often referred to as *Z*-contrast (especially at the atomic scale) as contrast levels in HAADF are very strongly dependent upon the atomic numbers *Z* of elements present in the specimen. As previously discussed in Section 2.3.1, *Z*-contrast is attributed to incoherent Rutherford scattering, which dominates at the high angles subtended by the HAADF detector. However, recent experimental and theoretical studies have argued that HAADF *Z*-contrast instead derives from inelastic scattering from phonons [176, 177].

In the last few years, a recent development in STEM imaging is the use of fast hybrid-pixel array detectors in place of the annular detectors described above. One such detector, the MediPix3 electron counting detector [178], has been used in some of the work presen-

ted here. Detectors such as these provide direct detection of electrons to record full images of the STEM probe at each position in the raster scan. As each probe position involves recording a 2d image with the detector, and 2 scan dimensions are typically used, STEM data involving these detectors comes under the name *4dSTEM*. In recording the complete image of the scattered electrons, 4dSTEM has a substantial range of applications [179], the breadth of which is still being explored. In addition to the ability to reconstruct the annular images conventional STEM detectors would yield, 4dSTEM data can be used to produce annular images with arbitrary (even overlapping) angles [180], produce phase images through pytchographic reconstruction [181, 182], provide improved magnetic phase contrast [183] and probe structural information through scanning nanobeam diffraction [184]. Unlike conventional CCD pixel-array detectors – which are prone to many sources of noise and the 16-bit-depth per pixel is easily saturated – direct electron detectors like the MediPix3 boasts incredible counting statistics and signal-to-noise, with rapid sub-millisecond readout times, up to 24-bit-depth per pixel and zero readout noise [166, 185]. These properties make the MediPix well-suited to recording the STEM probe and diffraction patterns, where intensities can vary by several orders of magnitude within a single image. These strengths are exploited here in the recording of scanning precession electron diffraction (SPED) patterns for structural nano-analysis, which is introduced in the next section.

2.3.6 Transmission Electron Diffraction

Diffraction, which was introduced in Section 2.3.1, forms a staple of materials analysis in the TEM. The influence of diffraction contrast in TEM and STEM imaging has already been discussed in Sections 2.3.4 and 2.3.5, however imaging of the diffraction pattern itself is sometimes of greater use than the contrast it generates in images. In real-space imaging in the TEM, the image plane recorded on the detector or screen (at the bottom of Figure 2.9) is a conjugate plane of the specimen; i.e. a focused image of the specimen plane is formed at the detector plane. With a properly focused TEM image, the microscope optics effectively perform a Fourier transform on the beam that first brings the reciprocal-space diffraction pattern into focus at the back-focal-plane (bfp) of the objective lens. Thus, observing the diffraction pattern instead of the real-space image is a matter of adjusting the projector system, so the image formed at the screen/detector is instead the conjugate plane of the bfp. The high-energy 200 keV electrons used in TEM have a de Broglie wavelength of 2.5 pm that is significantly smaller than the spacings between atoms. Consequently, the Ewald sphere of

TEM diffraction is very large and it is possible to observe a large number of diffraction peaks at once [155]. For the single-crystal/epitaxial specimens studied in this thesis, typical diffraction patterns are dominated by scattering from ordered atomic planes, resulting in arrays of discrete peaks representative of the crystal lattice.

Diffraction patterns are typically set up adjusting the C2 lens to spread the beam and ensure parallel illumination. Under these conditions, Bragg peaks in the diffraction pattern appear as sharp spots, giving the best reciprocal-space resolution [186]. Parallel illumination tends to cover a large area of the specimen, and so the diffraction pattern may contain contributions from regions we have no interest in observing. To record diffraction information from a smaller area under the same conditions, a selected-area aperture can be inserted below the bfp – shown in Figure 2.9(a) – to form a selected-area diffraction pattern (SADP) which only admits contributions from the region of the specimen image that fall within this aperture.

Sometimes, the area from which we wish to extract a DP from is smaller than the available selected-area apertures, the smallest of which can usually be used to select an area with diameter ~100 nm. In this instance, the beam can be converged – usually to form a point-like spot – to illuminate the small region of interest only. While the use of convergent-beam electron diffraction (CBED) improves the spatial resolution of the diffraction pattern, converging the beam sacrifices some of the reciprocal-space resolution that would be available in parallel-illumination diffraction. This occurs because the convergent beam contains a range of incident angles, which translate to a variation in the direction of the incident wave-vector described in Figure 2.8. Such variance in the diffraction conditions manifests in the diffraction pattern as a broadening of the peaks to form 2d discs instead, where the angular radius of each beam is determined by the convergence angle of the incident beam. Thus, although CBED is an excellent technique for achieving nanoscale spatial resolution in diffraction (convergent-beam probe sizes down to ~1 nm are possible), distinction of finely separated Bragg peaks may be lost.

Whether forming a diffraction pattern by parallel illumination or using a convergent beam, electron diffraction patterns contain information from complex dynamical scattering events that can obfuscate interpretation of the structure they represent. Diffraction intensities differ from kinematical predictions and, in the case of CBED, diffracted discs can contain strong internal variations in contrast. To return to a diffraction pattern that is a better representation of kinematical scattering, precession electron diffraction (PED) is incredibly useful. In this

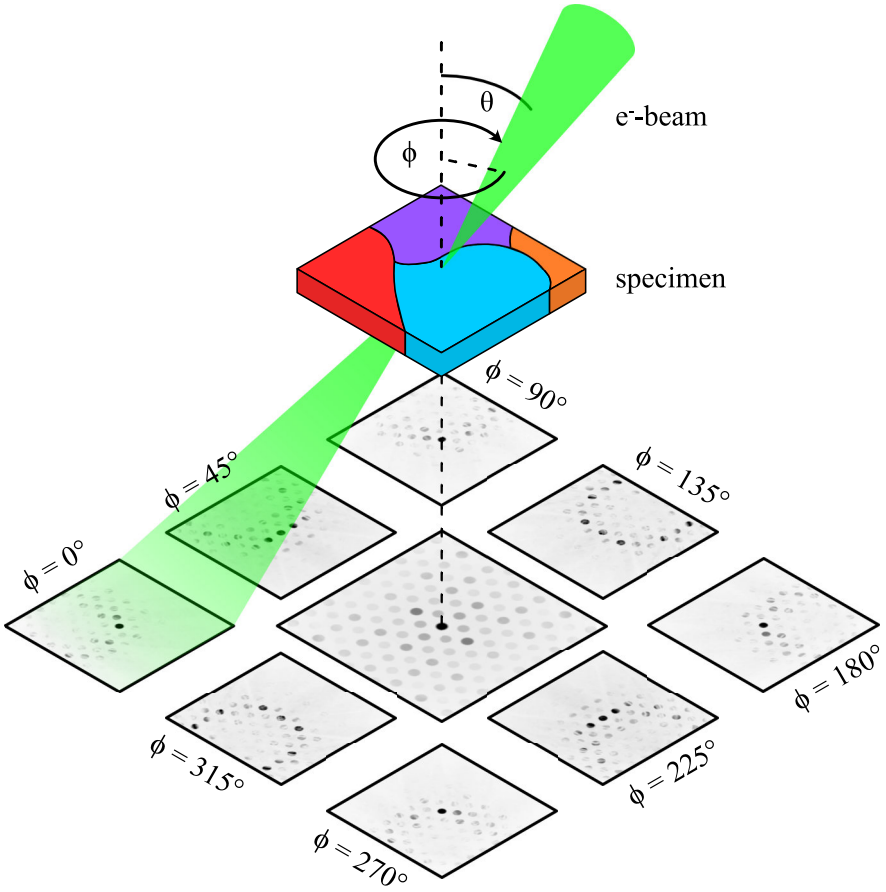

Figure 2.11: Illustration of precession electron diffraction (PED), where the electron beam is pivoted about its position on the specimen. As the precession progresses, different dynamical diffraction conditions are satisfied (outer patterns). These are deflected back onto the detector plane by the de-scan coils, and averaged over to produce a pseudo-kinematical diffraction pattern (centre).

technique, the beam is tilted off-axis and precessed about a point on the specimen, as shown in Figure 2.11. While the beam is precessed, a range of different diffraction peaks are excited as the Ewald sphere shifts and satisfies different Laue conditions [187]. Combining all of these different diffraction patterns in a single exposure results in the incoherent summation of all the different excitations and has the effect of 'averaging out' the dynamical scattering effects to produce a diffraction pattern which is pseudo-kinematical [188]. The PED pattern gives much more uniform spot/disc intensities and, as more spots are excited due to the beam tilt, many more diffraction peaks are visible than in a normal electron diffraction pattern. This makes the diffraction pattern far easier to interpret and extract structural information from, including very fine lattice vector and strain measurements [189] or for orientation measurements similar to EBSD in the SEM [190].

2.3.7 Electron Energy-Loss Spectroscopy in the TEM

Fast electrons passing through the specimen sometimes undergo inelastic scattering. These events result in the electron beam becoming polychromatic upon exiting the specimen, with a fraction of the beam having lost part of its original energy. The energy-losses of the beam electrons are characteristic of the material involved in the interaction, and can therefore be used to extract information about the specimen being studied. This is the premise of Electron Energy-Loss Spectroscopy (EELS), where a spectrometer (usually) situated at the end of the microscope column is used to discriminate electrons by their energy. In a modern post-column spectrometer, either a portion of the energy-loss spectrum can be measured, or a filtered image can be formed by selecting electrons of a specific energy, the latter being referred to as energy-filtered TEM (EFTEM). Both of these modes of operation rely on the same physical principles to separate electrons by energy-loss.

The post-column spectrometer used throughout this work is a Gatan GIF *Quantum* ER 965, for which an approximate schematic is presented in Figure 2.12. The primary component of

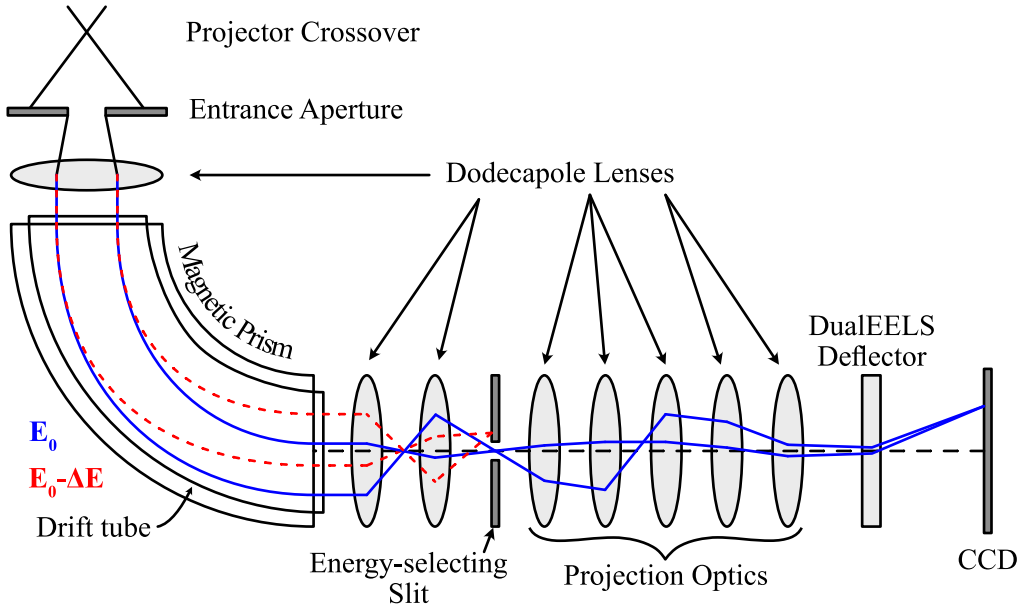

Figure 2.12: Schematic of the Gatan Image Filter (GIF) Quantum *post-column EELS spectrometer. The polychromatic electron beam is dispersed by the magnetic prism, optionally applying a voltage to the drift tube that lines the prism to accelerate the beam and 'shift' the spectrum. The three dodecapole lenses between the entrance aperture and the selected-energy slit are used for focusing and aberration correction of the beam/spectrum, bringing the spectrum into focus at the plane of the slit. A series of dodecapole lenses after the slit magnify and project the spectrum or energy filtered image onto the CCD. In dualEELS mode, the CCD is divided into two, with an electrostatic deflector projecting the low-loss spectrum onto one half, and the high-loss spectrum on the other.*

the post-column spectrometer is the magnetic sector prism. This electromagnet generates a magnetic field which imposes a Lorentz force upon the incoming electron beam, causing the beam path to curve through 90°. The actual curvature of the path created by the magnetic field is dependent on the velocity of the electrons entering the spectrometer, with faster electrons (i.e. those which have lost less energy) experiencing a smaller deflection than those which have undergone more significant energy-losses [111], as illustrated by the blue and red paths in Figure 2.12. In typical operation, to avoid thermal loading of the electromagnet which can lead to long-term drift in the magnetic induction, the prism current is fixed at a specific value. Thus, the energy spread of electrons at the dispersion plane of the spectrometer also has a fixed value. To vary the dispersion, additional post-prism electromagnetic lenses are used to magnify and focus the spectrum, as well as to remove some higher-order aberrations. These aberrations are similar to those in the discussion of the C_S corrector in Section 2.3.3, however the importance of chromatic effects dramatically increases the number of aberrations which need to be considered. The lenses in the spectrometer are complex, dodecapole elements and the extent of the user control over these in spectrum (as opposed to EFTEM) operation is limited to spectrum focusing and manual compensation for low order aberrations [165]. Other alignments and tuning of the spectrometer are carried out at the service level or automated, and obscured from the typical user. The corrected spectrum is then brought into focus at the energy-selecting slit, which is shown between the third and fourth dodecapole lenses in Fig.2.12. This slit is primarily used in EFTEM, where it is used to admit electrons in a specific energy-range to form an energy-filtered image, but it is also used when recording spectra to catch electrons outside the region of interest and prevent stray scattering contributions to the recorded spectrum. The remaining lenses then magnify the spectrum to the desired dispersion for parallel recording on a CCD.

One of the biggest strengths of EELS in the TEM is the ability to synchronise the spectrometer acquisition with STEM image recording – i.e. an energy-loss spectrum is recorded with the same spatial resolution of the STEM image to form a STEM-EELS ‘Spectrum Image’ (SI) [191–193]. The essence of this methodology is illustrated in Figure 2.13, which shows a representation of the contents of an SI dataset. For each point in a STEM raster scan, the spectrometer records a single spectrum, thus gradually building up a 3-d array of data about the specimen [191]. The STEM-EELS spectrum image can be considered analogous to an EFTEM datacube, where the energy filtered by the slit is varied to collect many images while scanning through a range of energy-losses [194]. The reciprocity of EFTEM and STEM-EELS is indicated in Fig.2.13, where a 3d dataset could be build up using either

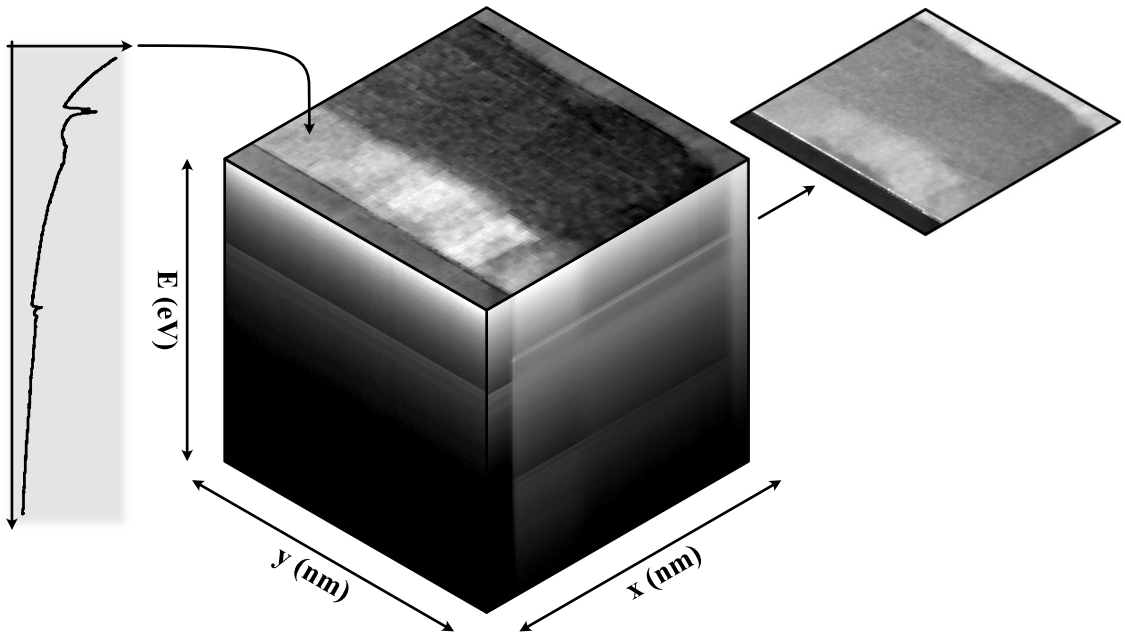

Figure 2.13: 3-dimensional representation of an EELS SI data-cube from a cross-section of a thin film multilayer, with spatial scan dimensions in the x and y directions, and the energy-loss data contained in the z direction. Either side of the data-cube, a representation of a typical portion of an energy-loss spectrum from a single (x,y) coordinate (left) extending from ~400–1200 eV, and an image formed by selecting a single energy (E) value (right).

site-specific spectra in STEM – as shown left of the cube – or by collating images at different energies in TEM, like the energy-slice shown to the right of the cube.

Another method in EELS which has been critical in this work to the accurate processing of spectra is Dual-EELS. This method circumvents issues in attempting to record data with such a large dynamic range using a charge-coupled-device (CCD). Instead of trying to acquire the full signal of interest in one exposure, which will inevitably result in a severe degradation of the signal-to-noise ratio at higher energy-losses, dual-EELS exploits the ability to rapidly displace the electron beam using an electrostatic shutter [195], creating two exposures of the spectrum on different halves of a CCD detector. On one half, the very intense zero-loss and low-loss range of the spectrum are recorded using a short exposure time then, at the same time the spectrum is switched to the other half of the CCD and the drift tube can be used to shift the spectrum in energy to record a high-loss region with a longer exposure [196]. This fast switching between low and high-loss regions of the spectrum is also compatible with the STEM-EELS spectrum imaging methodology, enabling acquisition of both low and high-loss spectrum images simultaneously [197].

The nuances of acquiring and processing STEM-EELS data are described throughout

Chapter 4, which includes detailed discussion of some finer points involved in EELS methodologies, including refinements in processes which have been made as part of this work.

2.4 Other Microscopies and Techniques

Throughout this thesis, the primary tool for performing analytical work and characterisation is the transmission electron microscope (TEM). Other techniques and methods outside of the TEM can often provide information that is complementary to that found in the microscope, or can fill in gaps in understanding where certain information is beyond the capabilities of the TEM. This is especially relevant when attempting to draw connections between properties observed on different length-scales and can facilitate the analysis of bulk material properties in relation to the observed micro and nano-structure. Herein, two techniques which have been used to complement TEM work are outlined; atomic force microscopy (AFM) and single-crystal X-ray diffraction (XRD).

2.4.1 Atomic Force Microscopy

Atomic force microscopy (AFM) is a scanning probe microscope technique used to image and make measurements of the surfaces of materials. In AFM, a sharp tip placed on the end of a cantilever is rastered across the specimen surface. Images are formed by recording the deflections of this tip due to Van-der-Waals interactions with the surface, which makes AFM universally applicable to conducting and insulating specimens, unlike the similar scanning tunneling microscopy technique [198, 199]. There are various ways of implementing AFM that vary in whether the tip is brought in contact with the surface. Here, a non-contact tapping mode has been used, where the cantilever oscillates with a drive frequency close to resonance conditions. As the tip is rastered, variations in the specimen-tip separation change the strength of the van-der-Waals interaction, which have a damping effect on the tip oscillation. This damping can convey two types of information about the sample, delivered through the amplitude and phase of the tip oscillation. Changes in amplitude directly relate to changes in separation, while any change in phase introduced by damping indicates a change in the chemical interaction between specimen and tip, which can be used to differentiate between different materials [200]. The AFM is illustrated in Figure 2.14, showing the tip cantilever

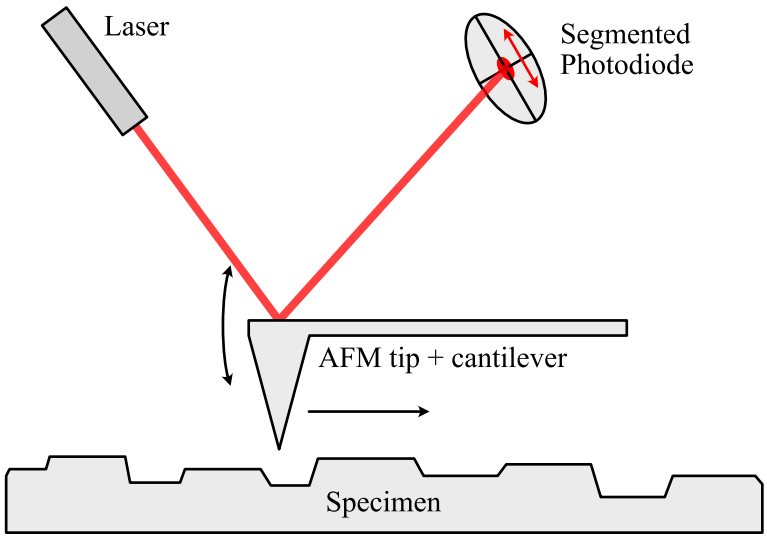

Figure 2.14: Cartoon of tapping-mode AFM. The silicon cantilever has a reflective back side which acts as a mirror for the laser system. The laser is centred on a segmented photo-diode, and small shifts in the cantilever height deflect the laser which is measured as a difference in the signal between diode segments.

oscillating above the surface. The magnitude of the damping effect on the tip by van-der-Waals forces is very small, so an optical system where a laser beam is reflected from the back of the tip amplifies the effect of the cantilever motion, increasing sensitivity to the small changes [201], which is also indicated in Figure 2.14.

All AFM measurements presented throughout this work were recorded using the tapping method on a *Digital Instruments* Dimension 3100 atomic force microscope. Antimony-doped silicon AFM probes from Bruker [202] (model TESPA-V2) with a 320 kHz cantilever resonance frequency were used.

2.4.2 X-Ray Diffraction

The diffraction concepts introduced in Section 2.3.1 apply equally to X-rays as they did to electrons in the TEM. The key differences lie in the volume of material probed in each technique, and the wavelength of radiation used. In TEM, as discussed in Section:2.3.6, diffraction yields structural information from a relatively small nano- or micro-scale volume of material and a large number of diffraction peaks can be recorded because of the relatively short wavelength of 200 keV electrons. Conversely, X-ray diffraction (XRD) typically probes millimetre-scale volumes of material, but the typical wavelengths of X-rays used (~1 Å) is comparable to the lattice spacings in materials, so the Ewald sphere for XRD is very small

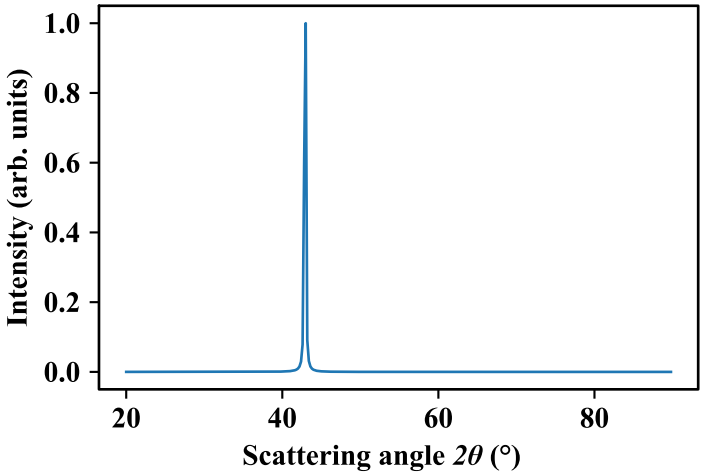

Figure 2.15: Example of a single-crystal XRD $\theta - 2\theta$ measurement simulated for a pristine MgO substrate with a surface hkl *of* 001*, using a Cu Kα X-ray source. Only the* 002 *reflection can be found when probing planes parallel to the surface.*

and typically very few peaks can be observed. This becomes apparent in Figure 2.15, which shows a simulated XRD pattern of single-crystal MgO where only a single peak is observable. Although XRD patterns contain fewer peaks than TEM diffraction patterns, X-ray crystallography is a highly complementary technique to TEM diffraction, as it provides summary structural information from a much larger volume of material with excellent precision. This is useful in developing an understanding the broader structural characteristics of a specimen, which can ensure that TEM observations from a much smaller sub-section are representative of the whole.

An X-ray diffractometer consists of an X-ray source and monochromator, a six-axis specimen manipulator stage and a counting detector which admits X-rays reflected from the specimen at one specific angle. To assess the crystal structure of a thin film using XRD, the diffractometer is operated using the $\theta - 2\theta$ method. In this procedure, the specimen and detector are tilted so that the angle of incidence and the angle of the detected reflection θ match. This establishes a geometry like that shown in Figure 2.8(a) on p.64, where the incident and reflected rays are symmetrical relative to the normal of some set of atomic planes. The angle θ is adjusted through a specified tilt sequence, with the X-ray count at each θ recorded by the detector. The intensity observed at a given angle is dependent on whether the Bragg condition is satisfied for that θ.

XRD $\theta - 2\theta$ measurements were performed using a PANalytical X'Pert3 diffractometer with a monochromated source of Cu Kα_1 radiation (wavelength 1.541 Å [97]). A scan step

size of 0.001° was used in these measurements, with a typical dwell time of 3 seconds to record sufficient counts from the thin films. With these settings, a typical wide-angle scan covering 2θ values from 25° to 65° took roughly 15 hours to acquire. As the nature of the data obtained from XRD did not vary significantly between specimens, the peak corresponding to the |002| reflection of the MgO substrate was used for calibration.

2.5 Utilisation of methods in this thesis

The methods, techniques and instrumentation which have been outlined in this chapter form the basis of the experimental investigations presented throughout the results chapters that follow. Thin films grown by PLD as described in Section 2.1 are the basis of investigations throughout the entire thesis and the optimisation of their growth is presented in Figure 5 along with TEM & STEM nano-characterisation of them, complemented by XRD and AFM. PLD-grown thin films are also studied in Chapters 6 and 7 and all TEM specimens are prepared using the FIB sectioning methods presented in Section 2.2.

STEM-EELS spectrum imaging, as described in Section 2.3.7, forms the core of the STEM analyses presented throughout. Developments in spectrum calibration are described in Chapter 3 and absolute elemental quantification of EELS spectra in Chapter 4, with these refinements used in results presented in the remaining results chapters. The use of SPED in conjunction with STEM-EELS for correlative structural and chemical analysis in STEM is introduced in Chapter 7.

It's so tedious writing cookbooks or writing the recipes
because I've never been much of a measurer.
But to write a book, you have to measure everything.

Maya Angelou

3

Measurement and correction of remanent aberrations in a post-column electron energy-loss spectrometer

Electron Energy-loss Spectroscopy (EELS) is an incredible addition to the techniques available in the transmission electron microscope, complementing images with a wealth of data from the inelastic interactions which occur within the specimen [111]. Spatially resolved measurements of inelastic interactions with the specimen provide compositional [203], valence [204] and even vibrational [205] properties of materials down to the atomic scale. The popularity of the technique has increased over time, as improvements in spectrometer design [165, 192, 196, 206, 207] and control hardware/software [191, 193, 208, 209] have simplified the acquisition of EELS datasets. The ease of operation of the spectrometer enables EELS to be combined with the scanning transmission electron microscopy (STEM) methodology to obtain spectral information at the nanoscale.

Measurements of the energy-losses of features in STEM-EELS spectra are typically made

in a relative sense. There are, however, situations where an absolute measurement is preferable. This is most obviously pertinent to the analysis of fine structure close to the onset of core-loss edges. These features provide a representation of a material's unoccupied electronic density of states, and thus vary with the atomic bonding geometry and oxidation states of elements. There has been extensive study of such effects in the literature for the first-row transition metals where, broadly speaking, the onset of the $L_{2,3}$ edge shifts on the order of 1 eV per unit of formal charge [210, 211], reflecting an increase in the binding energy of the 2*p* electronic state of the transition metal atom. Thus, accurate measurements could enable identification of bonding configurations by oxidation state. As measurements such as this are typically carried out without absolute calibration, the position in energy of core-loss features found in published literature can vary by over 2 eV [210, 212] and the opportunity for greater chemical information is lost. Verifying the accuracy of measurements onto an absolute scale usually requires comparison to be made with a well-understood and relatively stable reference material under the same spectrometer conditions [207, 211, 213], effectively relying on calibration of a single channel in the spectrum and extrapolating the calibration of the rest of the spectrum using the reference. Such a procedure is an arduous undertaking and thus is rarely performed in day-to-day use, as such a calibration would be susceptible to time-dependent environmental factors such as the electromagnetic and thermal conditions in the microscope room, hysteresis effects in the magnetic electron-optics, changes to the alignment of the microscope and even the presence of magnetic materials in the lab [207–209, 214, 215]. In practice, all these effects can alter the energy-dispersion – the rate of change of electron trajectory by energy – of the spectrometer, causing a problem in comparing data collected under different acquisition conditions or at different times, even on the same microscope.

In this chapter, several factors affecting the capacity for absolute energy calibration in the spectrometer are explored and a method is presented which enables the measurement, characterisation and post-acquisition correction of non-uniformities in the dispersion. Ideally, if chemical shifts are to be analysed adequately on an absolute scale, an accuracy of 0.1 eV or better is desirable, providing sufficient energy-resolution for accurate energy measurements. Calibration errors observed to be as small as 1% of the nominal energy dispersion are still sufficiently large as to prevent absolute measurements of the energy of a feature in the energy-loss spectrum. Without altering the existing spectrometer alignments, the new method for characterising the spectrometer rapidly probes the energy dispersion of the spectrometer while avoiding the need for reference materials for calibration. These standard-less measurements greatly simplify the characterisation of the spectrometer behaviour and facil-

itate our ability to correct the energy scale of real data, reducing the calibration error by an order of magnitude, to within 0.1% of the nominal dispersion. The effectiveness of the correction algorithm is demonstrated through implementation on real data, and the reduced error is found to be sufficiently low to consider the spectra in terms of absolute energy-loss. This, as already discussed, is of great benefit to measurements of chemical shifts and fine structure. These improvements are also useful for the absolute measurement of chemical composition described in Chapter 4, ensuring proper energy alignment of spectra with data from experimental reference materials.

The experimental protocols and results presented throughout this chapter have also been featured in a co-authored article in *Ultramicroscopy* [216].

3.1 Behaviour of a post-column EELS spectrometer

In scanning transmission electron microscopy (STEM), a focused, near-monochromatic electron probe is rastered across a thin specimen and interactions with the specimen at each location involve inelastic scattering which cause a fraction of the electrons in the beam to lose energy. A spectrometer placed at the end of the optic axis of the microscope ('post-column') collects the polychromatic electrons transmitted through the specimen and disperses the beam by energy. To achieve this, the post-column imaging filter exploits the Lorentz force electrons experience when passing through a magnetic field, and how the force experienced varies with the electron kinetic energy/momentum. The primary component of the EELS spectrometer which achieves this is the sector-magnet prism. Electrons passing through the prism experience a magnetic field perpendicular to their propagation, which typically bends their path through 90°. Complex electron optical lenses after the prism then magnify, focus and remove multiple orders of aberrations to transfer the spectrum generated by the prism onto a planar CCD camera [165, 192]. The energy dispersion – the amount by which the electron path is changed as a function of energy – created by the magnetic prism in the spectrometer should ideally be a straightforward linear spread of energies in the dispersion plane. This is critical to the operation of the spectrometer in parallel-EELS (pEELS) mode, where a range of the energy-loss spectrum is collected simultaneously through exposure on a CCD camera. However, the spread in energy due to Lorentz force is inherently non-linear and must be linearised by the post-prism optics.

3.1.1 A simple model for the dispersive effect of a sector magnet

The energy dispersion of the prism, through consideration of Lorentz force and of relativistic effects, does not behave linearly in energy and complex electron-optical elements are required to remove this and other aberrations affecting measurements in the spectrometer. Ignoring these complexities for the moment, the dispersion created by the Lorentz force on the beam from passing through the prism is described – including a relativistic correction – by

$$BR = \sqrt{\frac{2m_0E}{e^2}\left(1+\frac{E}{2m_0c^2}\right)}\,, \tag{3.1}$$

where B is the magnetic flux inside the sector magnet, R is the radius of curvature of the path of the electron beam, E is the kinetic energy of electrons passing through the prism, e is the magnitude of charge on an electron and m_0c^2 is the electron rest energy. This expression derives from equivalence of the Lorentz and classical centripetal forces, factoring in a relativistic correction to account for the high velocity of the in-going electrons. The energy of an electron (which originally had a primary energy, $e \times V$) passing through the prism, including an energy-loss ΔE and an energy gain due to acceleration by the drift tube with a positive potential V_{DT} is

$$E = e(V + V_{DT}) - \Delta E\,. \tag{3.2}$$

Throughout practical use of the spectrometer, the current through the sector magnet is fixed to maintain a stable field. Taking the differential over a fixed magnetic flux, Equation 3.1 can be used to determine the dispersion of the spectrum to be

$$D(B,R) = \left(\frac{\partial R}{\partial E}\right)^{-1}_{B} = \frac{Bec}{1+\frac{E}{2m_0c^2}}\sqrt{\frac{2E}{m_0c^2}\left(1+\frac{E}{2m_0c^2}\right)}\,, \tag{3.3}$$

thus illustrating that, for a fixed, uniform magnetic field, the dispersion of electrons through a given bend radius is not uniform, and varies non-linearly as a function of energy. Therefore, the image of the spectrum formed immediately after the prism is not scaled uniformly. This monotonic variation in the dispersion must be corrected by the post-prism lenses so that the spectrum which is projected onto the planar CCD detector is – ideally – linearly varying in energy. The dependence of the dispersion on the prism magnetic induction highlighted in Equation 3.3 also indicates that calibration of the optics to produce a linearised spectrum should ideally be carried out with the same prism current as that which is used for experi-

ments.

3.1.2 Spectrometer aberrations and transfer matrix theory

Moving beyond the basic effect of the sector magnet prism, some consideration needs to be given to aberrations in the spectrum, and how the post-prism lenses are used to correct for these aberrations. Although the description of the dispersion in Equation 3.3 gives a reasonable approximation of how electrons will be dispersed while travelling through the prism, it gives no consideration to how electrons react when entering and exiting the magnetic field in the drift tube. Edge/fringe effects of the magnetic field are important in understanding how the sector magnet influences the electron paths, and there is a significant body of work (both in electron microscopy and in high energy particle physics) dedicated to understanding their effects [111, 217–221].

The theory concerning spectral aberrations has been distilled into a relatively convenient mathematical description called the *transfer matrix*, which converts the properties of the incoming electron to the trajectory it would have upon exiting the prism, describing the effect of the magnetic field on the electron. Much as in the microscope itself, there are different orders of spectrometer aberrations which can be considered, and the transfer matrix can be expanded to include the effects of higher order aberrations. First order effects – which include the primary focusing, magnification and dispersive effects – are represented by the 6×6 transfer matrix [219];

$$\begin{pmatrix} x_i \\ \theta_i \\ y_i \\ \varphi_i \\ l_i \\ \delta_i \end{pmatrix} = \begin{pmatrix} R_{11} & R_{12} & 0 & 0 & 0 & R_{16} \\ R_{21} & R_{22} & 0 & 0 & 0 & R_{26} \\ 0 & 0 & R_{33} & R_{34} & 0 & 0 \\ 0 & 0 & R_{43} & R_{44} & 0 & 0 \\ R_{51} & R_{52} & 0 & 0 & 1 & R_{56} \\ 0 & 0 & 0 & 0 & 0 & 1 \end{pmatrix} \begin{pmatrix} x_0 \\ \theta_0 \\ y_0 \\ \varphi_0 \\ l_0 \\ \delta_0 \end{pmatrix} \tag{3.4}$$

which relates the electron properties at the image plane (position (x_i, y_i), angle (θ_i, φ_i), path length (l_i) and fractional deviation in momentum (δ_i)) to those corresponding properties at the object plane. Meanwhile, higher order aberrations are described by matrices which become exponentially more complex; resulting in 216 matrix terms for second order [111] and 2401 third order terms [220], resulting from the larger number of combinations available in higher-

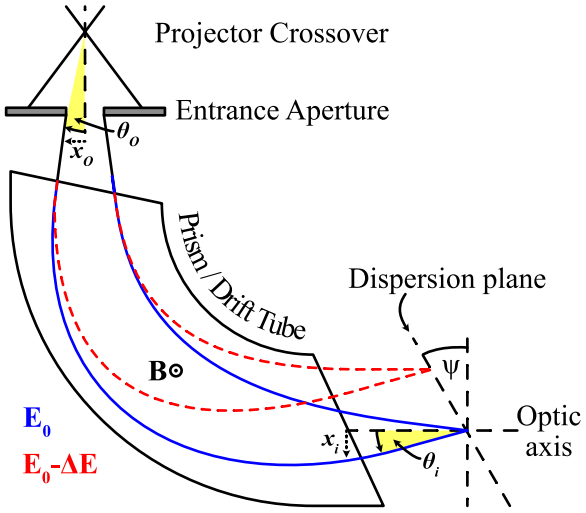

Figure 3.1: Illustration of the dispersive properties of a magnetic prism. In the Gatan GIF Quantum*, the flat, inclined faces of the drift tube are designed to create a gradient field effect, which is self-focusing. The directions of the x and θ terms of the prism geometry are labelled at either end of the prism, with the y and φ terms pointing out of the page.*

order derivatives. It is understood, thankfully, that many of these terms are either zero, or are inter-related through symmetries in the system, thereby reducing the number of coefficients which actually have to be compensated.

For the conditions which are specific to EELS, many of the aberration matrix terms mean very little, and only a handful of the terms we started out with have an important effect on the energy-loss spectrum. Significant first order properties include lateral and angular magnifications in x (R_{11} and R_{22}) and y (R_{33} and R_{44}) as well as the energy dispersion ($R_{16} = \partial x_i/\partial\delta_0$). The focusing properties of the prism are effectively represented by the coefficients R_{12} and R_{34} for the x and y directions, respectively. From these, and some of the second order terms, we can start to build a slightly more sophisticated image of how the sector magnet operates. In Figure 3.1, an illustration of how the prism operates in the Gatan GIF *Quantum* 965 ER, which is designed with straight, inclined pole faces to provide double-focusing (i.e. simultaneous focusing in both x and y) [165]. The geometries of the x and θ terms of the transfer matrix are indicated for both the image and object planes, with the y and φ terms pointing out of the page. As illustrated, the self-focusing nature of the prism in the *Quantum* means that electrons with the same energy follow a different path depending on their entry angle, resulting in all the electrons of that energy coming to a point on the dispersion plane (i.e. focused in x). However, a combination of the first order dispersion (R_{16}), first order magnification (R_{22}) and a second order dispersion aberration (T_{126}) dictate the position of the dispersion plane. As seen in Figure 3.1, the dispersion plane does not have to be perpendic-

ular to the optic axis and can instead lie some angle, ψ, away from the vertical. For imaging on a planar CCD camera parallel to the vertical, it is desirable to correct this spectrum tilt so the dispersion plane is correctly projected onto the detector. All of the aberration correction in the *Quantum* is achieved using the post-prism optics (shown in a full schematic of the spectrometer in Fig.2.12 on p.76), and includes correction of the spectrum tilt as well as aperture aberrations (T_{122}, T_{144}) which degrade the energy resolution [111] and some further third, fourth and fifth order aberrations which have been identified as important for EELS. It is worth noting, however, that the lowest order aberration coefficient which describes the non-linearity of the energy-loss axis (the second order coefficient $T_{166} = \partial^2 x_i / \partial^2 \delta_0$) is not targeted in the *Quantum* for correction [165] and is likely a major source of the non-uniformities which have been observed throughout this chapter.

3.1.3 Beam stability and spectrometer responsiveness

The data acquisition for the standard-less dispersion measurement protocol (which is described in full in Section 3.2) relies on precise control of the spectrometer to rapidly and incrementally shift the position of the spectrum on the detector many times. To understand the fidelity of the controls available for use in the automated measurements, as well as the stability of the microscope/spectrometer during operation, it is necessary to use easily reproducible tests to characterise the behaviour of some of the core functionality. In this regard, there are two key properties which need to be understood: the short- and long-term stability of the equipment as characterised by apparent variations in the beam energy, and the response times of the various modes of deflecting the spectrum to different positions along the energy axis of the spectrometer.

Tests of the beam stability were carried out by monitoring the position of the zero-loss peak over a 30 minute interval. To be sensitive to the long-term energy drift and also somewhat sensitive to high-frequency jitter, the sampling rate of the ZLP was set to be approximately 10 Hz. Results of the stability measurement are shown in Figure 3.2. The cumulative effect of beam instabilities and environmental factors led to an apparent drift in the primary energy of the beam at a rate of 0.07 eV/minute, as shown in Fig.3.2(a). The residuals of this measurement indicate a high-frequency jitter (Fig.3.2(b)) which is superimposed on this drift pattern, which has an RMS value of 0.06 eV. To obtain an accurate frequency spectrum for the rapid energy jitter, a shorter measurement – taken over the course of 5 minutes – was obtained using

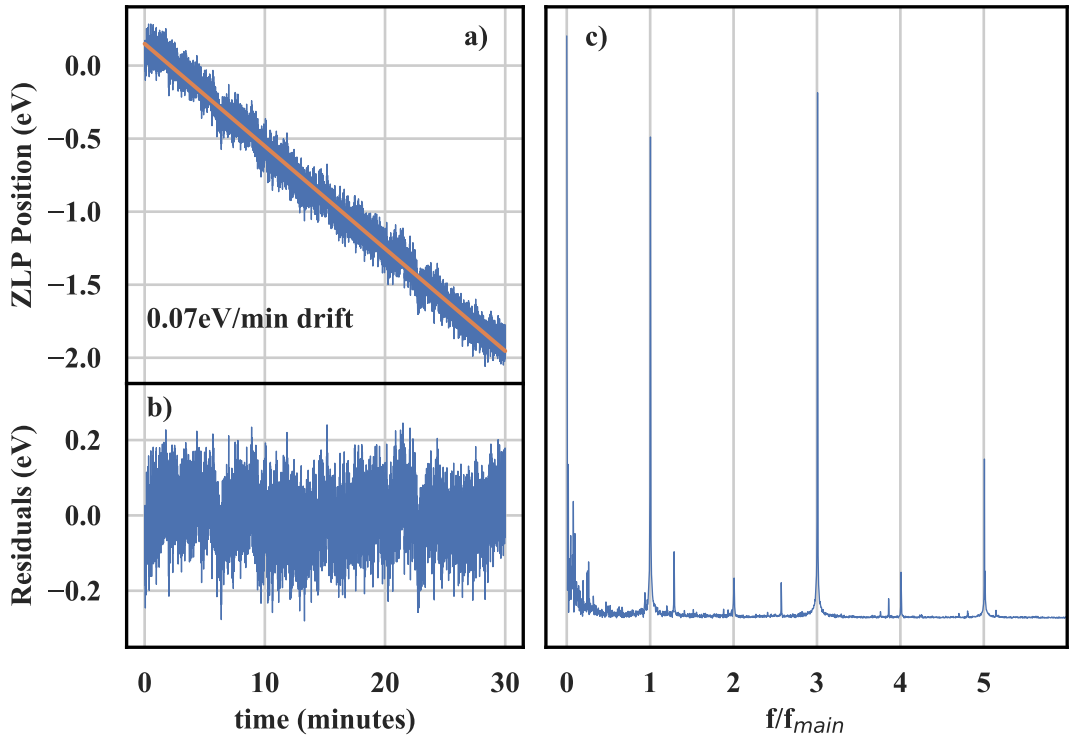

Figure 3.2: (a) Zero-loss peak (ZLP) position tracked over the course of 30 minutes (measured at a dispersion of 0.025 eV/ch). A linear fit indicates the overall rate of energy drift and is labelled. (b) Residuals of the linear fit indicate the extent of the high-frequency energy 'jitter', which has an RMS value of 0.06 eV. (c) A fast Fourier transform of the jitter is dominated by a series of harmonic frequencies. The frequency of the first dominant peak, f_{main}, likely corresponds to 50 Hz mains frequency.

the Digital Micrograph spectrum imaging tool. This allowed for higher fidelity acquisition than the live spectrum view and, for the same exposure time, improved the sampling rate to around 300 Hz. The frequency spectrum of this highly-sampled data was calculated using a fast Fourier transform which is presented in Fig.3.2(c). As there is some uncertainty in the sampling rate due to lack of knowledge of overheads in the hardware timings, it is not possible here to precisely calibrate the frequency spectrum to identify the strong, periodic peaks which feature throughout it, so the spectrum is presented with reference to the frequency of the first strong peak. It is not entirely unreasonable, however, that within the uncertainty of the sampling rate, these peaks correspond to multiples of the 50 Hz UK mains electricity frequency (the error range places the frequency of the first peak at somewhere between 40 and 60 Hz).

When it comes to user control over the portion of the energy-loss spectrum which is observed, there are three main methods which are available. Although there are nuances in the advantages and disadvantages of each method, the metric of interest here is their response times (i.e. the time taken for the spectrum to settle once an instantaneous offset is applied).

These have been measured and are presented in Figure 3.3. The first method is the 'prism adjust,' which controls the current on the sector magnet coils to vary the magnetic induction. Changes in the prism conditions settle relatively slowly (on the order of 1 second) and can also be subject to hysteretic effects. As such, the prism adjust control is not suitable for dynamic use in rapid data acquisition, though is frequently used to make minor adjustments to the position of the spectrum on the detector prior to a measurement. As is evident from our discussion in Section 3.1.1, use of the prism adjust control will introduce further complications, in that variations in the magnetic induction will also alter the dispersion from its nominal alignment.

The second available control of the spectrum position is the 'HT offset' which involves adjusting the primary beam energy by modulating the accelerating voltage (i.e. the high-tension, or HT) of the electron microscope. The key advantage of this method is that the microscope post-specimen lenses, the spectrometer prism and post-prism optics can all be aligned for a single electron energy, which can be selected within the spectrometer by placing a slit in the dispersion plane, as is typically done in the energy-filtered transmission electron

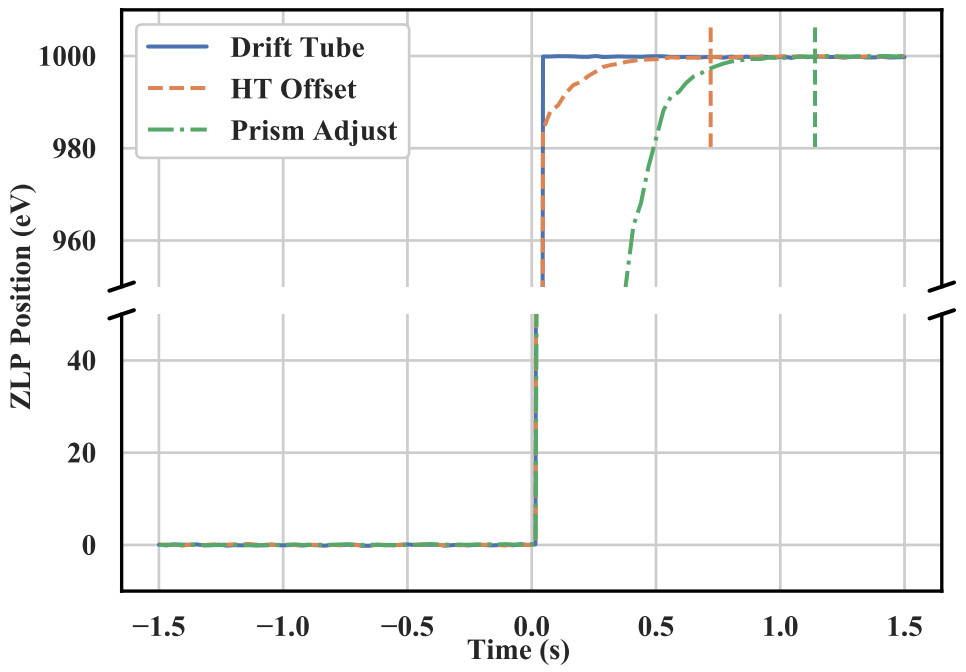

Figure 3.3: Measurement of the zero-loss peak position over a short period of time during which a sudden, 1 keV offset was applied to either the prism adjust, HT offset or drift tube offset. ZLPs were acquired using a 1 eV/ch dispersion. The times taken for the ZLP to settle to within 1 eV of its final value are 720 ± 15 *ms and* 1140 ± 10 *ms for the HT offset and prism adjust, respectively. The fast drift tube offset settled within the 5 ms sampling time used for the measurements.*

microscopy (EFTEM) methodology. Unfortunately, as the beam energy changes, chromatic aberrations in the microscope lenses result in a defocusing at the specimen plane, which must be manually corrected by refocusing the condenser lenses. Though faster to settle than the prism adjust, the HT offset is also slow (of order 100 ms, see Figure 3.3) and thus is also insufficiently dynamic for rapid STEM spectrum acquisitions.

Finally, the spectrum position can be set using the drift tube offset, whereby a positive potential is applied to the tubular electrode lining the drift tube. This potential accelerates electrons upon entering the prism, so that the feature with energy-loss ΔE that matches the energy $e \times V_{DT}$ passes through the prism with the original primary beam energy. The beam subsequently decelerates upon exiting the prism, and none of the other electron optics are changed [207]. The drift tube liner electrode is designed to have a low capacitance, such that the potential upon it can be changed rapidly (on the order of 10 µs) with minimal hysteresis so that it is suitable for dynamical adjustment during rapid spectrum acquisitions. The use of the fast drift tube offset already underpins the dualEELS methodology [196], where two regions of the energy-loss spectrum are acquired in quick succession by switching the drift tube voltage. The offset spectrum is also deflected onto a different, dedicated portion of the detector, so that the two regions are exposed rapidly in the same readout [165]. Using our measurement protocol, the drift tube offset appears to switch instantaneously and the timing of it cannot be ascertained. As the drift tube is designed for rapid switching faster than 10 µs during acquisition of dualEELS spectrum images, it should not be possible to resolve the motion of the spectrum due to drift tube offsets in the live spectrum view, which has a low frame rate.

3.2 A standard-less algorithm for measuring non-uniformities in the energy dispersion of a dual-EELS spectrometer

To measure the non-uniformities in the energy dispersion, a bespoke, automated acquisition routine was written using the Digital Micrograph (DM) scripting language. Operationally, it uses a similar principle to the method used for the ‘engineer alignment’ of the spectrometer dispersion, and also a recently published procedure for ‘energy offset correction’ of spectra, which shifts spectra through a small energy range for the purpose of averaging out fixed-pattern noise [222].

Prior to executing the script, the microscope is aligned using an amorphous specimen to optimise the Ronchigram and ensure the excitation of the objective lens is at a nominal, reproducible value (referred to as standard focus), with a STEM magnification which is sufficiently high ($\geq$ 1.5 $M\times$) to ensure the beam is close to the optic axis of the microscope. This is intended to minimise the variability in the microscope setup and reduce variations in the dispersion from sources external to the spectrometer. With the microscope optimally aligned at standard focus, the specimen is removed from the path of the beam, so that the zero-loss peak (ZLP) can be made as sharp and focused as possible by aligning the spectrometer focus controls and positioning the ZLP at the 'zoom point' (this is the 200th channel from the left-hand (high energy) edge of the CCD camera on the GIF *Quantum*).

Once set up with a focused ZLP at the zoom point, the acquisition script is initialised, opening a background thread in DM which grabs frames from the live view of the dualEELS spectrum. The process which the script follows as it monitors the live view is outlined in Figure 3.4. As the drift tube voltage offset can only be assigned positive values (i.e. can only be used to add energy to the beam passing through the drift tube), the ZLP must first be shifted to the right hand (high energy-loss) side of the CCD by another method, so that the drift tube can be used to displace the ZLP to any other point on the CCD. Two options for this initial peak shift are available to the user, and are indicated in the workflow by a separation into two paths in Figure 3.4. One is to use the prism adjust control to alter the prism current, and therefore the bend-radius of the zero-loss energy electrons. The other option is to keep the prism current constant, and instead reduce the primary beam energy using the 'HT offset.' When using the HT offset, the chromatic effect of the microscope optics mean that the lenses are now over-focusing for the reduced-energy beam, resulting in a defocus of the probe which must be rectified using the microscope condenser system. The choice of prism adjust versus HT offset has consequences which will be discussed later but, in either case, it was not necessary to refocus any of the spectrometer optics.

After the initial peak shift, the drift tube was then used to incrementally deflect the ZLP across the detector, taking advantage of the dualEELS system to rapidly acquire both the deflected and undeflected peak for each increment of the drift tube voltage. These can be seen in the 'high-loss' and 'low-loss' images in Figure 3.4, along with a graph showing a small section of the measurement, with the ZLP position changing with increasing drift tube voltage. The deflection is incremented until the ZLP has been positioned at points that span the full field of view of the detector. This results in two spectrum images (SIs), one which

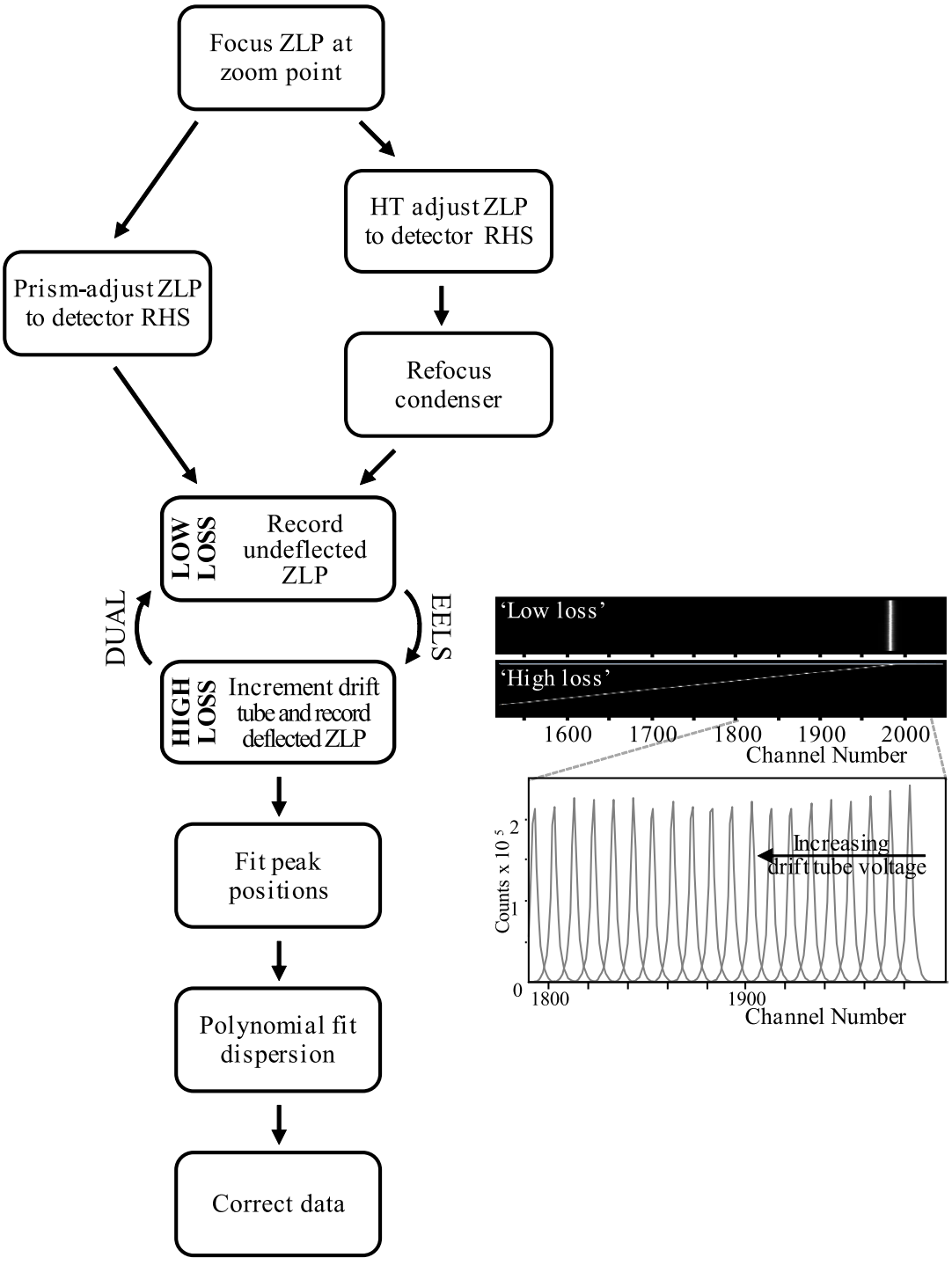

Figure 3.4: Flow diagram illustrating the procedure for measuring non-uniformities in the dispersion. After using either the prism or beam energy offsets to shift the spectrum, the drift tube is used to step the ZLP toward the left of the CCD camera. An example of the kind of data gathered by this procedure is shown. This diagram is adapted from the co-authored paper describing this work [216].

contains the undeflected peak which sits stationary at the right hand side of the detector, and the other which contains the deflected ZLP, which appears at a different position in each row of the dataset.

3.2.1 From data to measurement I: calculating the observed dispersion

The spectrum images produced by the standard-less measurement contain all the data required to measure details about the energy dispersion of the spectrometer, including position dependent variations. Processing the data initially involves mapping the position of the ZLP in all frames of the acquisition. Position-mapping is achieved in two stages, the first of which is a simple location of the position of maximum intensity (which should always be the centre of the ZLP), providing the ZLP centre position with pixel-level precision. Once the ZLPs have been located, the result of this rough calculation was used to provide the estimate for the centre position in a Gaussian fit of the peaks. The Gaussian fit also takes as estimates the intensity value of the centre pixel, and the initial condition for the width was taken as the reciprocal of the nominal dispersion (e.g. a width of 2 pixels for a 0.5 eV/ch dispersion), which provides a reasonable approximation of the ~1 eV peak FWHM. The low intensity tails of the ZLP are omitted from the fit by thresholding at a fraction of the peak intensity, as the tails typically do not follow a Gaussian distribution. This fitting stage in the processing enhances the original estimate of the peak centre to sub-pixel precision. Other peak shapes, such as Lorentzian or pseudo-Voigt, were tested but were not found to confer any advantage over the Gaussian profile.

With the positions of the zero-loss peaks accurately determined, the next step in processing is to relate the measured peak shift to the applied energy offset (using the drift tube). Plotting the peak positions against the applied offsets yields a relationship that is predominantly a straight line, as shown in Figure 3.5. The line shown in this figure – which intersects the x-axis at the position of the reference ZLP position – is the result of calculating peak positions for a measurement probing the 0.5 eV/ch dispersion using an initial HT offset. The gradient of this line provides directly an overall value for the observed energy dispersion which, in this case, is 0.4976 eV/ch; about 0.5% lower than the nominal value. It is at this point that we begin to observe differences in outcomes depending on whether the initial offset was made using the prism adjust or the HT offset. For the same measurement as in Figure 3.5, but using an initial prism adjust, the dispersion was observed to be 0.4996 eV/ch; which agrees

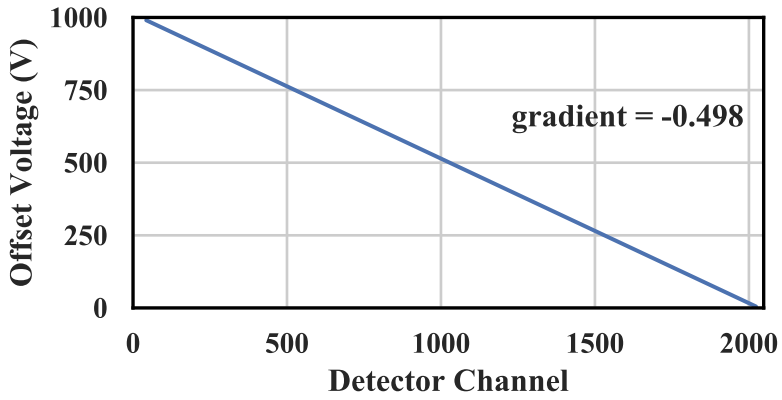

Figure 3.5: Applied voltage offset as it relates to the position of the deflected ZLP on the detector for a dispersion which is nominally 0.5 eV/ch. Calculating the gradient of this line provides the dispersion which is actually observed. Note that the data used to create this line used an initial HT offset; using an initial prism offset instead provides a gradient which agrees with the nominal dispersion to within 0.1 %.

with the nominal dispersion to 0.08%. This, in the absence of anything else, highlights the impact of varying the prism adjust control on the dispersion. Although this difference may appear small, the dispersion is a differential term which will accumulate when considering an increasing number of channels. Across the full field of view, this small deviation can result in an error as large as 10 eV at a dispersion of 0.5 eV/ch.

Considering now all the available dispersion settings in the spectrometer, we wish to know more about the position-dependent variations in the dispersions. To calculate these, the linear trend corresponding to the expected peak positions for the nominal dispersion is subtracted from the observed trend. The remaining profile corresponds to the position specific deviations from the nominal dispersion and these are shown for all available dispersion settings on the *Quantum* in Figure 3.6. As has already been established, the effective dispersion that is observed is dependent upon the initial offset method that is used, as changes to the magnetic induction of the prism are known to affect the energy dispersion. Consequently, we should also anticipate that the deviations from the nominal dispersion will differ depending on which offset method is used. As such, the deviations from the nominal energy of a channel are presented for both the HT offset and the prism adjust in panels (a) and (b) of Figure 3.6, respectively. The largest differences between the two datasets are in the lowest dispersions (1, 0.5 & 0.25 eV/ch) as these require the largest initial shift of the spectrum and, therefore, utilise the largest prism adjust (and implied change in the dispersion). The measured dispersion values for all settings are laid out in Table 3.1 and are also indicated in the legend of Figure 3.6. Similar characterisation of dispersion errors as shown in the prism-adjust meas-

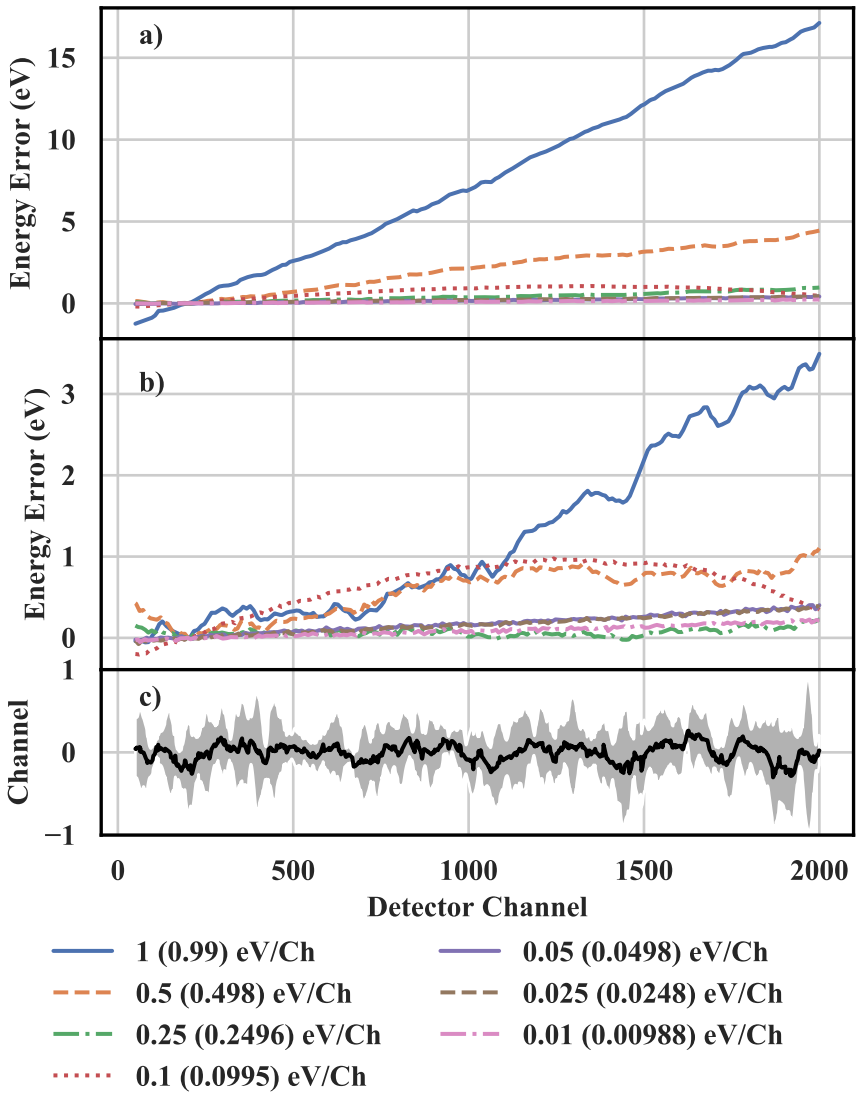

Figure 3.6: Measured dispersion deviations for each of the nominal dispersion settings, found by using (a) a starting offset in the primary beam voltage and (b) a starting offset in the prism adjust. (c) The mean (black line) and standard deviation (shaded region) of the residuals for all dispersions after a polynomial fit has been subtracted from each non-uniformity profile. The legend indicates the nominal dispersion for each trace, along with the measured dispersion (in brackets) for the HT offset data.

urements in Fig.3.6(b) and Table 3.1 have previously been reported [213]. The authors of that study proposed only making use of spectra recorded on regions of the detector where errors were sufficiently small, guaranteeing accurate calibration of the energy axis. As the HT offset method leaves the prism in its normal operating condition, this is the preferred method for measuring the dispersion and its non-uniformities. Given the difference (especially for the lowest dispersions) between the magnitude of errors observed when using an initial prism-adjust or HT offset, the errors in Fig.3.6(a) suggest that the calibration of the dispersion can only be relied upon very close to the zoom point, necessitating correction of dispersion errors. Further, when it comes to using these measurements to correct real data,

δE (Nom.)	δE (HT)	% Error	δE (Prism)	% Error
1 eV/ch	0.990	1 %	0.9982	0.18 %
0.5 eV/ch	0.4976	0.4 %	0.4996	0.08 %
0.25 eV/ch	0.2495	0.2 %	0.2499	0.01 %
0.1 eV/ch	0.0995	0.5 %	0.0996	0.4 %
0.05 eV/ch	0.0497	0.6 %	0.0498	0.4 %
0.025 eV/ch	0.0248	0.8 %	0.0248	0.8 %
0.01 eV/ch	0.00986	1.4 %	0.00988	1.2 %

Table 3.1: The dispersion (δE) settings on the Quantum *and the observed dispersion values found using the HT offset and prism adjust methods, along with their respective errors relative to the nominal value.*

the energy deviations described by the prism-adjust datasets do not sufficiently account for observed errors in the positions of real features.

3.2.2 From data to measurement II: calculating other properties

The primary purpose of the automated measurement outlined in Figure 3.4 is to facilitate calculation of position-dependent errors in the energy dispersion, as is illustrated in Figure 3.6. However, the data produced by the measurement – which is just a collection of ZLPs – can be used to characterise other properties, such as position-dependent variations in spectrum focus. Relative differences in focus across the detector can be estimated extracting the peak width of the ZLPs, which is calculated as part of the Gaussian fit used to determine the peak position. The peak width of a ZLP is directly related to the spectrum focus, as the peaks should progressively broaden as the spectrum defocuses. One source of inconsistent focus throughout the spectrum would be a misalignment of the spectrum tilt. As discussed in Section 3.1.2, the spectrum tilt encapsulates the compounded effect of first order dispersion and magnification, as well as second order dispersion aberrations. If the spectrum tilt has not been properly compensated by the post-prism optics, the dispersion plane will not coincide fully with the detector plane and only part of the spectrum will be properly focused. Spectrum tilt represents the lowest order effects which can cause the described misalignment; higher-order aberrations can potentially introduce more complicated effects that would effectively lead to curvature or ‘crinkling’ of the dispersion plane, creating more complex defocusing effects.

Results of measuring the peak width as a function of detector position are presented in Figure 3.7, where the widths of the deflected peaks in the scan have been normalised relative to the undeflected reference peak. For the three highest dispersions (0.01, 0.025 and

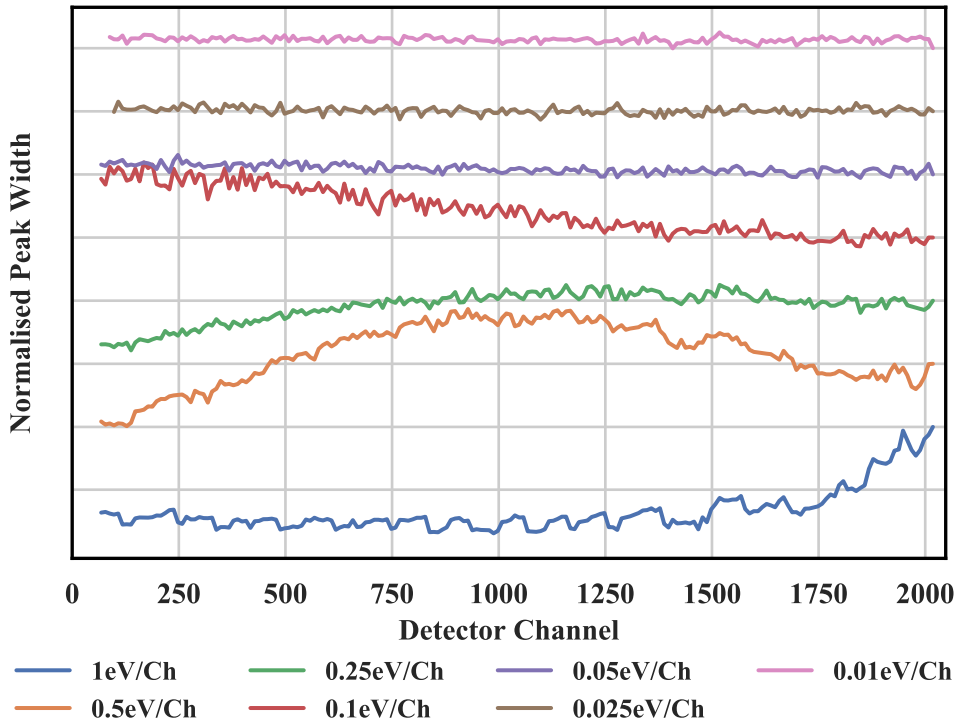

Figure 3.7: Variations in spectrum focus across the detector field of view, represented by the measured width of the scanned zero-loss peak from the automated dispersion measurement. All peak widths are normalised to the width of the reference peak (i.e. the right-most value) and each trace is offset for clarity. Variations in focus across the field of view are indicative of a misalignment of the dispersion and detector planes. Each horizontal gridline represents a 25 % increment in deviation from the reference peak width.

0.05 eV/channel) the focus of the ZLP remains uniform across the whole field of view, indicating a good alignment of the dispersion and detector planes. The lower dispersions, however, all show some variation in the ZLP focus, with the largest relative change shown for the 1 eV/ch dispersion setting (this dispersion also shows a lot of stochastic variation in width, demonstrating how the calculation is prone to errors when the peak width falls within a single channel). Observed variations in focus follow approximately parabolic trends that are consistent with an error in the spectrum tilt. If more complex behaviour is present, it is difficult to distinguish, suggesting the effect of higher order aberrations on the dispersion plane are negligible compared to the effect of tilt. The fact that the lowest dispersions are worst affected is most likely a symptom of the spectrometer alignment, as the prism settings have to be driven farthest away from nominal operating conditions to verify the calibrations at these dispersions (i.e. the same reason the deviations in calibration in Fig.3.6(a) are largest at the lowest dispersions).

Further to the slight position-variant defocus of the spectrum shown in Figure 3.7, the error in spectrum tilt can also introduce an error in spectrum magnification (matrix term R_{22}

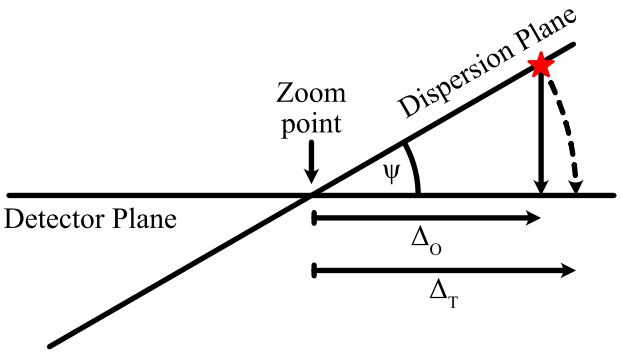

Figure 3.8: Graphical representation of the (exaggerated) impact of spectrum tilt on projection of the spectrum onto the detector. A feature at some energy loss in the spectrum (red star) is projected directly onto the detector plane along the solid arrow and observed at position Δ_O. If the spectrum tilt were compensated – i.e. the dispersion plane is rotated – the position of the red star feature would be translated onto the detector plane following the dashed arrow and observed at position Δ_T.

on p.87). The impact of the magnification error, which is illustrated in Figure 3.8, can be understood in terms of the projection of the dispersion plane onto the detector plane. When the dispersion and detector planes are not parallel, projection onto the detector introduces a contraction in the size of the image of the spectrum proportional to the mis-tilt. The magnitude of the projection error is energy-dependent, with the energy calibration error increasing for energy-loss features further from the primary beam energy. Additionally, as the spectrum tilt is different for each dispersion mode, the calibration error described by this effect is dispersion-dependent as well as energy-dependent.

Evidence for this error is presented in Figure 3.9, which shows part of the near-edge structure of the carbon *K* edge of diamond recorded using different spectrometer dispersions. These spectra were recorded with a drift tube offset of 302 eV, which should centre the large trough in the ELNES at the zoom point on the detector. Instead, the position of the spectrum on the detector is found to vary with the dispersion. This was surprising, as the calibration of the zoom-point is expected to be reliable. The discrepancy is understood in terms of chromatic effects, as the post-prism optics are effectively aligned for the primary beam energy only. Thus, when the drift tube offset is used to place a feature at the zoom point by acceleration of electrons through the prism, the subsequent deceleration of electrons upon leaving the prism means that loss electrons do not pass through the post-prism optics correctly, leading to the observed error at the zoom point (hereafter referred to as the *zoom-point error*). The energy-dependence of the zoom-point error is easily tested using the ZLP. In principle, applying a HT offset to the beam and compensating with an equal but opposite drift tube offset should not affect the position of the ZLP on the energy axis; it should remain

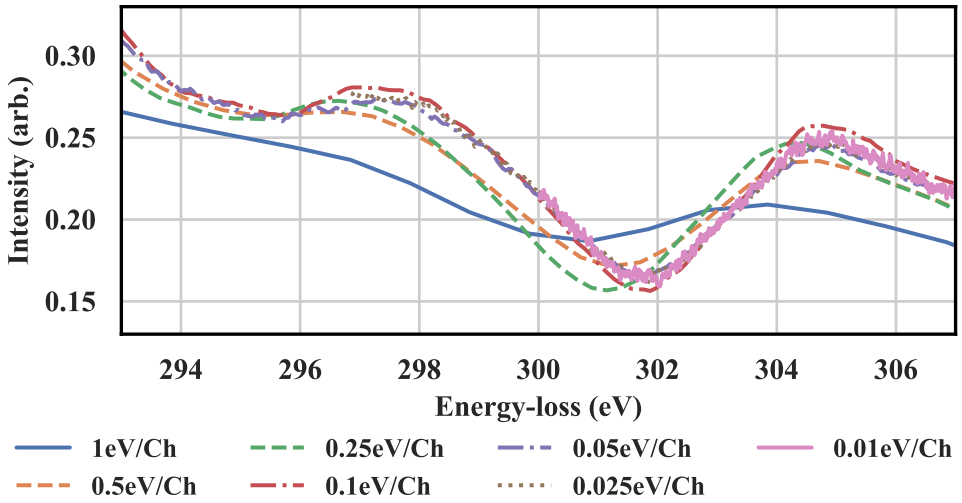

Figure 3.9: Acquisition of the carbon K edge of diamond, using a drift tube offset of 302 eV. This offset should place the band-gap trough in the fine structure at the zoom point of the detector and should therefore be free from errors. Yet a clear systematic error is present.

at the zoom point. In the presence of the discussed effects, the zoom-point error introduce a shift in position proportional to the size of the energy offset, ΔE. A cursory test of this nature reveals that zoom-point-errors of 1.5 eV and 3.5 eV are found for ΔE values of 270 eV and 900 eV respectively.

The same information about the zoom-point-error can also be extracted from the standard-less dispersion measurement data. Using the un-deflected reference ZLP, which has only been shifted by a HT offset, there is a discrepancy between the observed position of this peak, and the target position which the HT offset should have achieved. This discrepancy is the same as would be found for the zoom-point-error if a matching drift tube offset had been applied, and so can be used as a correction factor to modify the dispersion non-uniformity profile. With this difference determined, it can be used to calculate a linear, energy dependent scaling factor which pragmatically describes how to modify the dispersion;

$$C = D\left(\frac{\Delta_O - \Delta_T}{\Delta_T}\right), \tag{3.5}$$

where Δ_O is the observed shift, Δ_T is the target shift and D is the nominal dispersion value. These shifts are illustrated in Figure 3.8, which demonstrates the chromatic discrepancy which is compensated by this correction. C then represents the gradient of a linear term in energy which is added to the existing position-dependent non-uniformity profile; i.e. C will modify the slope of the profiles in Fig.3.6(a). As this term is a function of energy, rather than position on the detector, integrating this term into the correction algorithm will slightly

change the nature of the correction between low-loss and high-loss regions of a dualEELS spectrum, as equivalent positions on the detector will have different energy calibrations due to the drift tube offset.

3.2.3 Restoring data to its nominal dispersion

The dispersion measurements discussed in Section 3.2.1 provide the key to correcting spectra for a uniform energy-loss calibration that matches the nominal dispersion. The non-uniformity profiles shown in Figure 3.6(a), which denote position-dependent deviations from the nominal calibration, provide a 'map' which can be used to convert between the expected and observed positions of features in the spectrum, allowing the spectrum to be re-sampled by interpolation. Fitting a fifth order polynomial to the non-uniformity profile provides a smoothly-varying, continuously differentiable map, which can be used to interpolate the data from its non-uniform binning onto a uniform grid representative of the nominal dispersion. The choice of a 5^{th} order polynomial is ultimately arbitrary, but is found to provide a good approximation to the trends shown in Figure 3.6. The use of the polynomial is reasonable as the electron-optical aberrations leading to non-linearities in the dispersion are differential terms (like the previously discussed T_{166}) which should be smoothly-varying across the field of view.

The residuals of the polynomial fits contain higher frequency variations which appear to be common to all dispersions (see Figure 3.6(c), especially variations between channels 1500 and 1800). As they manifest independently of the dispersion, they are likely a feature of the detector which arise from the kind of fixed-pattern variations which has been explored elsewhere [209, 222]. It is probable that they derive from the physical construction of the detector, which involves a scintillator coupled to a pixelated CCD camera by way of a honeycomb fibre-optic lattice [165]. The mismatch in shape of the pixel array and the fibre-optic lattice may cause a slight redistribution of counts between channels. This is important because such redistribution would cause an apparent sub-channel shift in an edge and limit the precision to which the energy-loss of a feature can be determined. As the magnitude of these fixed-pattern variations is about one-fifth of a channel in the worst cases, this likely places a lower-bound on the level of precision we can expect to achieve in the corrected spectra. This lower-bound could be overcome by adopting the approach of Wang *et al.* [222], where the spectrum offset is shifted incrementally over a small range during measurement, moving

the spectrum relative to the fixed pattern so that these variations are averaged out when the shifted spectra are aligned and summed.

Re-sampling of the data from its observed, non-uniform dispersion onto a uniform grid is achieved by using the fitted polynomial profile as an interpolation map. The interpolation map acts as a set of instructions for how to construct the uniformly binned spectrum from the original, non-uniform data. Considering the dispersion profiles in Fig.3.6(a), if the *x*-axis denotes the channel numbers of the corrected spectrum, the value of the profile at each channel instructs the interpolation algorithm to pull intensity from a position *y* channels away from the current channel, where *y* is the observed deviation. For example, a positive deviation of 5 channels is an instruction to populate the channel in the corrected spectrum with the intensity from a position 5 channels to the right of that index in the original spectrum. Similarly, negative deviations are instructions to interpolate from channels to the left of the current position. Interpolation is carried out by a polynomial interpolation algorithm written in the DM scripting language which has been adapted from that provided in *Numerical Recipes for C* [223] and optimised for use on spectrum images in DM. The polynomial interpolation routine supports any degree of polynomial; a cubic interpolation was chosen as there is minimal improvement in precision of the interpolation when using higher order terms to be worth the trade-off in increased computational time. Care is also taken to correctly redistribute the channel intensities to take account of the non-uniform sampling, using the first derivative of the interpolation map to pre-adjust the recorded intensities and provide an intensity-preserving, Jacobian transformation of the data [224].

3.3 Improving the precision and accuracy of energy-loss measurements by correcting the energy dispersion

In testing the efficacy of the correction algorithm two specimens were studied. The first was a relatively thick specimen of nickel oxide (NiO). This was provided by Gatan and is routinely used for calibration of the fast drift tube offset in the spectrometer. The energy of the Ni L_3 peak maximum is commonly accepted as 852.75 eV[111, 225], though is taken as 853 eV during the engineer alignment of the spectrometer drift tube [226]. The use of NiO as a calibration standard is particularly advantageous because the impact of beam damage is minimal, with reduction of nickel to its metallic state only shifting the position of the L_3 peak maximum by about 0.2 eV [213, 227–229] as the d-band occupancy for the final state is

largely unchanged. The second material investigated was a single-crystal diamond specimen which was studied previously to understand the properties of laser-induced defects [230]. Diamond was chosen as it produces a strong EELS carbon *K* edge with fine-structure which is well characterised and the positions of features in the fine structure can be readily compared with X-ray absorption fine-structure (XAFS) measurements [231]. Here, we were interested in the undamaged regions of the diamond and, while beam damage effects may be subtle in NiO, beam damage in diamond can be rapidly identified due to the resulting reconfiguration of the near-edge structure in EELS.

Using dispersion non-uniformities measured using the standard-less protocol, the data for the energy-loss features of interest in both materials was corrected. The dispersion measurements were carried out immediately prior to data acquisition, to ensure that the measured dispersion accurately reflected the dispersion of the real spectra, eliminating the effect of any potential time-dependent variations. The sections that follow discuss the improvements brought by correcting the spectrum dispersion.

3.3.1 Nickel Oxide

Figure 3.10 shows the improvement in the alignment of the Ni $L_{2,3}$ edge spectra from nickel oxide that have been measured under a number of spectrometer settings. The spectra here are collected using a variety of combinations of dispersions and drift tube offsets to place the edge on different regions of the detector, intentionally exposing each spectrum to different parts of the dispersion non-uniformities. The result of varying the acquisition conditions in this way is quite apparent in Figure 3.10(a), which shows the as-acquired spectra. The only processing applied to the as-acquired spectra involves **1:** calibrating the spectrum to ensure the peak of the ZLP sits at 0 eV, **2:** subtracting the pre-edge background from the Ni $L_{2,3}$ edge and **3:** Fourier ratio deconvolution of the edge. Simply by varying the drift tube offset and dispersion setting in this way, the measured position of the L_3 peak maximum differs by more than 5 eV. This discrepancy is too large to be corrected by the non-uniformity profile generated by the prism-adjust-based measurements which were shown in Fig.3.6(b) and confirms that the use of the HT offset in the dispersion measurement provides accurate characterisation of the dispersions in normal operation of the spectrometer.

The spectra shown in Figure 3.10(a) were then passed through the dispersion correction algorithm prior to the other processing steps, with the corrected spectra shown in Figure 3.10(b).

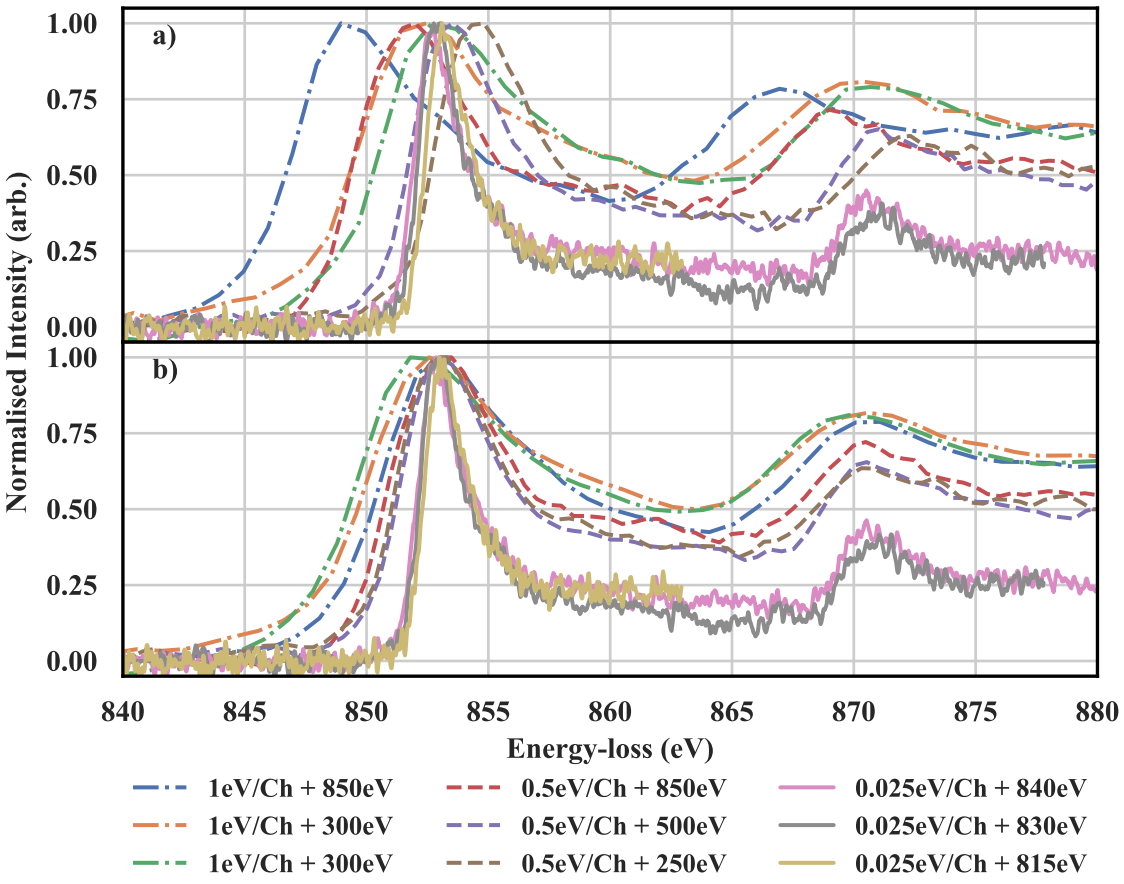

Figure 3.10: Correction of the core-loss EELS measurements of the Ni $L_{2,3}$ edges of NiO showing (a) as-collected spectra for three dispersion settings and (b) the same spectra after correcting dispersion non-uniformities. All traces are normalised to the Ni L_3 peak maximum.

The Ni $L_{2,3}$ spectra now overlap at all dispersions and drift tube offsets. The mean Ni L_3 peak position of 852.9 eV, in a range of 0.1 eV, is in very good agreement with the nominal drift tube calibration of 853 eV. This suggests that, with the dispersion correction algorithm, the energy-loss calibration is sufficiently accurate to identify energy-loss of a feature under any set of spectrometer conditions; i.e. the energy-loss is calibrated on an absolute scale.

3.3.2 Diamond

Diamond, which is one of the most mechanically-hard natural materials on Earth, is also incredibly radiation-hard. Indeed, 200 keV electrons are only slightly higher in energy than the threshold where it becomes possible for electrons to induce damage in diamond [232]. Owing to this relatively inert behaviour under exposure to the electron beam of the STEM, any ambiguity brought about by factors such as variability in oxidation state are presumed to be absent. If this should not be the case, the carbon *K* edge in EELS exhibits behaviour which can be used to easily identify spectra which come from damaged regions, allowing for a greater

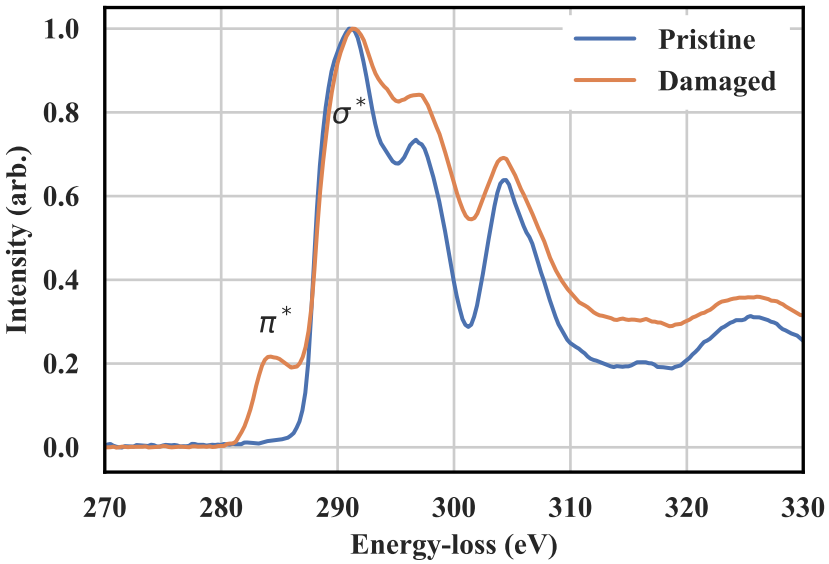

Figure 3.11: Comparison of the carbon K *edge from diamond in the absence and presence of damage. The damaged region introduces an additional π^* edge at lower energy-loss than the main edge which corresponds to a change from sp^3 hybrid bonding to sp^2 hybridisation resulting from the damage. Damage also significantly increases the density of states in the band-gap at 302.5 eV. These spectra were obtained using a dispersion of 0.25 eV/ch.*

degree of trust in the data. There are two spectral features in particular which can be used to readily identify defects in diamond, which are shown in a comparison of spectra recorded from pristine and defective diamond in Figure 3.11. The first is the presence of a pre-edge peak at 285 eV which arises as a result of sp^2 bond hybridisation in carbon. Normally, only sp^3 hybrid bonds exist in diamond and so this π^* peak should not be present in the spectrum. The other feature is a band-gap in the unoccupied density of states of diamond, which manifests as a significant trough in the *K*-edge structure at 302.5 eV [230]. The presence of this trough is indicative of the strongly insulating character of diamond and can therefore be used to diagnose damage in the specimen.

An improvement in energy measurement similar to that demonstrated for NiO above was achieved for diamond. Implementing the correction algorithm on data gathered from diamond, Figure 3.12 shows spectra which have been recorded under a larger set of spectrometer dispersions than was presented for NiO. The uncorrected spectra in Fig.3.12(a) – which have been collected with various drift tube offsets at five different dispersions – show similar disagreement to that found in the nickel oxide data, with the maximum of the initial σ^* peak varying in position by ~3 eV. Processing for these spectra was the same as described for as-collected NiO spectra in Fig.3.10(a). The dispersion-corrected spectra are then presented in Fig.3.12(b), again showing an improvement in the alignment of spectra. Here it is worthwhile to note that, not only are the features close to the onset in good agreement, but the alignment

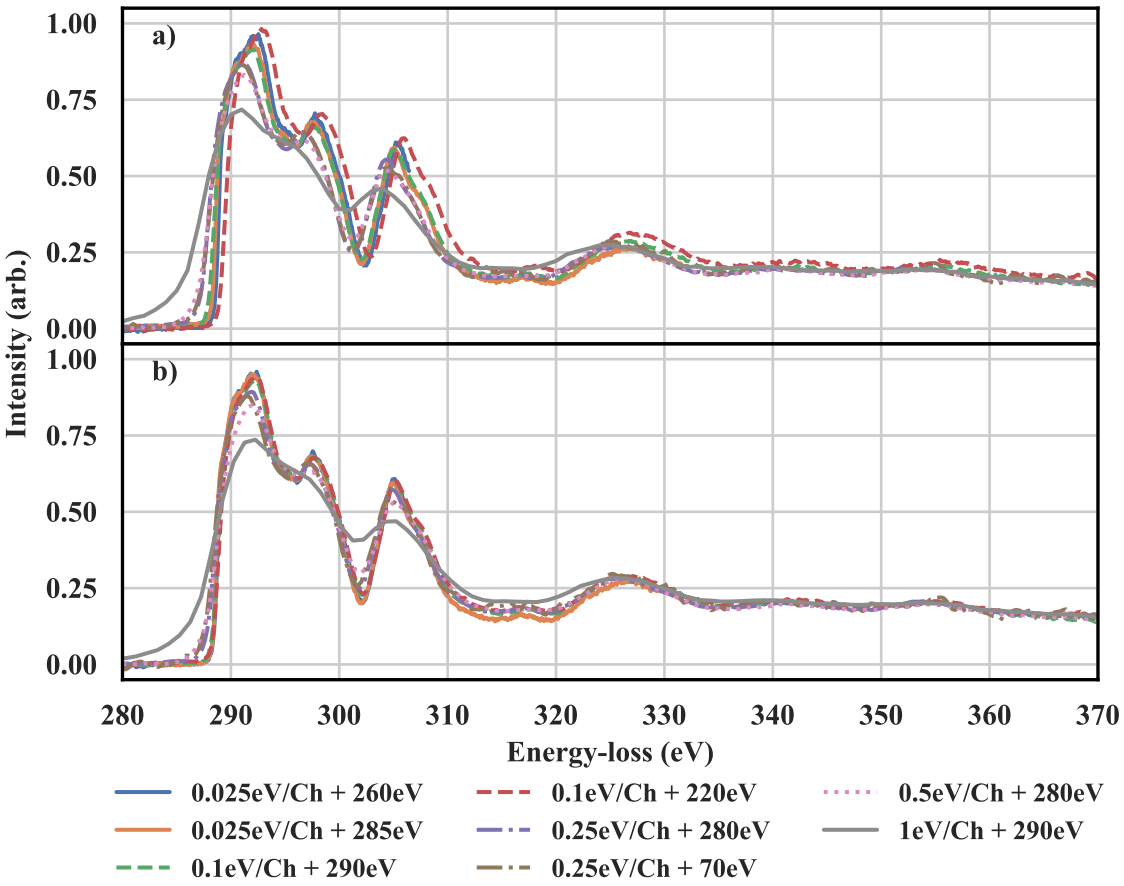

Figure 3.12: Correction of the core-loss EELS measurements of the C K edge of diamond showing (a) the as-collected spectra and (b) the same spectra after compensation for non-uniformities in the dispersion.

persists for all spectral features beyond the onset. This particular observation is important in regard to accurate measurements from extended energy-loss fine structure (EXELFS). Ensuring that the energy-loss calibration is accurate over a large energy-range is also important for splicing for dualEELS spectra, where the overlap region common to the low-loss and high-loss spectra are recorded at different positions on the detector [233].

3.3.3 Further considerations

Although there is a clear variation in peak broadening corresponding to the difference in resolution at different dispersion settings, the aligned spectra presented in Figure 3.10 and Figure 3.12 show that it is feasible using the methods developed here to maintain a reliable energy calibration where EELS edges are acquired under different conditions. Having verified the accuracy of the dispersion for the two test materials, we can further assure an absolute energy-loss calibration by looking at a range of materials. To verify our measurements, comparisons are drawn with techniques dominated by similar processes to EELS, such as X-ray

Absorption Spectroscopy (XAS). The fine structure that can be observed in XAS should be easily compared with that observable in EELS, but the poor energy-loss calibration in EELS has previously been a limiting factor in making reliable comparisons. XAS has not suffered in the same way from issues in the accuracy of the energy dispersion, so measurements of energy made from XAFS are generally more reliable [234]. In some situations, however, XAS suffers charging artefacts which can affect the accuracy of absorption spectra [235], highlighting that care should always be taken in ensuring accurate calibration, no matter the technique.

Having developed the corrections needed to get accurate measurements of energy from EELS, the main challenge in drawing comparisons between electron-loss near edge structure (ELNES) and X-ray absorption near-edge structure (XANES) is in finding references in the literature with measurements of the same edges which are readily accessible in EELS. Typically, XAFS measurements are carried out for the high-binding-energy *K* edges, but EELS core-loss measurements tend to focus on energy-losses within 1 keV, which can also be for *L* or *M* edges, depending on the element in question. Table 3.2 shows a selection of measurements from various materials, as well as a corresponding reference energy from XANES spectra for comparison. The positions of peak maxima are preferred for comparisons, as there is less ambiguity in determining the position of the maximum than there is in determining the edge onset, which is subject both to the instrumental broadening of the chosen dispersion (for EELS) and also a degree of subjectivity in choosing how to represent the onset [111, 213, 234].

Previously, in Section 3.1.3, the long-term energy drift of the ZLP was measured and estimated to be 0.07 eV/minute. In principle, the standard-less protocol will correct for drift in absolute beam energy, since positions on the detector are directly calibrated and a drift in energy will produce a corresponding drift in ZLP position that can also be measured. There is, however, the possibility that some drift arises from thermal and relaxation effects in the spectrometer prism, which would alter the magnetic induction experienced by the beam and

Material	**Feature**	**Reference Energy (*eV*)**	**Ref**	**EELS Measurement (*eV*)**
NiO	Ni L_3 max.	852.75	[111]	852.97 ± 0.11
Cu	Cu L_3 onset	932.68	[236]	932.6 ± 0.25
V	V L_3 max.	515.5	[237]	515.1 ± 0.25

Table 3.2: Measured energies of near-edge features in various materials, compared with reference values from literature.

have a more complex effect which cannot be removed. These errors are expected to have a cumulative effect over time, thus it is best to deploy the dispersion measurement immediately before or after critical measurements. This will also help to eliminate environmental factors, the impact of which can be difficult to predict.

3.4 Conclusions

The standard-less measurement of the energy dispersion of a post-column spectrometer presented in this chapter provides a post-acquisition means of correcting for aberrations in the energy-dispersion which prevent accurate calibration/measurement of features in terms of their energy-loss. The most striking sources of improvement arise from effects which, in future, may be desirable to correct during the full alignment of the spectrometer. The first of these is the error in dispersion introduced by alteration of the prism current during the engineers dispersion alignment. This is known to change the dispersive power of the prism, and effectively changes the optimisation of the alignment while it is carried out, providing the worst discrepancies at the lowest dispersions, where the prism will have had to be pushed farthest from nominal operational conditions. The second item is a chromatic effect, which may describe a compounded observation of errors in the spectrum tilt and drift-tube focusing which introduce an additional, energy-dependent term into the required correction. This has proven necessary to correct calibration errors of energy-loss features found at the zoom channel and the standard-less measurement also contains the data needed to determine the extent of this portion of the correction.

Accounting for all the effects which have been described throughout this chapter, the standard-less dispersion measurment has successfully reduced the energy-loss calibration error on the Glasgow ARM from around 1 %, down by an order of magnitude to approximately 0.1 %. At this level, the energy error is at the point of becoming sub-0.1 eV, which in many cases will be sufficiently small to enable meaningful analysis of near-edge structure. The limiting factors at this point, preventing greater accuracy of calibration, likely arise from the stability of the specific microscope/spectrometer combination used for this work, as well as the fibre-optic detector coupling issues that have been addressed elsewhere. We have shown from measurements that both the long term drift and high frequency jitter of the beam energy are in the region of 0.05 eV. The correction protocols used here may provide even greater precision in microscopes and spectrometers which boast greater stability.

The human mind always makes progress,
but it is progress in spirals.

Madame de Staël

4

EELS for absolute quantification of chemical composition

QUANTIFICATION of material composition on an *absolute* scale using electron energy-loss spectroscopy (EELS) in TEM is not common practice. Similarly, other chemically-sensitive methods inside the transmission electron microscope (TEM) – such as energy-dispersive X-ray spectroscopy (EDS) – are often only used to determine chemical compositions of materials in relative quantities because determination of chemical ratios circumvents the need for accurate knowledge of instrumental factors. For EELS, several developments have been made in past decades which improve the ease of acquisition of spectra, improving the veracity of quantitative analysis. Most notably, the spectrum imaging methodology [191] allows for rapid acquisition of site-specific spectra while dual-EELS [196] methods allow multiple energy ranges of the spectrum to be recorded in the same measurement. The ability of dual-EELS in particular to allow for more complete recording of the energy-loss spectrum lends itself (with proper treatment) to absolute quantification of spectral features, as the 'low-loss' region of the spectrum can be used to accurately normalise features of interest at high energy-

losses. These developments are critical to the success of work in this chapter, where we aim to use core-shell energy-loss edges for accurate, absolute quantification of the elemental composition of unknown specimens.

Standard practices for the processing and quantitative analysis of EELS data may, for a few reasons, provide an insufficient level of precision making compositional analysis unreliable. For some circumstances, the core-loss edges used to quantify elemental composition may be in close proximity to each other, complicating their separation or the background subtraction procedure required to extract an edge from the spectrum. In other situations, the core-loss edge available for quantification (preferring to examine edges with an onset energy-loss below 2 keV) may be an *M* or *N* edge which are poorly described by the theoretical Hartree-Slater scattering cross-sections. The errors that can be introduced by either of these sources are sufficient to compromise the veracity of elemental quantification in certain applications, such as the evaluation of dopant-level concentrations. In overcoming these problems throughout this work, a number of recent developments have been adopted and refinements made in both spectral processing and the quantitative analysis of composition. Principal among these has been the use of experimentally-defined reference spectra based on methods developed by Craven *et al.* for the analysis of nano-scale precipitates in steels [238–240]. This approach markedly improves the extent to which the measured cross-section is representative of all features present in a core-loss edge, providing a model that is superior to the Hartree-Slater cross-sections and also avoids the need for spurious background subtraction. Overcoming these effects has been instrumental in accurately characterising the half-Heusler alloys.

To demonstrate the improvements in quantitative analysis and also their relevance to the investigations throughout this thesis, the elemental quantification of a copper-doped TiNiSn half-Heusler is examined. This material provides a model example of the difficulties in quantifying overlapping features, as the titanium L, tin M, nickel L and copper L edges all lie in close proximity to one another. Reference-based quantitative modelling of the spectra from this material fits quantities of individual elements effectively, despite the expectation that differences in the bonding environment of such a complex specimen will affect the near-edge structure. The route to obtaining the experimentally-derived scattering cross-sections is outlined in Section 4.2. Then, the workflow for data treatment and processing to prepare spectra for the reference-based quantification is discussed in Section 4.3. Finally, to tie everything together, Section 4.4 discusses the improvements in precision of elemental analysis brought about by implementing reference-based quantification. Quantification results

from the reference-based approach are compared to the use of Hartree-Slater cross-sections. The comparison demonstrates the benefits to fitting precision and also in the case of mis-identification of elemental quantities, such as in the case of fitting the tin *M* edge. Then, after exploring the relative improvement from adopting the standard-based method, we consider the absolute limitations of quantification in this framework, discussing estimates for the ultimate precision of measured compositions and the minimum viable concentrations of elements which can be discerned with certainty.

Much of the progress and results outlined throughout this Chapter have relied heavily on computer code to produce them. In the interest of future replicability of the protocols discussed, some references are made to code modules or specific elements of code. Some of the code which has been custom-written for the contents of this chapter have been packaged into a Python module called *SQuEELS* (**S**tandard-based **Qu**antification of **E**lectron **E**nergy-**L**oss **S**pectra), which is hosted at the web-address in reference [241]. References in the text to the names of specific elements of code will be made in the `typewriter` font.

4.1 Quantitative Electron Energy-Loss Spectroscopy: A Recap

A typical TEM electron energy-loss spectrum has a large dynamic range. Signals in the spectrum may span as much as 7 orders of magnitude in intensity across the first ~1,000 eV of energy-losses. A representative example of an energy-loss spectrum is depicted in Figure 4.1, showing; the intense zero-loss peak (ZLP) which contains electrons that have scattered elast-

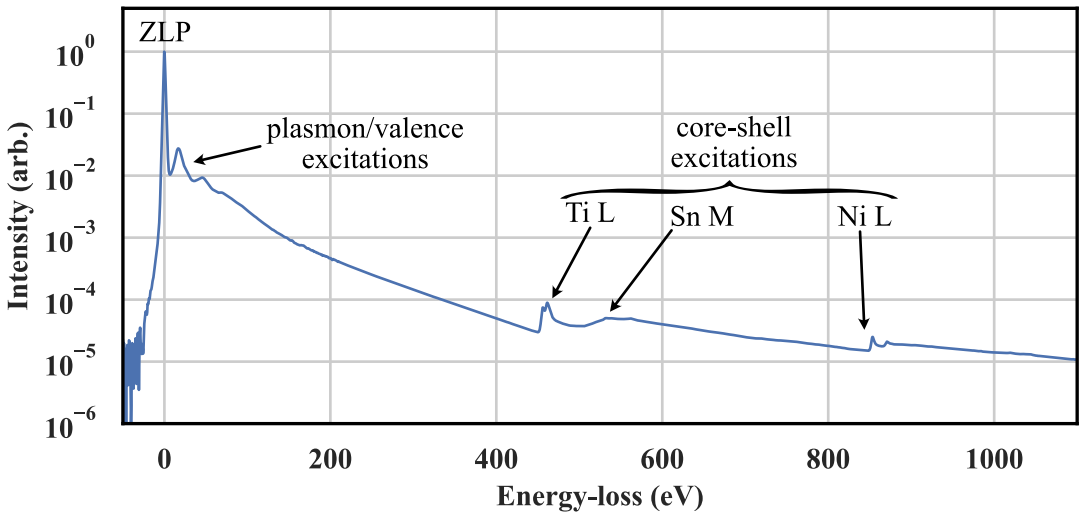

Figure 4.1: A typical electron energy-loss spectrum representative of the Heusler materials studied throughout this thesis.

ically, features at low energy losses (< 100 eV) which are dominated by plasmon excitations and valence electron interactions, then edges at higher energy-losses which derive from excitation of more tightly-bound core-shell electrons and appear as weak features on a stronger, decaying background. Unlike valence electrons, which are involved in chemical bonding and whose characteristics will change significantly from material to material as a result of their bonded states, the properties of core-shell electrons are dominated by the atomic physics of the parent element and vary to a lesser extent with differences in chemical bonding. This comparative invariance makes core-loss features useful for identifying the presence of specific elements and can be used to quantify the amount of an element which is present.

4.1.1 Extracting core-loss edges

The basic premise behind quantitative analysis of electron energy-loss spectra for elemental composition involves integrating the signal deriving from a core-loss EELS edge which is present in the spectrum. As can be observed in Figure 4.1, the energy-loss spectrum contains a continuum of decaying intensity extending to higher energy-losses arising from excitation of electrons with low binding-energies [111]. The core-loss edges are superimposed atop this

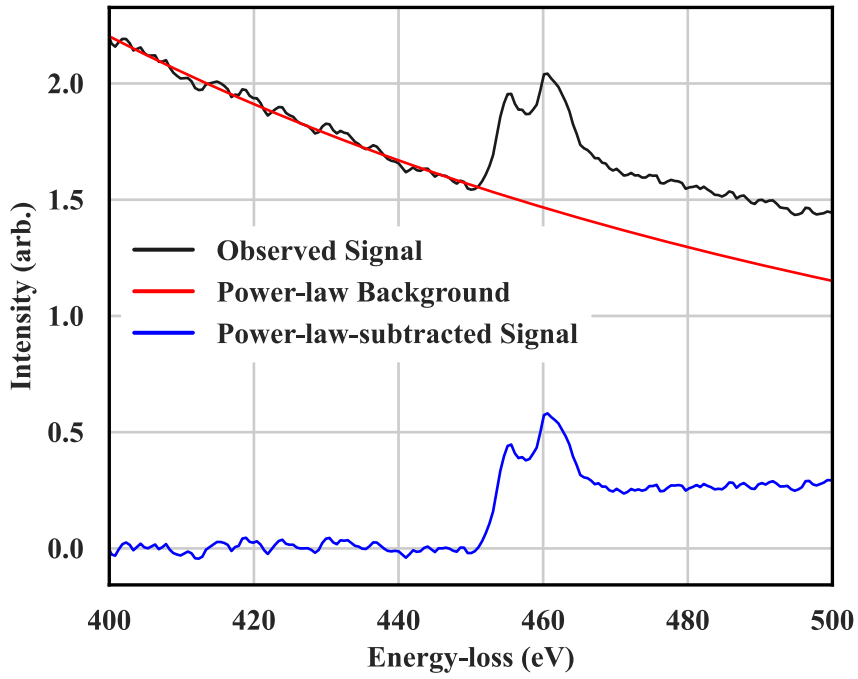

Figure 4.2: Example of a power-law (AE^{-r}) relationship fitted to a pre-edge background in an as-recorded spectrum containing the titanium $L_{2,3}$*-edge. The edge after subtracting the background is also shown.*

'background', which can have intensity similar to or greater than the edge itself. It is therefore imperative for quantitative analysis to accurately separate the signal of the core-loss edge from that of the underlying background. Removal of the background from under a core-loss edge is typically achieved by fitting a functional form to the background at energy-loss values immediately below the energy of the edge of interest. The high energy-loss tail which forms this background is usually approximated by a power-law dependence on energy-loss – AE^{-r} – due to functional similarity with plasmon high energy-loss behaviour expected from Bethe theory [242]. Despite commonplace use, the power-law form is somewhat controversial because it fails to accurately describe the background shape over large ranges in energy-loss and care should be taken to ensure it's use is appropriate. No definitive alternative to the power-law decay has been proposed, however any smoothly decaying function that provides a better model could be used [243]. After fitting a function to a region before the edge in energy-loss, the function can then be extrapolated to higher energy-losses to model the background under the edge, which can then be subtracted from the spectrum. This process is illustrated in Figure 4.2, which shows a power law relationship fitted to the pre-edge background in the region of 400 - 450 eV, which is then extrapolated under the edge and subtracted. Background subtraction is usually regarded as fairly routine [111] and is easily carried out in relevant electron microscopy software/code, such as DigitalMicrograph (DM) [208] or HyperSpy [244].

4.1.2 Multiple scattering in the spectrum

Throughout the energy-loss spectrum, unless the specimen is very thin (less than roughly 1/3 of the mean-free-path for inelastic scattering), there is a non-negligible probability of recorded counts from electrons which have interacted with the specimen more than once, undergoing multiple scattering events. This typically involves a mixture of core-shell and plasmon interactions (though double core-shell scattering is possible [209]) which leads to thickness-dependent changes in the intensity and near-edge structure of core-loss edges. For accurate interpretation of core-loss edges for elemental quantification, it is preferable to consider electrons which have *only* scattered once from the core-shell of interest. The spectrum which does not contain plural/multiple scattering events is called the *single-scattering distribution* (SSD) and can be obtained from a measured spectrum by using deconvolution to remove multiple scattering features.

There are a few methods for spectral deconvolution in EELS to recover the SSD. The most

commonly-used of these are the Fourier methods, based on the use of operations on Fourier transforms. The Fourier deconvolution method assumes that an observed and complete spectrum, $J(E)$, contains not only the SSD, but also a sum of contributions from plural scattering, where each new term includes a greater number of scattering events. This description of the energy-loss spectrum – from Misell and Jones [245] – requires the complete spectrum to have been collected, so that Poisson statistics are valid, and further describes the observed spectrum as having been broadened by an instrumental resolution function, $R(E)$:

$$J(E) = R(E) * [I_0\delta(E) + S(E) + D(E) + T(E) + ...] \ , \tag{4.1}$$

where $I_0\delta(E)$ is a delta function of height I_0, which describes the elastic contribution to the spectrum (i.e. the zero-loss peak). $S(E)$ denotes the single-scattering distribution, while $D(E)$ and $T(E)$ are the double and triple-scattering terms, respectively. These plural scattering terms are described by repeated convolution of the SSD, such that $D(E) = (S(E) * S(E))/2!$ and $T(E) = (S(E) * S(E) * S(E))/3!$ and the series continues to an arbitrary number of scattering events. The Fourier transform of Equation 4.1 gives the frequency-space representation of the spectrum, in which the convolutions in the series become products

$$j(v) = z(v)\left[1 + \frac{s(v)}{I_0} + \frac{s(v)^2}{2!I_0^2} + \frac{s(v)^3}{3!I_0^3} + ...\right] \ , \tag{4.2}$$

where the terms from equation 4.1 are now denoted by the same lower-case letters and are now a function of frequency (v). The elastic contribution and resolution function are now combined into one term to describe the observed ZLP, $z(v)$. This Fourier-transformed, non-truncated description of the spectrum can be recognised as a Taylor expansion of $e^{s(v)/I_0}$, so can be simplified. Then, as outlined by Johnson and Spence [246], equation 4.2 can be rearranged to represent the deconvolution which recovers the SSD,

$$s(v) = I_0 \ln\left[\frac{j(v)}{z(v)}\right] \ . \tag{4.3}$$

Taking the inverse Fourier transform of $s(v)$ would then complete the deconvolution to recover $S(E)$. This method is referred to as Fourier-Log deconvolution [247]. Completely deconvolving the spectrum like this introduces a lot of noise, as high-frequency terms are amplified relative to the rest of the spectrum. When removal of plural scattering, rather than correcting instrumental broadening, is the main purpose of Fourier-log deconvolution, Equation 4.3 can be modified so the logarithm is multiplied by $z(v)$ – representing a convolution

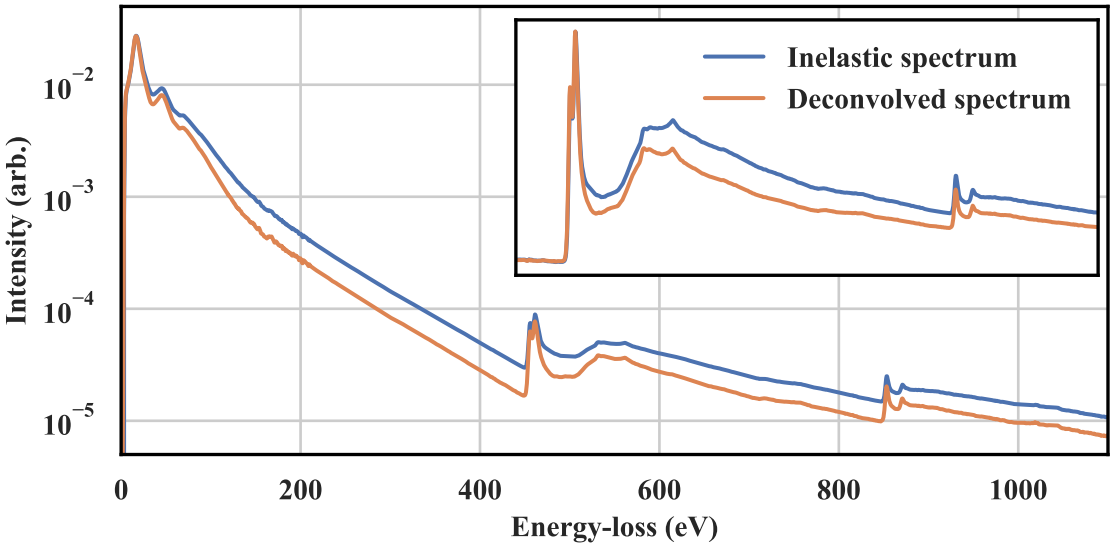

Figure 4.3: The contributions to the TiNiSn energy-loss spectrum in Fig.4.1 from inelastic scattering, before and after Fourier-log deconvolution. Core-loss edges are more pronounced in the single-scattering distribution. Inset compares the core-loss edges, background subtracted prior to the Ti L *edge at ~450 eV, emphasising difference made by deconvolution.*

with the ZLP – rather than simply multiplying by the elastic intensity I_0,

$$s(v) = z(v) \ln \left[\frac{j(v)}{z(v)} \right] . \tag{4.4}$$

This approach dramatically reduces the noise introduced by the deconvolution, but at the expense of retaining instrumental broadening in the spectrum [246]. Fourier-log deconvolution, including the instrumental resolution function retained by convolution with $z(v)$, is demonstrated in Figure 4.3, where the inelastic contributions to the energy-loss spectrum from Fig.4.1 are shown before and after deconvolution. The specimen this spectrum was recorded from is relatively thin, with a relative thickness of 0.33 mean-free-paths, yet a significant amount of plural scattering is eliminated by deconvolution. As plural scattering is removed from the entire spectrum, including the pre-edge background regions, the core-loss edges present in the spectrum become more prominent.

Fourier-log deconvolution requires measurement of a complete spectrum containing everything from the ZLP up to energies far beyond a feature of interest. It is not uncommon, however, for spectral measurements to not satisfy this level of completeness. This might be due to a limited spectral range, or difficulty in recording the entire spectrum with sufficient SNR. In these situations, a variant on Fourier deconvolution called Fourier-*ratio* deconvolution can be more appropriate. This approach lends itself well to dualEELS data, where

a high and low-loss region of the spectrum have been measured separately. Fourier-ratio deconvolution involves taking the ratio of the Fourier transforms of the high and low-loss spectra [248],

$$s(v) = z(v)\left[\frac{j_{CL}(v)}{j_{LL}(v)}\right] , \tag{4.5}$$

where the subscripts *CL* and *LL* denote the core-loss and low-loss regions of the spectrum, respectively. As in Equation 4.4, the Fourier ratio is multiplied with the Fourier transform of the ZLP to limit noise in the SSD. An important distinction which must be made between these two methods is that the core-loss region to be Fourier-ratio deconvolved must first have the background subtracted from the lowest-energy edge of interest. This ensures that, as in the complete spectrum, the extrema of the spectrum both tend to zero, which is a requirement of the Fourier series [111]. So long as this step is carried out, the SSD of a spectrum which has been background subtracted and Fourier-ratio deconvolved, or which has been Fourier-log deconvolved then background subtracted, should be identical [247].

4.1.3 Scattering cross-sections

Having extracted a core-loss edge from the rest of the spectrum and deconvolving to remove plasmon & valence scattering, we now need to relate the intensity in the edge to a chemical quantity. This is achieved through scaling the measured intensity by the scattering cross-section for the excitation which produced the edge. The theoretical scattering cross-sections for core-shell excitations are derived from Bethe theory, which describes the energy that will be lost by relativistic electrons from excitation or ionisation of an atom [111]. In Bethe theory, the differential cross-section for an excitation transition – based on the first Born approximation [249] – is

$$\frac{d\sigma_n}{d\Omega} = \left(\frac{m_0}{2\pi\hbar^2}\right)^2 \frac{k_1}{k_0} \left|\langle\psi_n|e^{i\mathbf{q}\cdot\mathbf{r}}|\psi_0\rangle\right|^2 , \tag{4.6}$$

where k_0 and k_1 are the initial and final wavenumbers of the scattered beam electron. The wavefunctions ψ_0 and ψ_n denote the initial and final states of the atomic electron, respectively, so that the exponent in the transition matrix element (where $\mathbf{q}$ and $\mathbf{r}$ are the momentum transfer and electron position, respectively) describes how the beam electron induces an excitation of the atomic electron from a core-shell to a continuum state. Collectively, the square modulus of these terms effectively describes the transition rate for each matrix element [249]. The differential cross-section here is dependent on the solid angle of scattering, Ω. Compared to

EDS, where X-rays are emitted isotropically through 4π steradians, the electrons in the TEM are mostly scattered at angles close to the optic axis of the microscope ($\lesssim 10^{-2}$ steradians). Because of the geometry of the TEM, it is often more convenient to consider scattering in terms of angle from the optic axis and define the angular dependence of scattering in terms of the collection angle, β, at the spectrometer entrance; this convention is used hereafter.

To determine the scattering cross-section for an excitation, the initial and final wavefunctions of the atomic electron have to be computed. The calculation of atomic, single-electron wavefunctions is described by the Hartree-Fock (self-consistent field) method [32]. To simplify the Hartree-Fock calculations, the wavefunctions are assumed to be spherically symmetric, so that only the radial components of the wavefunction are critical; this is the Hartree-Slater (HS) approximation [111]. The HS solutions to the atomic electron wavefunctions are then used to calculate the partial scattering cross-section. As the HS approximation considers only atomic physics, the calculated cross-sections do not contain contributions from collective effects where intensity close to the edge onset reflects the material-specific unoccupied electronic density-of-states [111]. The partial cross-section is calculated by integrating the differential cross-section in Equation 4.6 across both the collection angle (β) of the spectrometer and the energy-loss range (ΔE) over which the edge is integrated for quantification [111].

4.1.4 Quantitative analysis of elemental content

When the SSD has been recovered from the measured spectrum, the intensity in a core-loss edge should derive only from core-shell scattering and the intensity which has been extracted from the core-loss edge – integrated over an energy range Δ beyond the edge onset – is described by

$$I(\Delta, \beta) \;=\; N\, I_0\, \sigma(\Delta, \beta)\;, \tag{4.7}$$

where I_0 is the integrated intensity of the zero-loss peak (ZLP), which represents the electrons in the beam which have undergone elastic or no scattering. N is the atomic area-density of the element in the specimen, which is a product of the volume-density and the specimen thickness. The scattering cross-section, σ, is integrated across an energy-range (Δ) and the collection angle of the measurement (β). For meaningful comparison of the quantities of more than one element, scaling the integrated intensity I by the cross-section σ is necessary to recover the absolute values of N. The area-density gives an absolute measure of an elemental quantity,

though the relative atomic ratios of two elements, a and b, can also be calculated by

$$\frac{N_a}{N_b} = \frac{I_a(\Delta_a, \beta)}{I_b(\Delta_b, \beta)} \frac{\sigma_b(\Delta_b, \beta)}{\sigma_a(\Delta_a, \beta)} , \tag{4.8}$$

where the edges for a and b can be for two different shells, and the integration window Δ for the two edges need not be identical, either.

Measured intensity is related to the area-density in equation 4.7, rather than volume-density as the TEM energy-loss spectrum represents a 2-d projection of the specimen where signal is integrated across the specimen thickness. Estimation of the volume-density from the area-density would therefore require an estimate of the specimen thickness. Accurate, absolute measurement of specimen thickness from spectra is not routine as this typically requires prior calibration which can be time consuming or inconvenient [111]. Instead, the relative thickness of the specimen (t/λ), where the thickness is defined relative to the material-specific inelastic electron mean-free-path (mfp), can be readily determined from a low-loss spectrum using the log-ratio method [250], where

$$\frac{t}{\lambda} = \ln\left(\frac{I_t}{I_0}\right) . \tag{4.9}$$

Here, I_t denotes the sum of all intensity throughout the spectrum. If the electron mfp is known, then the quantity t/λ can be translated into an absolute thickness. Two theoretical parametrisations are commonly used to estimate the inelastic mfp of materials; the Malis parametrisation [250], where atomic number Z is the material-specific parameter, and the Iakoubovskii parametrisation [139] which instead uses the material density. Although the Iakoubovskii mfp appears more appropriate for STEM measurements – as it also factors in the beam convergence angle α – neither parametrisation is universally superior when compared with experimental measurements [111]. We therefore opt to experimentally measure the relevant mfps and this is described in Section 4.2.

4.1.5 Practical challenges in EELS quantitative analysis

The basic protocols for quantitative compositional analysis outlined above are not infallible. For certain applications, including those required throughout this thesis, there are numerous issues which may emerge that compromise the accuracy of elemental quantification. The main complications which are relevant to the work contained herein – which lie in the back-

ground subtraction procedure and the Hartree-Slater approximation – are described below.

The description of the background energy-dependence with a power-law relationship is contingent on sufficient separation (typically greater than 100 eV) from the preceding edge such that the power-law-like high-energy tail lies in the background fitting region. Issues in the background subtraction procedure can arise in situations where energy-loss features are close together. In this situation, the energy-loss near-edge structure (ELNES) or extended energy-loss fine structure (EXELFS) reflect contributions from the unoccupied electronic density of states (DOS) and chemical bonding geometries and contains features which do not follow a power-law relationship in energy. When these features are present in the fit-region for the background, the power-law fit is compromised and becomes highly unreliable. Furthermore, these ELNES/EXELFS features, if present immediately pre-edge, may also overlap the edge of interest and become very difficult to separate in a quantitative model of the spectrum using these protocols. Of the core-loss edges to be used for elemental quantification here, the Ti *L*, Sn *M* and O *K* edges are in very close proximity (onset energies of 456, 485 and 532 eV, respectively) and proper background subtraction is impossible to carry out for all edges individually.

The other complication relevant to the presented work lies in the use of the Hartree-Slater partial scattering cross-sections. Due to the spherical symmetry assumption made in the HS approximation, the reliability of the partial scattering cross-section calculation varies depending on the exact excitation the cross-section describes. EELS *K* edges, which denote an excitation from an electronic 1*s*-state, are described by the HS cross-sections with relative accuracy as *s*-states have spherically-symmetric wavefunctions. Other core-loss edges, including *L* and *M* edges which denote excitations from 2*p* and 3*d*-states respectively, have an angular dependence which leads to lobed wavefunctions [249] which are not spherically-symmetric and so are not as well described by the HS approximation. For the thermoelectric Heusler alloys which have been studied in this and the following chapters, there are five edges of interest for quantification; the titanium *L*, nickel *L*, tin *M*, copper *L* and oxygen *K* edges. The partial cross-sections from Hartree-Slater approximation are reasonably well defined for *K* edges and Egerton *et al.* [251] quote the error in the HS approximation of the oxygen K edge at 3 %. For the other edges of interest, the error in the parametrisation of the HS cross-sections increases dramatically. Errors for Ti *L*, Ni *L* and Cu *L* cross-sections are quoted (also by Egerton *et al.* [251]) at 15 %, while the error in the Sn *M* cross-section is 25 %, arising from underestimation of the near-edge white-line contributions to the edge.

Evidently, conventional quantification routines are unsuitable for compositional analysis of TiNiSn-based Heusler alloys, where identification of elemental composition to within 1 % precision is desired to ensure sensitivity to dopant-level concentrations of elements which are important to optimising thermoelectric properties. Theoretical approaches to calculating scattering cross-sections which are more sophisticated than the HS approximation are possible within the framework of density functional theory (DFT) calculations [252, 253]; these can take account of chemical bonding and collective effects which are important at energies close to the edge onset [254]. However, even in a DFT approach, there are still outstanding problems to be solved, such as modelling the effect of the core-hole left by a core-shell excitation on the density of states [255]. As an alternative to quantification using theoretical scattering cross-sections, we have opted to use experimental reference standards. Standard specimens can be used to experimentally ascertain the scattering cross-section of a material under a given set of conditions within the microscope. These experimentally-derived cross-sections can then be used as references for quantification of spectra from unknown specimens measured under the same conditions. This approach avoids the pitfalls of HS parametrisation, as it requires no assumptions about the atomic physics involved. Further, because the shape of an edge is known with greater precision, the challenge of quantifying overlapping edges becomes diminished, as the shape of a preceding edge can be used as the background for the next. The use of elemental reference standards is outlined in the next section.

4.2 The energy-loss zoo: experimental references for elemental quantification of EELS data

To redress the inadequate precision associated with elemental quantification using the Hartree-Slater partial cross-sections, the use of experimentally measured scattering cross-sections is implemented. A reference-based system for chemical quantification should also overcome the issue of proximity in core-loss features discussed in Section 4.1.5. The method chosen for implementation of experimental references is based on the use of tomography-style, needle-shaped specimens originally described by Craven *et al.* [239] and has also been reproduced by others since [256, 257]. Tomography specimens have clear variations in thickness which can be accurately measured and correlated with obtained spectra to provide experimental measurements of both the inelastic mean-free-path and differential scattering cross-section. This is critical to realising accurate and absolute quantification of composi-

tion using STEM-EELS data. Furthermore, the method takes advantage of the dualEELS methodology for recording spectra [196], which allows the low-loss and core-loss regions of the energy-loss spectrum to be recorded near-simultaneously. The key benefit to the use of dualEELS here is the ability to acquire a more complete spectrum containing both the very intense zero-loss peak and also the core-loss region of the spectrum, without sacrificing the signal-noise ratio of either portion. By capturing all important spectral features, data can be properly normalised and treated in preparation for quantitative analysis.

The implementation of experimental reference standards for absolute quantification used here differs from the method prescribed by Craven *et al.* Here, the objective is to accurately determine the elemental make-up of a specimen of 'unknown' chemical composition, whereas Craven *et al.* focused on accurately analysing the quantity of a phase of known composition [239, 240]. The exact nature of the experimental reference specimens required must change to reflect this difference in objective. Instead of using specimens which exactly match a composition of interest, the reference standards should be made from individual elemental sources. A further alteration to the method is necessitated by the range of energy-losses of interest. Features to be examined in this work lie at greater energy-losses than in the original experimental reference work. Consequently, in the proper treatment of data, splicing the dualEELS spectra together for Fourier-log deconvolution is no longer practical. SSD's are therefore obtained by Fourier-ratio deconvolution, relaxing the constraint on the SNR required throughout the low-loss spectra.

The reference spectra required here are all for individual elements, so TEM specimens were prepared from high purity (99.9+ %) d.c. sputter targets by FIB liftout and milling of the material to form a needle shaped specimen. These reference needles are similar to those used for 3d atom-probe (3DAP) tomography (or, indeed, TEM tomography) and their preparation has already been outlined in the methods chapter in Section 2.2.2 on p.61. To facilitate quantitative analysis of the materials of interest in this and future chapters, TEM reference standards were prepared from titanium, nickel, tin and copper sources; producing four tomography needles from which to measure differential scattering cross-sections.

In principle, any specimen which has been deliberately prepared to have a large variation in thickness – such as a wedge-shaped specimen – can be used to determine the differential scattering cross-section of the material. A spectrum image obtained across this thickness variation, containing both the measured intensities and encoding relative information about

the specimen thickness, is sufficient to calculate the differential scattering cross-section

$$\frac{1}{I_0}\left.\frac{\partial I}{\partial E}\right|_{\beta} = N\left.\frac{\partial \sigma}{\partial E}\right|_{\beta}, \tag{4.10}$$

where $1/I_0$ denotes a normalisation of the spectrum by the integrated elastic intensity (i.e. the ZLP). The product of the number of atoms, N, in the interaction volume and the differential of the scattering cross-section, σ, describes how the quantity of material involved in the measurement contributes to the intensity I observed at a given value of energy in the spectrum. In using a tomography needle, however, the reference standard can also be used to directly measure the specimen thickness, allowing for accurate measurement of the inelastic mean-free-path of the material. This will feed into the calculation of the scattering cross-section and further improve accuracy. The calculation of both the mean-free-paths and the differential scattering cross-sections are discussed in the rest of this section.

4.2.1 Calculating the inelastic mean-free-path

To measure the inelastic mean-free-path (mfp), the relative thickness (t/λ) which can be calculated from EELS data must be correlated with direct measurement of the specimen thickness. Relative thickness is calculated by the log-ratio method as described in Section 4.1.4. Use of a needle-shaped specimen is advantageous because the absolute thickness of the specimen is then determined from a HAADF or ADF STEM image of the needle recorded with a specimen tilted 90° from that of the spectrum image. Thresholding of the image can be used to calculate a profile of the diameter of the needle along its length. It is then presumed that the needle has a circular profile so that the largest value of t/λ at each point along the length of the needle corresponds to the observed thickness in the perpendicular STEM image. Though the relationship between the absolute thickness and the EELS t/λ measurement should be linear, the mfp is calculated by finding the gradient of the squares of these quantities

$$t^2 = \lambda^2 \times \left(\frac{t}{\lambda}\right)^2. \tag{4.11}$$

As noted by Craven *et al.*, using the squares of the two observables weights the linear regression toward contributions from thicker material and significantly diminishes the influence of the surface of the needle, which may be chemically different from the bulk [239]. This treatment of the data for the calculation results in a gradient which derives primarily from the

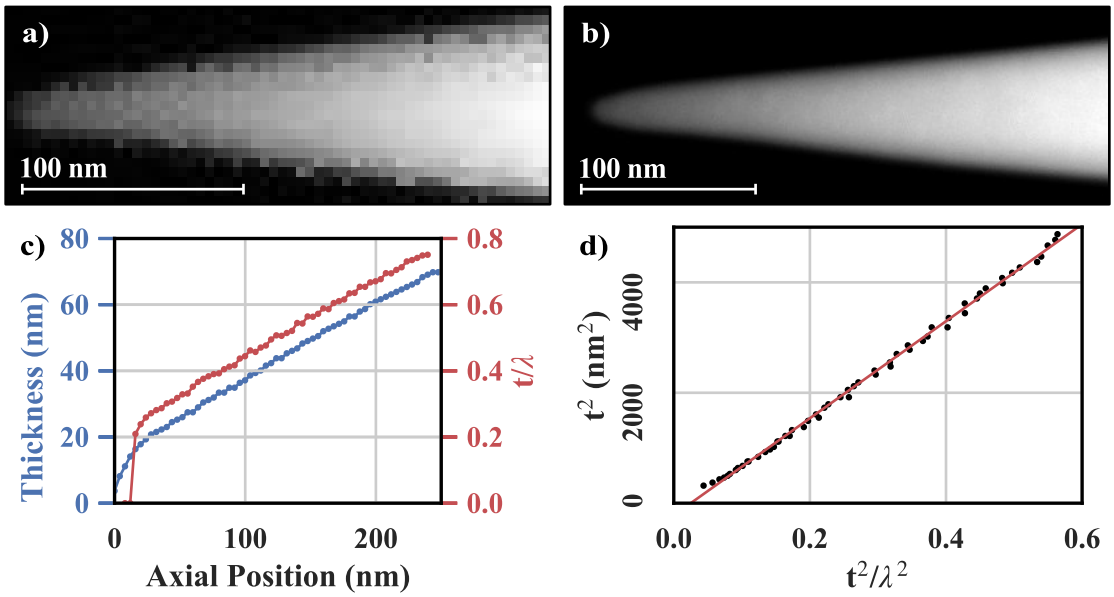

Figure 4.4: (a) Log-ratio relative thickness (t/λ) map calculated from the STEM-EELS spectrum image of a nickel needle specimen. (b) The HAADF-STEM image recorded at a 90° tilt from the SI. (c) The measured absolute diameter and maximal t/λ values as a function of axial position along the needle. These profiles are then used in a linear regression in (d) from which the inelastic mfp is calculated as $\sqrt{m}$.

bulk mfp, rather than a combination of the bulk and surface properties.

Figure 4.4 illustrates how the images obtained from a needle are used to calculate the inelastic mean-free-path. The image in Fig.4.4(a) is the log-ratio thickness (t/λ) map calculated from the EELS low-loss spectrum-image, while Fig.4.4(b) contains the HAADF-STEM image of the needle recorded with a tilt orthogonal (90°) to the SI. From these images, the axial profiles in Fig.4.4(c) are determined. A threshold is applied to the image to distinguish quickly between specimen and vacuum, allowing the column containing the needle apex to be identified. For each column from the apex, the largest value of t/λ is selected from the EELS map, while the number of pixels in the HAADF image identified as belonging to the needle by the threshold is counted to determine the absolute thickness from the image calibration. Finally, these profiles are fed into a regression as in Fig.4.4(d); the inelastic mfp (λ) is determined by taking the square root of the gradient.

The results of calculating the mean-free-path for each of the different elements from their needles are presented in Table 4.1. For comparison, the theoretical mfp's have been calculated using the Iakoubovskii [139] and Malis [250] parametrisations and provided alongside the experimental measurements performed here. These calculations have been carried out using code written by D.R.G. Mitchell [258] to return mfps for 200 keV electrons with probe convergence and collection angles of 29 and 36 mrad, respectively, to reflect the experimental

Material	Measured mfp (nm)	Iakoubovskii (nm)	Malis (nm)
Titanium	118.5 ± 1.2	129.2	88
Nickel	91.0 ± 1.6	109.6	81.79
Tin	121.9 ± 0.9	115	68.64
Copper	91.9 ± 0.4	109.4	80.92

Table 4.1: Measured inelastic mean-free-paths for 200 keV electrons in the denoted reference materials. Presented alongside are the inelastic mfp values calculated from the two common theoretical parametrisations (Iakoubovskii [139] and Malis [250]) using convergence and collection semi-angles of 29 and 36 mrad, respectively, to reflect the experimental conditions used throughout.

conditions of the measurements. Though the experimentally measured values do not show strong agreement with either parametrisation, the accuracies of the calculated mfps are relatively poor, with both Iakoubovskii *et al.* and Malis *et al.* [139, 250] quoting a ~5 - 10 % error which may be due to solid-state effects that are not included in either parametrisation. The experimental measurements of the mfps, which have regression errors of ~1 %, are carried forward into the calculation of the differential scattering cross-section.

4.2.2 Calculation of experimental scattering cross-sections

Accurate determination of the scattering cross-sections requires an approach which takes full advantage of the dualEELS [196] methodology. In addition to the low-loss spectrum image, from which the inelastic mean-free-path has already been measured, a high-loss spectrum image is recorded with a much greater exposure time to record core-loss edges with good signal-to-noise. From the observed spectra and some knowledge about both the acquisition conditions and the material properties, the description of the observed intensity in Equation 4.10 can be expanded upon to give

$$\frac{1}{I_0}\frac{I(E)}{\Delta E}\frac{1}{\tau} = n\lambda\left(\frac{t}{\lambda}\right)\sigma(E)\ , \tag{4.12}$$

where $I(E)$ is the intensity observed in a channel at a given energy E in the spectrum. This is normalised by the integrated elastic intensity, I_0, which is further scaled by the energy-width of the channel (ΔE) and also by the time ratio, τ, to take account of the difference of exposure times between the high-loss and low-loss spectra. The channel intensity $I(E)$ is then related to a physical quantity of material by the scattering cross-section evaluated at the same energy, $\sigma(E)$. The total quantity of an element, which was denoted N in Equation 4.10, is calculated by taking the product of the measured t/λ, the previously measured inelastic mfp (λ) and the

atomic number density of the material n, which has been calculated from standard values for each metal. Note that while equation 4.12 concerns the energy-dependence of the relationship between intensity and scattering cross-section, the angular dependence of scattering, β, which was discussed earlier is still implicitly present. It is not necessary to explicitly include β here as the use of experimental references has been adopted in the understanding that all measurements must be made using consistent conditions in the microscope, including the collection angle.

In addition to providing an experimental measure of the inelastic mfp, the varying specimen thickness of the needles provides a means to use Equation 4.12 to extract the differential scattering cross-section for the element. The relationship in Equation 4.12 is presented in Figure 4.5, which examines the dependence of observed intensity in the nickel $L_{2,3}$ edge on the quantity of nickel being probed. Fig.4.5(a) shows a Fourier-ratio deconvolved Ni L edge.

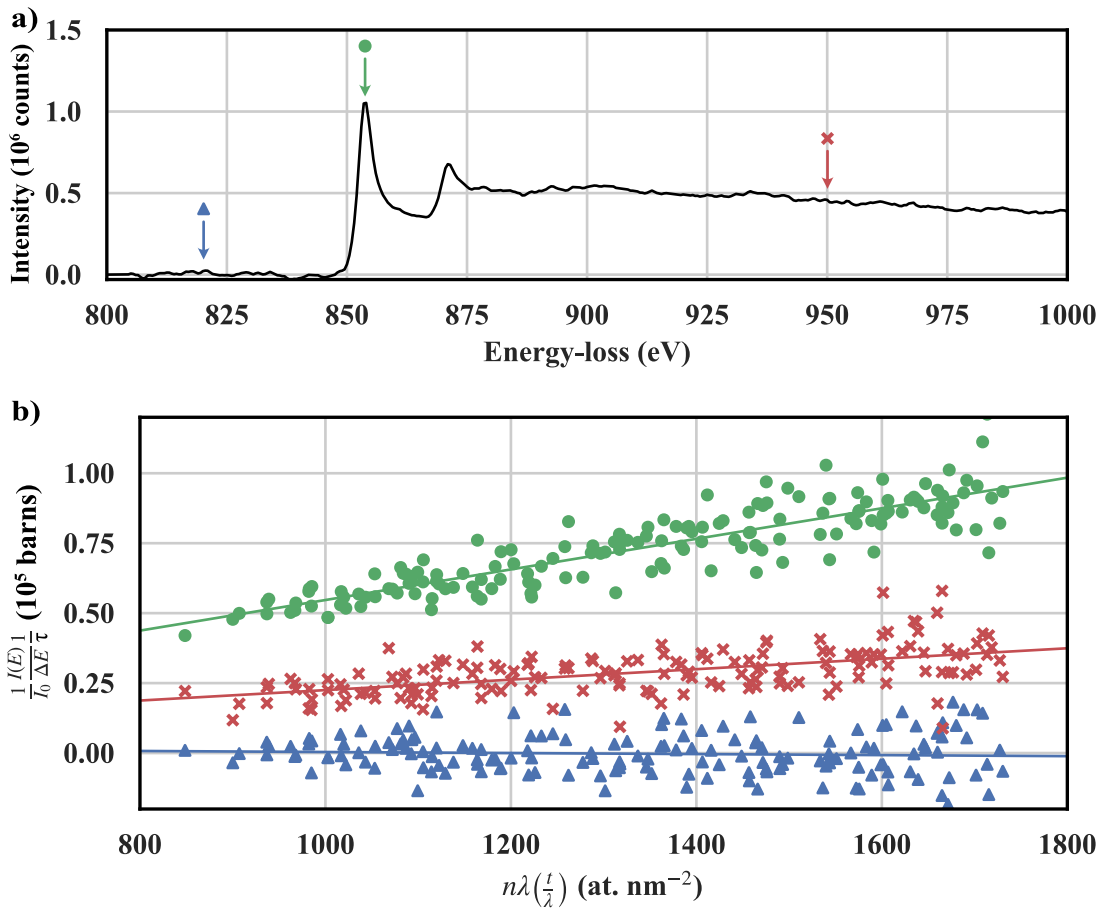

Figure 4.5: (a) Fourier-ratio deconvolved nickel $L_{2,3}$ edge summed across an entire spectrum image. (b) Normalised intensity plotted against the quantity of nickel (calculated from the log-ratio thickness) for three different values of energy-loss (820, 854 & 950 eV) as indicated by the arrows on the nickel spectrum in (a). The differential scattering cross-section at each energy is determined by the gradient of the shown relationship, as described by Equation 4.12.

Three points in the spectrum are marked by arrows – a pre-edge energy at 820 eV, the apex of the Ni L_3 peak at ~854 eV and a point further from the onset at 950 eV – for which the normalised intensity is plotted against the calculated areal density of nickel in Fig.4.5(b). The data in this graph come from an EELS spectrum image covering a region of a nickel specimen with a significant variation in thickness across the measurement region. The spectrum image – which contains the Ni L edge – has been treated for dispersion non-uniformities as described in Chapter 3, recalibrated to the energy of the ZLP, background subtracted to extract the Ni L edge and Fourier-ratio deconvolved to recover the SSD. For the intensities in the SSD to be consistent with the description in Equation 4.12, the spectra are normalised by I_0, τ and ΔE. Areal densities of nickel are calculated from the log-ratio specimen thickness (t/λ), the experimentally determined inelastic mfp (λ) and the atomic density of nickel (which has been calculated from the standard bulk density as 91.4 at.nm^{-3}). The trends observed between intensity and areal density directly relate to the scattering cross-section evaluated at each energy, such that $\sigma(E)$ corresponds to the gradient of the line of best fit. Spectra in the SI with a t/λ greater than 1.0 have been excluded from the calculation, as the linear relationship in Equation 4.12 is no longer accurate above these thicknesses. This is because Equation 4.12 does not capture the effects of the convergence angle of the electron probe, which results in an interaction volume which grows more rapidly at large thicknesses.

The three energies selected in Figure 4.5 illustrate the connection between the scattering cross-section and the gradient. 820 eV (blue triangles in Fig.4.5(b)) precedes the Ni L edge, so the calculated gradient is approximately zero. At the maxima of the Ni L_3 peak (green circles), the Ni L edge is most intense and so has the largest gradient/scattering cross-section. Further beyond the onset, the edge intensity gradually decays and so the calculated gradient – as with 950 eV (red crosses) – decreases with increasing distance from the edge onset. Although data for only three energies are shown in Fig.4.5, the complete differential scattering cross-section is evaluated at all energies in the spectrum image. This can then perform the same role as the Hartree-Slater partial scattering cross-section in quantitative analysis.

Finally, the completed evaluation of the differential scattering cross-sections calculated from experimental data are presented in Figure 4.6. The core-loss edge cross-sections for Ti $L_{2,3}$, Ni $L_{2,3}$, Sn $M_{4,5}$ and Cu $L_{2,3}$ which have been measured are also shown alongside the corresponding cross-sections calculated by DigitalMicrograph using the Hartree-Slater approximation. Of the four elements of interest, the most obvious discrepancy between the measured and calculated cross-sections is for the Ti L edge in Fig.4.6(a), where the intensity

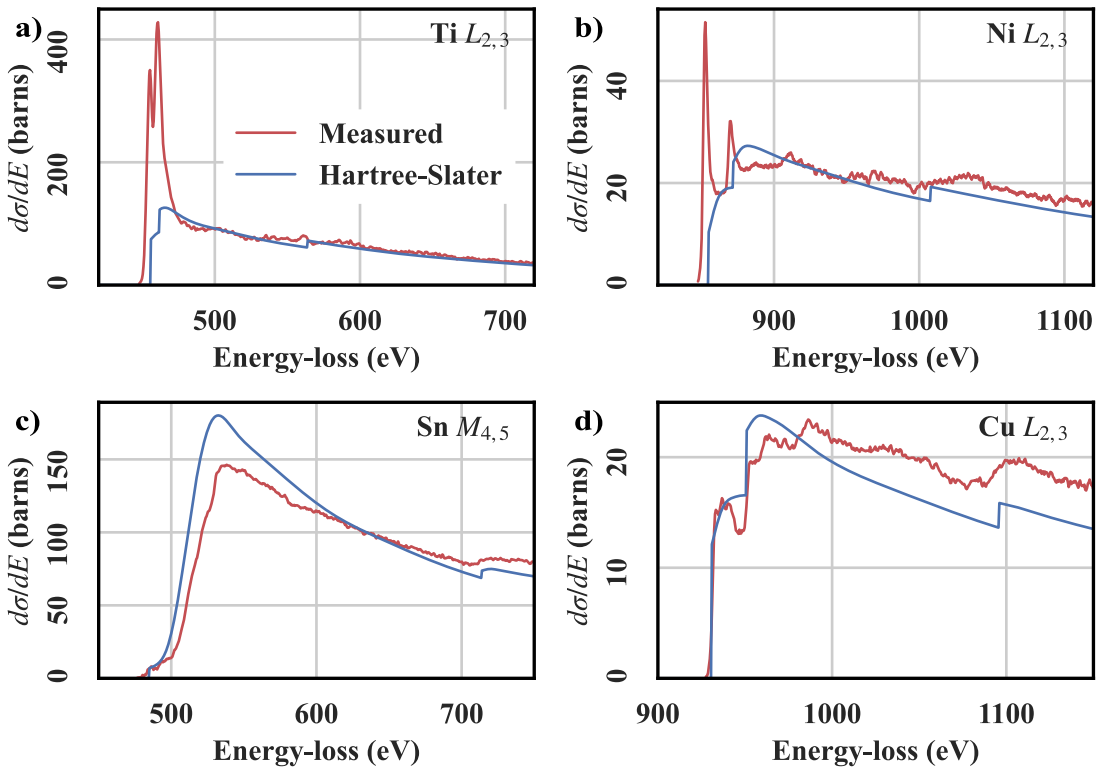

Figure 4.6: The Hartree-Slater (blue) and experimentally measured (red) differential scattering cross-sections for the (a) titanium $L_{2,3}$, (b) nickel $L_{2,3}$, (c) tin $M_{4,5}$ and (d) copper $L_{2,3}$ edges.

in the vicinity of the Ti white lines is grossly underestimated by the HS approximation. The discrepancy found to have the most profound effect on quantification, however, is in the Sn *M* edge cross-section in Fig.4.6(c) where the HS approximation significantly overestimates the magnitude of the cross section up to ~100 eV from the offset. Consequently, quantification of Sn using the HS cross-section would under-estimate the quantity of tin present in the material; by approximately 30 % compared to the experimental cross-section. Meanwhile, the key difference between the experimentally-measured and the HS cross-sections is the improved sensitivity of the experimental measurements to the near-edge structure for all the edges. In some cases this is a clear advantage, which should improve the quality of elemental quantification by reducing errors in fits. Inspection of DFT-calculated electronic DOS for Ti, Ni, Sn [259] and TiNiSn [260] shows a strong similarity between the unoccupied DOS of TiNiSn and elemental Ti, suggesting the change in the unoccupied DOS is small and the experimental cross-sections for the individual elements provide a reasonable approximation for the hH DOS. In other compounds such as oxides, however, significant alteration of the density of states and binding energy can result in chemical shifts in the edge onset or changes in near-edge structure [211, 227] which might compromise the quality of fitting procedures. A further advantage of the experimentally measured cross-sections over the HS cross-sections

comes from the parity of experimental conditions, which ensures that the instrumental broadening of the spectrum is included in any quantification using the experimental references.

4.3 A refined workflow for processing EELS data for absolute quantification

For absolute compositional quantification in EELS to be accurate, diligent measures are required for both spectral acquisition and processing. In this section, the workflow developed for processing EELS data for elemental quantification by experimental references is described. The workflow contains a series of steps which are a mix of physical and practical considerations for getting the best results from dualEELS spectra. Starting with existing wisdom about the processing of EELS spectra and spectrum images, Figure 4.7 outlines the workflow for taking as-acquired spectra to the point of being ready for absolute elemental

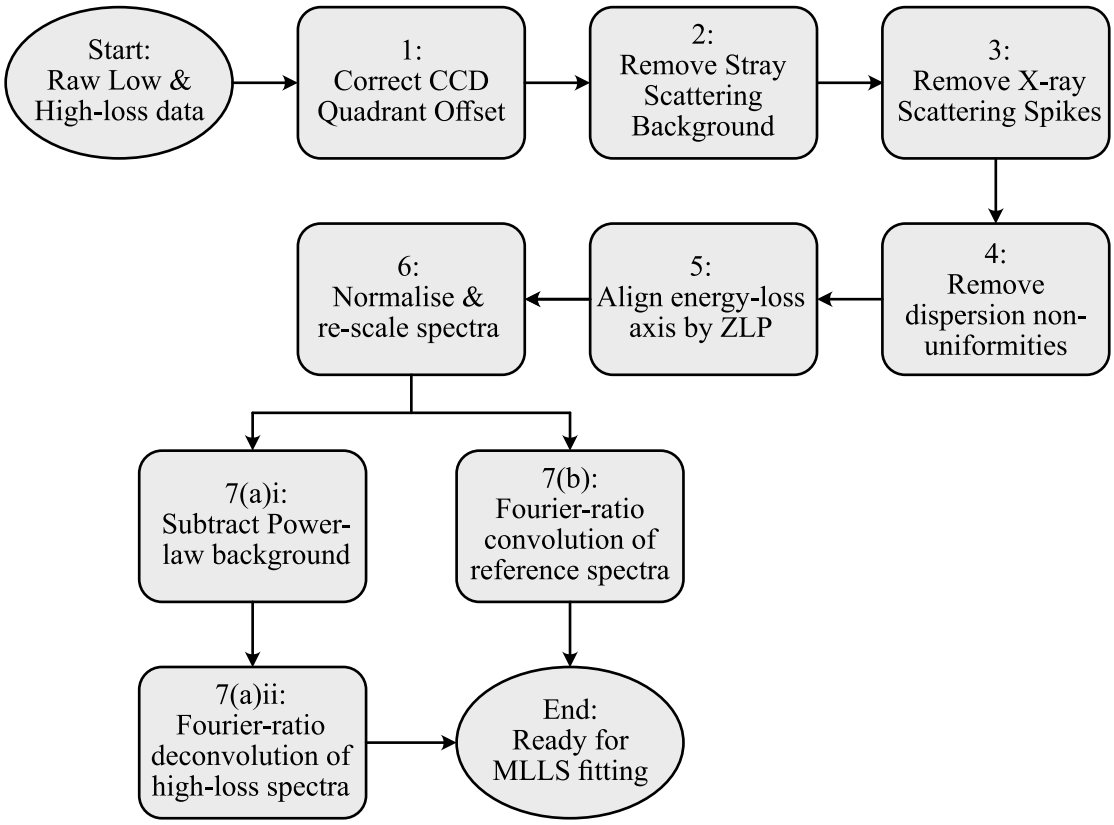

Figure 4.7: Workflow for preparing dualEELS datasets for standard-based elemental quantification. Note that either the high-loss spectra can be deconvolved to recover the SSD for fitting (step 7(a)), or the experimentally measured cross-sections can be convolved with the low-loss (step 7(b)).

quantification. The workflow starts with a series of steps to remove unwanted artefacts from the data, before calibrating both the energy-loss axis and the recorded intensities. Then, for compatibility between the spectra and the experimental cross-sections, plural scattering needs to be treated. This can be achieved either by deconvolving the spectrum to recover a SSD, or by convolving the cross-sections so they also contain the plural scattering effects present in the spectrum. The rationale for the two different approaches is discussed on p.134 and all of the steps are summarised below. This protocol is used for all EELS elemental analysis presented throughout this thesis, in this and all the following chapters.

1: CCD quadrant offset balancing The construction of the CCD detector on the Gatan GIF *Quantum* [165] provides 2048 × 2048 pixels divided across four quadrants. This segmentation of the CCD allows the four quadrants to be read out simultaneously and reduce overheads from readout times. In dualEELS operation, the high and low-loss spectra are exposed on different halves of the CCD, such that each spectrum is measured from two of these quadrants. Small artefacts in the dark reference of the CCD have been found to lead to a constant offset between the two quadrants on which a spectrum is exposed, resulting in a step in the spectrum between the two quadrants (i.e. between channels 1024 and 1025) [233], as illustrated in Figure 4.8.

This ‘glitch’ in the spectrum is most apparent in the low-loss spectrum where, at the centre CCD channels, the spectrum intensity is low and any step between the quadrants will be a significant feature. The first step in processing EELS spectra in Fig.4.7 is to correct this artefact. The offset between quadrants can be corrected post-acquisition by a pragmatic ‘balancing’ of the magnitude of the step which takes account of the constant offset introduced through an error in the dark reference [233]. The size of the offset is determined by averaging over a few channels (about 10, typically) either side of the step at the centre after applying a top-hat smoothing function to mitigate noise levels. The difference in intensity found determines the size of the offset to be applied, with half the offset being added to the quadrant at the bottom of the step, and half the offset removed from the other quadrant [233].

It is worth noting that, with sufficiently good detector dark and gain references, this step should be unnecessary. Checking for whether a noticeable step is present and requires removing is recommended, even if a correction is not found to be needed. This procedure is complicated, however, if an edge onset lies on the midpoint of the spectrum, at which point we would be at risk of doctoring real spectral features.

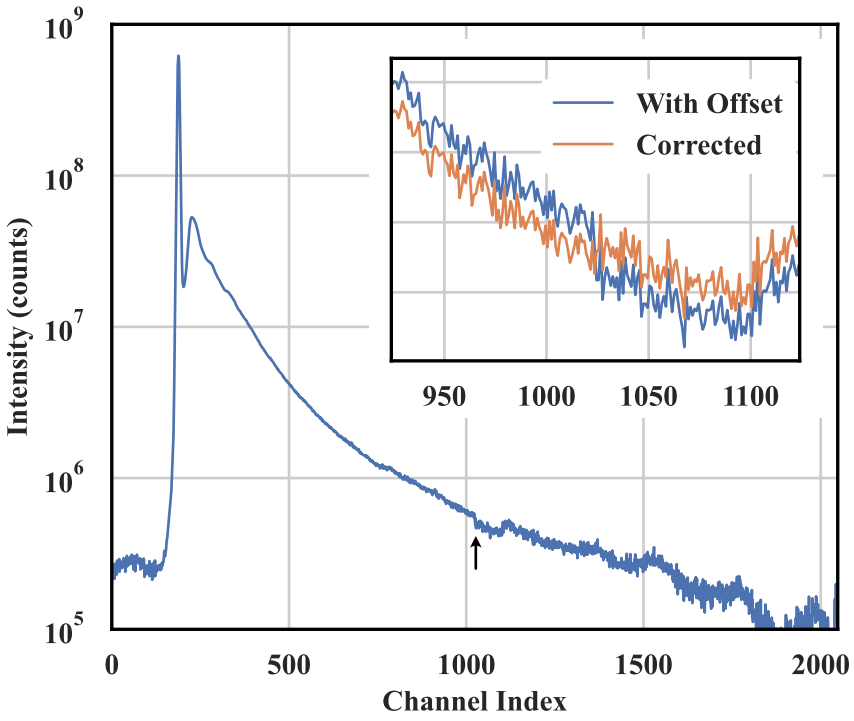

Figure 4.8: An as-recorded dualEELS low-loss spectrum, shown here in terms of CCD channel number, instead of energy calibration. At channels 1024-1025, which mark the edges of the two CCD quadrants, there is a small step indicated by the arrow. Inset is a close-up of the offset between the two halves (blue), along with the same spectrum after the offset has been corrected for (orange).

2: Removal of stray electron scattering There are two sources of stray scattering which can contribute unwanted counts to an energy-loss spectrum. These derive either from stray electron scattering from the interior of the spectrometer, or from the generation of hard X-rays inside the microscope. First, we will handle stray electron scattering, which is step two in the workflow in Fig.4.7. This describes when electrons strike solid material other than the specimen inside the microscope column, generating backscattered or secondary electrons with a range of energies. This stray scattering has implications for the recorded intensities in dualEELS, where the low-loss is recorded on one half of the CCD and the high-loss on the other. Although the low-loss spectrum is only exposed on the CCD for a brief time, the CCD still records counts across the entire CCD while the high-loss is exposed [196]. The difference in exposure times can often be as large as a factor of 10^3, so stray scattering 'measured' on the low-loss during the high-loss exposure can become a non-negligible contribution to the low-loss spectrum, which can have implications for spectral splicing or deconvolution [233].

To limit the effects of stray scattering such as this in the spectrum, the energy-selecting slit of the *Quantum* is used as a beam trap for the low-loss spectrum during the high-loss acquisition. However stray scattering contributions can still arise in the low-loss if the beam

trap does not perfectly contain the intense features of the low-loss during dualEELS acquisition [261]. Previous characterisation of the energy-profile of the stray signal by Craven *et al.* demonstrate that it has a persistent profile which can be used to scale and subtract stray scattering of its kind from any spectrum or spectrum image [233, 261].

3: Removal of stray X-ray scattering A further consequence of high-energy electrons scattering from solid material in the column or spectrometer is the generation of X-rays. If any of these X-rays arrive at the CCD detector during a spectrum acquisition, the incident channel records a localised spike in intensity which is often orders of magnitude larger than the recorded spectrum. Because the pixels illuminated by X-rays record such a high intensity, it is relatively straightforward to remove them from spectra, and this is done as step three of Fig.4.7. In a spectrum image, the mean and standard deviation of each single-energy slice is computed. X-rays are then defined as any feature with an intensity greater than the mean value by some threshold, defined as a multiple of the standard deviation (σ). Intensity values recorded as being above the threshold are replaced with the median of the surrounding pixels. If the threshold factor is set too low, real contributions to the energy-loss spectrum may be unintentionally filtered; a threshold value of 20σ has been used throughout this work.

4: Correction for dispersion non-uniformities Step four of Fig.4.7 involves handling any dispersion non-uniformities. Correcting the spectral dispersion ensures that the energy-loss scale is replicable between experiments which is important in having the experimental cross-sections correctly aligning with spectral features. The procedures for measuring and correcting for dispersion non-uniformities were discussed in great detail in Chapter 3 and will not be repeated here.

5: Energy-loss alignment of spectra Instabilities in the microscope and spectrometer, when observing an energy-loss spectrum, manifest as variations in either energy or focus as time passes. These instabilities occur with a variety of timescales, ranging from high-frequency energy jitter (~10 ms) to long-term energy drift (over many minutes or hours). Such instabilities have already been documented in Section 3.1.3. When making parallel-EELS measurements on the spectrometer, the channel calibration is fixed so that, for an undeflected spectrum, the zero eV energy is fixed at channel 200: the zoom point. In the presence of system instabilities, however, the centre of the zero-loss peak need not lie at the 0 eV channel

in the as-recorded data. This is especially true for large spectrum images where, over the course of their acquisition, the ZLP can drift continuously and appear in a different position of the detector for each spectrum in the dataset.

Step 5 of the workflow in Fig.4.7 is to take care of this spectral drift, which is easy to fix post-acquisition, owing to the dominating intensity of the ZLP. Each spectrum can be shifted so that the ZLP appears in the same position in all spectra by using a simple algorithm to find the position of the value of maximum intensity in the spectrum. For typical TEM specimens, this most intense value should always correspond to the apex of the ZLP. The centre of the ZLP can be found with sub-channel precision using the 'Align SI by peak' tool in DigitalMicrograph, which calculates the peak position throughout a spectrum image and the offset required to calibrate the ZLP to 0 eV. Spectra can then be interpolated along the energy-loss axis by the offset to 0 eV, so that all spectra in the spectrum image are aligned consistently in energy.

6: Spectral Normalisation For elemental concentrations to be quantified absolutely, spectral intensities must first be properly normalised. In the same way that needle-specimen spectra were treated for extracting the differential scattering cross-sections, spectra from an unknown specimen must be scaled in keeping with Equation 4.12 so that the measured intensities unambiguously relate to an absolute physical quantity, as follows. First, the low-loss spectrum image is multiplied by the high/low-loss time-ratio, so that the intensities are consistent with a single exposure time for both halves of the dualEELS data. The integrated elastic (ZLP) intensity is then calculated from the low-loss and used to normalise the high-loss spectra. Intensities in the high-loss data are then further divided by the value of the spectrometer dispersion setting (in eV/channel) to scale the data consistently with Equation 4.12. Finally, the spectral intensities are multiplied by a factor of 10^{10} to convert into units of barns.

Background subtraction (optional) If opting to remove plural scattering and recover the single-scattering distribution (SSD) by Fourier-ratio deconvolution of the spectrum (steps 7(a) of Fig.4.7), the pre-edge background must first be removed. This is achieved by fitting a power-law relationship to a region prior to an edge, which is then extrapolated under the edge and subtracted from the spectrum, as discussed in Section 4.1.1. Removing the pre-edge background from the lowest-energy-loss edge of interest is sufficient for successful deconvo-

lution. If, instead, the reference cross-sections are to be convolved, background subtraction becomes purely optional, as the power-law can be modelled as part of the quantification.

7: Accounting for plural scattering Finally, for accurate use of the experimental cross-sections, plural scattering has to be taken into account. This can be done by one of two methods; either the data to be quantified is deconvolved to recover the SSD as described in Section 4.1.2, or the experimental cross-sections are convolved with the low-loss data. Convolution of the reference standards is based on the work of Verbeeck and others on model-based quantification [243, 262] and operates on the basis of using the inverse of the Fourier-ratio deconvolution. If Fourier-ratio deconvolution is described by Equation 4.5, then convolution of the cross-sections is described by,

$$j_\sigma(v) = j_{LL}(v)\left[\frac{s_\sigma(v)}{z(v)}\right] , \tag{4.13}$$

where $j_\sigma(v)$ is the Fourier transform of the convolved scattering cross-section. The motivation for this approach, instead of simply deconvolving the spectrum, is that division by the Fourier transform of the low-loss amplifies the high-frequency terms, increasing the high-frequency noise in the spectrum and reducing the SNR [243]. As we are instead multiplying by the low-loss frequency-spectrum, the same noise-amplification does not take place when convolving the spectrum. As with deconvolution, the zero-loss term in the convolution, $z(v)$, encapsulates the instrumental resolution function, and ensures that energy-resolution of the spectrum is not affected by convolution.

Fourier-ratio convolution has been implemented in `SQuEELS` [241], making use of the NumPy array processing module to perform fast Fourier transforms [263]. Convolution of the data can introduce artefacts, including the apparent introduction of an offset in the convolved spectrum, or an apparent 'wraparound' effect where the high energy-loss slope is superimposed on the low energy-loss end of the spectrum. Effects such as these have been explored before in literature [243] and are remedied by 'padding' the spectrum to ensure that, at both ends, it tends smoothly toward zero across a sufficiently long range. The convolution function (`SQuEELS.fourier_tools.fourier_ratio_convolution`) provides the method outlined by Equation 4.13, further treating the spectra to ensure the convolution process does not introduce any of the unwanted artefacts above. In `SQuEELS`, artefacts are prevented by filling the empty space introduced by padding with a Hanning function [264], which can be set up to smoothly vary between the last value in the measured spectrum and zero. This

treatment is applied both to the spectrum to be convolved, and also the low-loss used in the convolution, to ensure that all spectra tend to zero at the edges and do not introduce unwanted effects during convolution.

4.4 Precision of elemental quantification achieved using experimental reference standards

Coming full-circle, the main objective throughout this chapter has been to evaluate best practices in recording and processing EELS data with a view to establishing how precisely the chemical composition of a material can be quantified. After all these steps, it remains to examine the available possibilities for carrying out the quantitative modelling of the data itself. Two approaches based on linear regression are examined. One, the 'model-based' approach representing the current standard practices using the Hartree-Slater cross-sections. The other is the 'reference-based' approach which has been set up in the previous sections of this chapter. To delve deeper into understanding the limitations of elemental quantifications in the reference-based approach, a survey of literature surrounding detectability limits in EELS creates a path to establishing the minimum detectable concentrations of elements based on the Rose criterion for detection. This approach is used to assess the detectability limits of low concentration dopants added to TiNiSn half-Heusler alloys, focusing on the use of copper-dopants.

4.4.1 Comparison of linear regression techniques for EELS quantification

Typical elemental quantification in EELS as described in Section 4.1.4 relies on comparison of intensity integrated over a window of energies typically tens of eV in size. To use the experimentally-measured scattering cross-sections for reference-based elemental quantification in EELS, a multiple linear least-squares (MLLS) approach was used instead. MLLS quantification of EELS, which has previously been demonstrated elsewhere [265, 266], involves describing the observed spectrum as a linear combination of terms,

$$y(E) = a_1\sigma_1(E) + a_2\sigma_2(E) + a_3\sigma_3(E) + \dots , \tag{4.14}$$

where each $\sigma_n(E)$ are the components of the fit represented by the reference differential cross-sections for each element. The coefficients a_n for each component will then represent the quantity of each element present. If the spectra have been collected under similar conditions, then treated and normalised properly according to the procedures set out in Section 4.3, the coefficients directly relate to the number of atoms of each element.

To compare the effectiveness of quantification using reference standards versus the standard practice of using the HS cross-sections, a specimen of half-Heusler TiNiSn doped with copper was examined. This specimen has a nominal composition of $TiNiCu_{0.1}Sn$, however microscopic grain-by-grain variations are expected to deviate from this macroscopic nominal composition [104]. Accurate characterisation of composition is therefore desirable to enhance understanding of these variations and STEM-EELS is an appropriate tool for the length-scales involved. A STEM-EELS spectrum image, recorded over a uniform region within a single grain of the specimen, was provided by J. Halpin for elemental analysis. The nature of the specimen was verified during FIB extraction by electron back-scatter diffraction (EBSD) - to confirm the location is within a single grain - and by energy-dispersive X-ray spectroscopy (EDS), to verify the chemical homogeneity of the liftout region (within the sensitivity limits of SEM-EDS). The spectrum image covers a 250 by 50 nm region in 100 by 20 spectra, corresponding to a spatial pixel separation of 2.5 nm. Acquisition conditions including the spectrometer dispersion, convergence and collection angles are nominally the same as those used for the reference standards. The SI was processed post-acquisition using the procedures outlined in Section 4.3 to ensure that energy and intensity calibrations are consistent prior to least-squares fitting.

Elemental quantification based on the use of Hartree-Slater partial scattering cross-sections was carried out using Gatan DigitalMicrograph (DM) 2.3 [267] and the Elemental Quantification plugin. This plugin mimics the full model-based approach of Verbeeck and Van Aert [243], where the HS cross-sections are ‘forward-convolved’ with a low-loss spectrum, similar to the convolution procedure described on p.134, however the DM implementation does not consider instrumental broadening. Further, near-edge fine structure is included in the model by assuming that the observed unoccupied density of states in the ELNES region, which contains solid-state effects, is the same as that in the atomic approximation of the HS cross-section [262]. This method effectively uses the fit residuals to take account of ELNES and such a fit can be compromised in circumstances where multiple core-loss edges are in close proximity, as is true for TiNiSn.

	Model-based (at./nm^2)	% St.Dev	Reference-based (at./nm^2)	% St.Dev
Ti	1770 ± 177	10	1799 ± 26	1.4
Ni	1768 ± 177	10	2141 ± 69	3.2
Sn	1534 ± 354	20	1703 ± 22	1.3
Cu	89.5 ± 56.1	62.7	406 ± 88	21.7

Table 4.2: Areal densities of specimen determined by model-based and reference-based quantification methods. Results and standard deviation errors are the mean values from individually fitting all spectra in the spectrum image.

Reference-based quantification routines were implemented using Python and incorporated into the *SQuEELS* module for easily replicable use [241]. In the reference-based approach, the desired experimentally-measured scattering cross-sections are each Fourier-ratio convolved with the low-loss spectra from the data to be quantified, as described in the previous section. Adding the effects of plural scattering to the reference standards by convolution, rather than recovering the SSD from the data to be quantified avoids increasing the noise content of the data by deconvolution [243]. The MLLS fitting procedure for elemental quantification used here was an implementation of the Levenberg-Marquardt [268, 269] non-linear least-squares algorithm available in the Python module *SciPy* (`scipy.optimize.curve_fit`) [270]. Although we have set out that the spectrum should be described by a linear combination of reference spectra (Equation 4.14), the non-linear algorithm further allows the incorporation of non-linear terms including power-law backgrounds in the model. Including the background in the fit model, rather than using a small pre-edge region to fit and subtract the background before modelling, is preferable as extrapolation across large energy ranges can be unreliable [111, 243]. Spectra were fitted for titanium, tin, nickel, copper and a power-law background across an energy range covering 400 eV up to 1100 eV. This ensures the fitted region includes a sufficient region of potential copper signal to reduce fit errors from limiting the available counts.

The mean composition of the specimen as determined by each method is found to be $TiNiCu_{0.05}Sn_{0.87}$ for model-based quantification and $TiNi_{1.19}Cu_{0.19}Sn_{0.95}$ for standard-based modelling. The corresponding absolute mean elemental quantities in terms of areal densities are presented in Table 4.2 along with typical standard deviations deriving from the fitting procedure for both methods. These average results are represented in Figure 4.9, which shows the mean high-loss spectrum, as well as the Fourier-ratio convolved experimental cross-sections and power-law background fitted to the measured spectrum. A comparison of the fit errors, based on the standard deviations in Table 4.2, shows that the reference-based fitting gives a marked improvement in the precision of the quantities of all elements. It is worth noting

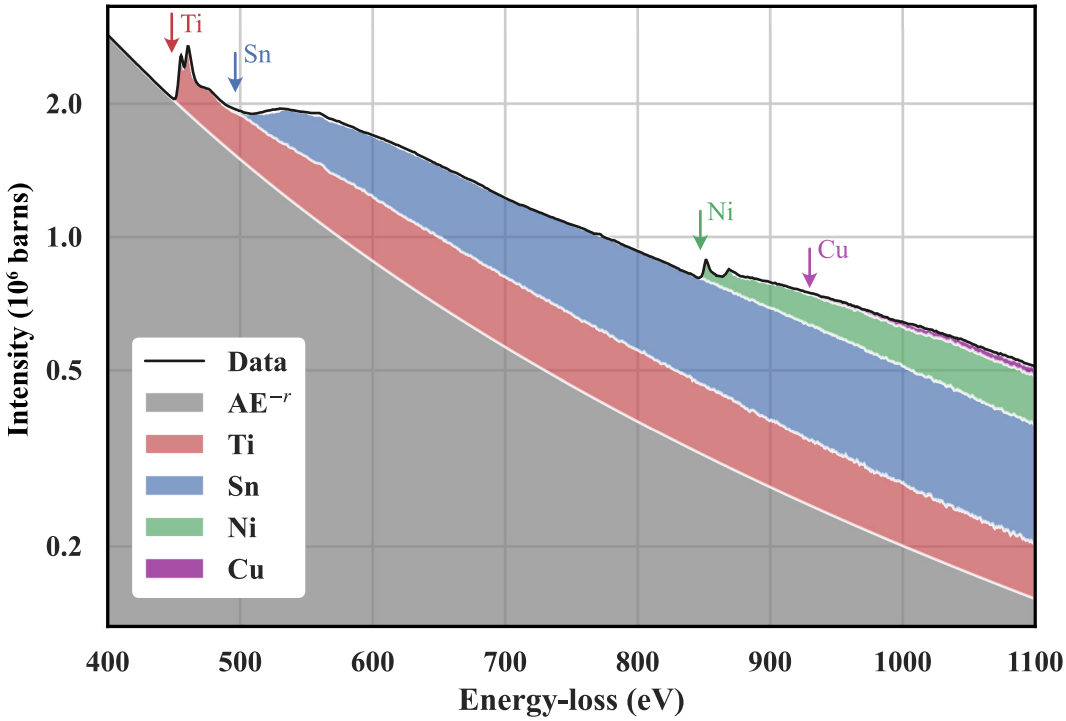

Figure 4.9: The mean high-loss spectrum (black line) from the spectrum image. The shaded regions denote the components of the spectrum described by the mean elemental quantities in Table 4.2 found using the reference-based method.

that the standard deviations for Ti, Ni and Sn in the model-based quantification appear to have been given a default value based on the approximate uncertainty in the Hartree-Slater partial cross-sections [251]. This naive approximation of the quantification error does not reflect the real standard deviation of the fitting procedure which, if smaller than these values, is unfortunately obscured from the user.

In an attempt to make a more meaningful comparison between the two methods, the results of fitting spectra across the entire spectrum image are compared. Results of both the model-based and standard-based quantifications for all spectra were compiled into histograms presented in Figure 4.10. These plots show the distributions of absolute quantification values for titanium, nickel, tin and copper, with line-traces overlaid showing the normal distributions used to model them and extract statistics. The standard deviations in the distribution of results yields a poorer precision than the statistics from an individual model, which is indicative of noise contributions in the spectra. Still, the standard-based quantification performs better than the model-based method, with a significant reduction in the variance of results for both Ti and Sn. Further, as noted earlier in Section 4.2.2 when discussing the discrepancies between the HS and experimental cross-sections, the apparent deficiency in the quantity of tin is remedied by use of the experimental tin standard for quantification and nearly matches

the absolute quantity of titanium.

In addition to the improved precision of elemental quantification and reliable determination of absolute quantities of elements, the results of reference-based quantification can be used to infer the inelastic mfp of the specimen. Based on the 5.95 Å lattice constant determined by colleagues [104], and the mean density of titanium calculated from reference-based quantification, the specimen is estimated to have an absolute thickness of 94.7 ± 2.2 nm. This absolute thickness corresponds to a mean log-ratio relative thickness of 1.02 mfps, indicating that the inelastic mfp for TiNiSn-based Heusler alloys is about 92.8 nm.

Examining both model-based and reference-based methods for elemental quantification,

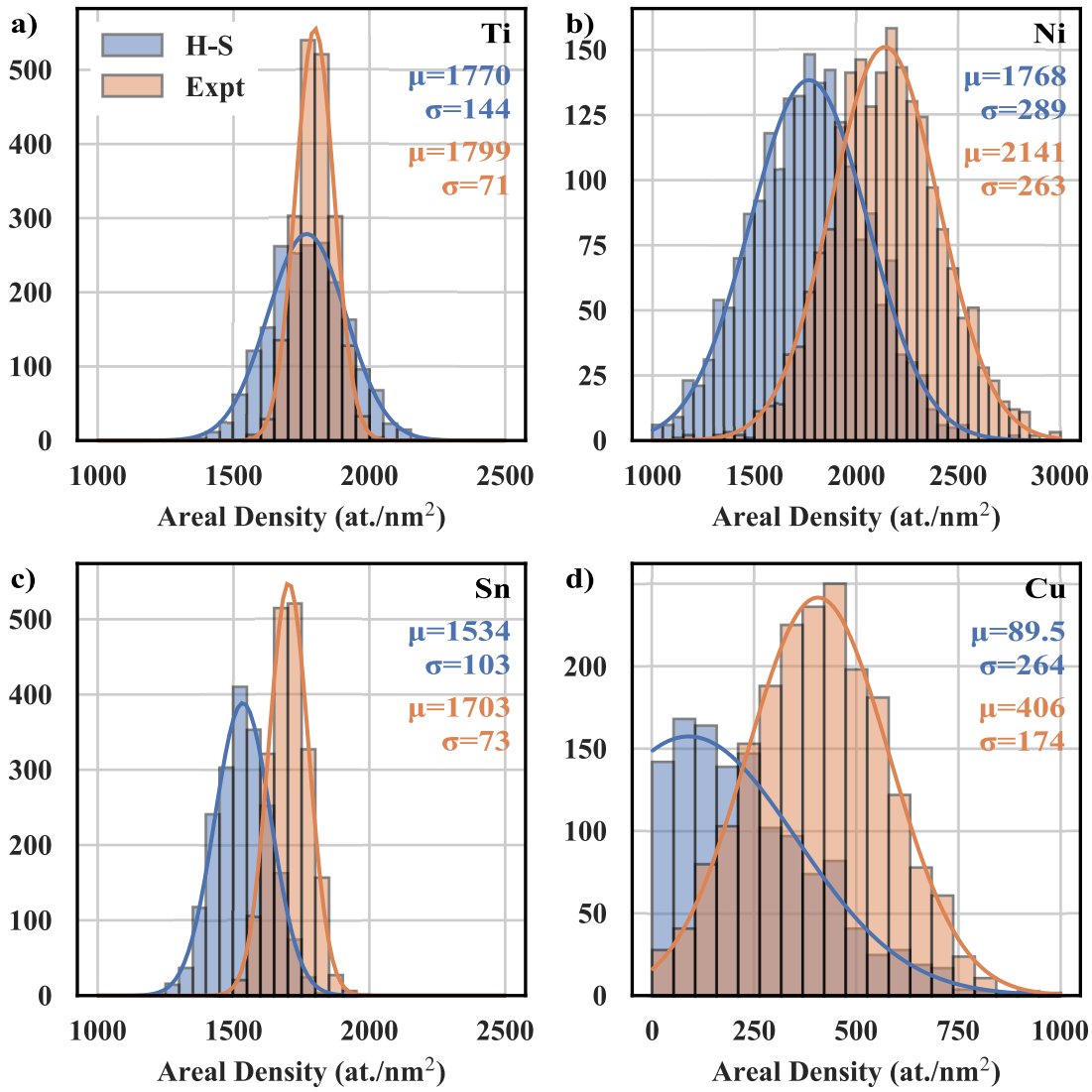

Figure 4.10: Distribution of results of elemental quantification of individual spectra within the spectrum image by model-based (blue) and reference-based (orange) methods for (a) titanium, (b) nickel, (c) tin and (d) copper. The means (μ) and standard deviations (σ) of each distribution are also presented for each method and each element.

the use of experimentally-measured scattering cross-sections provides not only absolute chemical quantification, but also a measurable improvement on the use of the Hartree-Slater partial cross-sections. Although a relative improvement in precision has been established, this comparison does not provide information of the absolute degree of precision for elemental quantification. The absolute limitations of reference-based quantification shall be explored in the next section.

4.4.2 Detectability limits in the reference-based approach

Although the improvement in precision gained using a reference-based method rather than a model-based method for elemental quantification is now established for characterising TiNiSn-based half-Heusler alloys, this comparison does not consider the ultimate limits of the quantification. It is worth noting that the distribution of copper quantities determined in either approach in Figure 4.10 intersects with a zero-quantity of copper. Nearly half of the results in the model-based approach register no copper, while about 2 % of results in the standard-based approach do not return a valid quantity of copper. In such a situation, the key question revolves around how to distinguish between a real signal and a false positive (or conversely, no signal and a false negative) when searching for elements in low concentrations.

The question of detectability limits – the minimum elemental quantity which can be discerned in a spectrum with absolute (or near-absolute) certainty – in EELS is a challenging one, involving a degree of subjectivity. This subjective nature stems from the interpretation of the work of Albert Rose [271, 272], who set out a mathematical framework for describing the certainty with which a signal is real, based on probabilities of a measured signal being a false-positive. In essence, Rose states that, for credible detection, a signal must be a factor h larger than the RMS (root-mean-square) of the background noise. Larger values of h correspond to a lower probability that a single measurement is actually of the background, rather than a real signal. This probability is based on the normal distribution, such that h effectively represents the number of standard deviations above the mean background; i.e. there is a 15, 2.3, 0.13 % probability of detecting counts from the background above h-values of 1, 2 and 3, respectively, with increasingly diminishing probability for higher h [272].

Rose acknowledged the subjectivity in choosing an appropriate h-value and opted for choosing a value of h which effectively limited the prospect of a false result. For instance, in the spectrum image in the previous section – which contains 2000 spectra – there are effect-

ively 2000 chances to generate a false result; so the there needs to be a smaller than 0.05 % chance of making an erroneous detection. From this logic, an h of 4 would be an appropriate level to set for the Rose criterion. In other work which has addressed the use of EELS to detect trace elements, this criteria has been treated in a more relaxed, less stringent manner, with $h = 3$ typically seen as being universally sufficient [273, 274]. To consider the Rose criterion in terms of EELS analysis Egerton and others developed an ansatz to describe the minimum atomic fraction (*MAF*) of an element which is detectable [111, 273],

$$MAF = \frac{N}{N_T} = \frac{SNR}{\sigma_k}\sqrt{\frac{he\sigma_b}{IT}}\,, \tag{4.15}$$

where N/N_T denotes the quantity of one element as a fraction of the total, *SNR* is the signal to noise ratio of the spectrum, σ_k is the cross-section of the element in question in the fit range, while σ_b is the corresponding cross-section for the background. The term e/IT takes into account the beam current and exposure time, while h here is referred to by the authors as a 'background extrapolation parameter' [273], though it is drawn directly from the Rose criterion definition of the SNR required for a valid detection,

$$SNR = \frac{I_k}{\sqrt{I_k + hI_b}}\,, \tag{4.16}$$

where I_k and I_b denote the signal and background intensities. The SNR is then dictated by the choice of h-value. This description of the *MAF* has been found to be incompatible with quantification by MLLS fitting and subsequent studies of detectability limits have outlined adjustments which allow determination of *MAF* compatible with MLLS quantification [274].

Looking further into how Riegler and Kothleitner framed the problem of detectability limits in MLLS quantification of trace elements in ruby [274], there are a couple of useful definitions. The first of these is a convenient description of the SNR of an element, described by the MLLS fit properties as,

$$SNR_i = \frac{a_i}{u_i}\,, \tag{4.17}$$

where a_i is the MLLS fit coefficient of element i, and u_i is the uncertainty, or standard deviation, of the fit coefficient, which provides an equivalent description of the noise if the fitted region is large enough [275]. As a result of this definition, the description of the *MAF* can be recast in terms of MLLS uncertainties as,

$$MAF = \frac{N}{N_T} = \frac{3}{\sigma_k}\frac{u_k e}{N_T IT}(DQE)^{-\frac{1}{2}}\,, \tag{4.18}$$

where the factor of 3 derives from the Rose criterion, and the new term, *DQE* is the detector quantum effiency, which takes into account that the detector does not record the spectrum with perfect efficiency [274]. Considering the data introduced in Section 4.4.1, the physical properties of the microscope, such as the DQE, have little bearing on a relative interpretation of the *MAF*, so the expression in Equation 4.18 simplifies greatly,

$$MAF = \frac{N}{N_T} = 3\frac{u_k}{\sum_i a_i}\,, \tag{4.19}$$

where u_k is still the uncertainty in the fit coefficient for the element of interest and the total atomic quantity N_T is described as the sum of the fit coefficients for all elements. The factor of 3 is retained here as the default value of for interpretation of the Rose criterion though, as discussed earlier, a more stringent factor may be desired.

Using the definition of the MAF in Equation 4.19, the minimum atomic fraction of copper which can be determined with certainty from a single spectrum in the SI is 4.3 %; the composition found for this specimen indicates 6.7 % copper. This detectability limit for Cu is quite large, and there are a couple of points to consider here. First, spectra contained in 3d spectrum images are typically sampled with a low exposure time, and therefore poor SNR. The exposure time for this spectrum image is 50 ms per spectrum; several orders of magnitude smaller than the typical exposure time used in any other detectability limit study, which count for tens or hundreds of seconds [192, 273, 274, 276, 277]. The second point to note is that, for a fixed pEELS exposure time, the SNR of the spectrum degrades with increasing energy-loss. Thus, an exposure time which gives suitable counting statistics for, say, the titanium or tin edges may not be sufficient for the higher energy-loss nickel or copper edges, as the fit distributions in Figure 4.10 would seem to indicate.

Without making new measurements, it is possible to 'increase' the SNR of the spectra post-acquisition by rebinning the spectrum image, emulating the effect of increasing the exposure time. Noise in the spectrum arises from multiple sources, some of which are additive and can be averaged out by increasing exposure times, including Poisson statistical noise [275]. Other sources of noise are fixed and remain constant in relative magnitude as the exposure is increased, such as fixed-pattern detector readout noise [209]. It is worth noting that integrating across multiple (or, indeed, all) spectra in the SI is only valid because the specimen is of uniform composition and thickness in the probed region; this approach would be of limited use in specimens which have either of such chemical or physical variations. To examine

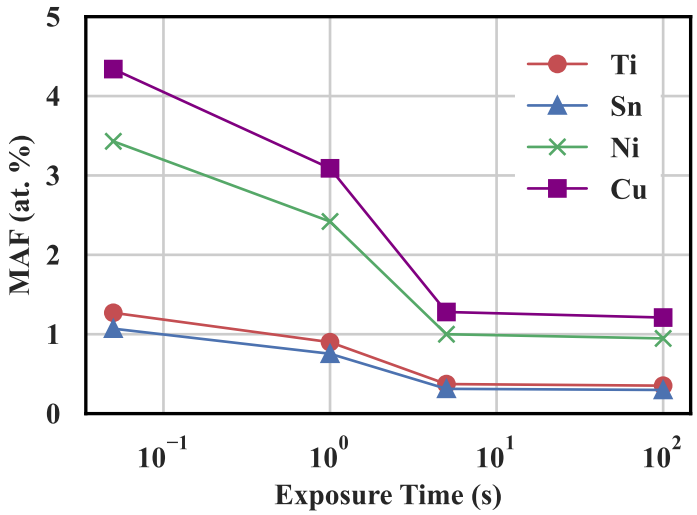

Figure 4.11: Minimum detectable atomic fraction (MAF) of each element at spectrum 'exposure times' of 0.05 s, 1 s, 5 s and 100 s.

what effect this has on the MLLS standard-based quantification, the MAF for each of Ti, Ni, Sn and Cu are calculated on the original individual-spectra basis and also for spectra which have been integrated across 20, 100 and all 2000 points in the SI; emulating exposure times of 1, 5 and 100 s, respectively. The results of these calculations are shown in Figure 4.11, where the MAF for each element and each 'exposure time' is plotted. Consistent with the degrading SNR at increasing energy-losses, the MAF for Ti and Sn is far superior to Ni and Cu, plateauing at ~0.3 at.% for the larger integrations. The reduction in SNR by integrating spectra is apparent up to the 5 s total exposure time, where the MAF for copper drops to 1.2 %, indicating the limit for detection in this particular dataset. There is minimal difference between the MAFs for 5 s and 100 s, suggesting all additive noise which can be mitigated by integrating multiple exposures has been eliminated and fixed-pattern effects now limit the SNR. In principle, detector fixed-pattern should be corrected by the detector dark reference, however there are known issues associated with the use of dark references [209]. Procedures for reducing the magnitude of fixed-pattern noise in the spectrum rely on energy-shifting the spectrum across multiple exposures, such that the position of the fixed pattern relative to the spectrum is different in each exposure [209, 222]. Alignment and summation of the individually exposed spectra is then capable of averaging out the effects of both Poisson noise and fixed-pattern noise, further improving the SNR.

4.5 Conclusions

Throughout this Chapter, the means for experimentally deriving scattering cross-sections has been discussed, along with introducing a workflow for processing spectra or spectrum images such that elemental quantification returns results which can be interpreted in an absolute sense. The reference-based elemental quantification has been shown to provide a marked improvement in precision of compositional results in comparison to a model-based approach grounded in the use of Hartree-Slater cross-sections. Applying these improvements to compositional analysis of a specimen of $TiNiCu_{0.1}Sn$ half-Heusler thermoelectric, the composition of the grain investigated is found to be $TiNi_{1.19}Cu_{0.19}Sn_{0.95}$. Not only does this grain contain nearly double the expected concentration of copper, but a significant excess of Ni is also measured, highlighting the importance of sensitivity to nano- and micro-scale variations in the composition of thermoelectric materials. Other grains which have been studied from the same specimen highlight grain-by-grain variations in the composition [104] that are presumed to tend toward the nominal bulk composition upon averaging over many grains. However, as it is the variations in the composition which are important in enhancing the thermoelectric efficiency, rather than the net composition, accurate assessment of the nature of such granular segregation is key.

An important aspect of elemental quantification of Heusler alloys which remains to be explored in detail is accurate comparison with other quantitative techniques. As focus in thermoelectric Heusler research shifts to characterisation across many lengthscales, reliable and comparable use of different analytical methods is desirable to complement STEM-EELS analysis. Without a Heusler specimen where the composition is reliably known, defining an accurate calibration which is consistent across different analytical techniques is challenging. Without a consistent cross-calibration, comparison of elemental analyses from other techniques can be subject to unique instrumental factors specific to each technique. This area is of active interest for future exploration and efforts to correlate STEM-EELS results with 3d atom-probe tomography and SEM-EDS analyses are ongoing.

Science, my lad, is made up of mistakes, but they are mistakes which it is useful to make, because they lead little by little to the truth.

Jules Verne

5

Growth of nanostructured TiNiSn half-Heusler thin films

HEUSLER ALLOYS are a versatile family of materials. This versatility is useful, as it may support a multitude of functionalities and applications. For instance, a great deal of interest in applications of Heusler alloys has been as magnetic materials for spintronics or magneto-optics, as some Heuslers exhibit interesting spin or magnetic properties without containing any of the traditionally ferromagnetic elements (iron, cobalt or nickel) [278–280]. As much as the versatility of the Heusler alloys is a boon, it can, however, also be a significant disadvantage. The ease with which so many different elements can be incorporated into the Heusler structure presents a highly-complex chemical phase-space which, from a growth perspective, makes fabricating a specimen of stoichiometric, single-phase Heusler quite challenging.

Though from a growth perspective creating a pure, chemically uniform Heusler alloy is technically challenging, it is precisely this difficulty which can be exploited to develop more efficient thermoelectrics. The versatility of the chemistry of the Heusler alloys translates into a remarkable capacity for tunability of the material properties, which is of particular interest

when designing materials for thermoelectric generators, where selective manipulation of electrical conductivity, thermal conductivity or carrier concentrations is desirable [35, 49, 281]. Within the Heusler alloy family, TiNiSn stands out as a candidate n-type semiconducting half-Heusler (hH) with a reasonable thermoelectric power factor [67, 83, 282, 283]. Further to its promising performance for thermoelectric applications, TiNiSn crucially exploits abundant, non-toxic natural resources which is an important point to consider when thinking about its widespread use. Others have demonstrated that the performance of TiNiSn can be improved through doping, which can either modulate the electronic properties of the material, or introduce structural and chemical complexity that impedes thermal transport [54, 55, 84, 86, 89, 108, 284–288]. However, doping the material in this manner raises the question of stability of the half-Heusler phase and segregation effects may arise, especially when the synthesis process might not occur at thermodynamic equilibrium.

Thin film growth presents a useful opportunity to fabricate model systems in which to explore phase segregation and nanostructuring within a Heusler alloy matrix. To that end, this chapter describes the growth of epitaxial TiNiSn thin films by pulsed laser deposition (PLD). TiNiSn thin films have been deposited by other processes before [289–291], but the ability of PLD to produce multi-component films and non-equilibrium phases and structures [292] could be advantageous here. PLD has been used for TiNiSn once before, but only to produce a solution of nanoparticles [293] under conditions that are atypical of PLD thin film research. The growth of high-quality, epitaxial films of TiNiSn is pertinent to all the work in the coming chapters of this thesis, so the optimisation of growth and characterisation of chemical and structural properties discussed in this chapter will be pertinent throughout. The optimisation of TiNiSn thin film growth and the subsequent nanoscale characterisation of these films is discussed in Sections 5.1 and 5.2, respectively. One of the features that TEM characterisation highlighted was a deleterious reaction with the substrate in the initial stages of growth. In Section 5.3, the use of vanadium as an ultrathin buffer layer to prevent that reaction is discussed.

The work presented in this chapter forms the basis for co-authored, peer-reviewed journal articles which have been published in *APL Materials* [294] and *Applied Surface*

Science [295].

5.1 Optimisation of conditions for pulsed laser deposition

The first efforts in preparing thin films needed to be spent in optimising pulsed laser deposition for TiNiSn. There is a broad parameter-space in PLD which must be investigated to locate the optimal conditions to produce epitaxial thin films. This investigation can be effectively reduced to a four-dimensional problem dependent upon: the ambient gas used during deposition, the temperature of the substrate, the fluence of the laser on the target and the pulse rate of the laser. Each of these parameters has a different role to play in how they affect thin film growth. The ambient gas pressure influences the laser-matter interaction at the target – affecting the deposition rate – and also the kinetic energy of the adatoms as they reach the substrate surface [296]. Substrate temperature controls the thermal energy available to adatoms for surface diffusion once they have arrived at the substrate, which can influence atomic ordering which occurs during growth [297, 298]. The deposition rate is also dependent upon the energy density delivered to the target for sputtering, so is affected by laser fluence [292]. The laser pulse rate can then be tuned to determine how rapidly material is delivered to the substrate, effectively drawing a distinction between deposition rate *per pulse* and deposition rate *per second*.

5.1.1 Optimising the ambient gas pressure

As the aim of this study was to promote the growth of smooth, epitaxial thin films, optimisation of the ambient gas pressure was carried out with respect to both the deposition rate and also the surface roughness of the films. To characterise these metrics, atomic force microscopy (AFM) was used. Films were deposited at room temperature onto silicon-wafer substrates which were marked with a straight line in acetone-soluble ink prior to deposition. The ink was washed away with acetone in an ultrasonic bath to lift off the deposited material directly above the mark and leave a trench with edges sharp enough to be imaged with AFM. The trench edges, whose depth spans the full height of the film, was used to determine the thickness of the deposited film and calibrate the deposition rate. Surface roughness was also determined using AFM, imaging 5×5 μm areas and calculating the RMS roughness from the topographic image.

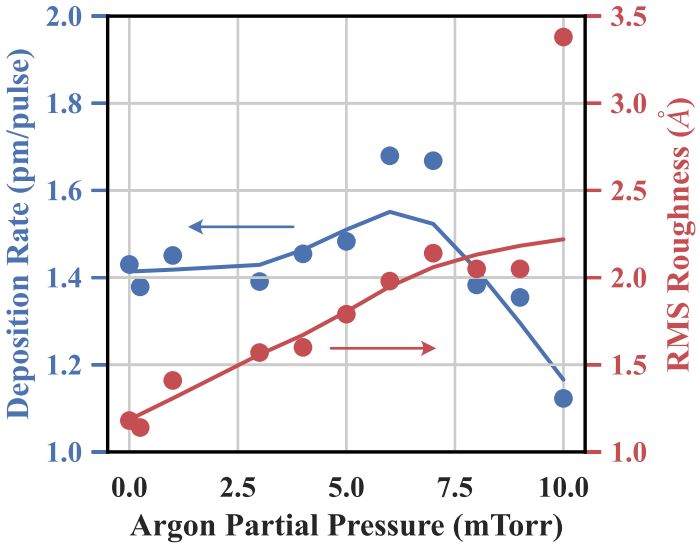

Figure 5.1: Investigation of the effect of ambient gas pressure on the TiNiSn deposition rate (blue, left scale) and surface roughness (red, right scale) at room temperature. Solid lines are Locally Weighted Scatterplot Smoothing curves which help highlight the trends in the data.

Argon (BOC *Pureshield*, 99.998% purity) gas was used to provide the ambient background during deposition of TiNiSn. Partial pressures ranging from 10^{-5} mTorr to 10 mTorr were tested, where 10^{-5} mTorr represents the base pressure of the growth chamber with no gas insertion. Results of probing the effect of argon partial pressure on surface roughness and deposition rate are shown in Figure 5.1. As there are several factors which contribute to the deposition rate, including a time-dependent depreciation of the rate as ablated material coats the laser window and attenuates the laser pulses, direct comparison of the impacts of different gas pressures on the deposition rate is challenging. To properly account for these time-dependent factors, a run of depositions was carried out with gas pressures selected in a non-monotonic order. A background pressure of 1 mTorr Ar was used as a calibration reference and depositions at this pressure were repeated periodically throughout the deposition run to monitor and correct for the time-dependent depreciation in deposition rate. The calculated pressure-dependent deposition rates are presented in Figure 5.1. From the graph, the observed variation in deposition rate is modest, apparently peaking around 6 or 7 mTorr. The sharper drop in the deposition rate at the higher pressure range can be explained by the increased scattering effect of the background gas, reducing the volume of material which reaches the substrate [296]. Consequently, depositing TiNiSn at pressures above 7 mTorr is clearly unfavourable.

As the deposition rate does not change significantly across much of the explored pressure range, it is useful to examine the impact on the roughness of the deposited film, which is also

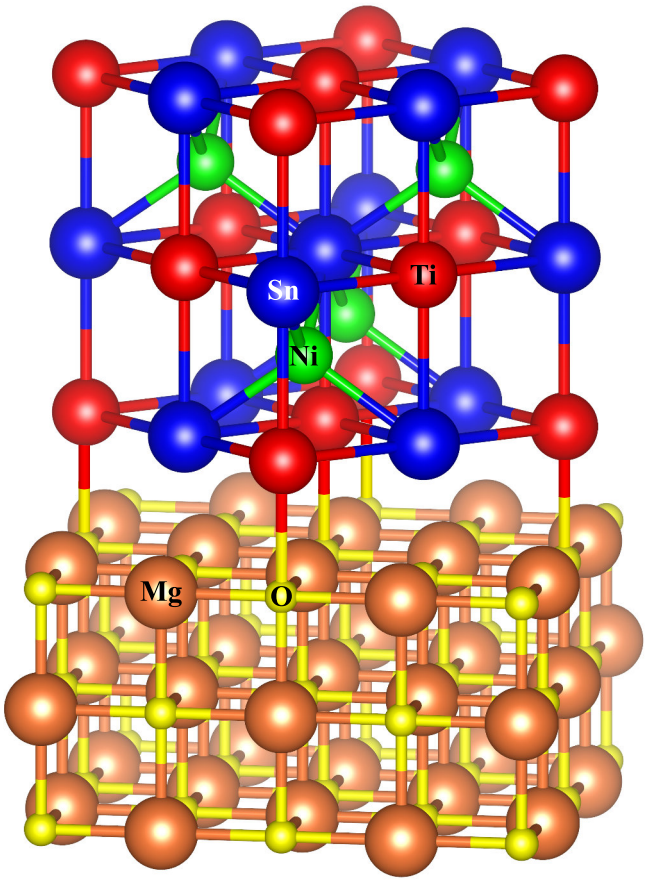

Figure 5.2: Ball-and-stick model of the anticipated epitaxial relationship between MgO and TiNiSn. A single unit cell of TiNiSn registers with the substrate across four unit cells of MgO.

shown in Figure 5.1. For the same films used to determine the influence on deposition rate, the argon partial pressure appears to have a much greater effect on the surface roughness, with the RMS roughness more than doubling between the highest and lowest pressures. This monotonic trend in RMS roughness with Ar partial pressure can be attributed to the increased scattering of the ablation plume by the ambient gas reducing the kinetic energy of the plasma arriving at the substrate. Preferring not to limit the adatom mobility and increase the surface roughness, TiNiSn thin films were deposited using the base pressure of the vacuum system. Low gas pressures reduce scattering and will enable more energetic species to arrive at the substrate, which should facilitate surface diffusion. Further, it emerged that this choice of pressure is consistent with optimal conditions found for PLD of other Heusler alloys [299, 300].

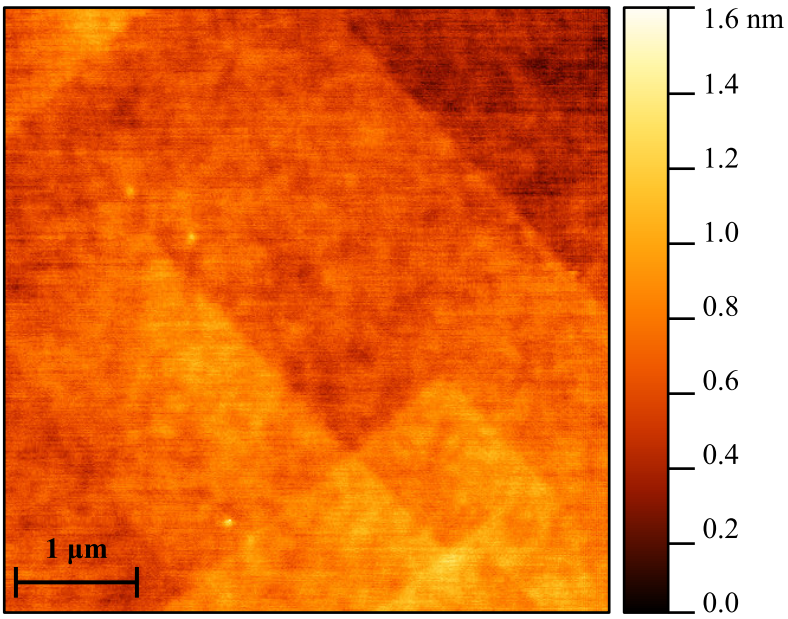

Figure 5.3: Atomic-force micrograph of the surface of an MgO substrate covering a 25 µm² area. Atomic-layer steps on the surface can be clearly seen, typically spread by at least one micron from each other.

5.1.2 Characterisation and preparation of substrates

To achieve epitaxial growth, single-crystal magnesium oxide (MgO) substrates were used. MgO, which has an *fcc* structure with a lattice constant of 4.212 Å [290], was chosen to provide a coincident lattice match with the bulk lattice constant for TiNiSn of 5.957 Å [282] by way of a relative 45° rotation of the unit cell about the z-axis so that the (110) lattice vector of TiNiSn is aligned with the (100) lattice vector of MgO. Figure 5.2 illustrates the expected hetero-epitaxial relationship between MgO and TiNiSn.

Commercial MgO substrates (Pi-Kem Ltd., UK) were used throughout this work. These are cleaved and epi-polished on one side to give an atomically-smooth, (001)-oriented surface. AFM characterisation of the topography, shown in Figure 5.3, shows a terraced surface with steps corresponding to half a unit-cell in height. The overall surface roughness has an RMS value of ~2 Å, as calculated from micrographs covering 5 × 5 µm and 10 × 10 µm areas and is representative of the atomic-scale terracing of the surface.

To prepare for subsequent deposition of thin films, the MgO substrates were first annealed in vacuum at 973 K for at least 1 hour. This *in situ* annealing serves the purpose of removing surface layer contamination by promoting desorption of carbonaceous materials [301]. Annealing under vacuum can also assist in mitigating surface defects caused by air exposure to some extent [302]. There is a possible trade-off for the reduction in surface contamination,

however, as the heat treatment may introduce a small amount of surface roughening through surface rumpling, as has been observed for annealing in air [303]. Since exposure to air is detrimental to the surface quality of the MgO, substrates were kept under vacuum between annealing and deposition.

5.1.3 Exploring the impact of deposition temperature

To promote epitaxial growth, deposition of TiNiSn must be carried out at elevated temperatures to provide energy for thermal diffusion which assists nucleation. Optimisation of the surface temperature was based on two metrics. The first is the crystallographic quality of the film, while the second is the surface roughness. The crystal structure of the film was primarily assessed by reflection high-energy electron diffraction (RHEED) and also through TEM diffraction or X-ray diffraction (XRD) in some cases. Surface roughness was once again assessed using AFM micrographs to examine the surface topography.

To test the effect of substrate temperature, TiNiSn thin films were deposited onto single-crystal MgO substrates at a range of elevated temperatures from 473 to 800 K and, in most cases, without an ambient gas at the base pressure of the vacuum system. Examining the literature surrounding deposition of TiNiSn by other techniques suggested optimal substrate temperatures of 723 K for molecular beam epitaxy (MBE) [290] and 773 K for d.c. sputtering [289].

Figure 5.4 provides an overview of the explored substrate temperature parameter-space. Characterisation of the thin films produced at a range of temperatures has led to identification of four main growth modes of TiNiSn in PLD: amorphous, polycrystalline, epitaxial and segregated epitaxial. Amorphous films, deposited at approximately room temperature (~300 K), have no long-range atomic ordering. A TEM cross-sectional image and diffraction pattern for an amorphous film are presented in the light-blue, 300 K box in Fig.5.4. The amorphous film is continuous with a very smooth surface and there is only slight, mottled contrast within the film. TEM selected area diffraction (SAD) of the film shows a continuous disc of intensity emanating from the direct-beam spot, consistent with cumulative contributions of random ordering typical of an amorphous structure. Bragg reflections arising only from the MgO substrate are also captured in the diffraction pattern and have been marked with red crosses. Amorphous growth occurs as a result of kinetically limited surface diffusion that restricts the capacity for crystalline ordering [121]. Increasing the substrate temperature

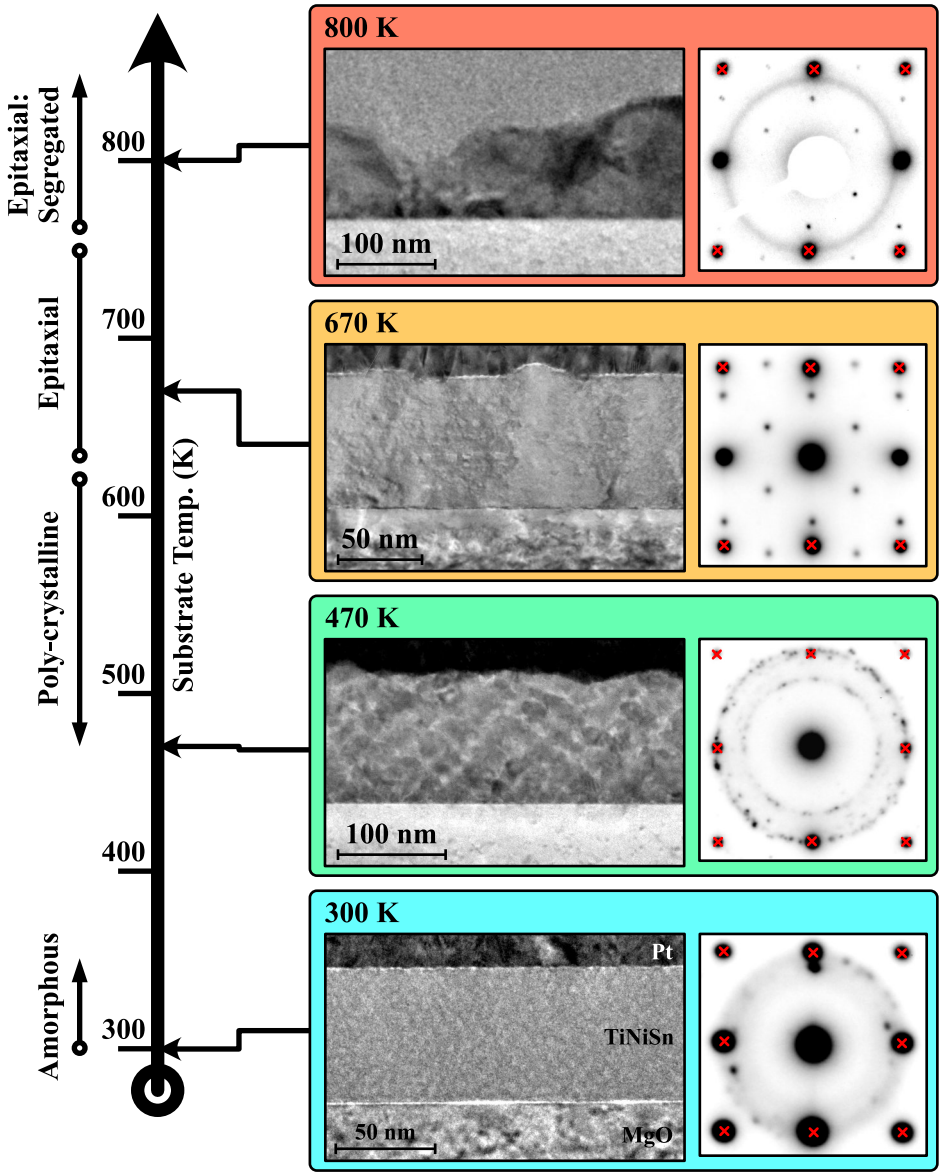

Figure 5.4: Effect of substrate temperature on the growth mode of TiNiSn during pulsed laser deposition. Four main growth modes are identified and examples are presented of thin films grown at temperatures in each of these modes. For each film, a cross-sectional TEM image and TEM diffraction pattern are shown. In the diffraction patterns for all temperatures, spots identified as originating solely from the MgO substrate are marked with red crosses.

during growth relaxes this limitation.

At moderate substrate temperatures, energy from thermal diffusion begins to assist growth and some crystalline ordering starts to emerge. Films grown between 470 K and 620 K have been observed to have polycrystalline character, where crystal grains have formed, but do not have coherent orientation. Examining a polycrystalline film deposited at 470 K in the green box of Figure 5.4, there is an irregularity to the surface compared to the smooth surface of the amorphous film. The increased surface roughness of the polycrystalline film is similar to the sizes of crystal grains which can be seen throughout the TEM image, where

contrast within the film is more pronounced due to the granular nature of the film. The SAD pattern here shows the introduction of some crystal ordering; the presence of many weak spots organised into rings reflects the polycrystalline nature of the film, where small grains have formed with the same crystal structure, but the structure of each grain is arbitrarily oriented. Polycrystalline growth such as this has been observed across a ~150 K range, extending up to nearly 620 K. As the main concern in tuning thin film growth was to achieve epitaxial growth, the low end of the temperature scale has not been explored as thoroughly as the more elevated temperatures. Consequently, the low temperature transition between amorphous and polycrystalline deposition is not marked in Figure 5.4.

Exploring higher substrate temperatures, the increased thermal energy supplied to arriving adatoms unlocks the potential for hetero-epitaxial growth. When the additional thermal energy sufficiently increases the relaxation time for surface diffusion, deposited material can nucleate to form a film which uses the substrate as a template for the structure and orientation of the atomic lattice, i.e., epitaxial growth. Epitaxial growth is typically described by one of three growth modes: 2d layer-by-layer (Franck-van-der-Merwe) growth, 3d island (Vollmer-Weber) growth and mixed layer-then-island (Stranski-Krastanov) growth [297]. For PLD of TiNiSn, epitaxial growth is observed to occur in some form at substrate temperatures above 620 K and, from observations discussed later in Section 5.2.1, always involves nucleation of 3d islands. An example of an epitaxial hH thin film grown at 670 K is shown in Figure 5.4. The SAD pattern for this film now consists of a unique set of Bragg spots corresponding to a single-crystal diffraction pattern, identifying the film as having a single coherent crystal structure and orientation. The TEM image indicates that the film is continuous and relatively smooth with only minor thickness variations. Contrast within the film is also minor, with the columnar variations in contrast arising as a result of separate nucleation sites which are also associated with subtle compositional variations discussed later. Films like this can be reliably produced up to temperatures of about 750 K, above which the deposited films coarsen significantly. An example of this is given using a film deposited at 800 K in Figure 5.4 where, although the SAD pattern indicates the same single-crystal epitaxial relationship as was observed at 670 K, the TEM cross-sectional images shows not only significant variation in film thickness, but also strong contrast variations within the film which likely indicate the occurrence of phase segregation to produce local regions of different chemical compositions. Chemical disordering of the film due to the elevated temperature may either be a result of bulk diffusion during deposition, or be introduced by a chemical imbalance due to the varying vapour pressures of the component elements of TiNiSn at temperatures this high, resulting in

the different elements from the target being delivered at different rates [304].

Although epitaxial growth of TiNiSn appears to be supported for a large range of substrate temperatures above 620 K, there is clear variation in the character and quality of epitaxial thin-films produced dependent upon the exact substrate temperature used. To illustrate, AFM images of film surfaces are presented in Figure 5.5, selected from films within the epitaxial regime grown at substrate temperatures of (a) 630 K, (b) 720 K and (c) 800 K. Morphological changes in the surfaces of the films are quite clear between the images in Fig.5.5(a-b), which highlight a transition from rounded and roughly hemispherical islands whose typical diameter is ~30 nm to large, flat islands that span as much as 200 nm each. The large, flat islands of the 720 K film are similar to the surface features observed in TEM for the 670 K thin film in Figure 5.4, suggesting the range of temperatures over which this particular morphology is accessible. Thin films deposited at temperatures below 670 K, including the film shown here grown at 630 K, are morphologically distinct, indicating a morphological transition between 630 and 670 K. The peak-to-peak range in both images is of order 10 nm which is substantially less than the film thickness, and is consistent with TEM images which show the islands to have coalesced to completely cover the substrate. A further morphological change is observed when the substrate temperature is increased further, as shown in Fig.5.5(c). At 800 K, the peak-to-peak range of the image is comparable to the film thickness and dark regions can be seen where the film has effectively failed to coalesce and fully coat the substrate. Three-dimensional island growth such as this typically arises from limited adatom mobility across step edges in the initial stages of growth by PVD [305]. Contrast in the TEM image in Fig.5.4, however, alludes to significant chemical inhomogeneity which is confirmed by studies of films grown at these temperatures in Chapter 6. It is worth noting that the substrate temperature of 800 K is greater than half the melting point temperature of TiNiSn (1453 K [106]) and so bulk diffusion is probable [121]. The activation of bulk diffusion is likely responsible for the chemical phase separation observed in Chapter 6 and this chemical disorder be linked to the extreme film roughness at these temperatures.

In addition to the AFM images of the final film surfaces, RHEED patterns recorded at the end of thin film deposition are presented in Fig.5.5(d-f). At all three deposition temperatures, the same lattice reflections are visible in RHEED, with variations in how the pattern presents due to the changes in the surface morphology. Both patterns in Fig.5.5(d) and Fig.5.5(e) have – to differing degrees – a spotty character produced by the three-dimensionally rough surfaces where the RHEED electron beam is transmitted through the outermost islands. This

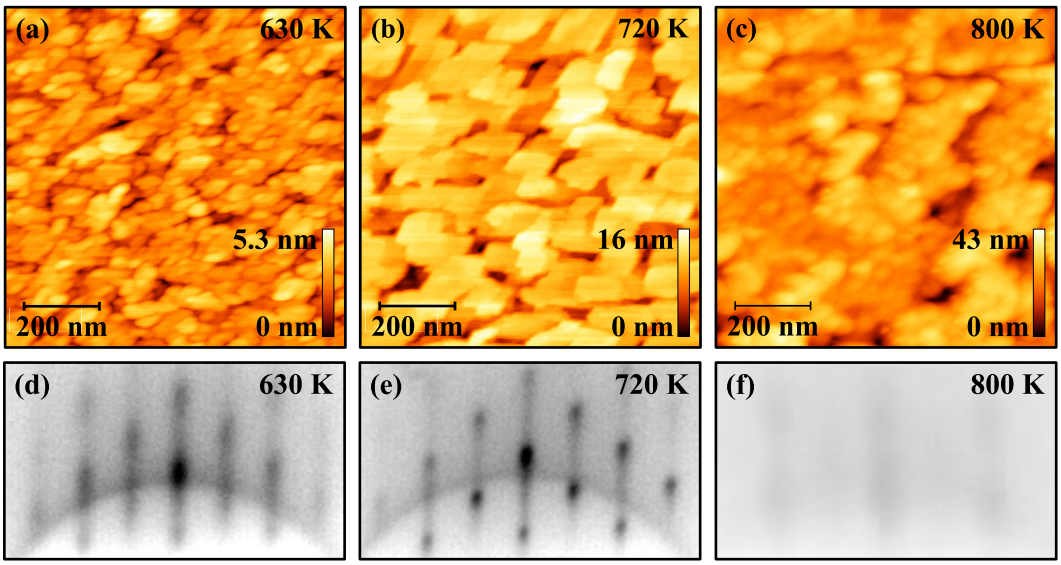

Figure 5.5: AFM micrographs of the surfaces of ~50-100 nm thick TiNiSn films grown at substrate temperatures of (a) 630 K, (b) 720 K and (c) 800 K, with [(d)-(f)] the corresponding RHEED patterns for (a)-(c) observed at the end of thin-film growth. RHEED patterns are collected with the electron beam at a grazing angle to the (100) direction of the MgO substrate. The RHEED pattern in (f) is incredibly diffuse and made difficult to observe due to the roughness of the film.

is taken further in Fig.5.5(f), where the more extreme surface roughness diminishes almost all Bragg intensity from the pattern and the lattice rods are barely visible over the diffuse background scattering. Neither pattern contains peaks which are notably sharp, however the diffuse background is least significant for the film grown at 720 K as the surface, whose structure is dominated by crystal faceting along TiNiSn(100) directions, is more ordered and contains large, flat regions which are individually significantly smoother than the surfaces of the other films. Below 670 K the faceted surface morphology no longer features and the specular reflection of the RHEED patterns starts to become more diffuse, indicating that the crystal structure at the surface is less ordered and subject to greater tendency for misorientation. In terms of film flatness – and the greatest prospect for creating coherent interfaces in any prospective multilayer deposition – ~720 K is nominated as the optimal deposition temperature. This is, interestingly, in agreement with a previous MBE study [290], which was not necessarily expected given the potentially large differences in adatom kinetic energies between these two techniques.

5.1.4 The role of the laser in tuning growth conditions

Typically, to achieve high-quality epitaxial growth in PLD, a laser pulse rate of order 1 Hz is used. This slow rate is intended to facilitate the characteristic relaxation time of island nucleation in the PLD-deposited material, which is typically up to 0.5 s [121]. Originally, a pulse repetition rate of 2 Hz was used in deposition of TiNiSn on MgO and, although epitaxial growth was possible under these conditions, the specular RHEED intensity always diminished significantly throughout the deposition, indicating a strong tendency toward highly three-dimensional growth.

As coarse films are preferably avoided, a different approach to laser operation was adopted, inspired by the Pulsed Laser Interval Deposition work of Koster *et al.* [306]. In this method, rather than employing a continuous and even pulse repetition rate, pulses are 'bunched' together at a much higher pulse rate, such that a unit-cell's worth of material is delivered rapidly, with a brief annealing interval between each burst of pulses. In the original investigation of the interval deposition approach, pulse rates of 10 Hz and 100 Hz were compared with uninterrupted deposition at 1 Hz. The intent of interval-based deposition is that one monolayer of material is delivered within the relaxation time of surface adatom diffusion, forcefully imposing a 2-d layer-by-layer growth mode [306, 307]. This requires a 100 Hz pulse rate (at least), which is beyond the specifications of the KrF laser available for the work in this thesis. The authors note, however, that even adopting the interval-based approach with the pulse rate increased by a factor of ten over the slow, uninterrupted deposition yields marked improvements in ability to preserve the specular RHEED intensity over time [307]. An interval-based approach to deposition has been adopted for TiNiSn here, using the highest available, reliable pulse repetition rate of 18 Hz.

A further side-effect of adopting the interval-PLD may in fact be a reduction of the quantity of contaminants accrued in the film during growth. Given that the typical base pressure of the deposition chamber reaches the low 10^{-8} Torr, 1 Langmuir (L) of gas exposure occurs approximately every 100 s [308]. Although the deposition rate of TiNiSn varies by several factors in PLD – pulse energy, transmission efficiency of the optics and laser window, target surface morphology etc. – it is typically on the order of 0.05 Å/pulse. Effectively, one unit cell thickness of TiNiSn is deposited by ~100 pulses. Therefore, at an uninterrupted rate of 2 Hz, each unit cell is deposited in ~50 seconds. Consequently, the film is exposed to 0.5 L for every unit cell of TiNiSn deposited. In the interval-PLD approach, one unit cell thickness

is deposited at ~20 Hz over a period of 5 seconds, with an annealing interval of 10 - 20 s. Thus, the gas exposure of the film is reduced to 0.15 - 0.25 *L* per unit cell deposited, which should improve the purity of the thin films.

5.2 Characterisation of nanostructured epitaxial TiNiSn thin films

Exploration of the PLD growth parameter-space for TiNiSn has highlighted a region where films are epitaxial with a surface morphology dictated by crystal facets producing large, flat islands. This occurs at substrate temperatures ranging from 670 K to 720 K, no ambient gas present and using a 'burst' laser pulse pattern. In this section, films deposited with a substrate temperature of 720 K are studied in detail. Going beyond the RHEED and AFM diagnostics used to optimise thin-film growth, XRD and TEM/STEM analyses are employed to explore in-depth the bulk and nanoscale characteristics of thin films.

To assess the bulk properties of a thin film deposited at 720 K, X-ray diffraction (XRD) measurements presented in Figure 5.6 show the $\theta - 2\theta$ diffraction pattern, which highlights Bragg reflection from atomic planes parallel to the surface. From the large-range pattern in Fig.5.6(a), the only peaks observed from the film are (00L) reflections, which is consistent with a single-crystal Heusler film whose out of plane orientation is (001), as expected from the epitaxial template in Fig.5.2. The most significant reflection is accounted for by the MgO substrate, while minor contributions to the pattern close to the MgO(002) peak arise from the polycrystalline platinum capping layer which was deposited after fabrication of the hH thin film. The (002) and (004) Heusler reflections which have been observed are noticeably broad, asymmetric and peaked at angles which lie between the expected positions for the bulk lattice constants for the full and half-Heusler. Examining the TiNiSn(004) reflection more closely in Fig.5.6(b), the position of the apex of the peak at an angle of 62.03° would suggest – assuming variation in only the nickel content – a mean composition of $TiNi_{1.3}Sn$. There is, of course, an uncertainty associated with using Vegard's law to approximate the composition based on relaxed bulk values of the lattice constants, arising both from the possibility of a strained epitaxial thin film, and further from a potential non-linear variation in lattice constant between the full and half-Heusler phases owing to a transition from metallic to semiconducting electronic behaviour [99].

The asymmetrical broadening of the TiNiSn(004) reflection observed in the XRD pattern

in Fig.5.6(b) tapers off in the direction of the bulk fH reflection and is attributed to incoherent summation of diffraction intensity from regions with differing lattice constants. The changes in lattice constant which contribute to this effect are due to variations in the nickel concentration of the Heusler film, which have been found in STEM and are discussed later. To model the asymmetric peak, a minimum of three pseudo-Voigt functions were required to provide a reasonable fit to the data. For contrast, the data which were discussed in the MBE study described observed XRD reflections using a pair of Gaussian profiles [291]. The results of fitting pseudo-Voigt profiles are also shown with the data in Fig.5.6(b). The need for three peak profiles, though not a unique solution for the fit, suggests the presence of at least three

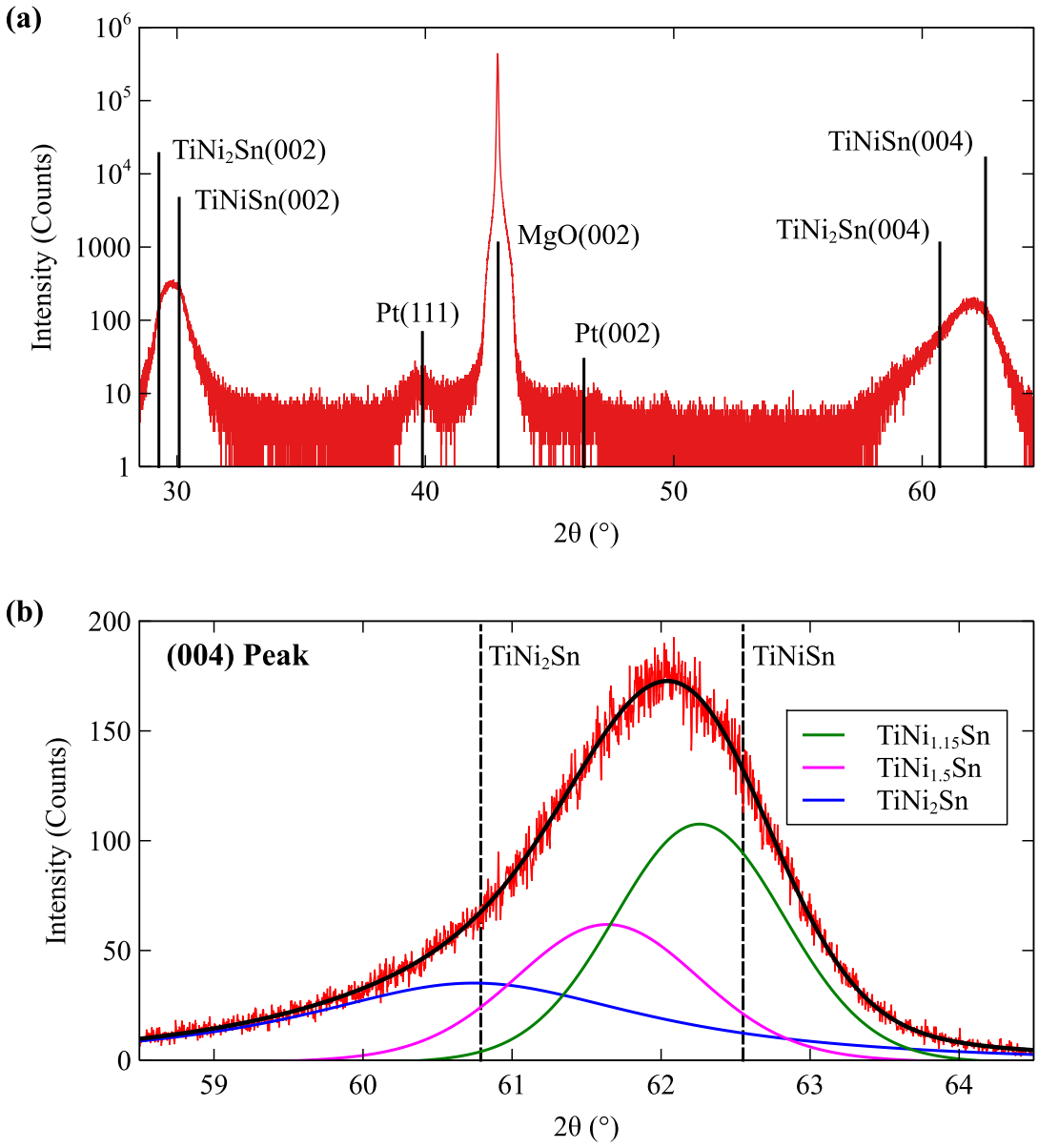

Figure 5.6: (a) XRD θ – 2θ scan of ~100 nm TiNiSn/MgO deposited by PLD at 720 K. Reflection angles based on the bulk lattice constants for TiNiSn, $TiNi_2Sn$, Pt and MgO are labelled. (b) The TiNiSn(004) reflection with bulk full and half-Heusler angles marked by dashed lines. A fit to the data and three pseudo-Voigt profile components are also shown.

Ni-rich Heusler phases in the thin film. The compositions which are inferred from the fit are approximately $TiNi_{1.15}Sn$, $TiNi_{1.5}Sn$ and $TiNi_2Sn$. For each of these compositions, the relative breadth of the pseudo-Voigt peak is used to assess the quantity and geometric extent of the phase. The sharpest of the three peaks, which corresponds to $TiNi_{1.15}Sn$, is understood to be the majority phase of the film on this basis. Conversely, regions containing the largest nickel concentrations are expected to be the smallest in size. The Scherrer relation, which connects the mean size of crystalline nanoparticles to the diffraction peak width [309], gives mean crystal domain sizes of 31 nm, 14 nm and 4 nm for the phases from lowest to highest Ni concentration.

To compare the compositions of the PLD target and the resulting thin films, SEM-EDS was used for chemical analysis of the target material. The Bruker *Esprit* proprietary software was used for elemental quantification, first involving a background fit and a Bayesian deconvolution to extract the net peak intensities before applying a standard-less approach which relies on calculating the peak-to-background (P/B) ratio and using theoretical models to account for material-specific atomic number, self-absorption and fluorescence effects (the *ZAF* factors) [310]. Due to the lack of availability of suitable standards and the use of a standard-less approach, the results of SEM-EDS quantification do not approach the precision of the STEM-EELS analyses using methods outlined in Chapter 4. Using this process, chemical analysis of the PLD target material yielded a net composition of $TiNi_{1.3}Sn_{1.4}$. Compared to the net composition of the film determined by STEM-EELS as $TiNi_{1.17}Sn_{0.92}$, the film does not reflect the composition of the target and highlights issues with stoichiometry transfer during PLD fabrication here. The largest discrepancy here is the difference in Sn concentration, which highlights the large difference in vapour pressure of the constituent elements as a likely source of the differences between target and film [305].

5.2.1 Interfacial reaction at the MgO substrate

When used during growth, the RHEED system provides a diagnostic tool which can give indications of how the crystal structure varies throughout the film thickness. This type of *in situ* analysis allows us to develop a better understanding of the evolution of the thin-film crystal structure and RHEED patterns recorded at various points during the deposition of epitaxial TiNiSn at 720 K are shown in Figure 5.7.

Starting with a bare MgO substrate in Fig.5.7(a), the RHEED pattern contains vertical

streaks, which are typical of a very smooth surface with atom-high terraces [138], consistent with AFM images of the substrates like that in Figure 5.3. Kikuchi bands are also present in the RHEED pattern, which have been used to identify correct alignment of the glancing electron beam along the (01) direction. When deposition of TiNiSn commences, significant surface roughening is observed during the initial stages of growth. This is shown in Fig.5.7(b) which corresponds to 2 monolayers (ML) of growth; at which point the pattern now consists of discrete diffraction spots and a greater degree of diffuse scattering. The spot-like nature of the diffraction pattern – which persists throughout the entire remainder of thin-film growth – arises from transmission of the electron beam through rough surface features, as opposed to reflection from a smooth surface. As well as the transition from a streaked to spotted pattern after 2 ML deposition, new spots are observed at one-third of the MgO(01) lattice rod spacing. A change in the fundamental periodicity of the diffraction pattern is indicative of a surface reconstruction; which in this case results in a surface superstructure with a periodicity three times that of the substrate. This type of pattern was observed in the initial monolayers of growth for all films deposited at or above 630 K. These superstructure spots, which are discussed in the context of TEM observations later, represent a transient surface reconstruction that is only apparent at this initial stage of the growth, and disappears shortly thereafter. The spotty nature of the pattern remains, indicating that island growth persists throughout much of the subsequent deposition, however the diffuse background is observed to diminish

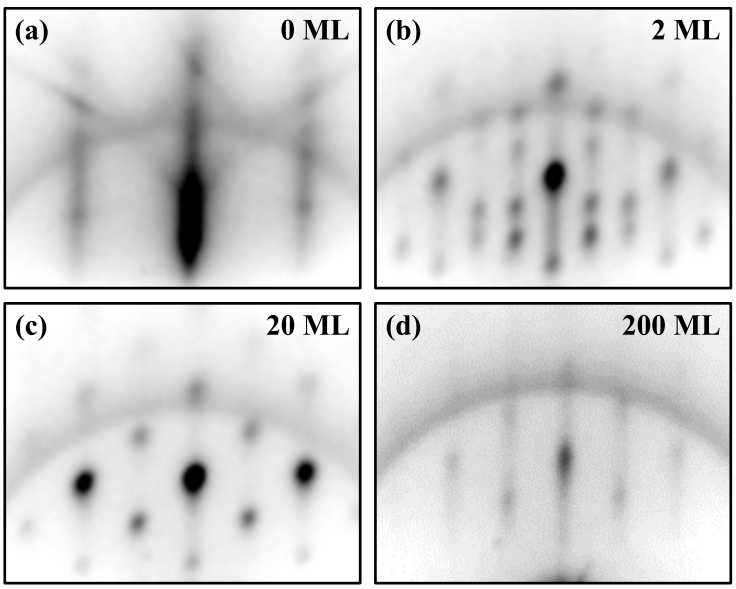

Figure 5.7: RHEED diffraction patterns recorded in situ during the growth of a TiNiSn thin film on MgO(001) at 720 K. The patterns shown correspond to (a) the bare MgO substrate, and then approximate coverages of (b) 2 ML, (c) 20 ML and (d) 200 ML of TiNiSn. The RHEED electron beam was at a grazing incidence to the (100) lattice vector of the substrate.

as shown in Fig.5.7(c) at a coverage of 20 ML. The reduction in diffuse scattering is tied to an improvement in the crystal quality at the surface, as more intensity in the pattern gets channelled into Bragg scattering from the surface. The pattern in Fig.5.7(d) then reflects the film surface after 200 ML of deposition. Here, the streaky nature of a pattern from a smooth, two-dimensional surface is partially recovered. This suggests a tendency toward island coalescence as the film becomes thicker, and is consistent with the broad, faceted, flat islands imaged by AFM in Fig.5.5(b).

Turning to TEM characterisation, a low magnification overview of a cross-section of a typical 720 K thin film, ~80 nm thick, is presented in Fig.5.8(a). The film is continuous, fully dense and lacks any obvious granularity. The large, flat islands which were observed in AFM (Fig.5.5(b)) are identified here as the trapezoidal features at the top of the film. Within the film there are subtle intensity variations running vertically which could be attributed to either compositional variations or slight differences in diffraction scattering. Both of these origins could arise from the merging of islands which grew from independent nucleation sites in the first few monolayers. Triangular-like features found at the interface with the substrate – circled in Fig.5.8(a) – are found to be nickel stannide phases that form as part of the decomposition of the hH structure and this will be discussed further later.

Convergent beam electron diffraction (CBED) patterns collected from three distinct regions are presented in Fig.5.8(b-d), using a focused beam with a diameter of 1 nm to acquire local diffraction information. In Fig.5.8(b), the diffraction pattern from the MgO substrate shows the square symmetry expected from alignment along the (100) axis. The in-plane lattice vectors of the MgO are coincident with those of the TiNiSn thin film, which is shown in Fig.5.8(d). The matching in-plane reflections provide further confirmation of successful epitaxial growth. The diffraction spots collected from the film, at a point about 10 nm from the substrate interface, can be indexed to the expected $F\bar{4}3m$ space group. At the interface, the pattern shown in Fig.5.8(c) is dominated by a superposition of the patterns arising from the substrate and film, however weak distinct spots (red arrows) are consistent with an out-of-plane expansion of the MgO lattice. This, together with a more subtle contraction of the in-plane lattice spacing, yields in- and out-of-plane lattice dimensions of 4.17 Å and 4.26 Å, respectively, representing strains of -0.96 % and 1.2 % relative to the unstrained MgO lattice constant. This elongation of the MgO unit cell at the interface does not appear to affect the overall unit cell volume, however the in-plane reduction in lattice constant here is surprising, as epitaxial strain is generally accommodated in the growing film, rather than the substrate.

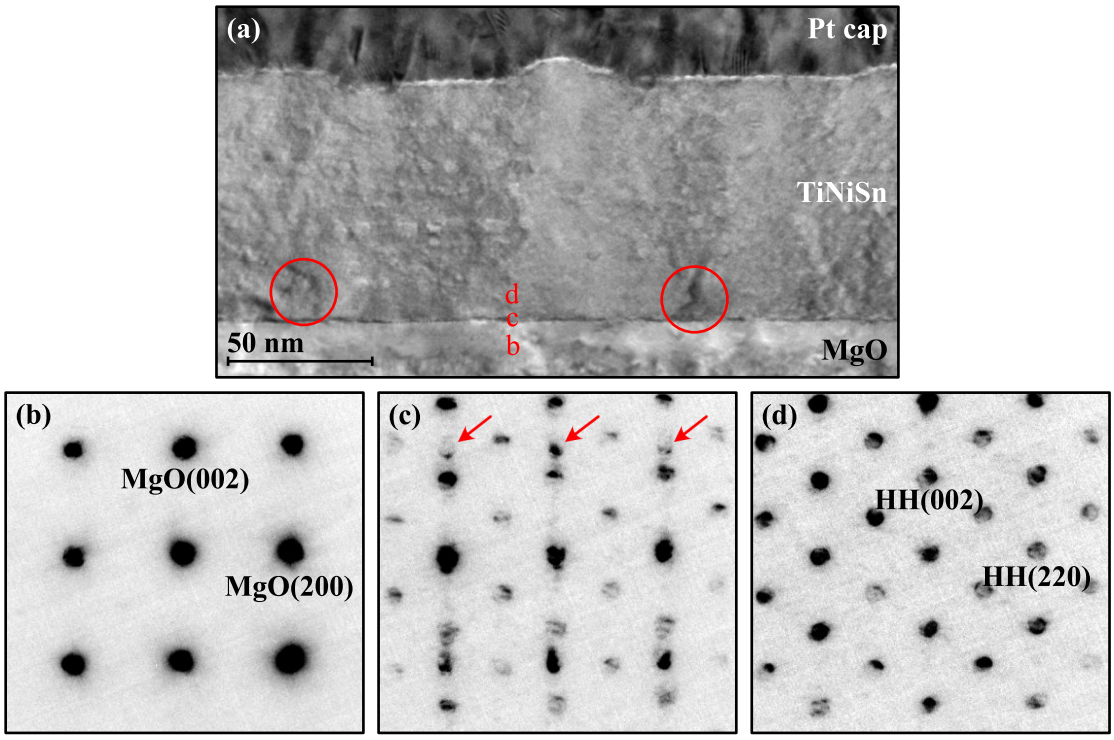

Figure 5.8: (a) TEM image of cross-section of a TiNiSn film deposited on MgO(001) at 720 K with features identified as nickel stannides encircled in red. (b)-(d) Nanoprobe convergent beam electron diffraction (CBED) patterns collected along a MgO (010) direction from positions marked in the TEM image. CBED patterns correspond to (b) the MgO substrate, (d) the TiNiSn film, and (c) the interface between the film and the substrate. The scaling is the same for all patterns. Red arrows in (c) point to some of the weak spots related to the expansion of the MgO lattice.

The observed contraction is also greater than required to compensate for the nominal lattice mismatch between MgO and the hH. The bulk lattice mismatch between TiNiSn and MgO is expected to be -0.32 %, but in light of the observed interface lattice this mismatch switches from being tensile to realise a compressive mismatch of 0.64 %. In the context of EELS measurements discussed below, this is understood to originate from chemical variations at the interface.

A key observation to be made from Fig.5.8(c) is the lack of evidence for significant structural reorganisation at the interface. If the surface reconstruction observed by *in situ* RHEED in Fig.5.7(b) were permanent, the additional spots at a third of the lattice period should once again be observed in the CBED pattern. The absence of a superstructure in the TEM diffraction pattern indicates that modulation of the lattice observed in RHEED reflected a transient reconstruction of the surface which reorganised to preserve the cubic structure upon further deposition. This lattice coherence is more evident in STEM imaging, where the atomic structure can be observed directly. Figure 5.9 shows a STEM-HAADF (High-Angle Annular Dark

Field) image of the cross-section of the MgO/hH interface, resolving the atomic columns directly. This image shows a distinctive layer at the interface – which is centred on the red dashed line in Fig.5.9(a) – following the same atomic structure as the MgO, but with a higher contrast level indicating the presence of an element with a higher atomic number. Further, Fourier-filtering by the in-plane component of the lattice shown in Fig.5.9(b) produces a Fourier-filtered version of the HAADF image which is presented in Fig.5.9(c). This filtered image highlights the in-plane lattice spacing across the interface and indicates the continuity of the epitaxial lattice, with only four lattice dislocations in the field of view.

Spatially-resolved chemical mapping was also carried out in the same region as Figure 5.9 by STEM-EELS spectrum imaging across the MgO/hH interface. Absolute elemental quantification was carried out using the protocols described in Chapter 4 and the results are presented in a line profile running across the interface in Fig.5.9(d), which is aligned to match the vertical position and scaling of the HAADF image in Fig.5.9(a). Here, relative concentrations of the main elements are shown and reveal the impact of substantial chemical reactions, resulting in the presence of an chemically distinct interfacial nanolayer. Examining the lower-half of the line profile, the MgO substrate composition is confirmed, but a small quantity of Ti is observed to extend into the substrate up to 6 nm from the interface. The Mg concentration drops to zero over a distance of 2 nm, which is substantially wider than anticipated from the extremely flat MgO substrates characterised by AFM prior to deposition. This is taken as evidence of substantial reorganisation and elemental diffusion at the interface during the

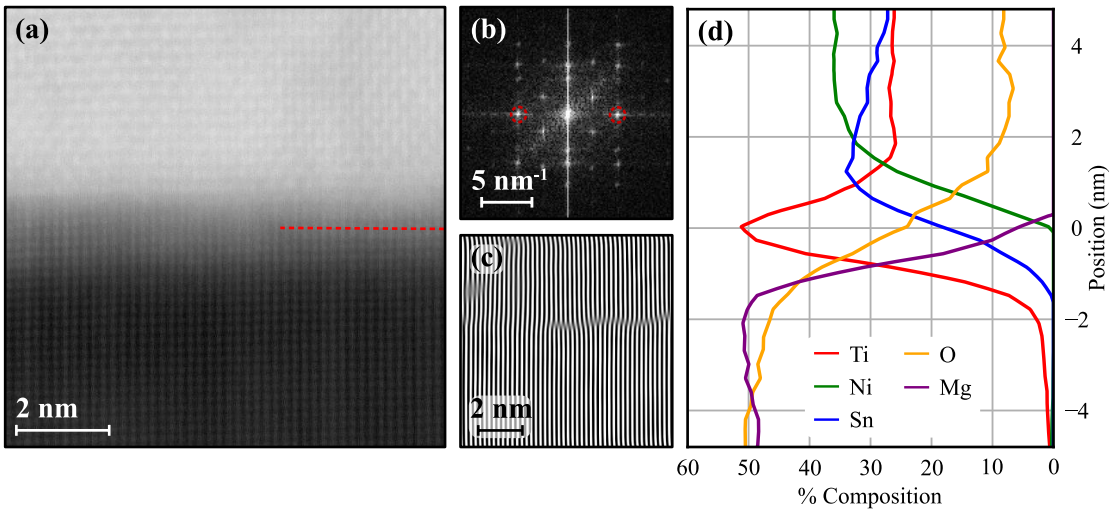

Figure 5.9: (a) STEM-HAADF image of MgO/TiNiSn interface. The MgO substrate occupies the bottom half of the image. (b) Fourier transform and (c) Fourier-filtered image of (a) (using spots circled in the fast Fourier transform) demonstrating crystalline and epitaxial ordering. (d) Result of elemental quantification across the interface aligned with the image in (a).

initial stages of deposition. The nanolayer at the interface itself seems to be primarily composed of titanium oxide having presumably drawn oxygen out of the substrate, explaining the more gradual termination of the oxygen concentration compared to Mg. The Ti enrichment at the interface results in a complementary enhancement of the Ni and Sn concentrations in the Heusler film immediately above the interface. The Sn concentration only drops to equal the Ti content of the hH about 5 nm beyond the interface. The enhancement in Ni in this region results in a local mean composition of $TiNi_{1.38}Sn$, which persists beyond the range of the line profile shown in Fig.5.9(d), up to 10 nm from the interface.

The formation of a Ti-rich interfacial layer implies that the nature of the substrates' epitaxial template differs from that which was expected from clean MgO. Evidence indicates that the layer adopts a very similar lattice spacing to that of MgO and the Fourier-filtered HAADF image presented in Fig.5.9(c) does not show any disruption to the epitaxial relationship. The MgO subsurface region is also clearly chemically modified by Ti implantation up to 6 nm beneath the centre of the nanolayer. This is clearly observed not only from elemental analysis of EELS data, but also in the contrast modification of the STEM-HAADF image, which shows a clear band of intermediate intensity below the interface, instead of an abrupt step between the relatively heavy TiNiSn and the elementally light MgO. Implantation may arise from the impact of energetic species present during PLD, but this should then also apply to Ni and Sn, which are not observed to penetrate the substrate. Instead, the Ti implantation is attributed to diffusion; previous observations showed facile diffusion of Ti into MgO by cation substitution [79]. This substitution mechanism was reportedly observed under a range of conditions, including at room temperature; suggesting that this interaction is unavoidable without taking further preventative measures. The preventative approach adopted in this work is discussed later in Section 5.3.

In Figure 5.10, variations in the Ti $L_{2,3}$ EELS edge across the nanolayer show a continuous change in near-edge structure (ELNES). The main changes in ELNES effectively amount to a chemical shift which encodes a change in the titanium oxidation state. The fine structure of the $L_{2,3}$ edge in the half-Heusler is very similar to that of elemental Ti, consistent with the covalent, uncharged nature of Ti within the hH alloy. Moving into the interface layer, the peak maxima undergo a small shift to higher energy-losses as the proportion of oxide increases. In the interface nanolayer and the substrate below, the Ti L_3 peak settles at 457.4 eV, in excellent agreement with expectations for Ti^{2+} arising from a cubic TiO phase [311]. This is a slightly more unusual titanium oxide phase, as TiO_2 is by far more common, however the evidence

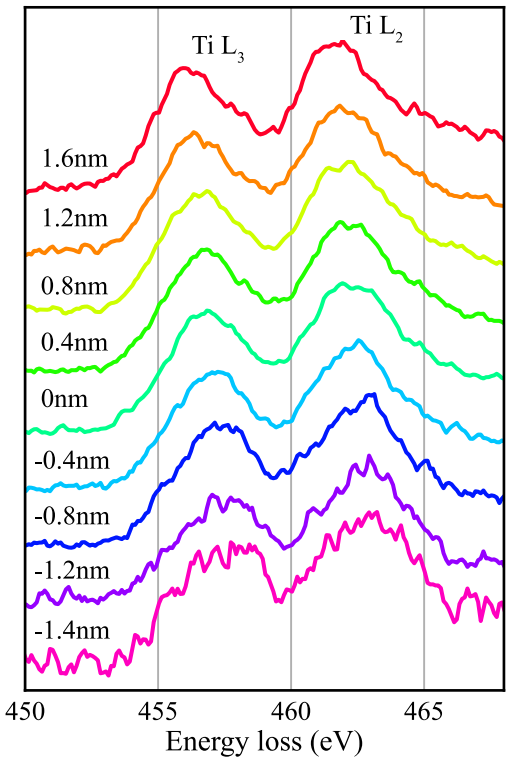

Figure 5.10: Ti $L_{2,3}$ near-edge spectra acquired from different positions scanning across the MgO/TiNiSn interface. Spectral intensities are normalised to the L_2 maximum. The centre of the Ti-rich interface layer is marked as 0 nm so that positive positions denote further into the Heusler film and negative toward the substrate.

here is incompatible with either the anatase or rutile phases, for which additional sub-peaks would be observed due to crystal field splitting effects [311]. The ELNES observed for all positions below the hH film are similar, although with worsening signal-noise ratios due to the diminishing Ti content further into the substrate. Comparison with composition analysis indicates that the concentration of oxygen throughout the interface layer is either similar or lower than the Ti concentration. The oxygen deficiency relative to a TiO composition highlights difficulties in making accurate assessments of chemical compositions at interfaces and the chemical shifts observed in Figure 5.10 provide a more accurate assessment of oxidation state (see Chapter 4). The exact nature of the interface is an outstanding problem, with many different phases and superstructures comprising Ti, Mg and O which could achieve an epitaxial match, as discussed later in Section 5.2.3.

5.2.2 Nanoscale phase-segregation and binary alloying

In STEM, contrast from nanoscale defects in the thin films was found to be much more pronounced than in conventional TEM. Examining the full thickness of a film, STEM-HAADF

imaging shown in Fig.5.11(a) confirms that films are continuous and do not exhibit polycrystalline characteristics. The STEM image does, however, reveal a network of nanoscale imperfections which were unexpected and appear as dark spots throughout the film. As HAADF imaging contrast arises from atomic numbers, the dark spots indicate the inclusions are atomically lighter than the hH matrix. A STEM-EELS spectrum image was recorded across the region bounded by the red box in Fig.5.11(a) and the elemental analysis carried out on the spectra is represented in Fig.5.11(b). The majority of the film has a broadly uniform composition but distinct, Ni-rich (green) stripes are found below the dark regions which were observed in STEM-HAADF. The composition of the majority phase, determined by EELS elemental quantification, is $TiNi_{1.12}Sn$; i.e. a half-Heusler with excess nickel. Regions of the film corresponding to this majority phase appear as a dull green in the false-colour representation of elemental quantification in Fig.5.11(b).

The dark regions which were observed in STEM-HAADF imaging in Fig.5.11(a) appear red in the false colour map in Fig.5.11(b) indicating that they are Ti-rich. A more detailed look at the results of absolute chemical quantification of EEL spectra is shown in Fig.5.11(c), which contains the results from a line-profile through the spectrum image denoted by the white arrow in Fig.5.11(b). The line profile here shows an equal increase in the concentrations of titanium and oxygen across the inclusion around the 11 nm point in the plot and suggests that the Ti-rich phase is the titanium oxide TiO. Assuming that the inclusion has an isotropic form (has the same extent in depth along the electron beam as the dimensions

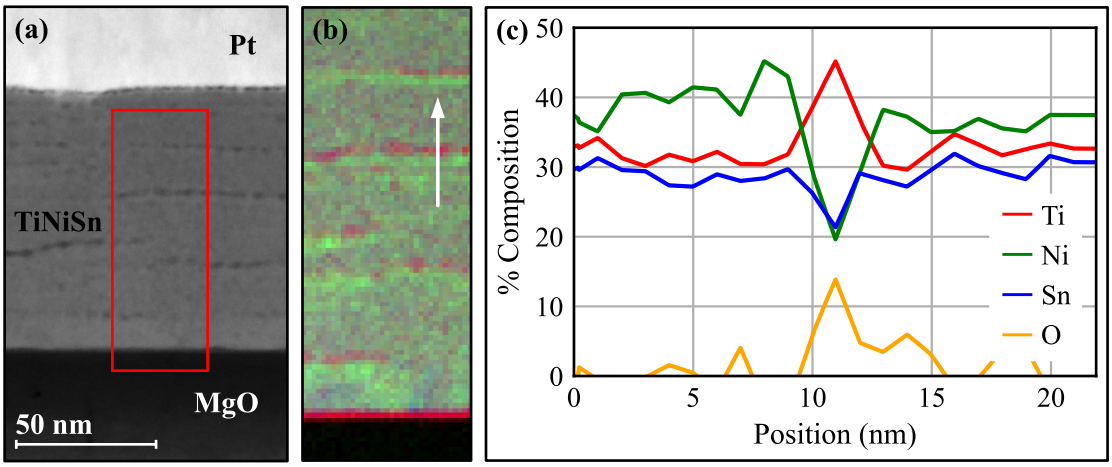

Figure 5.11: (a) A STEM-HAADF cross-sectional image of a ~100 nm thick film grown at 720 K. A protective Pt capping layer was deposited immediately after growth. (b) RGB colour map determined from a spectrum image collected within the area marked by the red rectangle in (a), showing the distribution of Ti (red), Ni (green) and Sn (blue). (c) Plot of a single line profile through the quantification results marked by the white arrow in (b).

observed in the image plane), the inclusions are approximated as roughly spherical volumes which likely decorated the surface of the film intermittently during deposition, explaining the clustering of inclusions into rows. If the hH matrix composition is subtracted from the absolute quantification, results indicate that the TiO inclusion inspected in Fig.5.11(c) contains approximately 1270 Ti atoms, corresponding to a volume of 23 nm^3 and a diameter of 3.5 nm. Extending this analysis to the full spectrum image indicates that ~2.5 % of the volume of the film is occupied by TiO.

The presence of TiO rather than TiO_2 is interesting as it has a structure that can be coherent with the surrounding hH matrix and support continued epitaxy, as with the interfacial TiO layer. The TiO phase, which is usually unstable and oxidises further to become TiO_2 [311], is perhaps stabilised within the film by lattice strain. A high magnification STEM-HAADF image which resolves atomic positions is presented in Fig.5.12(a). The brightest, most obvious atomic columns resolved in the image are Sn atoms, which is the heaviest element present. The Fourier filtered version of this image, presented in Fig.5.12(c) – selecting the spots highlighted in Fig.5.12(b) – demonstrates clearly the continuity of the hH lattice around the oxide inclusion. As the nano-inclusions are small enough to be embedded within the TEM cross-section (which here was about 32 nm thick) the energy-loss spectra unique to the inclusions are only ever present as a spectral mixture also containing significant contributions from the hH matrix. Machine learning methods can be used to 'unmix' the spectra and in this instance the spectral features arising from the oxide nano-inclusion were isolated from the hH matrix contributions using non-negative matrix factorisation (NMF) [312] as implemented in *HyperSpy* [244]. The spectra represented by the first two significant components found by NMF are presented in Fig.5.12(d) and not only show the different edges present in TiNiSn versus TiO, but also a clear chemical shift of the Ti *L* edge between the two phases. The energy of the Ti L_3 peak at 457.4 eV and the apparent absence of crystal-field splitting of the L_2 and L_3 white lines further support the results of elemental analysis with the inclusion assigned a Ti^{2+} oxidation state consistent with the cubic TiO phase [311].

Titanium segregation to form oxide inclusions has the added effect of perturbing the composition of the surrounding alloy. The false-coloured spectrum image in Figure 5.11 consistently shows complementary green (i.e. nickel-rich) stripes immediately beneath each red (TiO) region. If during deposition the atomic flux arriving at the substrate is both stoichiometric and uniform throughout, then it is likely that phase segregation into Ni-rich and TiO nano-inclusions occurs immediately following arrival of the atomic flux at the surface. One can

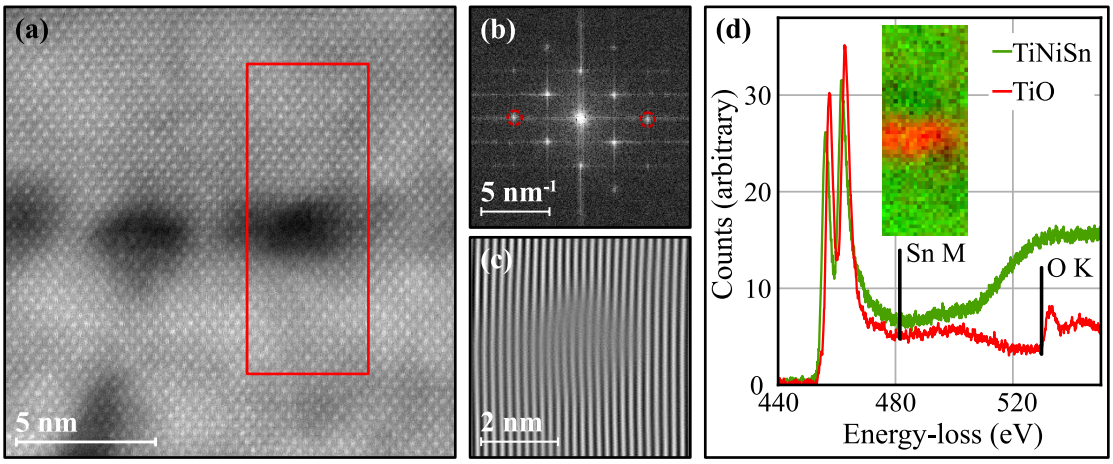

Figure 5.12: (a) Atomic-column resolved HAADF image of TiO nanoinclusions in the TiNiSn film. STEM-EELS spectrum imaging was conducted within the red outline. (b) Fourier transform of (a) and (c) a Fourier-filtered image of the nanoinclusion showing the in-plane lattice spacing, demonstrating the continued epitaxy across the inclusion. (d) Results of the NMF procedure, showing the two most significant NMF factors contributing to the data in the refion of Ti, Sn and O EELS edges. The coloured inlay shows a false colour distribution of these two components across the spectrum image, clearly identifying the inclusion as TiO.

speculate that trace amounts of oxygen which arrive at the growing film are adsorbed and draw Ti out of the underlying hH to decorate the growing surface with TiO nano-particles, which are subsequently buried as deposition continues. The concentration of Sn seems to be relatively unaffected by this process, as no modification of the Sn content is observed in the Ni-rich regions. Determination of an accurate chemical composition for the Ni-rich inclusions is challenging, as these are presumed to have a similar geometrical confinement as the TiO nano-inclusions and will be embedded in the TEM cross-section, surrounded by the hH matrix phase. In this situtation, NMF failed to produce spectral components which allowed clear identification of the Ni-rich phase. The NMF decomposition may have proven unreliable in this instance because the Ni-rich phase and the hH matrix phase differ only subtly by their Ni content. However, if the same geometric approximation as was applied to the TiO inclusions are used here, the composition yielded for the Ni-rich inclusions is approximately $TiNi_{1.85}Sn$; i.e. a near-full-Heusler phase. If accurate, the Ni-rich nano-inclusions would account for the minority full-Heusler fraction seen in XRD in Figure 5.6.

In some regions, the amount of titanium extracted from the surrounding half-Heusler matrix cannot be supported, leading to the demise of the half-Heusler crystal structure in a localised area. Under such circumstances, the result is the formation of a binary alloy phase from the excess nickel and tin; a nickel stannide. Although this is observed to happen throughout the thin films, it is most common at the substrate interface where, as already shown, titanium

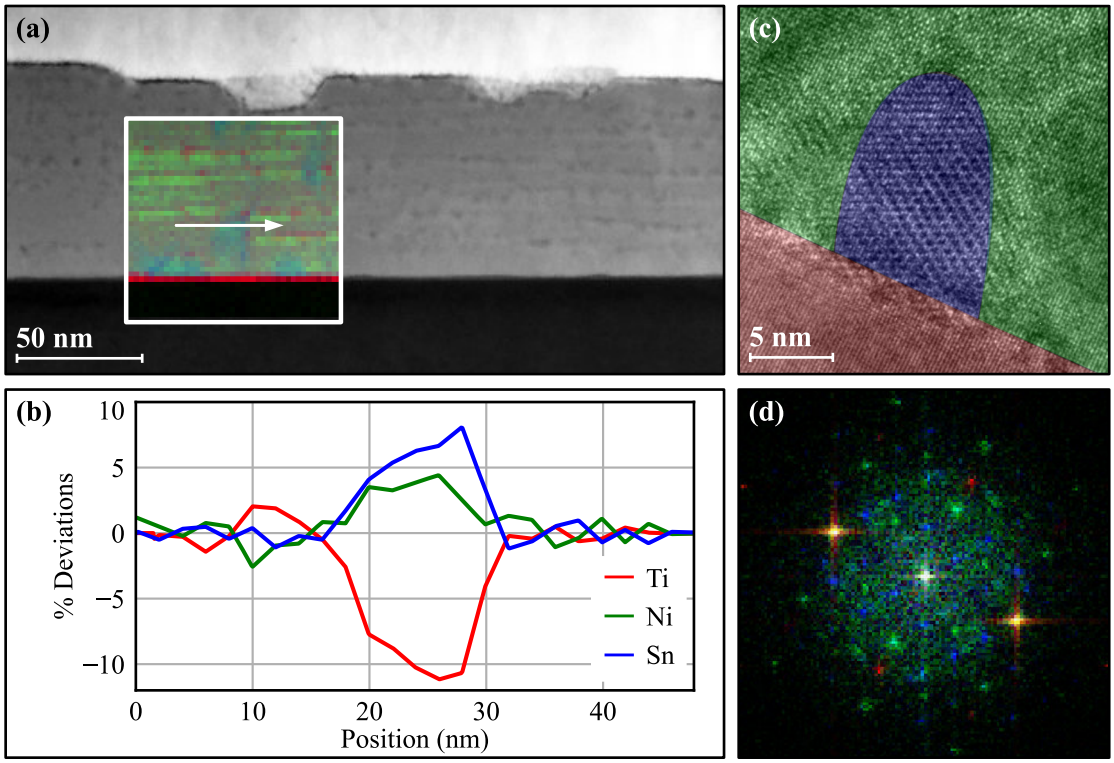

Figure 5.13: (a) STEM-HAADF overview of TiNiSn film containing nickel-stannide phases. The false-colour inlay shows the Ti, Ni and Sn distributions, using the same colours as (b). (b) Deviations from the $TiNi_{1.15}Sn$ matrix composition across the line profile marked by the white arrow in (a), which crosses a nanoscale grain of Ni_3Sn_4. (c) HRTEM image of a similar Ni_3Sn_4 grain at the substrate interface (note the TEM camera orientation makes the sample appear rotated w.r.t. the HAADF image). (d) Simulated diffraction pattern composed of Fourier transforms of regions in (c) with colours matching the associated areas. The nickel stannide phase FFT (blue) indicates a larger lattice parameter than the hH phase and matches Ni_3Sn_4.

extrusion is significant. Regions like these are explored in Figure 5.13. In this specimen, elemental quantification of an EELS spectrum image – inset in colour in Fig.5.13(a) – yielded a majority phase composition of $TiNi_{1.15}Sn$. This is similar to the $TiNi_{1.12}Sn$ majority phase found in the spectrum image analysed in Fig.5.11(a). These subtle differences in the level of excess Ni are potentially commensurate with the vertical striping in contrast seen in Fig.5.8(a). Variations in the composition of the majority phase like this are reminiscent of the grain-by-grain variations observed in a study of Cu-doped TiNiSn [104] and would indicate lateral diffusion of Ni, if the elemental flux during deposition is uniform. It is worth noting, however, that the minor difference between $Ni_{1.12}$ and $Ni_{1.15}$ is comparable to the detectability threshold for Ni in EELS found in Chapter 4.

Once again, nanoscale, Ni-rich inclusions present in the false-colour representation of the spectrum image appear as bright green stripes, paired with the presence of titanium oxides in red. In the spectrum image in Figure 5.13 however, additional nickel and tin-rich phases

can be found in the SI region in blue. A line profile through one of these nickel-stannide regions is shown in Fig.5.13(b) and very clearly indicates a composition rich in Ni and Sn. The combined increase in Ni and Sn content across the inclusion matches in magnitude the corresponding decrease in Ti, indicating that the inclusion contains only Ni and Sn, but is embedded within the TEM cross-section, so is still surrounded by Heusler matrix along the electron beam direction.

The structure of the Ni-Sn alloy was determined through analysis of the high-resolution TEM image shown in Fig.5.13(c). Here the inclusion region, coloured in blue, has a different atomic lattice pattern to both the surrounding Heusler matrix and the MgO susbtrate. Fourier transforms for each coloured region in Fig.5.13(c) are presented as a pseudo-diffraction pattern in Fig.5.13(d) and includes components corresponding to the substrate (red), Heusler matrix (green) and binary inclusion (blue). The three Fourier transforms show a geometric alignment of peaks corresponding to the in-plane lattice, indicating an epitaxial relationship between all three components. The Fourier component corresponding to the Ni-Sn alloy can be indexed using the structure of Ni_3Sn_4 [313, 314] observed along the [110] zone axis. The conclusion that the observed phase is consistent with Ni_3Sn_4 is also consistent with the chemical analysis in Fig.5.13(b), where the increase in Sn concentration is about one-third greater than the increase in Ni concentration. Ni_3Sn_4 is one of two nickel stannide phases predicted recently by *ab initio* thermodynamical calculations, the other being Ni_3Sn_2 [315]. No evidence was found for the Ni_3Sn_2 phase in these thin films.

5.2.3 Further discussion

Pulsed laser deposition of off-stoichiometric TiNiSn on MgO(001) between substrate temperatures of 670 K and 720 K produces thin-films which are smooth and epitaxial, possessing limited three-dimensional character that becomes less significant with increasing film thickness. Initial stages of growth occur with nucleation of three-dimensional islands, arising as a consequence of an interfacial reaction which substantially roughens the subtrate surface, limiting adatom mobility. The formation of a titanium-rich interface layer does not appear to impede the epitaxial growth of the hH film, but the introduction of a buffer layer to prevent this reaction may improve growth and will be discussed in the next section. Growth beyond the interface leads to three main Heusler phases, with compositions of $TiNi_{1.12}Sn$, $TiNi_{1.38}Sn$ and $TiNi_{1.8}Sn$ for the matrix, the Ni-enriched layer above the interface and the Ni-rich nanoin-

clusions, respectively. These phases occupy volume fractions of 78.4 %, 8.1 % and 11 %, respectively. This is in addition to the TiO nanoinclusion phase, which occupies a 2.5 % volume fraction which is attributed to the titania content of the PLD target, which shows a similar fraction of titanium oxide. The compositions determined by EELS do not exactly match those found by XRD but the fit which produced the XRD results is not unique and is therefore only broadly indicative. The uncertainty of the XRD analysis is further compounded by limitations to the application of Vegards law in this instance, as has been discussed elsewhere [99]. This is discussed further in Chapter 7, where STEM structural analysis is explored further in conjunction with STEM-EELS to correlate composition and lattice size.

The formation of TiO, which has a similar cubic structure to MgO and a very similar lattice constant ($a_0 = 4.176$ Å) [316] explains the continuation of the epitaxial relationship throughout growth. The more common titanium oxide phases, anatase and rutile, would be structurally incommensurate with both MgO and TiNiSn and expected to disrupt epitaxy. Where the interfacial layer is concerned, thin films of TiO on MgO have not previously been studied in detail, although the surface termination of bulk titanium oxides is known to reconstruct to form any number of superstructure phases, several of which would have the potential to lattice-match to the MgO substrate here [317, 318]. Incorporation of Ti into the MgO substrate increases the number of possible phases further. A spinel phase of Mg-Ti-O has previously been identified, which would have a coincident lattice match with a lattice parameter approximately twice that of MgO [319]. It is feasible that the transient reconstructed surface observed in RHEED was a metastable Mg-Ti-O spinel phase. Substitution of titanium in the MgO lattice also helps to explain the measured changes in lattice parameter at the interface, if interpreted as an intermediate MgO:TiO composition driving the in-plane lattice constant toward the smaller TiO value.

In comparing bulk film analysis to the TEM/STEM nanoscale analysis of the hH thin films, it is worth nothing that neither the TiO nor Ni_3Sn_4 nanoscale phases were observed by XRD and that these features could be easily overlooked without the nanoscale spatial resolution of the electron microscope. Thermoelectric measurements have not been carried out on the thin films, however the presence of the titanium oxides is not expected to impair the funtional performance of the Heusler alloy, as suggested in examination of experimental measurements [84] and theoretical calculations [315].

5.3 Preventing interfacial reactions with metallic contact layers

As is evident from the discussion in Section 5.2, it is not difficult to compromise the integrity of the half-Heusler alloy. The incorporation of nano-inclusions in the thin films is understood to arise from impurities and imperfections in the PLD target material, which suffers similar issues of phase separation in bulk synthesis of TiNiSn [67, 86]. Little can be done about this without modifying the synthesis of the bulk materials. The interfacial reaction with the substrate is, however, a factor which can be controlled in the deposition system. Instead of depositing the half-Heusler layer directly onto the oxide substrate, deposition of an intervening layer can be used to change the chemistry of the surface onto which the TiNiSn is grown. The objective of doing so is to prevent the interfacial reaction which has been observed between the deposited Heusler alloy and the MgO substrate to form a Ti-rich wetting layer. Preventing this reaction will make more titanium available for the deposited film, simultaneously improving the homogeneity of the thin film composition and preventing diffusion of Ti into the substrate.

5.3.1 Buffer layers and maintenance of epitaxial registration

To choose an appropriate material for a buffer layer, the key consideration is the anticipated lattice constant of the unit cell as this will dictate the likelihood of achieving an epitaxial relationship. Ideally, the buffer layer should also be uncomplicated to fabricate and thus should be chemically simple. A survey of literature on thin film growth – focusing on the available methods of pulsed laser deposition and d.c. magnetron sputter deposition – highlighted a few possibilities. Ultimately, three candidate buffer layer materials were considered: MgO, Pt and V. Although there is precedent for using MgO as a buffer for TiNiSn in MBE [290, 291] and PLD growth of MgO is achievable [320], our own attempts highlighted issues with deposition of exfoliational particulates and it was unlikely that the interfacial reaction with the MgO substrate would be any different for a buffer layer of the same material. Pt was also considered, as PLD of Pt on MgO has previously been demonstrated [321]. The use of a metallic buffer layer should avoid interfacial reactions between titanium and oxides and also potentially serve as an electrical contact. Though epitaxial growth of Pt on MgO is possible, large strains are involved, with a significant lattice mismatch of ~7% with MgO. The mismatch with TiNiSn is therefore also relatively large and therefore Pt is best avoided. Instead,

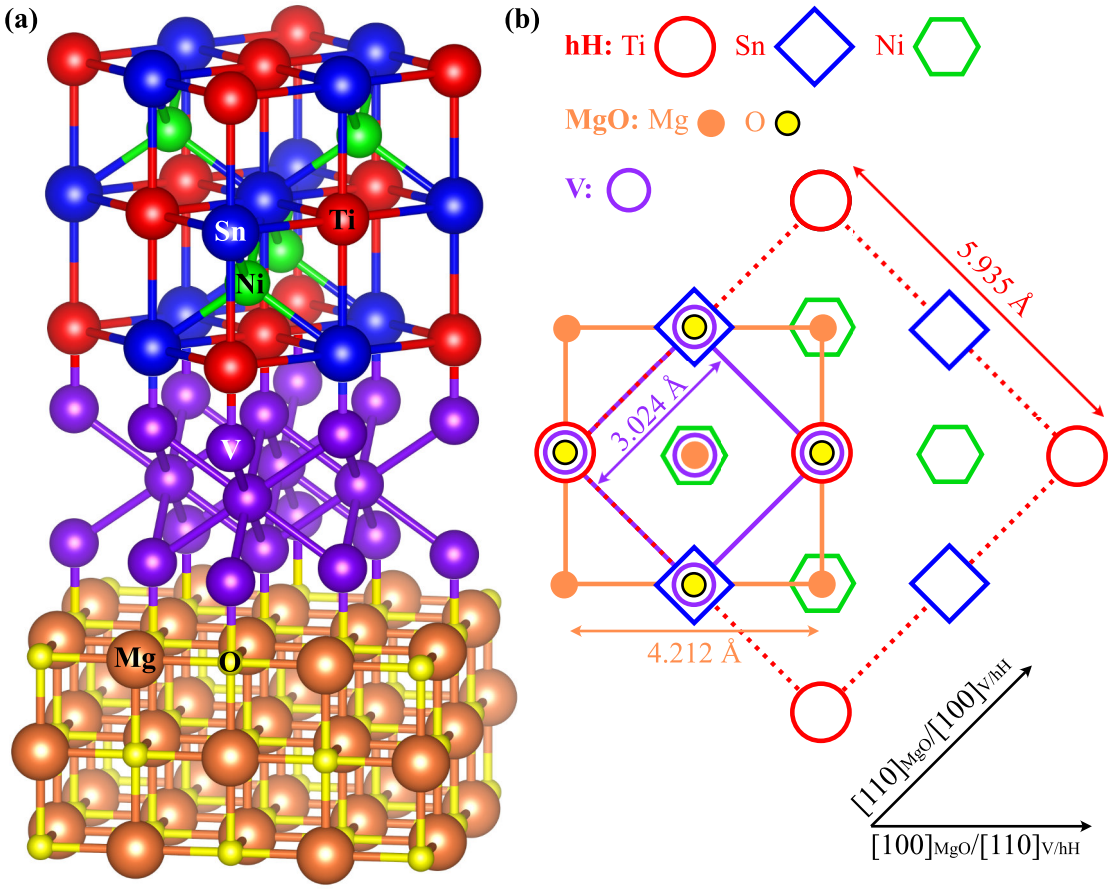

Figure 5.14: (a) Ball-and-stick model of the anticipated epitaxial relationship between MgO and TiNiSn when an intervening vanadium layer is present. The vanadium buffer layer has lattice registration with the MgO through a 45° rotation that is similar to that found for the half-Heusler. (b) A top-down view of the layer stack helps represent how the unit-cell dimensions for each material relate to each other. The boundary of each unit cell in the top-down view is outlined and bulk lattice constants of each material labelled.

a material which is more closely matched would be preferred and, for this reason, vanadium was chosen.

Elemental vanadium has a bcc unit cell with a bulk lattice constant of 3.024 Å for the [001] direction [322]. This lattice constant provides a coincident lattice match with MgO through a 45° rotation of the unit cell about the [001] axis, as found previously in studies of magnetic tunnel junctions [323] and for the use of contact electrodes with half-Heuslers [324]. This is similar in manner to that used to achieve epitaxy for TiNiSn directly on MgO in the previous sections of this chapter. This rotation aligns the [110] planes of the vanadium cell with the [100] direction of the MgO, as illustrated in Figure 5.14 resulting in a +1.5 % bulk lattice mismatch between vanadium and the MgO substrate ($\sqrt{2} \times 3.024$ Å $= 4.277$ Å for V, versus 4.212 Å for MgO [290]). The orientation of the vanadium layer is then consistent with that of the TiNiSn unit cell and epitaxy is expected with a lattice mismatch of -1.9 % between these

two layers (2×3.024 Å $= 6.048$ Å for V, versus 5.935 Å for TiNiSn [282]). Deposition of vanadium by MBE or d.c. magnetron sputtering is well documented [322, 323, 325, 326] and typical deposition temperatures are in the vicinity of the substrate temperatures used for TiNiSn.

5.3.2 Optimising the sputter-deposition of vanadium

Metallic vanadium thin films have been of scientific interest for a number of applications, particularly in magnetic systems, owing to the paramagnetism of vanadium [322, 327] and its role in magnetic exchange coupling in thin film multilayer systems [328, 329]. As such, there is a wealth of literature concerning the deposition of elemental vanadium, particularly by molecular beam epitaxy (MBE) and also for d.c. magnetron sputter deposition. As discussed in Chapter 2, The growth chamber of the pulsed laser deposition system provides the means to deposit thin films by both PLD and d.c. magnetron sputtering. Preferring to avoid the droplet problems associated with the PLD of metals [127], magnetron sputtering has been used for the deposition of vanadium thin films, using a commercially available vanadium sputter target (Pi-Kem Ltd., UK, 99.9+% purity, 2" diameter $\times$ 2 mm thick). Sputtering must be carried out with an ambient argon gas and partial pressures in the range 2.5 - 25 mTorr Ar were tested. Substrate temperatures from 298 K to 823 K were also studied. Prior to depositions, the vanadium target was sputtered to remove any oxide scale which may have formed on the surface. Aspects of the deposition regarding MgO substrate preparation and growth of TiNiSn were kept the same.

Understanding the deposition rate here is much simpler than when optimising the pulsed laser deposition rate of TiNiSn in Section 5.1, which was hampered by virtue of the laser being external to the growth chamber. For sputter deposition, the rate inevitably reduces with increasing gas pressure for the same reasons discussed for PLD growth [296]. To ensure that a vanadium nanolayer is fully continuous, surface roughness is a much more important factor than deposition rate. Thus, although the highest Ar partial pressure of 25 mTorr yields a low deposition rate on the order of 0.05 nm s^{-1}, it was this pressure which was found to produce the smoothest vanadium films on MgO, irrespective of substrate temperature.

To optimise the deposition temperature for epitaxial growth of vanadium, substrate temperatures from 298 K to 823 K were tested. *In situ* RHEED was again used to monitor the crystalline character of the deposited films, while AFM was used to assess surface rough-

ness after deposition. In terms of minimising surface roughness, the best films of vanadium were produced at 723 K, which had an RMS roughness of 1.6 Å when deposited on silica. However, no Bragg intensity was observed in the RHEED patterns from vanadium when deposited on MgO at this temperature which indicates a lack of crystallinity. This is consistent with a previously observed transition to amorphous deposition at temperatures above 673 K [322]. Thus, to maintain epitaxial growth, a substrate temperature of 623 K was used hereafter. There is only a minor sacrifice of surface quality at this temperature, which had a surface roughness of 3.4 Å when deposited on silica.

5.3.3 Characterisation of TiNiSn thin films deposited onto a V contact layer

To explore how the vanadium buffer alters the interface chemistry, a small amount of TiNiSn – approximately 20 - 25 nm equivalent – was deposited atop the buffer. Deposition conditions for the TiNiSn were not altered from previous optimal conditions found for direct growth onto MgO, so the substrate temperature was raised to 670 K for TiNiSn deposition after creating the vanadium layer. The PLD of TiNiSn is executed using the same 'burst' method described earlier. For the chosen thickness of TiNiSn, 40 repetitions of the pulse-burst/anneal cycle were used. The resulting film, though quite thin, is sufficient for exploring the interfacial relationship between the vanadium and the TiNiSn.

Where deposition of TiNiSn onto bare MgO was concerned, growth proceeded with the formation of flat-topped islands, that coalesce with increasing film thickness. Deposition of the hH onto the V buffer appears to follow a similar mechanism, suggesting that the 3d growth mode of TiNiSn is driven by strain effects within the hH film, rather than the kinetics of surface diffusion, which is expected to be characteristically different for a metallic vanadium surface compared to the oxide surface of the substrate. RHEED patterns recorded during thin-film growth are presented in Figure 5.15(a-c) and provide an overview of the data collected during deposition. First, Fig.5.15(a) was recorded from the MgO substrate, immediately prior to deposition. The vertical streaks observed are typical for a smooth surface whose main feature is atomic-scale terracing. This is consistent with the AFM topography, which indicated a surface roughness of 1.1 Å. The next pattern shown in Fig.5.15(b) was obtained from a 5 nm thick vanadium film grown at a substrate temperature of 623 K. The pattern is similar to the MgO pattern, indicating the formation of an epitaxial relationship with the underlying substrate, as well as minimal differences in surface roughness. AFM mi-

crographs show the RMS roughness increases marginally to 1.6 Å. The last RHEED pattern, shown in Fig.5.15(c), was recorded after deposition of ~25 nm of TiNiSn. This pattern is markedly different from the patterns of the preceding layers, with the appearance of discrete diffraction spots whose lateral periodicity is halved compared to the MgO or V. The change in period is the same as for deposition of TiNiSn onto MgO and is consistent with the model for epitaxial alignment shown in Figure 5.14. The spotty, rather than streaky pattern arises due to transmission of the electron beam through a 3-dimensional surface which exhibits significantly greater roughness than the substrate. The RMS roughness, as measured by AFM, for this layer increases dramatically to 22.6 Å, which is consistent with the propensity for 3d island growth in the initial stages of deposition.

Although the RHEED patterns obtained during growth provide a wealth of qualitative information, quantitative analysis of RHEED patterns – to assess epitaxial strain, for instance – was found to be unreliable. This was due to the variation in substrate temperature throughout the deposition process. As heating is achieved by a resistive coil behind the substrate, changes in the heater power produce changes in the electromagnetic field that the coil produces and therefore has differing electron lensing effects at different temperatures. As this effect is not well characterised, it is impossible to draw a reliable cross-calibration of the reciprocal-space dimensions of the RHEED patterns. Instead, nanoprobe convergent beam electron diffraction (CBED) patterns were recorded from each layer in the TEM from a cross-sectional specimen of the film. These patterns are presented alongside their RHEED counterparts for each layer in Figure 5.15.

To calculate the lattice parameters of each layer, the disc positions in each CBED pattern shown in Figure 5.15(d-f) are located using an implementation of the Hough transform algorithm [330] in the CrysTBox software [331, 332]. All the patterns, which were recorded sequentially under the same conditions, are calibrated against the *200* reciprocal lattice vector for bulk MgO at room temperature (0.4751 $Å^{-1}$). With this calibration, the corresponding reciprocal lattice vectors in vanadium and TiNiSn are found to be have values of 0.4747 $Å^{-1}$ and 0.4756 $Å^{-1}$ respectively. These values translate to real-space lattice constants of 2.979 Å for V and 5.947 Å for TiNiSn. Comparing the measurements between layers, these indicate that there is only a slight relaxation in the epitaxial relationship between the layers, with a small compressive strain of 0.05 % between vanadium and MgO, and a tensile strain of 0.18 % between TiNiSn and vanadium. For context, the anticipated lattice mismatches for fully-relaxed bulk materials would be 1.5 % and -1.9 %, respectively.

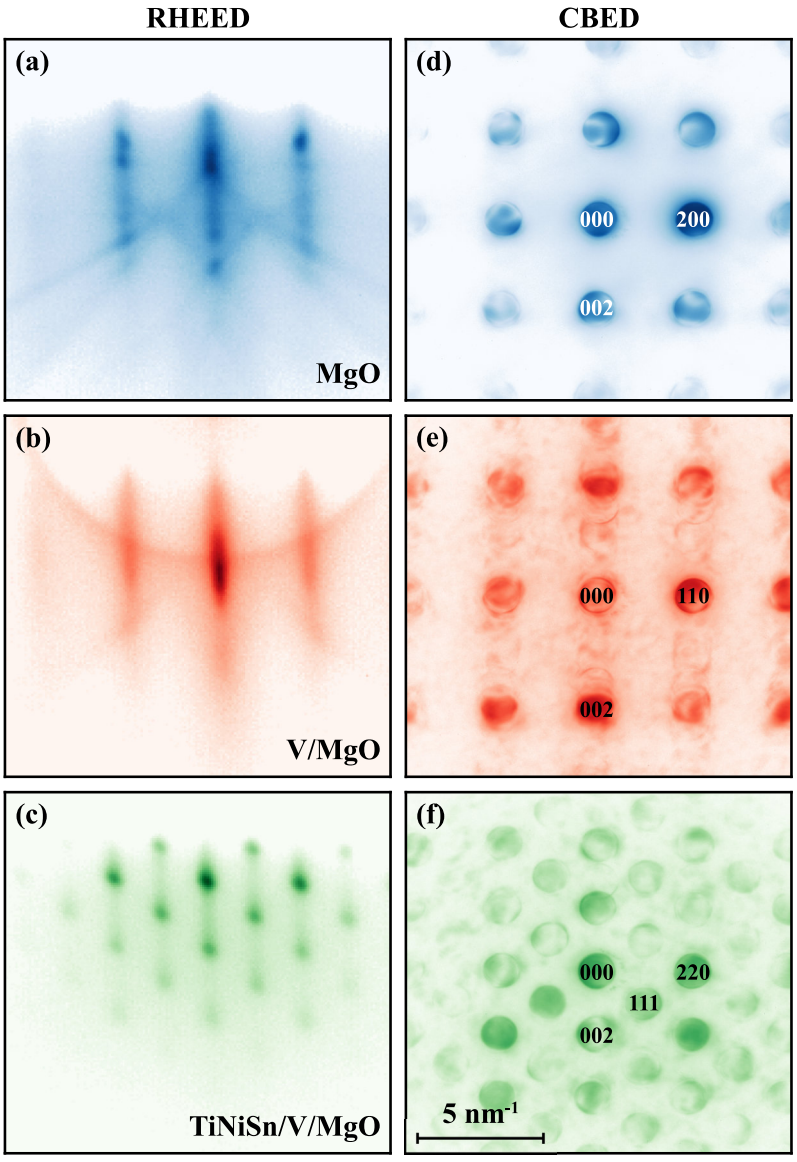

Figure 5.15: RHEED patterns for (a) MgO, (b) V and (c) TiNiSn surfaces collected during deposition of TiNiSn/V/MgO. (d)-(f) Cross-sectional TEM CBED patterns collected from the same layers after deposition, with the same scalebar. Miller indices for some reflections are indicated in (d)-(f), indexed with respect to the unit cells for MgO, V and TiNiSn structures, respectively.

Turning to STEM for further characterisation, images of the specimen provide direct evidence of the integrity of the thin-film system. Figure 5.16 presents an analysis of a cross-section through a MgO/V/TiNiSn specimen with a protective Pt capping layer. Approximately 5 nm of vanadium was deposited at $T_S = 623$ K prior to depositing ~25 nm of TiNiSn at $T_S = 723$ K, in keeping with the preferred deposition temperature which we previously used for TiNiSn in Section 5.2. A STEM-BF (bright-field) micrograph in Fig.5.16(a) clearly shows the TiNiSn with a trapezoidal top surface atop a relatively uniform and continuous layer of vanadium. The faceting in the surface structure of TiNiSn is no different to that previously observed for deposition without a buffer layer and is consistent with the forma-

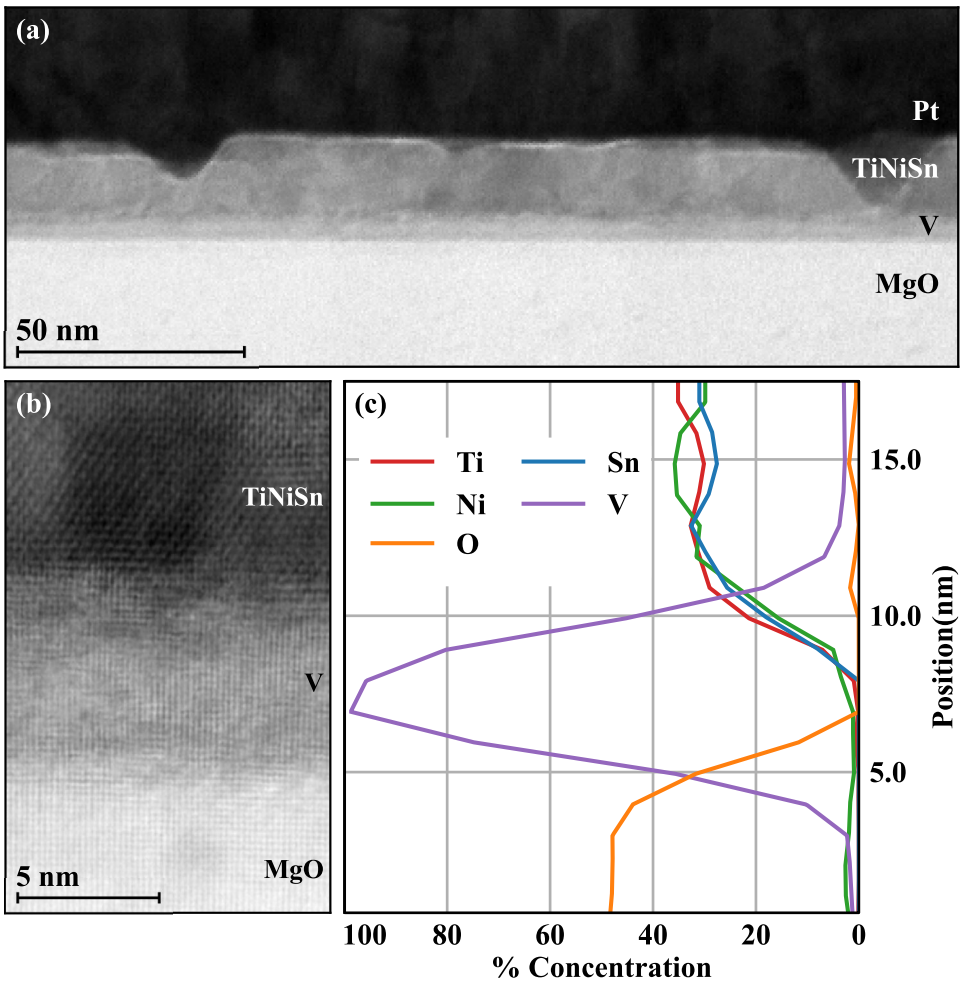

Figure 5.16: (a) Low magnification STEM-BF image of a MgO/V/TiNiSn/Pt cross-section. (b) HR-STEM-BF image of MgO/V/TiNiSn interface viewed along $[100]_{MgO}$ and (c) composition determined from EELS across that interface. The key result here is the emergence of a clean 1:1:1 TiNiSn Heusler allow without loss of Ti.

tion of 3-dimensional islands. As discussed previously, the large values of roughness found from AFM measurements are dominated by the gaps between islands, where there is large variation in film thickness, rather than the flat tops of the islands themselves.

Looking at the interface with greater magnification, Fig.5.16(b) shows another STEM-BF image of the V nanolayer and its interfaces with atomic resolution; confirming directly that an epitaxial relationship exists between all three layers. The specimen in this image is oriented with the beam passing along the (100) direction of MgO so that columns of atoms (bright spots) are arranged in a square symmetry which continues uninterrupted from the substrate into the vanadium layer. The uniform contrast across these layers in Fig.5.16(a) indicates minimal crystallographic variation across the specimen. Similar continuity of the structure is seen in the relationship between the V and TiNiSn layers, however the structure and orientation of the hH unit cell leads to a more complex arrangement of atomic columns in Fig.5.16(b).

Contrast variations are more noticeable throughout the hH layer and are attributed to minor misalignments of crystalline regions which nucleated separately. Loss of epitaxy in the film is discounted as the observed contrast variations are minor.

Elemental quantification of STEM-EELS data recorded from a region spanning the nanolayer is presented in Fig.5.16(c) as line profiles of the percentage elemental concentrations aligned vertically with the STEM-BF image in Fig.5.16(b). Unlike the EELS data presented in Fig.5.9, only the oxygen content from the MgO was quantified, as the Mg *K* edge was beyond the recorded energy-loss region. The oxygen concentration has been normalised to 50 % to account for the magnesium content. Above the MgO, there is a clear region of 100 % vanadium and the interface with the substrate is approximately 2 nm wide, which is consistent with the sharpness of the contrast variation observed in Fig.5.16(b). The interface width observed here is significantly larger than would be expected given the low roughness of the surface measured by AFM, but is understood to reflect the roughening which occurs to the MgO surface while held at high temperatures [333]. Deposition onto the coarser surface at high temperature acts to 'lock in' the increased surface roughness upon subsequent cooling to room temperature. The upper nanolayer interface, between V and TiNiSn is found to be slightly broader. This may be accounted for by a combination of the existing roughness of the V surface, a small amount of implantation during pulsed laser deposition and possibly a minute amount of interfacial alloying. The stoichiometry of the TiNiSn layer at the top of the dataset is observed to be close to the ideal 1:1:1 ratio; no vanadium was detected in the hH layer and negligible quantities of oxygen were present. From the STEM-EELS data, the key observations are in the quality of the vanadium nanolayer. No discernible oxide content is measured and no chemical shift or change in ratio of the V $L_{2,3}$ white lines – which would indicate a change in oxidation state [334] – is found. Furthermore, the common onset of the Ti, Ni and Sn signals in the elemental concentration profile, as well as the near-ideal stoichiometry, indicate that the previously observed diffusion of titanium out of the Heusler alloy is absent here. No Ti-rich interface or corresponding Ti-depleted alloy region are observed and the buffer layer has fulfilled its intended purpose.

The data presented in Figure 5.17 are used to probe in greater detail the crystallinity and epitaxy of the thin-film stack. Presented are a pair of STEM images containing high-resolution structural information which can be used to assess defect formation at the interfaces of the V nanolayer. The atomic-resolution STEM-BF image in Fig.5.17(a) shows a small portion of the MgO/V/TiNiSn interfaces, similar to Fig.5.16(b). The colour overlay illustrates the res-

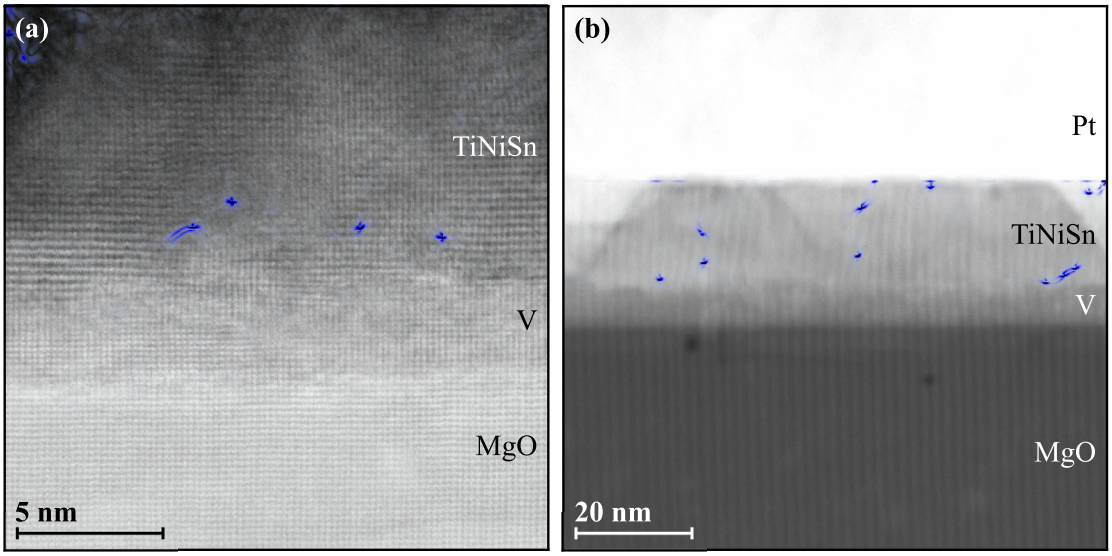

Figure 5.17: (a) HR-STEM-BF image showing close-up of vanadium interfaces with atomic resolution viewed along $[100]_{MgO}$ and (b) lower magnification STEM-HAADF image containing STEM-Moiré fringes. Colour contrast overlaid on images derives from differential phase maps from geometric phase analysis (GPA), where the singular points of blue denote a phase inversion indicative of a dislocation site.

ults of geometric phase analysis (GPA) of the atomic lattice, which is used to identify strain and dislocations [335]. Colour contrast in the overlay derives from the differential phase map, calculated from the image using the Strain++ software package [336]. The Sobel edge-filtered image of the phase map turns points of phase inversion – which indicate a dislocation site – into peaks. These peaks, highlighted in blue in the colour overlay, represent points where the lattice periodicity has been disrupted. No lattice defects were observed in connection with the MgO/V interface in the field of view. Meanwhile, for the V/TiNiSn interface, a lateral dislocation density of 0.021 $Å^{-1}$ was found.

To probe the epitaxial and crystalline properties on a larger lengthscale – with a view to achieving a more representative description of the specimen – Fig.5.17(b) presents a STEM-HAADF (high-angle annular dark field) image which contains contrast from STEM-moiré interference. This interference offers the same structural information as Fig.5.17(a), but across much larger length-scales [337] and has been analysed in an identical manner. Once again, no defects were observed in association with the MgO/V interface, across a field of view five times greater than in Fig.5.17(a). The lack of dislocations on this length-scale is consistent with diffraction data in showing excellent quality of epitaxial, largely unrelaxed growth of vanadium on MgO. There are once again defects associated with the V/TiNiSn interface, this time with a calculated dislocation density of 4.2×10^{-3} $Å^{-1}$. There is a significant difference in dislocation densities found between the high and low-resolution images, suggesting that

the dislocations are not uniformly distributed and that the 0.18 % epitaxial mismatch between the V and hH layers found from CBED is compensated by small, sparse clusters of defects which relieve the tensile strain so the hH layer is slightly relaxed. Both here and in growth directly onto MgO described in Section 5.2, these sparse dislocation networks not only mark the strain relief that occurs during thin film growth, but also provide an explanation for the exclusive observation of 3d island growth of TiNiSn. These dislocations indicate that the misfit strain associated with the mismatch of lattice constants is large enough that surface stresses during growth make 2d Frank-van-der-Merwe growth unstable, favouring the formation of 3d islands instead (Vollmer-Weber growth) [297].

5.3.4 Further discussion

One of the main concerns which arose surrounding the use of vanadium as a buffer layer was the apparent requirement to deposit it at a substrate temperature 100 K lower than the TiNiSn layer. There was anticipation that this could cause problems related to the integrity of the buffer layer upon annealing, through the possibility of either oxidation, amorphisation or alloying, especially given the capability of Heusler alloys to incorporate a large range of elements into their structures [70, 280]. Instead, the evidence which has been presented shows no cause for concern on any of these fronts and the vanadium layer remains metallic, crystalline and immobile. Vanadium mobility here is likely restricted as a consequence of the temperature range which has been studied, which is quite low compared to the melting point of metallic vanadium (2183 K). This is an important consideration for applications of the vanadium nanolayer as an adhesion layer or passivating coating, as mobility of the vanadium would have a deleterious effect on the half-Heusler stoichiometry. These considerations are important to the eventual incorporation of TiNiSn thermoelectrics into a TEG module, where contact layer materials should suppress any possible reactions with the thermoelectric. Diffusion of vanadium into the hH could lead to unintentional phase segregation of some form, which is known to have an impact on the thermoelectric efficiency of Heusler alloys [66]. Consequently, further study is required to develop an understanding of the behaviour of vanadium nanolayers at temperatures greater than 723 K. It would be useful to study this high temperature behaviour by annealing of the layer stack to temperatures of 900 K, which would then encompass a similar temperature range to those found in studies of the thermoelectric merit of TiNiSn-based Heusler alloys [66, 282, 283].

5.4 Conclusions

In this chapter, growth of TiNiSn thin films by pulsed laser deposition has been explored, with demonstration of amorphous, polycrystalline and epitaxial growth regimes dependent on substrate temperature. In a detailed investigation of epitaxial thin films, rich nanostructural character was discovered through high-resolution TEM & STEM studies. With the refinements to quantitative analysis detailed in Chapters 3 and 4, it was possible to accurately identify the compositions of the nanostructured minority phases and comparisons with XRD measurements emphasise difficulties in extracting similar information from bulk analytical methods, where some minority phases were characterised inaccurately and others – such as the TiO inclusions – were completely overlooked. In addition to the nanostructuring throughout the film, an interfacial reaction with the MgO substrate was also observed to produce a distinct, TiO interface layer. The formation of this layer robs the hH of Ti and perturbs film composition in the initial stages of growth. The use of nanometre-scale buffer layers of vanadium to suppress this reaction was demonstrated, and represents a potentially useful approach to incorporating TiNiSn thermoelectrics into TEG modules.

Epitaxial thin films grown at substrate temperatures between 670 K and 720 K represent the best quality films of TiNiSn achieved with PLD. The surfaces of these films consist of large, flat islands terminated by crystal facets. The atomically-smooth surface planes of these islands should prove ideal for providing smooth interfaces with other materials which may be deposited. Film quality benefits from using an interval-PLD approach to deposition, where monolayers of material are delivered as rapidly as possible with brief annealing intervals in between monolayer depositions. Film quality might be improved further if a laser with a higher maximum repetition rate were used, so that pulse bursts could be delivered within the relaxation time of island nucleation, as suggested by the authors of the original interval-PLD studies [306, 307]. Satisfying these conditions could overcome the tendency of TiNiSn for 3d island growth and impose a layer-by-layer growth mode for smoother films. Given that the number of pulses required to deposit one unit cell thickness of TiNiSn is typically 100 pulses, a pulse rate of 100 - 200 Hz should fulfil this condition and would be worth further exploration.

The spontaneous nanostructuring found in high-resolution STEM studies gives a glimpse into understanding phase segregation effects in thermoelectric half-Heusler alloys, where the micro-/nanostructure of the material can play a key role in improving thermoelectric per-

formance. Here, phase segregation appears to be driven by a proximity to TiO phases and the extrusion of Ti from the Heusler matrix which occurs in forming the oxide phase. The phase segregation of the nickel-rich half-Heusler primarily leads to the formation of near-full-Heusler nanoinclusions, which are likely stabilised due to the smaller enthalpy of formation of the full-Heusler phase [66]. These features are revisited in Chapter 7, where their impact on the lattice is also considered. The most curious feature here is the intermediate composition, $TiNi_{1.38}Sn$ Heusler phase found near the interface with the substrate. Conventional wisdom regarding Heusler alloys suggests only phases with stoichiometries close to either the half- or full-Heusler can be supported and that such intermediate concentrations of Ni are not soluble in the hH. The presence of this intermediate phase, which may be stabilised by either the chemical interaction with the substrate or the epitaxial relationship with the Ti-doped interface layer highlights a difference between states available at thermodynamical equilibrium, and those deposited under kinetically limited conditions. Further investigation of this effect is warranted.

Epitaxial growth of nanometre-scale thin films of vanadium on single-crystal MgO has been demonstrated for application as a buffer layer. The vanadium films are epitaxially strained and no evidence was found for defect formation to compensate for the structure of vanadium. As little as 5 nm of vanadium was successful in acting as a barrier to the titanium diffusion which had been observed in MgO and the result is a more uniform composition of the TiNiSn film during the initial growth. The half-Heusler layer still grows epitaxially atop vanadium, with the lattice mismatch supported by the formation of a low density of dislocations. No oxidation, amorphisation or alloying was discernible at or below the the half-Heusler deposition temperature of 723 K and no deleterious effect on the nature of the half-Heusler layer was found, which will be critical to successful application of these materials in thermoelectric generators.

Change is the essential process of all existence.

Spock

6

Thermal evolution of nanostructured TiNiSn half-Heusler thin films

NANOSTRUCTURING of TiNiSn-based Heusler alloys is a powerful route to realising high-performance thermoelectric power generation using these materials, however the thermal stability of nanoscale features is seldom investigated. Exploitation of the nano- and microstructure of Heusler alloys to improve thermoelectric efficiency relies on the complex compositional phase space, which contains more than one Heusler phase and many other binary intermediate phases [66, 67, 99]. The complexity of the Ti-Ni-Sn phases-space, combined with the narrow range of conditions within the phase-space where TiNiSn formation is possible, makes controlled synthesis of pure TiNiSn challenging [66, 99]. In bulk synthesis, simply mixing stoichiometric quantities of elemental powders rarely produces a phase-pure reaction product, as the constituent elements have a broad range of melting points. This leads to incongruent melting and the formation of intermediate phases during reactions, which has been highlighted in recent neutron powder diffraction (NPD) investigations [338]. TiNiSn can be produced by a range of bulk synthesis techniques, each of which represents a differ-

ent set of thermodynamic and kinetic conditions and so the exact nature of any secondary reaction products will depend on which synthesis protocol is used [46, 66, 84, 99, 109, 282, 339].

Phase separation in TiNiSn-based Heusler alloys has been widely reported [66, 84, 86, 109, 285], arising as a consequence of the relative properties of the half-Heusler (hH) phase compared to the possible secondary phases. Several of the non-hH phases possess a greater stability and therefore crystallise more readily than the hH [106]. In working TEGs, the presence of non-hH phases can increase phonon scattering to reduce the thermal conductivity. The inclusion of the other main ternary phase, the full-Heusler (fH) $TiNi_2Sn$, is especially beneficial [67, 86] and is observed to form within the hH in association with excess Ni beyond the solubility of the hH [85, 86, 340]. The metallic fH $TiNi_2Sn$ is a poor thermoelectric material on its own, but enhances the hH when incorporated as small inclusions (e.g. nanoscale precipitates [67]) as it reflects an excess of Ni associated with doping and, consequently, an increase in the carrier density and electrical conductivity of the composite alloy [86]. Meanwhile, coherent boundaries between the phases act to scatter phonons, leading to a reduction of the lattice thermal conductivity [46, 105]. Binary alloy phases are near ubiquitous in literature, primarily as nickel stannide inclusions [106, 338] and this is consistent with observations made here. There is speculation that the presence of metallic binaries negatively impacts the Seebeck effect [315], however this has yet to be verified.

The formation of non-hH phases, and their nano- or micro-structural character varies with synthesis method and they must be capable of withstanding prolonged exposures to high temperatures like those involved in thermoelectric power generation. However, the stability and practical reliability of composite Heusler compounds has seldom been examined in great detail. If it emerges that nanoscale inclusions and precipitates in TiNiSn are metastable, their usefulness would be significantly limited. Therefore the thermal evolution of nanostructured TiNiSn, with a focus on high-temperature stability of nano-inclusions, is of great interest. To investigate the high-temperature evolution of Heusler nanostructures, we build on the work presented in the preceding three chapters, taking the improved EELS chemical characterisation (Chapters 3 and 4) of thin films grown by pulsed laser deposition (Chapter 5) and extend this chemical analysis into the temperature domain through *in situ* transmission electron microscopy, specifically, the thermal annealing of specimens whilst inside the TEM.

The fabrication of epitaxial TiNiSn thin films by pulsed laser deposition was demonstrated

in Chapter 5. These films contained a rich variety of nanostructures, some arising from the kinetics of film deposition, and some driven by chemical imperfections found in the PLD targets used for their fabrication. By increasing the deposition temperature, the degree of phase segregation was observed to increase in tandem with increases in film roughness which can be interpreted as the thermally excited system tending towards a thermodynamic minimum. The thin film studied in this chapter, deposited at 800 K, is phase-segregated to the point of possessing comparable quantities of hH and fH TiNiSn phases, present alongside titanium oxides and nickel stannides [294]. A complexity of the experiment presented here is that the film was capped with a ~10 nm layer of elemental Ni, with the intent that incorporation of excess quantities of Ni into the Heusler structure and the consequences for phase segregation can be studied as part of the experiment. A detailed study of the as-grown thin film is presented in Section 6.1, so that the starting-point of the *in situ* experiment is clear. This section also introduces some of the analysis and visualisation of results which will be used throughout the chapter.

Section 6.2 introduces the thermal annealing experiment in detail, outlining the thermal treatment protocols and summarising the results. The objective of the *in situ* annealing ex-

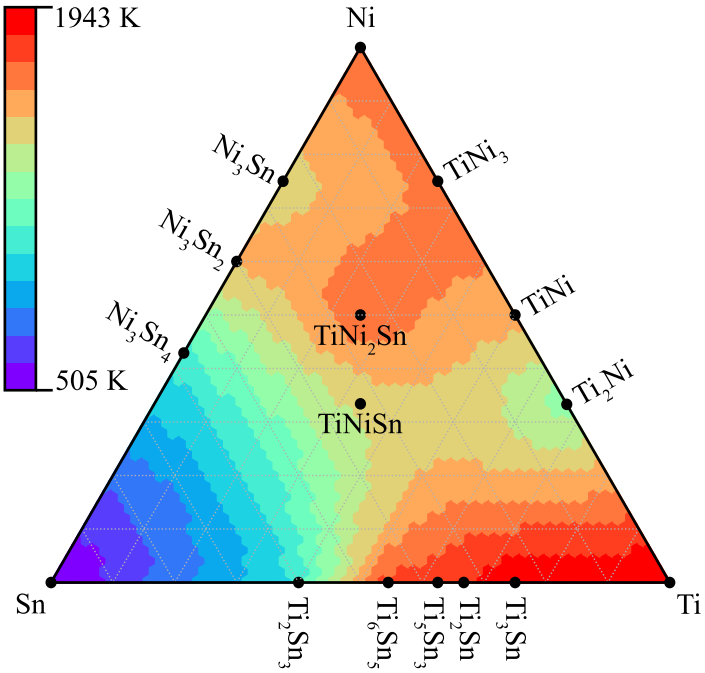

Figure 6.1: A representation of the Ti-Ni-Sn composition phase-space. Each corner denotes a single element, known binary alloys containing two of the three elements are found along the edges of the phase-space, while the ternary full and half-Heusler phases are found in the middle of the diagram. The colour contours derive from melting point data for the annotated phases found by Douglas et al. [66]. Linear radial basis function interpolation [223] is used to approximate variations in melting points between known temperatures.

periment was to use STEM-EELS to study thermally-activated diffusion within the specimen, with a special interest in the solubility of Ni and relationships between Ni excesses and phase segregation. Figure 6.1 is a ternary diagram which represents the Ti-Ni-Sn composition phase-space. Known alloys are identified, including the two Heusler phases TiNiSn and $TiNi_2Sn$. The colour scale superimposed on the diagram is an approximation of the variations in melting points of different compositions, derived from the melting points of the identified phases. These melting points provide a proxy for the relative stability of different phases. In this representation, the preferred TiNiSn phase sits at a saddle-point in the middle of the phase-space, with the fH phase sitting in a position of greater stability, which suggests that formation of the fH phase is favourable and points to difficulties in fabricating pure samples of TiNiSn. Thermal annealing, which has been achieved using TEM heating chips from DENSsolutions [145], was performed at temperatures up to 1223 K. Sn, Ni_3Sn_4 and Ti_2Sn_3 all have their melting points within this temperature range. Thus, if these phases are present within the specimen, heating is anticipated to have a severe effect on them.

Finally, in Section 6.3, results of the annealing experiment are discussed in detail. Annealing is found to profoundly impact the hH/fH phase segregation at temperatures above 1000 K, while the integrity of the Heusler alloy appears to be compromised at 1200 K as extrusion of Ti was observed. The merit of including the Ni cap is also discussed, as it appears to dissipate without significantly altering the Heusler film. The discussion of results concludes with an analysis of the mobility of Ni between Heusler phases, drawing comparisons with wider research and discussion of how observations should be interpreted.

6.1 Nanoscale segregation in as-grown TiNiSn thin films

The thin films studied in this chapter differ from those of Chapter 5, which were epitaxial, continuous and contained nanoscale inclusions embedded within a nickel-rich half-Heusler phase. These films were grown at temperatures ranging from 670 K to 720 K and it was noted that increasing the substrate temperature above 720 K crosses a morphological transition where the surface roughness of the film increases (see Figure 5.5 on pp.155). One such film, deposited at 800 K, is the primary subject for this chapter. Using TEM we find that films grown at these high temperatures are not only rougher but also undergo more pronounced chemical phase segregation. A TEM cross-section of a TiNiSn thin film deposited at 800 K is presented in Figure 6.2. The STEM-HAADF image in Fig.6.2(a) reveals a discontinuous film of large, discrete islands, all containing variations in intensity which betray the compositional

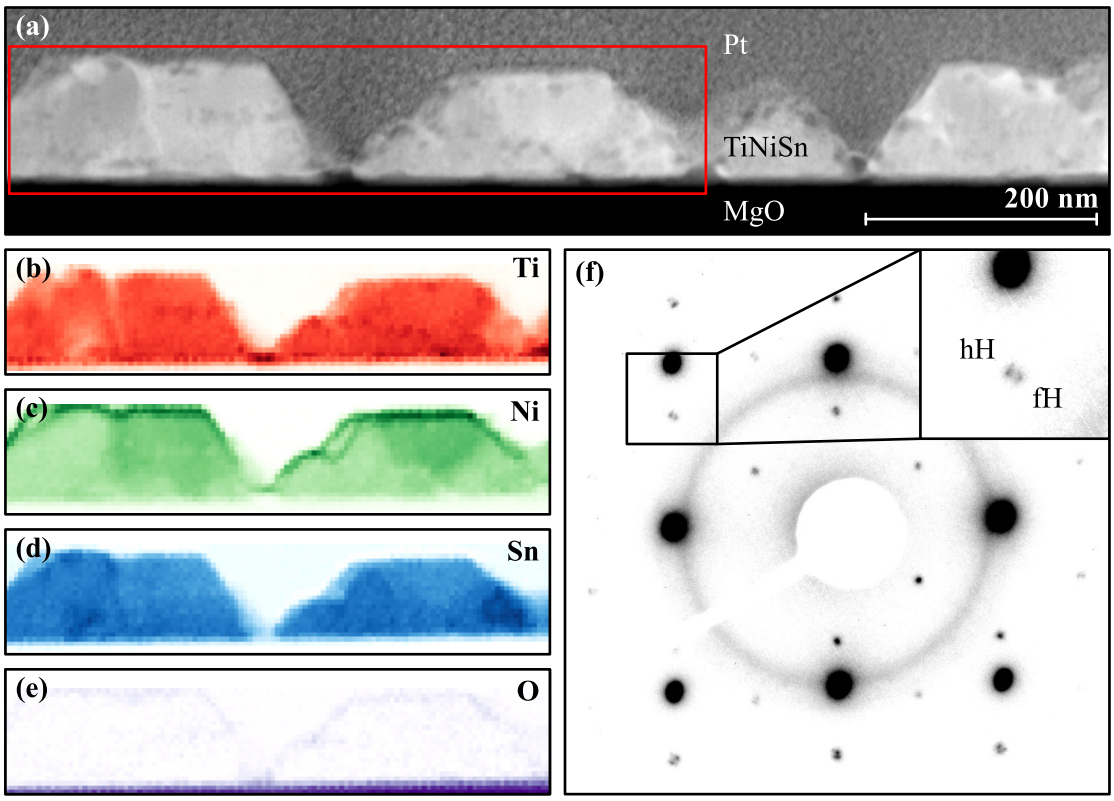

Figure 6.2: (a) STEM-HAADF cross-sectional image of a phase-segregated Heusler thin film. (b-e) Elemental maps of Ti, Ni, Sn and O, respectively, deriving from the results of elemental quantification of a STEM-EELS spectrum image recorded in the region marked by the red outline in (a). Greater intensity/darkness of colour in these maps denote greater absolute quantities of the element. (f) TEM diffraction pattern showing the epitaxial nature of the film, with intense spots in a square pattern arising from the MgO substrate, and a set of less intense spots deriving from the Heusler film. Inset in (f) is the 222 Heusler reflection, enlarged to emphasise the radial splitting into two spots caused by the difference between hH and fH lattice constants.

diversity within them. As established in Chapter 5, the chemical diversity present in the islands reflects the phase segregation found in the bulk materials.

STEM-EELS spectrum imaging highlights the chemical variations present in the islands, and elemental maps are presented in Fig.6.2(b-e). These images map the quantification results for each of the elements Ti, Ni, Sn and O from the STEM-EELS spectrum image recorded in the region marked by the red outline in Fig.6.2(a). In addition to being able to differentiate the Heusler islands from the nickel capping layer – which is clearly visible in Fig.6.2(c) – there is also notable variation in Ni content within the film, complementing the HAADF contrast observed in Fig.6.2(a). These two distinct Ni concentrations result in mean compositions of $TiNi_{1.04}Sn_{0.95}$ and $TiNi_{1.77}Sn_{0.9}$, which correspond to the half-Heusler (hH, light green) and a near full-Heusler (fH, dark green) alloy, respectively. Both Heusler phases are present in comparable quantities. The oxygen map in Fig.6.2(e) shows the majority of O

intensity arises from the MgO substrate. There is also some subtle evidence for surface oxidation on the upper surface of the Ni capping layer, though no oxidation is present in the Heusler islands.

The similar volumes of the hH and fH phases throughout the film found in chemical analysis by EELS is also reflected in the atomic lattice. TEM diffraction observed from this film, which is presented in Fig.6.2(f), contains a square array of large, intense spots containing diffraction contributions from the MgO substrate and a set of smaller, less intense Bragg reflections originating from the Heusler thin film. The Heusler pattern describes a single-crystalline thin film and the coincidence of the MgO(200) and hH(220) reflections demonstrates the epitaxial lattice matching of the film to the substrate. Studying the less intense reflections from the Heusler film in greater detail, a clustering of two peaks can be observed for each reflection. For emphasis, the inset in Fig.6.2(f) shows a close-up of the (222) Heusler reflection. The division of the reflection into two peaks along a radial direction relative to the direct beam indicates a uniform expansion/contraction of the lattice in all directions. Of the two peaks in each reflection, the peak closer to the direct beam has a larger unit cell and has been labelled as the fH phase in the diffraction pattern, while the peak representing the smaller unit cell is the hH phase. In Chapter 5, we discussed the epitaxial strain of the hH on MgO where, despite a very close lattice match, the hH film was partially relaxed. The diffraction peak splitting observed here is indicative of differing magnitudes of epitaxial strain relief for the hH and fH phases that likely originates from the difference in bulk lattice constants, where the relaxed fH unit cell is approximately 2.5 % larger than the hH cell.

For a quantitative assessment of the compositions which are present, the distribution of elemental quantities in the chemical phase-space is presented in Figure 6.3. To determine elemental concentrations, a full compositional analysis was performed on each spectrum in the SI, following the protocols in Chapter 4. The diagram presented in Fig.6.3(a) represents the Ti-Ni-Sn ternary phase space with the same axes as the ternary diagram shown in Figure 6.1. Here, the diagram contains a density plot deriving from the results of EELS elemental quantification. The colour scale – which is logarithmic to emphasise the presence of minority phases – indicates the prevalence of a given composition within the thin film, with darker colour representing a greater proportion of the thin film. In this representation, The half-Heusler (Ti = Ni = Sn = 33.3 %) and full-Heusler (Ti = Sn = 25 %, Ni = 50 %) compositions are easily identified close to the centre of the diagram and have been labelled

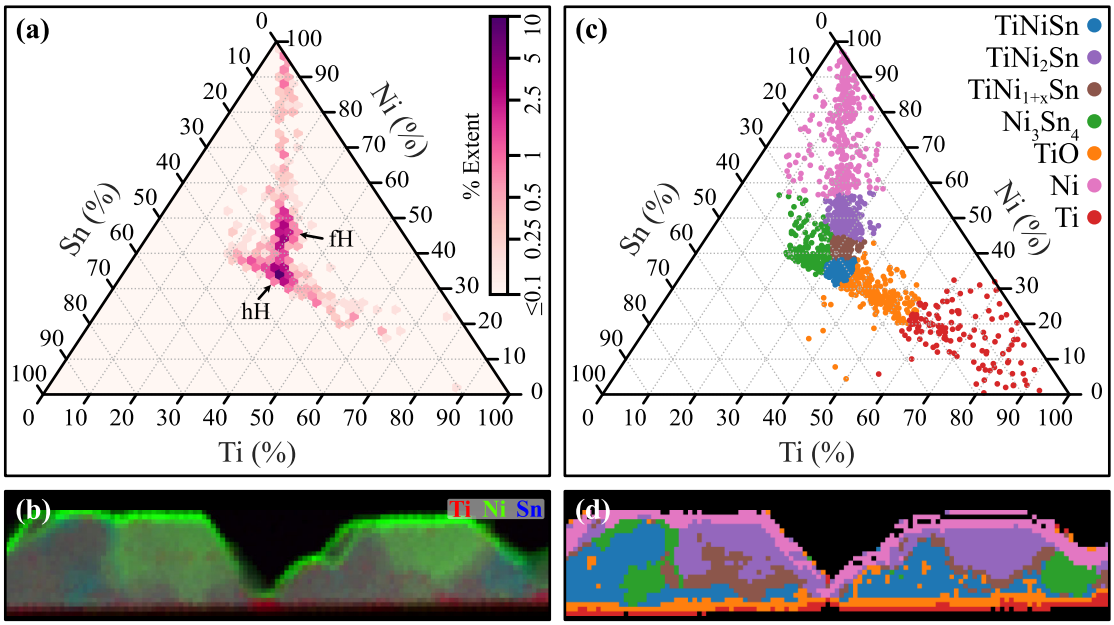

Figure 6.3: (a) Ternary chemical phase diagram showing the prevalence of different compositions in the Ti-Ni-Sn phase space; the axes are identical to the diagram shown in Figure 6.1. (b) False colour representation of the specimen, where red, green and blue denote quantities of Ti, Ni and Sn, repspectively. (c) A ternary phase diagram, where all quantification results are represented as points, labelled by colour according to chemical phase as identified by machine learning. The key identifies the phase each colour represents. (d) Another false-colour representation of the region probed by EELS. Here, the same colouring is used as in (c) to identify where within the specimen each chemical phase is located.

accordingly. In addition to the hH and fH populations, other phases are also present in the diagram, one of which is a notable concentration of near-pure nickel, which is present due to the elemental nickel capping layer atop the islands. A false-colour RGB image of the specimen in Fig.6.3(b) helps to visualise chemical variations throughout the specimen, with red, green and blue channels in the image corresponding to Ti, Ni and Sn respectively. In the image, hH regions appear grey-ish in colour, while fH regions, which are richer in Ni, appear green. The bright green top layer of the islands belongs to the Ni capping layer. Other regions, which appear slightly red or blue, identify titanium or tin enrichment, respectively, which can also be seen in the phase distribution in Fig.6.3(a), extending out from the hH population.

To aid the identification of the chemical phases present, clustering algorithms can facilitate classification of distinct populations by chemical composition. Spectral clustering is a method of cluster analysis with roots in graph theory, where a similarity matrix is computed from the data and cluster analysis is performed on the eigenvectors (the spectrum) of this matrix, typically by k-means clustering [341]. To perform cluster analysis on elemental quantities in this chapter, an implementation of spectral clustering in the Python module Scikit-Learn is used (`sklearn.cluster.SpectralClustering`) [342], taking advantage

of the '`discretize`' option which, instead of k-means clustering, implements a multiclass spectral clustering method which has the advantage of insensitivity to initialisation conditions [343]. Relative percentage quantities of Ti, Ni and Sn are used as inputs for the clustering algorithm. Clusters are calculated based on compositions calculated from all spectrum images in the annealing sequence, however data-points which returned poorly conditioned percentage quantities (values beyond the range 0 - 100) were excluded from the model, effectively eliminating contributions from the substrate and FIB protective Pt layer. The number of clusters, which has to be manually defined, was set at 7 clusters as this was found to give a reasonable classification of the phases present.

The outcomes of using spectral clustering on the EELS elemental quantification results are presented in Fig.6.3(c-d). The ternary phase diagram in Fig.6.3(c) shows all classified data-points from the initial spectrum image (the as-grown film/room temperature dataset), with the colour of each data-point denoting the cluster to which it belongs. Comparing the ternary diagram representation to the false-colour image in Fig.6.3(d) makes an identification of the compositions of different clusters straightforward. First, blue and purple in the diagram are attributed to the fH and hH phases, and the pink-labelled cluster identifies the nickel capping layer. Between these populations in the phase diagram there is an 'intermediate-Heusler' phase labelled in brown which represents Heusler regions with a nickel concentration between the fH and hH phases; i.e. a composition of $TiNi_{1+x}Sn$. Spatially, this phase is found at the boundaries between the fH and hH grains in each island, suggesting there is no sharp boundary between the two phases and the composition transitions between hH and fH over several nanometres. The green-labelled cluster, which is deficient in Ti and rich in Ni and Sn compared to the hH phase, is attributed to binary nickel stannide inclusions, with a mean composition tending toward to Ni_3Sn_4. Titanium-rich compositions are labelled by red and orange in the phase diagram and are predominantly found at the interface between the substrate and the Heusler film. Drawing on the analysis made in Chapter 5, the differentiation between the two clusters is interpreted as follows. The orange cluster corresponds to the partially-oxidised, titanium-rich interfacial wetting layer at the substrate, while also appearing to mark the locations of some TiO nanoinclusions within the islands. The red cluster, which is only present immediately below the the Ti layer at the interface, marks the Ti implantation in the MgO substrate beyond the interfacial layer and generally indicates impurity-level concentrations of Ti.

Given the established benefit of forming TiNiSn as a nano-composite alloy, this chapter

seeks to address the practicality of this approach to enhancing thermoelectric performance. In context of the application of these materials in a thermoelectric generator, nano-inclusions in TiNiSn need to be resilient to high temperatures of up to ~1000 - 1100 K. *In situ* TEM presents an opportunity to chart the thermal evolution of nanostructured Heuslers and the thermal annealing of the thin film presented in this section is discussed hereafter.

6.2 *In situ* annealing of the nano-segregated TiNiSn thin film

6.2.1 Experimental

An *in situ* annealing experiment was carried out on the specimen described in the previous section to investigate the thermal evolution of nano-composite TiNiSn. Observations by STEM annular dark field imaging and STEM-EELS spectrum imaging facilitated the investigation by providing compositional 'snapshots' with nanoscale spatial resolution. Annealing was performed in a sequential progression of increasing temperatures, heating the specimen to temperatures from 673 K to 1223 K in steps of 50 K. Heating *in situ* during STEM observation was enabled through the use of a DENS Solutions Wildfire heating chip/TEM specimen holder and controller [145]. For each stage in the annealing sequence, the specimen was heated from room temperature to the target temperature at a rate of 100 K per minute. The target temperature was maintained for 5 minutes before cooling the specimen to room temperature, also at a rate of 100 K per minute. After each 5 minute annealing cycle, both a STEM-HAADF survey image and a STEM-EELS spectrum image were recorded. Taking spectroscopic measurements at room temperature effectively quenched any thermally-actived processes, ensuring the nature of the specimen remained unchanged during the measurement period. Performing all measurements at room temperature also circumvented the need to repeatedly refocus/realign the microscope to compensate for specimen drift.

To analyse EELS data, elemental quantification was carried out following the methods set out in Chapter 4, recovering maps of absolute chemical quantities throughout the specimen. Data treatment in preparation for elemental quantification was performed in DigitalMicrograph; fitting and all subsequent processing was carried out in Python. To compensate for small spatial differences in the region surveyed by EELS after each heating stage, the accompanying STEM-HAADF images are used for spatial registration and alignment of data throughout the sequence, aligning and cropping datasets to ensure they cover the same region

of the specimen. Absolute elemental quantities can be converted into percentage compositions and these are used to populate the ternary Ti-Ni-Sn phase space for representations identical to Fig.6.3(a). From the percentage compositions, phase classification is achieved using spectral clustering as outlined in Section 6.1.

6.2.2 Results

In Figure 6.4, a sequence of STEM-HAADF images are presented, starting with the as-grown thin film in Fig.6.4(a) and providing snapshots of the specimen after each cycle up to a temperature of 1223 K in Fig.6.4(l). Throughout the series, contrast arising from different chemical phases which were present at the beginning gradually disappears before 1023 K (Fig.6.4(h)). Above 1000 K, the evolution of the specimen continues apace with the introduction of much greater variations in contrast, indicating the emergence of different chemical phases. This

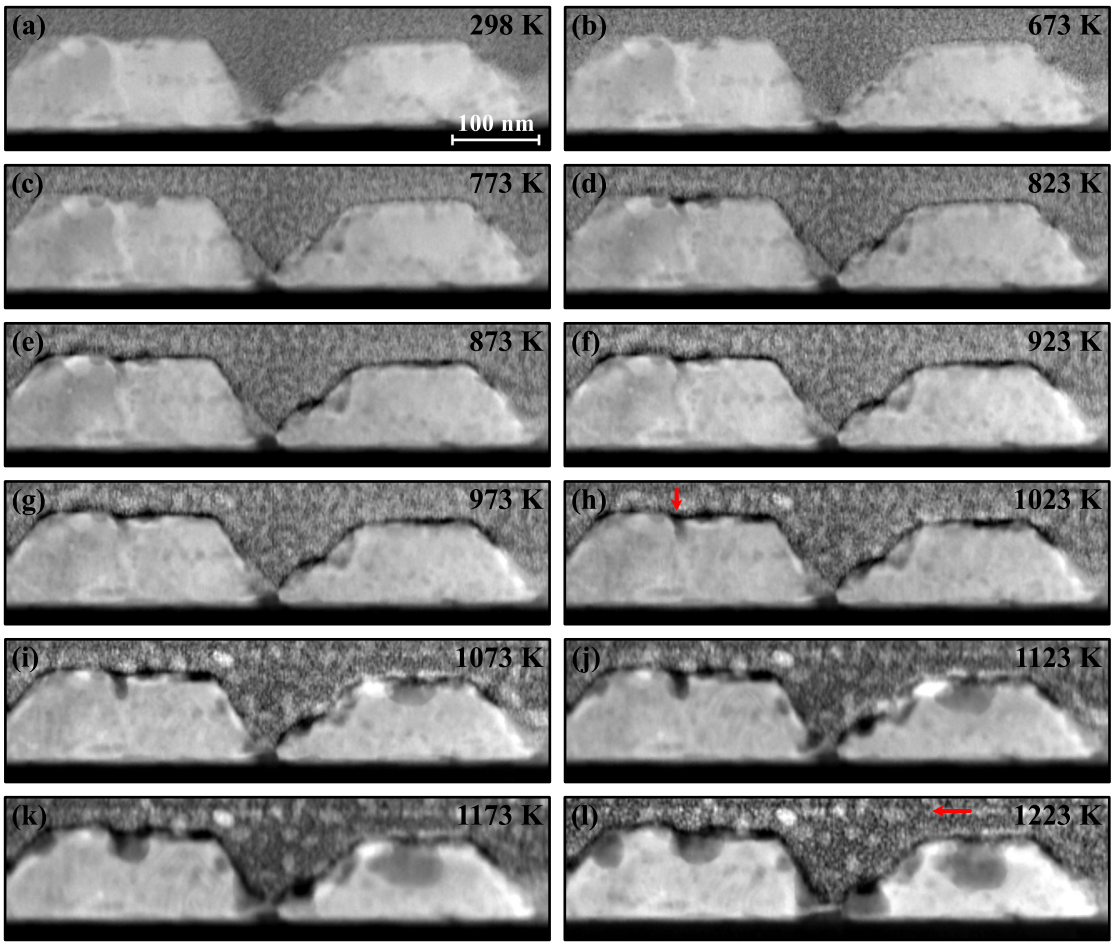

Figure 6.4: STEM-HAADF images recorded after each cycle in the annealing series. Annealing temperatures are annotated in the top-right corner of each image. All images are presented with the same scale as (a). Arrows in (h) and (l) point to potential void formation, and indications of carbonaceous contamination, respectively.

would be driven by the thermal increases in atomic mobility to promote bulk diffusion and greater intermixing of the phases present. Such changes at high temperatures may be driven by features such as that indicated by the red arrow in Fig.6.4(h). Here, at the top of the left island, a dark region of low HAADF intensity forms and then expands at higher temperatures, marking mass loss leading to the formation of a void within the island. The redistribution of material here and also from a similar site in the right-hand island will be examined in greater detail within the context of EELS results.

Although there is no immediate evidence for electron beam-induced damage, note that recording a STEM-EELS spectrum image of the same area a dozen times still has an influence on the specimen. In Fig.6.4(l), a red arrow points along the upper edge of the region probed by STEM-EELS. Increased contrast along this line emerges late in the annealing series and is typical of deposition of carbon by the electron beam as it is scanned, a result of migration and cracking of hydrocarbon contamination on the TEM specimen.

Further to the observation of HAADF contrast from carbonaceous contamination, there is a clear change in texture of the e-beam deposited platinum from the FIB preparation of the cross-section. The coarsening with increasing annealing temperature to produce a more granular layer is a result of the separation of the Pt/C mixture to form Pt nanocrystals which are present as the bright grains in the later images of the series in Fig.6.4(h-l) [344, 345]. This isn't perceived to impact the Heusler islands in this instance. As the analysis is continued, the potential permeability of the Pt layer should be considered. Ideally, the region covered by the spectrum images should be representative of the thin film. As diffusion rates increase, the influence of material beyond the surveyed area may become harder to ignore. Unfortunately, very little of the Pt layer was included in the SI. Given the new understanding of diffusion in these specimens, the Pt layer should be considered a part of the specimen in similar, future experiments.

Turning to analysis of STEM-EELS data, results of elemental quantification throughout the annealing series are presented in Figure 6.5. These false-colour RGB maps – where red, green and blue represent Ti, Ni and Sn, respectively – aid visualisation of the thermal diffusion of different elements within the specimen as the annealing temperature is increased. The first significant modification of the specimen was the disappearance of the Ni capping layer. This layer, which appears as the intense green in the false colour images in Fig.6.5(a-e), was no longer discernible in the EELS maps above 900 K. The Ni cap does not appear to modify

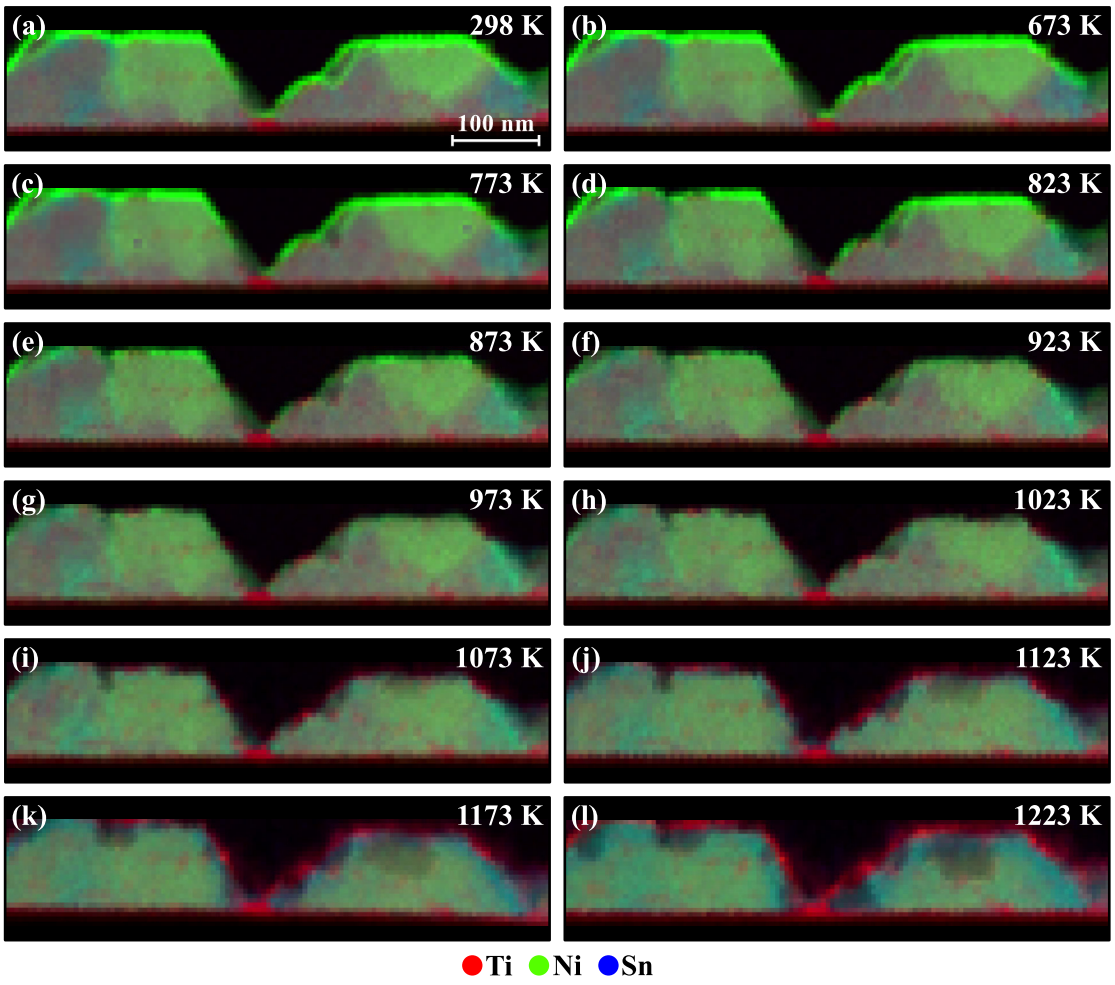

Figure 6.5: False-colour RGB images showing the results of elemental quantification of EELS data. Red, green and blue denote the presence of Ti, Ni and Sn, respectively. The intensity scaling in the images are consistent across the whole series.

the Ni content of the Heusler islands in this temperature range and is presumed to diffuse beyond the scope of the spectrum images out through the Pt layer instead. At higher temperatures a gradual redistribution of the Ni content between the fH and hH regions of the specimen is activated such that, by 1123 K, the Ni distribution is visually homogeneous throughout. Additionally at 1123 K, the extrusion of titanium to form a titanium-rich outer layer is observed, forming a red outline at the top surface in Fig.6.5(j). Signal in the oxygen map at this temperature (not shown) which is coincident in location suggests that the formation of the Ti overlayer is driven by preferential oxidation of titanium. This is followed at temperatures above 1170 K by the apparent extrusion of tin to form a Sn-rich band immediately below the newly-formed Ti overlayer.

In this section the broader details of the *in situ* annealing experiment have been outlined, including a first presentation of the results. In the next section, experimental results will be discussed in greater depth along with ramifications for practical applications of Heusler

materials in thermoelectric devices.

6.3 Discussion

6.3.1 Influence of annealing on the overall phase distribution

Phase diagrams selected from throughout the annealing series are presented in Figure 6.6. These ternary diagrams have been selected to emphasise changes in the phase distribution throughout the annealing series. At the lower annealing temperatures, the dispersal of the Ni capping layer is clear, as intensity at the upper (Ni-rich) corner of the distribution disappears. In this same temperature range, there is also a change in the exact nature of the nickel stannide phases present in the specimen. The stannide region of the phase distribution – marked by the green circle in Fig.6.6(a) – shifts to greater Ni content, potentially indicating the transformation of the Ni_3Sn_4 phase into other intermediate phases. This would be consistent with observations from *in situ* neutron powder diffraction (NPD) experiments where, above 763 K, Ni_3Sn_4 transformed into other nickel stannide phases with the incorporation of more nickel [338]. Thus, the change of state of Ni_3Sn_4 may indicate partial integration of Ni from the capping layer into the stannide regions exposed to the top surface of the film. Although the Ni cap might be influencing these binary alloys, there is no evidence that the fH and hH populations are modified throughout the same temperature range.

Above 1000 K, mobility of nickel extends to the Ni content of the Heusler phases. At 1023 K, which is shown in Fig.6.6(d), the fH and hH populations have begun to change in Ni concentration and there is less distinction between the two populations at this temperature. The shift in Ni content of these phases resulted in the eventual merging of the two phases populations to form a single phase with a mean composition of $TiNi_{1.5}Sn$ by 1123 K, shown in Fig.6.6(e). The observation of this composition is highly interesting because it contradicts current wisdom regarding limitations to the solubility of excess Ni in the hH, which is discussed further in Section 6.3.3. Due to the strong tendency of the hH to segregate in the presence of Ni excesses [84, 85], we attribute the existence of this intermediate phase to the behaviour of sub-stoichiometric full-Heuslers, where off-stoichometries can be stabilised through a repulsive interaction between Ni-vacancies which prevent clustering [346]. The migration of Ni in the Heusler phases indicates increased atomic mobility commensurate with the annealing temperatures above which the half-Heusler phase forms; observed to occur

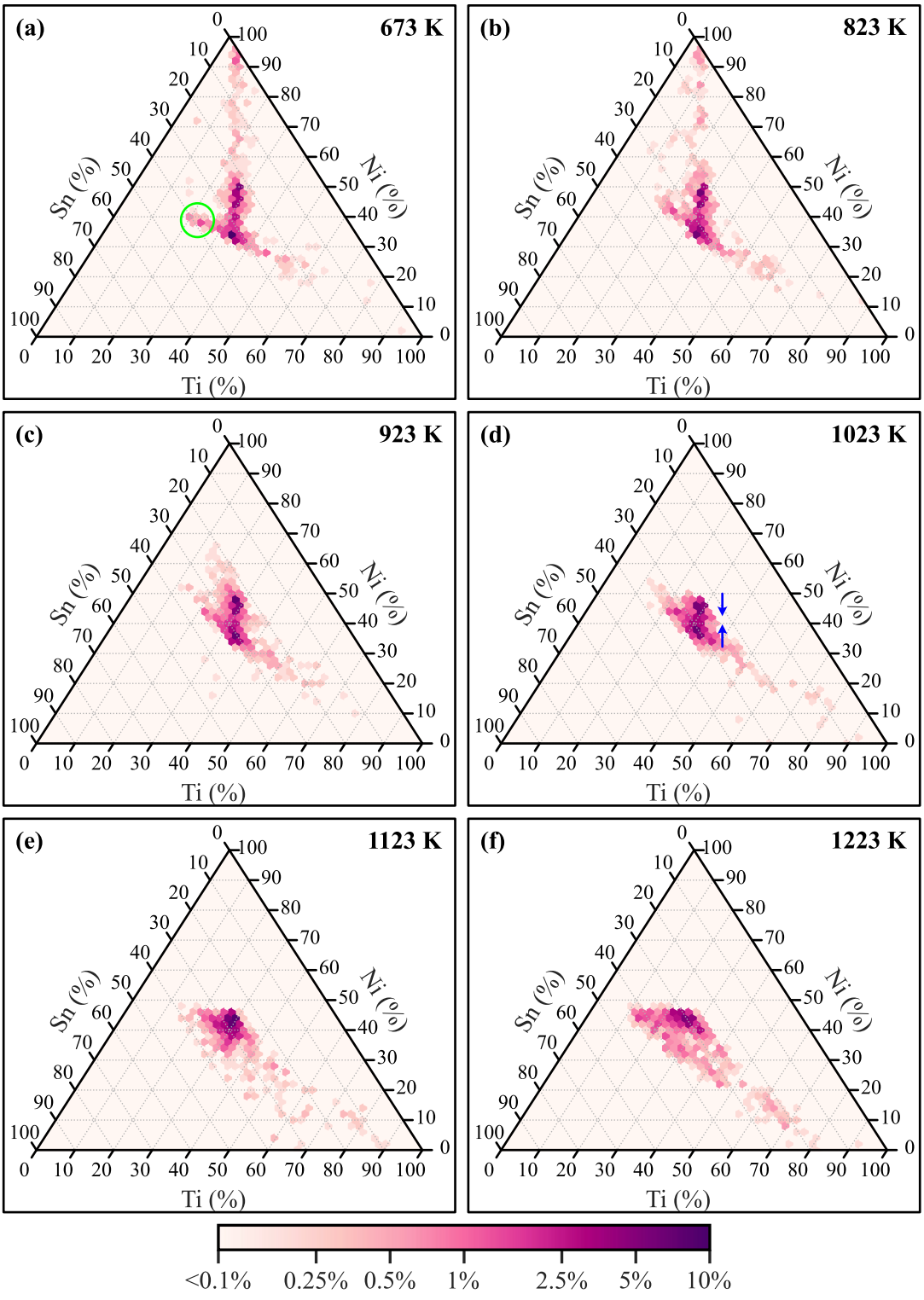

Figure 6.6: Selected distributions of measured compositions throughout the Ti-Ni-Sn phase-space during the annealing series. (a) the distribution after the first annealing cycle (673 K). (b-f) phase distributions after annealing at higher temperatures as annotated, concluding with (f) the final and highest temperature in the series (1223 K). Scale bar indicates percentage of spectrum image accounted for by compositions within a 2% wide bin. Annotations are described in the main text.

above 1013 K by NPD [338]. From 1100 K, extrusion of titanium from the Heusler matrix becomes evident in the false-colour maps in Figure 6.5 as the formation of an overlayer in red. In the phase diagrams in Fig.6.6(e-f), this manifests as a cluster of points which tend toward the bottom-right, Ti-rich corner of the phase-space. Points which cluster toward the Ti-rich corner are found not to represent pure, elemental Ti and should be interpreted instead as the absence of Ni and Sn. Comparisons of the elemental maps show coincident signal for Ti and O at the island surface, indicating at partially oxidised Ti overlayer of approximately $TiO_{0.5}$. The extrusion of titanium, which signals the decomposition of the Heusler phase, is also accompanied by transformation of some of the Heusler content into binary nickel stannides, as indicated by the shift of the phase distribution to left-of-centre in Fig.6.6(f).

The spectral clustering algorithm used to identify different chemical phases from the elemental quantification results in Section 6.1 was also used to classify the compositions throughout the entire annealing series. In applying the phase classification to the full dataset, the relative abundance of each chemical phase can be determined for each temperature. The percentage breakdown of each phase in the composite throughout the experiment is shown in Figure 6.7. At the start of the experiment, the dominant phases are the fH and hH phases, which account for approximately 50 % of the specimen. The Ni capping layer and Ti interface layer each account for approximately 15 % of the film. In this plot, thermally-driven decomposition or formation of different phases is recognisable by changes in the height occupied

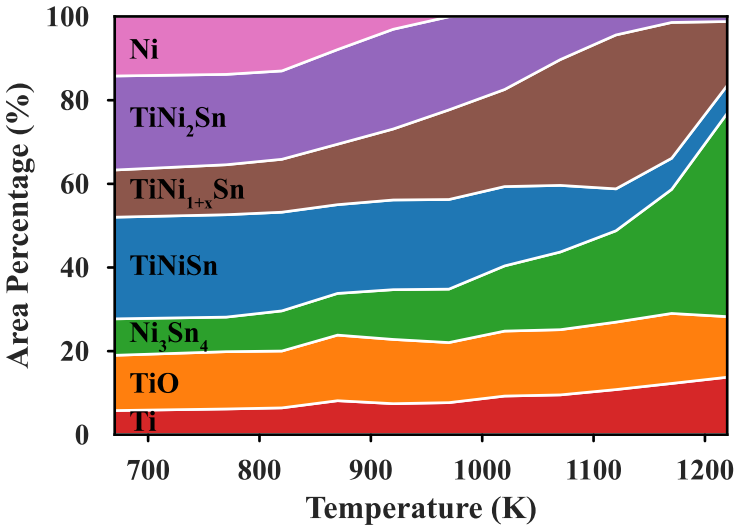

Figure 6.7: Stack-plot which illustrates the relative area of the TEM specimen occupied by each composition. Compositions are assigned by spectral clustering, with steps in the annealing series spread along the x-axis to show variations with annealing temperature. Results shown cover the temperature range 670 K to 1220 K. Results for the as-grown film are not shown as there is no material difference between these and the results for 673 K.

by each chemical phase. Transformations occur above 800 K, starting with the disappearance of the Ni capping layer. This is followed by reduction of both fH and hH in favour of an intermediate Heusler phase then the decomposition of the Heusler, which diminishes at the expense of nickel stannides. The titanium extrusion that provided an easily recognisable indicator of the decomposition of the Heusler in Figure 6.5 only results in a minor increase in the combined percentage content of Ti impurities and TiO. In terms of interpreting these results for thermal stability, changes which aren't directly related to the disappearance of the Ni capping layer only occur above 1000 K, indicating that nanostructured TiNiSn thermoelectrics would be suitable for use in industrial furnaces up to temperatures of approx. 950 K and is a considerable safety margin from the optimal conditions for thermoelectric efficiency zT, which typically peaks at 800 K or lower [67, 338, 339]. It is worth noting, however, that these results only cover a relatively short annealing period and further study of these materials at operating temperatures for a more prolonged period would be of great interest.

6.3.2 Addressing the loss of Ni from the specimen during the experiment

As well as tracking spatial changes in nanoscale features in the specimen, the total quantities of Ti, Ni and Sn in the spectrum image region can be monitored throughout the experiment. These measurements are presented in Figure 6.8 and show the absolute quantity of Ti and Sn to be roughly constant throughout the annealing series, while the quantity of Ni gradually decreases. The consistent quantity of Ti and Sn throughout the series, despite the extrusion

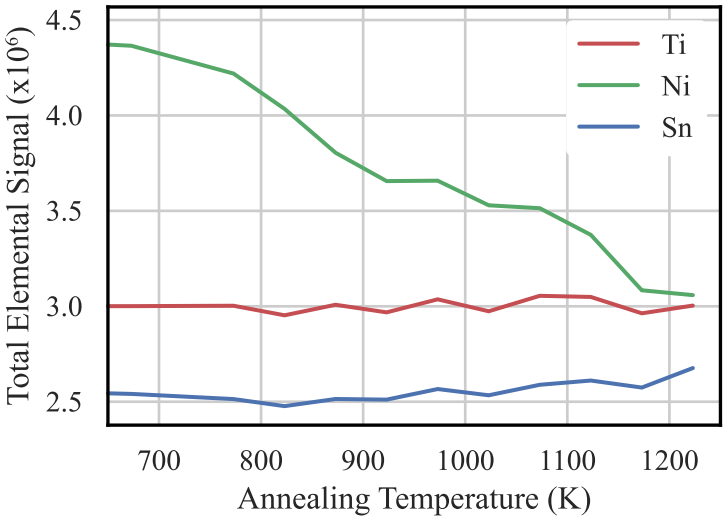

Figure 6.8: Total quantities of Ti, Ni, Sn within spectrum image at each temperature. Shows consistent amounts of Ti and Sn throughout, but the quantity of Ni starts high and decreases significantly.

of both of these elements observed at the highest temperatures, suggests that the region of the thin film surveyed in STEM-EELS is sufficiently representative of the specimen at large. If an insufficient area of the thin film was studied, the total quantity of Ti and Sn might be subject to variations throughout the series, as diffusion dynamics beyond the scope of the spectrum image influence the properties in the field of view. There is approximately 15 % more Ti than Sn across the spectrum image. The difference between these quantities is accounted for by the Ti-rich nanolayer at the substrate interface present in the as-grown film.

To address the loss of nickel shown in Figure 6.8, the quantitative Ni maps are studied in greater detail. Figure 6.9 shows Ni maps taken from the first half of the annealing series. The maps in Fig.6.9(a-b) are from data recorded after the 673 K and 923 K annealing cycles, respectively. By 923 K, the Ni capping layer has disappeared completely. Line traces through the full and half-Heusler sections of the left island are shown in Fig.6.9(c) for temperatures

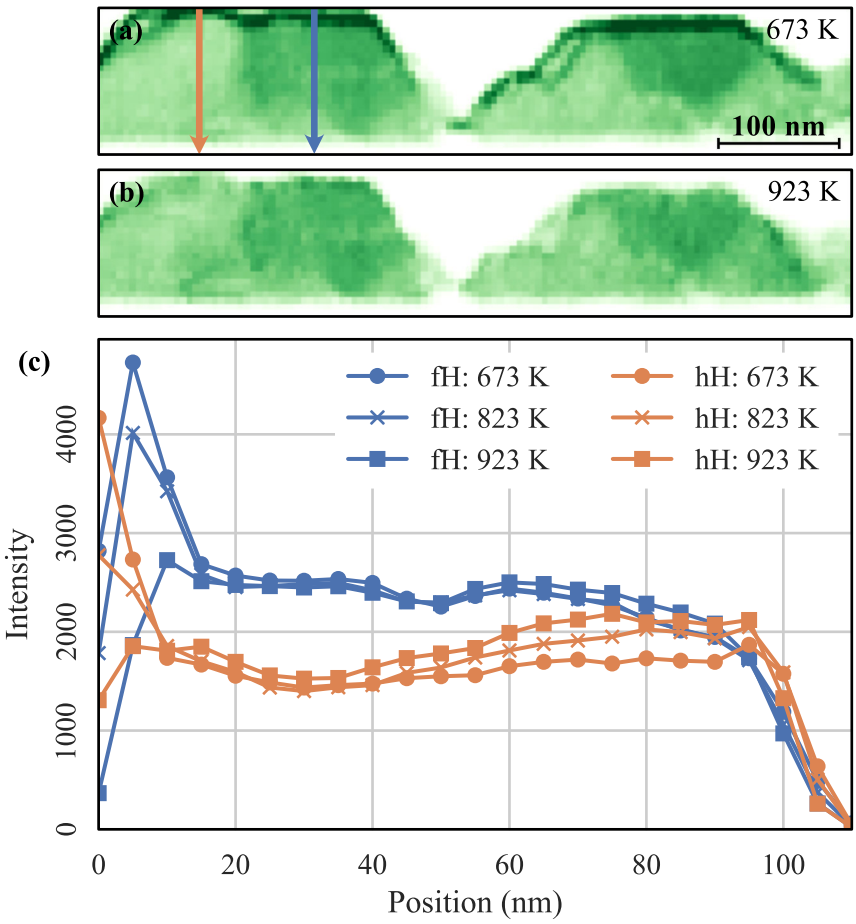

Figure 6.9: Nickel quantification maps for (a) 673 K and (b) 923 K. Between these two temperatures, the Ni capping layer disperses completely and the dark green top layer indicating this pure Ni layer has disappeared. The character of the Heusler islands appears to have not otherwise changed significantly. (c) Line profiles taken from the 673 K, 823 K and 923 K stages of the annealing series along the cuts shown by the arrows in (a).

of 673 K, 823 K and 923 K. For both sets of line plots, the Ni cap is on the left and the substrate on the right. For the fH line traces, the only substantive difference is the presence of the Ni capping layer; no material difference is made to the Ni concentration throughout this section of the film. The unchanged nature of the fH portion of the film suggests no diffusion of Ni from the capping layer into these regions of the film. Some enhancement of the Ni concentration was observed in the hH segment, however this only occurs toward the substrate side of the film while the Ni content near the top surface of the film is unchanged. This suggests that the increase in Ni content here is not due to the capping layer, as this would affect the uppermost region of the film first. The changes to the Ni profile for the hH segment must therefore have a different origin, as attributing this to the capping layer would be inconsistent with Fick's laws of diffusion [347]. In the absence of any clear permeation of Ni from the capping layer into the Heusler islands, we surmise that the Ni capping layer must completely or near-completely diffuse outward into the FIB-deposited platinum. Such dispersal of the capping layer beyond the scope of the spectrum images would thus explain the Ni loss observed in Figure 6.8 up to 923 K.

Throughout the second half of the experiment, the total Ni content, shown in Figure 6.8, continues to decrease although the capping layer has fully dispersed. Above 1000 K, the loss of Ni appears to be tied to the void formation/general loss of material commented on earlier. The decrease in intensity at certain sites observed in the HAADF images, such as that marked in Fig.6.4(h), is complemented in the elemental quantification by an overall reduction in the amount of material present. The localised loss of material manifests in the false-colour maps in Fig.6.5(h-l) as an overall darkening of contrast. This gives credence to the hypothesis of void formation within the specimen, rather than possible chemical variations which would not only lead to changes in HAADF Z-contrast, but also changes in hue in the false-colour maps. Looking at the spectral clustering map for 673 K in Fig.6.10(a), the location of a void formation site previously marked in Fig.6.4(h) is also marked here and occurs at a binary alloy interface layer, denoted by the green sliver at the white arrow. The link between void formation at high temperatures and the locations of Ni_3Sn_4 inclusions can be attributed to the low melting point of 1071 K for this phase [66]. The molten Ni_3Sn_4 present in the final 4 cycles of the annealing series, from 1073 K and above, could be lost by rapid diffusion through the FIB platinum above. Alternately, the vapour pressure of the liquid stannide phase may have resulted in the evaporation of material into vacuum from the surfaces of the TEM cross-section. However, examining the phase diagram in Fig.6.1, one would expect direct evaporation of Sn before Ni, which points to other origins for the loss of Ni; perhaps via

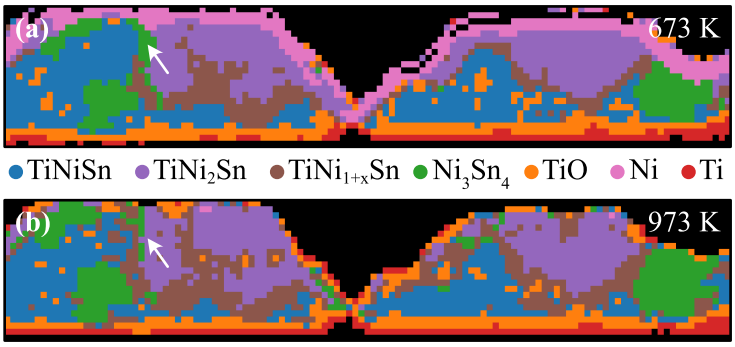

Figure 6.10: Representations of the specimen where chemical phases are colour-coded according to the key below (a). The maps correspond to annealing temperatures of (a) 673 K and (b) 973 K. The white arrow in (a) denotes the Ni_3Sn_4 region which is coincident with the void formation site annotated in Fig.6.4(h). At the same position in (b), the stannide region at the white arrow is significantly diminished.

thermally-assisted beam damage ejecting Ni from the specimen into vacuum. Diffusion of material in the Ni-Sn binary system can be activated at relatively low temperatures, with formation of Ni_3Sn_4 reported at temperatures as low as 453 K [348]. In support of this, Fig.6.10(b) shows the chemical phase map for 973 K and there is evidence that elemental diffusion leads to some spatial redistribution of the stannide phase. Changes in the Ni content along the line profile could therefore arise from redistribution of the Ni content within the stannide regions at temperatures below 923 K.

6.3.3 Nickel mobility between Heusler phases

Although in the early stages of the annealing series, very little change was observed in the Heusler phases, significant changes throughout the specimen were observed to occur at the higher temperatures in the series. Modification of the Heusler regions in the thin film was observed to occur above 1000 K and primarily manifests as redistribution of the nickel content of the islands. The increasing Ni concentration in the hH regions and decreasing Ni concentrations in the fH regions are illustrated in Figure 6.11, which shows a line profile of Ni occupancy through one of the Heusler islands at different temperatures. The occupancy is calculated as the ratio of Ni content versus the measured Ti/Sn content such that, at $x = 0$, all elements are present in equal amounts. The line profiles in Fig.6.11(b), which are taken along the arrow shown on the map in Fig.6.11(a), show two regions which are initially well-defined and identifiable as hH and fH. At the higher temperatures the distinction between fH and hH blurs and the Ni occupations tend toward an intermediate value which was previously identified as a mean composition of $TiNi_{1.5}Sn$ at 1123 K, as shown in Figure 6.6. By the end of the

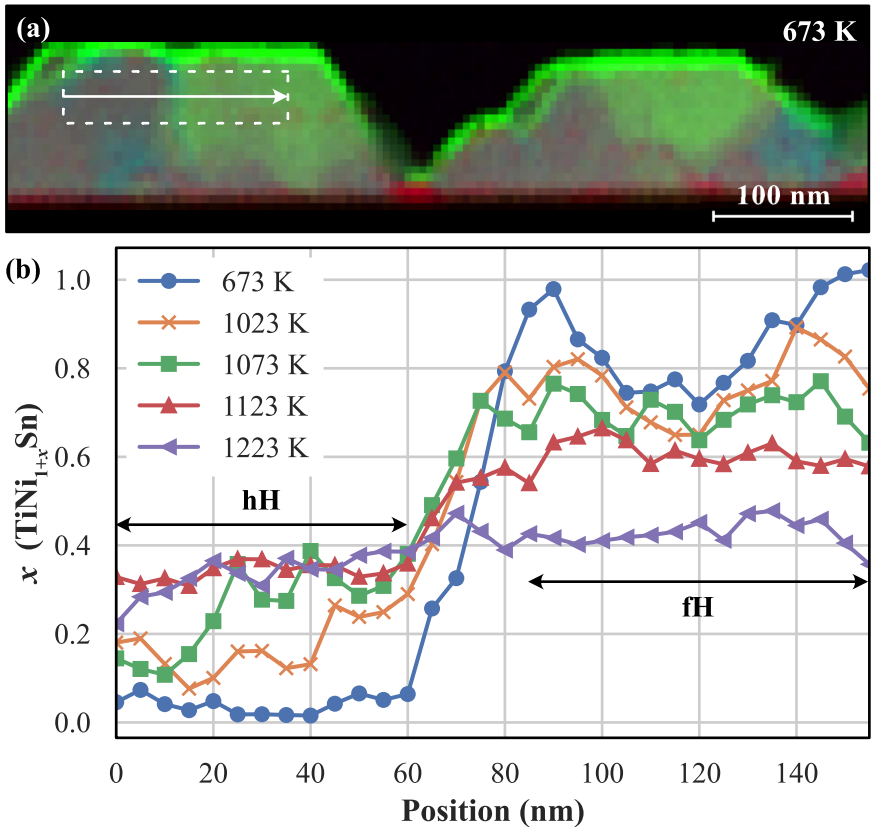

Figure 6.11: False-colour elemental map for 673 K, where Ti, Ni and Sn are coded by red, green and blue, as in previous figures. (b) Heusler Ni occupation levels measured across the region shown by the white arrow and outline in (a). Line profiles represent the occupancies after annealing at the specified temperatures.

annealing series, the occupancy has completely homogenised between the two regions, with $x = 0.4$. However, the absolute Ni content along the line profile is uniform from 1123 K and does not change significantly in the remainder of the series. This suggests that the apparent change in occupation level is driven by diffusion of Ti and Sn, instead.

The final Ni occupancy of $x = 0.4$, as remarked upon earlier, is of special interest as it is inconsistent with current understanding of solubility limits for excess Ni in TiNiSn. The Ni solubility limit, which indicates the level where incorporation of excess Ni results in segregation to form both hH and fH phases, is typically understood to be quite low. The highest soluble Ni concentration is found to be ~8 % (i.e. $x = 0.08$), however there is some variability between reports [66, 67] and even contention with theoretical calculations, which indicate a much smaller limit of 1 % [101]. Although the tension between experimental and theoretical results highlights the potential to overcome thermodynamic limitations on Ni solubility, the intermediate phase found here represents a composition never before observed in bulk materials. This points to two key differences between this and experiments on bulk materials, one or both of which may be responsible. The first possible source is thin foil effects;

that annealing of an ultra-thin TEM specimen, where the material is mostly confined to two spatial dimensions, leads to different pathways for modification which cannot be accessed in bulk materials, highlighting potential dangers in drawing comparisons between TEM experiments and the properties of bulk materials. Second, it is possible the small size of the islands leads to a nanoscale confinement effect which would not be observed in bulk materials. As the TiO which eventually envelops each island acts to passivate the interfaces with the film and provide an impermeable barrier, the competing ordering mechanisms must be resolved within each island separately. The observed behaviour might then be a natural consequence of the competition between the attractive interaction between Ni interstitials [349] and a repulsive Ni vacancy interaction [346] when confined to these lengthscales. Clearly, further investigation will be required in future to pinpoint the origin of this unusual phase.

To learn more about the mobility of nickel between the different Heusler phases and the energetics of diffusion behind the observed mobility, the redistribution of Ni within the specimen was modelled. Changes in the concentration profile as the annealing progresses are described by Fick's second law, which concerns non-steady-state diffusion. The law describes the relationship between the rate of change of concentration (c) in both time (t) and position (x);

$$\frac{\partial c}{\partial t} = D\frac{\partial^2 c}{\partial x^2} \ , \tag{6.1}$$

where D is the diffusion coefficient which describes the temperature-dependent rate of diffusion [350]. To treat the migration of Ni in the Heusler thin film in the framework of Fick's law, approximating the problem as a 1-dimensional hH/fH junction where the boundary between the two phases is initially well-defined yields a simple solution to Equation 6.1 which describes the concentration profile after some time, t, as

$$\frac{c_x - c_h}{c_f - c_h} = 1 - \mathrm{erf}\left(\frac{x}{2\sqrt{Dt}}\right) \ , \tag{6.2}$$

where c_x here represents the quantity of Ni at a distance x from the fH/hH boundary, c_f is the original concentration of Ni in the fH region and c_h is the original concentration of Ni in the hH region. These terms, which define a relative change in the concentration profile at position x, are related to the diffusivity, D, and the annealing time t by the gaussian error function (erf) [347]. As the duration of each annealing cycle is known (300 s), and the distance x can be determined from the STEM image calibration, the diffusivity of Ni between the fH and hH can be calculated for most of the temperatures in the annealing series.

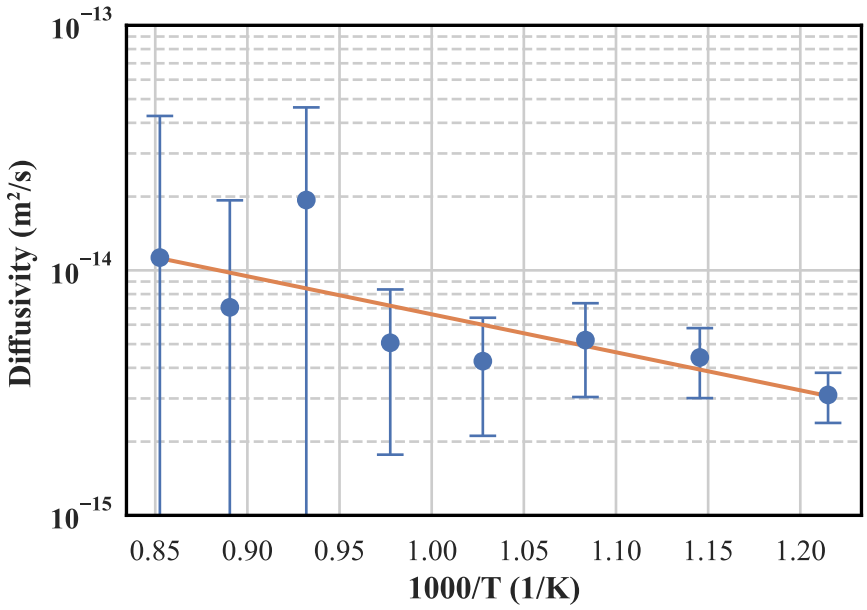

Figure 6.12: Arrhenius plot of Ni diffusivity as an inverse function of temperature. Data points represent the diffusion coefficients calculated for temperatures from 773 K to 1173 K. The line of best-fit, shown in orange, is used to determine the activation energy for diffusion between the fH and hH regions.

The results of calculating the temperature-dependent diffusion rates, using Equation 6.2, are illustrated in an Arrhenius plot shown in Figure 6.12. The presented diffusivities are calculated based on data in the region identified in Figure 6.11, which is taken to be closest in representation to the model solution in Equation 6.2. To make the calculation at the n^{th} temperature in the annealing series, the Ni concentrations found away from the hH/fH interface in the n-1^{th} Ni quantification map are used as the original concentrations, providing the values c_f and c_h. A point was chosen within the hH region which was 50 nm from the boundary to provide the value of c_x. In the figure, the diffusion coefficients are plotted on a logarithmic scale against reciprocal temperature $(1/T)$. In this representation, linear relationships indicate an Arrhenius-type temperature dependence of the diffusion coefficient [350], i.e.

$$D \propto \exp\left(-\frac{E_a}{k_B T}\right) , \tag{6.3}$$

where E_a is the activation energy for diffusion and k_B the Boltzmann constant. The linear trend shown in Fig.6.12 is the line of best fit between the values of $\ln(D)$ and $1/T$, such that the gradient of the slope represents the value E_a/k_B. Consequently, the activation energy for Ni diffusion in this situation is determined to be 0.3 ± 0.1 eV/atom.

Theoretical studies in the literature can help provide insight into why diffusion is observed at certain temperatures and what the calculated activation energy reveals about the diffu-

sion mechanism. First, enthalpies of formation of TiNiSn and $TiNi_2Sn$ are -0.715 eV and -0.622 eV, respectively [66]. The gap between these energies (0.093 eV) can be spanned by thermal excitations corresponding to a temperature of ~1070 K. This may explain why observation of Ni diffusion is clear in the upper temperatures of the annealing series.

The mechanism for diffusion of Ni in this situation would appear to be connected to the freedom to adjust the ordering of Ni atoms in the Heusler unit cell. Theoretical studies by Kirievsky *et al.* [108] explore all the possible ordering configurations of Ni and Ni vacancies on the tetrahedral sites of the TiNiSn hH and fH unit cell. The largest difference in energy of formation of any of the identified configurations was ~0.3 eV [108]. Similarly, other studies which explore the role of Ni interstitials in the hH calculate a binding energy of 0.33 eV/atom for a Ni interstitial [349, 351] while the energy required to add a single Ni atom to a vacant tetrahedral site in the hH is reported as being 0.19 eV/atom [351]. This suggests that the value of 0.3 eV/atom calculated here as the activation energy for Ni diffusion is connected to the energy required to release a nickel interstitial in the hH or, equivalently, the energetic freedom to redistribute the Ni into any configuration of tetrahedral site occupation. If all orderings of the Ni sub-lattice are energetically available, then there is also no distinction between Ni atoms in one unit cell versus another, so swapping of Ni atoms and vacancies between unit cells leads to the diffusion which has been observed between fH and hH. As the activation energy for diffusion is comparable with the energy required to mobilise a Ni interstitial, and greater than the energy required to implant a Ni interstitial into the hH structure, the diffusivity in this situation is driven by the properties of the fH phase. This conclusion is consistent with the purported greater stability of the full-Heusler phase and indicates that the liberation of Ni from the fH is the rate-limiting factor.

6.4 Conclusions

In this chapter, the use of *in situ* heating in conjunction with STEM imaging and STEM-EELS spectrum imaging has been demonstrated for use as a tool to probe chemical diffusion in TiNiSn Heusler thin films. Elemental quantification using methods presented in Chapter 4 provides useful snapshots of the elemental make-up of a nano-composite TiNiSn thin film after increasingly severe heat treatments. The information which can be extracted from such experiments is vital to understanding the thermodynamic stability of nanostructural phases within the Heusler material and assess their practical use in applications. The chemical ana-

lysis which has been presented supports the use of nanostructured TiNiSn at moderate temperatures (~500 - 800 K) where the thermoelectric efficiency zT is typically at its best. At higher temperatures, Ni diffusion between fH and hH occurs relatively rapidly across the small lengthscales probed in the experiment, however these observations were limited to temperatures greater than 1000 K and are not anticipated to interfere with practical applications of such materials. The nickel capping layer was effective in preventing interactions between the Heusler film and the Pt protective layer. The Ni cap was also selected to serve a second purpose, which was to assess the receptiveness of the Heusler to excess Ni. However it had dispersed completely before any other Ni mobility was observed in the Heusler regions.

While the study presented here has answered some questions about the evolution of phase-segregated material, there are still outstanding areas of interest to be addressed. Two further *in situ* experiments have been identified to be relevant. The first involves examination of not just chemistry but also the structural evolution of Heusler thin films. This would entail the annealing of an amorphous thin film, obtained by pulsed laser deposition at room temperature. By starting with an amorphous precursor film, this experiment would qualitatively amount to a TEM equivalent of the NPD study referred to earlier [338]. Preliminary attempts of this experiment – where STEM-EELS spectrum imaging was carried out in a similar annealing series to the one shown here – were carried out. However, issues were encountered preventing the amorphous TiNiSn from alloying with surrounding material and further investigation is required to establish a suitable buffer material to suppress external reactions. In the event a suitable buffer is found, STEM-EELS chemical analysis would be complemented by a 4d-STEM technique for structural analysis, such as scanning precession electron diffraction as is explored in Chapter 7.

The second concept for a future *in situ* experiment takes advantage of the improvements brought about by depositing TiNiSn on a vanadium buffer layer. A nanostructured half-Heusler thin film, similar to those analysed in Chapter 5, sandwiched between V contact layers would be held at an operational temperature for a more prolonged period to determine if there is any longer-term degradation of nanoscale features. This experiment would be more pertinent to real-world applications, instead of driving the specimen to temperatures that intentionally lead to the demise of the Heusler. In any *in situ* experiment however, it is important to be cautious in extrapolating observations from TEM cross-sections to processes in bulk materials. This is perfectly embodied by the observations made throughout this chapter, some of which represent reactions that have never been seen in bulk materials. Though no

bulk equivalent exists, the intermediate Heusler compositions observed in PLD-grown thin films still represent an interesting avenue of research, where there are lessons to be learned about solubility of Ni in these alloys.

I could be chasing an untamed ornithoid without cause.

Lt. Cdr. Data

7

STEM correlative nanoanalysis of coherent interfaces in TiNiSn thin films

NANOSTRUCTURING plays a significant role in modifying the properties of thermoelectric materials. As discussed in Chapter 1, phonon scattering by coherent nanostructures can successfully reduce the thermal conductivity of thermoelectric Heusler alloys [84, 109], where increases in scattering result from a combination of the introduction of mass contrast, strain fields and coherency effects [39]. In Chapters 5 and 6, the primary focus of nanoscale characterisation has been the use of STEM-EELS to provide precise information about the chemical composition of specimens using protocols detailed in Chapters 3 and 4. While absolute elemental quantification can be useful to assess compositional variations which can be beneficial to thermoelectric materials, this does not yield information about related modification of the crystal structure which can further influence the phonon properties.

The objective throughout this chapter is to introduce high-resolution, high-precision structural analysis which provides crystallographic information complementary to the nanoscale chemical analysis provided by STEM-EELS and the absolute elemental quantification pro-

tocols outlined in Chapter 4. To achieve this, a novel experimental set-up was used which combines the application of scanning precession electron diffraction (SPED) with pixelated direct electron detector (DED) technology. Throughout the last decade, pixelated detectors, originally developed for particle physics [352], have been adapted for electron imaging and provide superior performance compared to CCD-based devices, boasting higher detection efficiencies, greater radiation hardness and zero readout noise [185, 353]. Combining these advantages with SPED, which can provide high precision strain analysis [189], confers the benefits of both aspects by improving imaging of weak diffraction features and opens opportunities for dose-efficient, high-precision lattice mapping. The exact combination used to produce the data for this chapter involves a Nanomegas Digistar scan/precession control system [354] and a MediPix3 DED [166].

Building on the expertise of the Materials and Condensed Matter Physics (MCMP) group in Glasgow, which has been pivotal in developing the MediPix3 DED for use in TEM and STEM [166, 183, 185], a protocol for analysis of precession diffraction patterns obtained from SPED is described in Section 7.1. The processing methods are well suited to analysis of epitaxial thin film systems and build on existing code developed for processing DED-generated, 4-dimensional-STEM data: the *fpd* Python library [355]. In Section 7.2, the use of the lattice analysis protocol is demonstrated on an epitaxial $TiNi_2Sn$/TiNiSn thin film bilayer system. The results from lattice analysis presented here are then used in Section 7.3, where 'correlative-STEM' analysis is introduced, relating the lattice information from SPED to compositional information extracted from STEM-EELS spectrum imaging. This initial exploration of correlative analysis is discussed for the bilayer specimen, highlighting interesting coherency-strain effects associated with fH/hH interfaces and suggesting approaches to improve the joint spatial resolution of the correlated SPED/EELS datasets.

A significant motivating factor for taking advantage of the new developments in SPED was the potential to relate crystallographic information from SPED investigations with the high-precision chemical analysis which has been developed throughout this thesis in Chapters 3, 4 and 5. Ideally, to minimise the electron dose, SPED and STEM-EELS datasets would be collected simultaneously, in a 'pseudo-5dSTEM' methodology. However, the two methods are mutually exclusive, not only because of significantly different requirements on the microscope alignment for the two techniques, but primarily because the positioning of the MediPix3 DED in the microscope blocks the beam from the the EELS spectrometer. Instead, measurements were recorded sequentially, covering the same region at similar scan resolu-

tions, enabling the information captured at the nanoscale to be correlated between techniques in the electron microscope. With the specific combination of SPED and STEM-EELS envisaged here, the proposed approach leads to nanometre-scale correlation of structural and chemical information, which may shine a light on how modulated chemical doping in thermoelectric materials influences the structural properties which are important to increasing phonon scattering.

Some of the code and methods used in processing 4dSTEM data shown in this chapter have also been presented in co-authored manuscripts which are in press and available as pre-prints at time of writing [356, 357]. The Python code used for characterising the direct beam in Section 7.1.1 was written by Dr Gary Paterson. The protocols described throughout the rest of Section 7.1 and the Python code which implements them were developed in collaboration with Dr Gary Paterson.

7.1 4dSTEM data and structure analysis

The modern TEM user has at their disposal a myriad of techniques with which to investigate the atomic lattice of materials. This could be through direct inspection of diffraction patterns, such as selected area diffraction (SAED), nanobeam diffraction (NBED), convergent-beam diffraction (CBED) or precession diffraction (PED) [187], for instance. Alternately, diffraction contrast in images can also be useful in analysing crystallographic defects and strain with typical approaches including the use of high-resolution TEM (HRTEM) imaging, geometric phase analysis (GPA) [335] and STEM-moiré imaging [337]. Of these techniques, SPED presents the most promising approach to high-precision strain analysis with nanometre-scale spatial resolution, because it eliminates the strong intensity variations within diffracted peaks which can compromise the accuracy of peak-finding [189].

As a 4dSTEM technique, SPED provides individual diffraction patterns for each position in a STEM raster scan. The main challenge in any manner of analysing 4dSTEM data post-acquisition derives from the large size of the raw datasets. The data acquired from fast pixelated detectors, including the SPED datasets used throughout this chapter, can easily be greater in size than the available computer memory. For example, a STEM spatial scan containing $1,000 \times 1,000$ points, recording data from a detector like the MediPix3 which has 256×256 pixels would amount to ~250 GB when recorded as 32-bit integers. For the SPED data presented in this chapter, the scan size is typically much smaller but the more

modest dataset size is typically still on the order of 10 GB or greater, which means the available system memory is still a prevailing issue. To address this, an approach has been adopted which builds on the previous experience of the materials and condensed matter physics group (MCMP) at Glasgow, incorporating processing of SPED data into the pre-existing framework of the *fpd* Python library [355]. The *fpd* package provides code to facilitate analysis and visualisation of data from pixelated DEDs and operates on a principle of 'out-of-core' processing, whereby a dataset is only partially loaded into memory at any one time. This can significantly reduce the memory demands of analysing 4dSTEM data to something much more modest, easing computational constraints while retaining efficiency in processing.

There is no single 'correct' method for extracting lattice information from diffraction patterns. For instance, the software used to analyse individual diffraction patterns in Chapter 5 – CrysTBox – provides a plethora of different options with which to optimise analysis [332]. Commercial solutions dedicated for SPED use a template matching approach, where diffraction data is compared against a large number of computed patterns to find the best match [358]. While this 'top-down' approach is good for characterising polycrystalline materials with varied grain orientations, it can be quite inflexible more generally, requiring significant prior knowledge of the materials involved, and struggles to accurately capture the effects of strain in the lattice.

Though a pre-existing package (CrysTBox [331]) has been used for diffraction pattern analysis in Chapter 5, its design is intended for analysis of single patterns and is not an appropriate tool for the scale of SPED data. Thus, in this chapter, a bespoke, scalable protocol for structural analysis is presented which is well-suited to the epitaxial systems which were studied. The processing method outlined below is a statistical approach where the properties of the lattice described by the diffraction pattern are extracted without assuming any prior knowledge of the materials involved. This 'bottom-up' method provides a framework which starts with a high-precision approach to locating diffraction peaks, which can then be built upon by adding steps to the analysis from which lattice properties can be characterised, knowledge of materials involved introduced, and more advanced data analysis or machine learning applied to the results. The fundamental approach used here to characterising the lattice represented by the diffraction patterns is broken down into three sections. The first (Section 7.1.1) involves characterising the direct beam and creating a reference image of the beam, using the measured features, which will be used as a template for cross-correlation. In Section 7.1.2, the positions of the diffracted peaks are identified with deep-sub-pixel pre-

cision using a combination of edge-filtered cross-correlation with the direct-beam reference and functional peak-fitting. Together, these two sections represent the extension of methods developed by Krajňák and others [183] for pixelated differential phase contrast (DPC) STEM imaging, applying the disc location procedure to all peaks in the diffraction pattern. The third and final stage (Section 7.1.3) involves identifying lattice vectors which describe the relationships between the peaks identified in the previous stage, which can be used to extract crystallographic information about the material, such as strain, in a way that works well for the epitaxial thin films studied throughout this thesis. Although the code for the protocols described here is optimised for the analysis of epitaxial systems, the sections have been implemented in such a way that, if other applications called for it, different processing methods could be inserted or even replace existing sections entirely. An analysis of the precision of the methods described below is provided in Section 7.1.4, characterising the level of sensitivity which can be expected from typical SPED experiments using a DED. The precision levels found here, which already approach the previously reported limits of other techniques, do not necessarily reflect the best that can be achieved with this setup and there is much which has not yet been done in optimising either the acquisition of data or its processing.

7.1.1 Beam characterisation

The first stage of diffraction pattern analysis is to identify and characterise the direct beam in the diffraction pattern. The approach described below is based on the work of Krajňák *et al.* [183], in which the disc of the direct beam is characterised and used to create a template image where the shape of the beam – defined by the edge profile – is the important factor

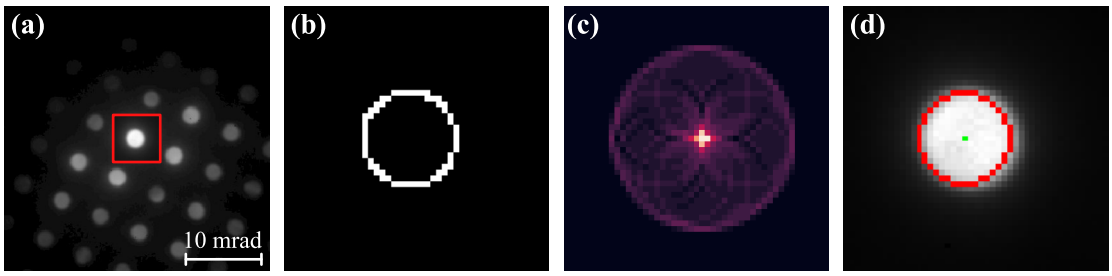

Figure 7.1: Illustration of the procedure for finding the direct beam in (a) a typical precession diffraction pattern from an MgO substrate where the beam is incident along the (001) direction. (b) Canny-edge-filtered image of direct beam in outlined region of (a). (c) Section of the circular-Hough space representation of (b) when an accurate radius is selected, giving a sharp peak. (d) The original image of the direct beam as outlined in (a), but with the circle identified by the CHT marked in red.

in peak-finding by cross-correlation. It is preferable to use the shape of the beam for peak finding rather than the intensity which, even in SPED patterns, can be subject to intensity variations that can compromise accuracy because excitation errors can lead to intensity maxima which are not at the peak centre [189]. The steps needed to find the position and size of the direct beam are illustrated in Figure 7.1. The original image containing the diffraction pattern in Fig.7.1(a) was processed with a Canny edge detection algorithm [359] to produce an image of the edges, as shown for the direct beam in Fig.7.1(b). Edge detection effectively transforms the discs in the original image into circles which can be used as the input of a circular Hough transform (CHT) [360, 361]. The CHT, which here uses an implementation of the algorithm in the Python module *scikit-image* [362], generates a set of 2D images of the Hough-space for a range of potential circle radii provided by the user. As shown in Fig.7.1(c), the position of the beam is represented by a sharp peak in the Hough-space when the correct radius is identified. For radii too large or small, the peak illustrated in the figure becomes a circle. The results of applying the CHT are shown in Fig.7.1(d), where the red circle overlaid on the image indicates the position and size of the circle found by the transform. There is an assumption in this approach that the direct beam is the most prominent feature in the diffraction pattern. If this assumption were inaccurate, the anticipated outcome would be the identification of a disc other than the direct beam, creating issues in the following processing stages. For the data examined in this chapter, the assumption was sufficient and no contingency was required.

Further to the position and radius of the direct beam, it is also important to characterise the edge of the direct-beam disc so the edge-profile of the template provides an accurate representation of the diffracted peaks. This is achieved by up-sampling the image of the beam and converting it to a polar space where the edge appears as a straight line at constant radius, as illustrated in Figure 7.2(a). The radial profile of the spot is then used to estimate the width of the edge, assuming a Gaussian-like behaviour at the edge. Width estimation is thus achieved by fitting a Gaussian error function to the radial profile at a range of angles, as shown by the solid blue lines in Fig.7.2(a) fitted to the image data represented by the sets of crosses. Together with the calculated disc centre-position and radius, the edge-width is used to generate a template of the direct-beam which can be used as a reference image for locating diffracted beams in later steps. The original and processed template images of the direct beam are shown in Fig.7.2(b) and (c), respectively. In the reference image, the disc has uniform intensity throughout. This eliminates intensity variations throughout the disc in the original image, which are highlighted as texture in the image of the difference between

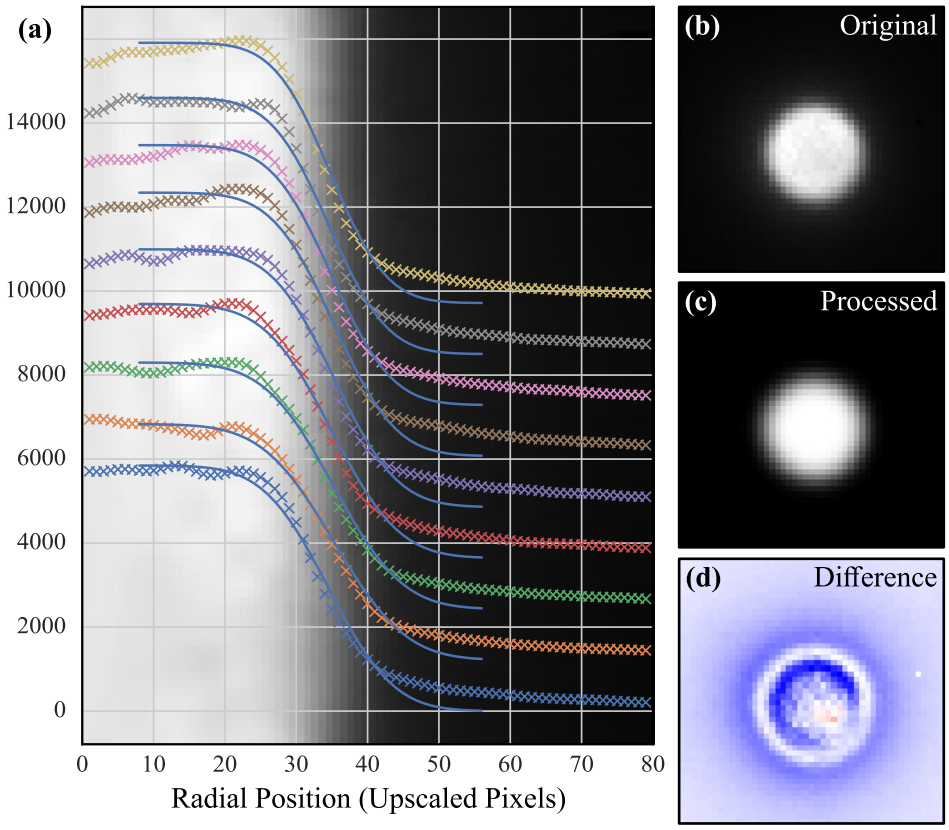

Figure 7.2: Process for creating a reference template of the direct beam. (a) Background image shows image of direct beam when up-sampled and transformed into polar coordinates about the peak centre. The sets of crosses, which are offset along the y-axis for clarity, are the radial profile of the direct beam at different angles, which are then fitted using an error function to estimate the width of the edge. (b) Original image of the observed direct-beam peak. (c) The template image of the direct beam generated using the calculated position, radius and edge-profile. (d) The difference between the direct beams in images (b) and (c), highlighting the intensity variations in the disc which are present in the original image, but not the template.

the original and template discs in Fig.7.2(d). In creating a reference image free of internal intensity variations, the emphasis of cross-correlation techniques for peak-finding is placed on the shape of the beam, rather than the beam intensity. Using the disc-shape instead of intensity-based correlations in peak-finding is acknowledged to yield improved precision in image registration, especially in edge-filtered approaches [183, 363]. This shape-dependence is most significant in nanobeam diffraction techniques, where dynamic diffraction effects can lead to intensity variations within each disc [364].

Unless the position of the direct beam changes significantly throughout the dataset, this first step to create a beam template only needs to be carried out once, saving on computation time. Otherwise, the direct beam position can be estimated for each scan position, simply repeating the same method each time it is required.

7.1.2 Peak identification

The second step in processing the SPED data is to locate all the Bragg reflections in the diffraction pattern. The candidates for potential lattice peaks are identified using Laplacian of Gaussian (LoG) blob detection, searching for features of a range of radii based on the direct beam radius determined in the previous stage [365]. The features identified by the LoG are indicated in Figure 7.3(a) by the red circles on the image. The pattern shown here is the same pattern as Fig.7.1(a) but with a logarithmic intensity scaling to improve the visibility of weaker features. Though the LoG peak detection reliably identifies most of the diffracted peaks in the image, the precision of peak positions can be improved upon. As has been noted by others for applications in pixelated DPC-STEM, NBED and energy-filtered TEM (EFTEM), cross-correlation of the edge-filtered image provides the most robust route to precise location of features in an image [183, 363, 364]. Thus, edge-filtered cross-correlation of the diffraction pattern and the template image of the direct beam created in the previous section was used to provide accurate peak positions. The peaks identified through cross-correlation are indicated in Fig.7.3(b) as red crosses. Although the positions found by cross-correlation are more accurate than the LoG blob detection method, this approach was found to generate a significant number of false-positives, identifying many more peaks than actually present in the diffraction pattern, as is evident from the figure. Using the LoG blob detection in combination with edge-filtered cross-correlation provides an approach which retains the accuracy of the latter, while the reliability of the former is used to discard the false-positives. The peaks which are retained by this combination approach are highlighted by the black circles in Fig.7.3(b).

In the typical microscope conditions for SPED, there is a very real possibility that small structural variations result in changes in the diffraction pattern where peak positions shift by less than one detector pixel. It is therefore imperative to locate peak positions with sub-pixel precision to maximise the utility of 4dSTEM data for structural analysis. Thus, once the relevant peaks have been identified in the image of the diffraction pattern using the edge-filtered cross-correlation, the sub-pixel position of the peak centre can be estimated by fitting 2d Gaussian functions to the peaks in the correlation-space [366, 367]. The peaks in the cross-correlation image generally have the same shape irrespective of the real profile of the beam. Consequently, this approach to fitting the peaks works whether the Bragg peaks in the diffraction pattern are discs from convergent beam diffraction, or point-like as would be

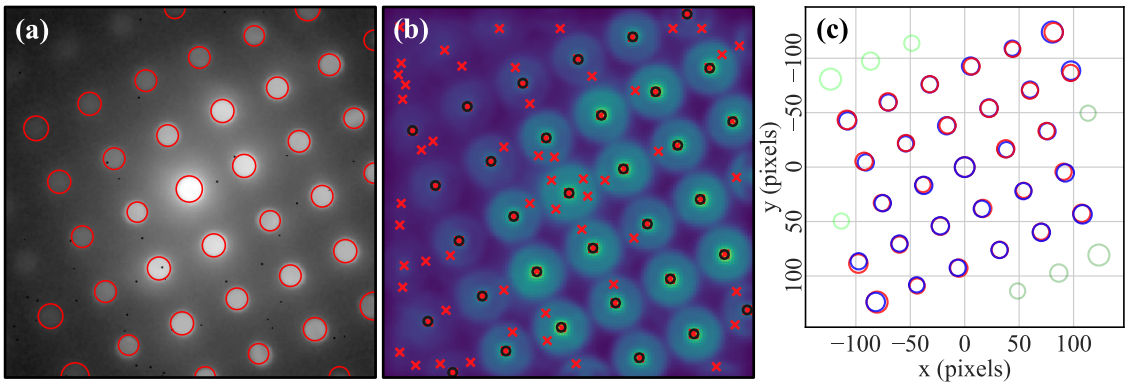

Figure 7.3: Stages involved in identifying, locating and filtering peaks in the diffraction pattern. (a) Original diffraction pattern, with log-scaled intensities to reveal weaker reflections. Peaks identified by LoG blob detection are circled in red. (b) The edge-filtered cross-correlation image, where peaks mark positions where the direct-beam reference image directly overlaps with a peak in the diffraction pattern. Peaks identified in the cross-correlation are marked by red crosses, including a significant number of false positives. The peaks retained after comparison with the peaks found in (a) are marked with black circles. (c) Illustration of the Friedel filter step, where red circles denote the original position of a peak and blue the reflected position. Peak positions filtered out because no reciprocal peak was found are shown in a faint green.

found under Fraunhofer diffraction conditions.

Finally, the measured peak positions are checked for consistency with Friedel's law, which specifies that any observed Bragg peak must have a matching peak at the coordinates given by reflection of the peak position about the pattern centre. Typically, Friedel's law fails for TEM diffraction as a result of dynamic effects [368], however this is mitigated in SPED by incoherent integration over a large number of dynamical diffraction conditions. This 'Friedel filter' acts as a further check that all the identified peaks are valid, removing points which – within some margin for error – have no equivalent point at the inverse position directly opposite the coordinates of the pattern centre. This is illustrated in Fig.7.3(c), where all peaks marked by overlapping red and blue circles indicate peaks that have been matched with their inverse position and are retained. The Friedel filter has the added advantage of acting as a check for errors in the peak positions. If there is a systematic difference between points and their inverses when reflected about the centre, this indicates that there is an error in the position of the direct beam, and the centre coordinates can be refined to eliminate this systematic error. Such an error is most likely to arise from small changes in the position of the direct beam throughout the dataset. By including the Friedel filter in this step, the centre position can be updated for each scan position in the dataset.

7.1.3 Lattice mapping

The data processing steps up to this point, having extracted the positions and sizes of all the Bragg reflections, have so far involved no assumptions about the relationship between these reflections, which contain the information about the atomic lattice we aim to extract. In the remaining processing, a 2d lattice is identified from the filtered set of peak positions and reduced to a simple expression which can be used to extract information about the unit cell.

Several routes to estimating lattice parameters from the diffraction pattern exist. Here, a

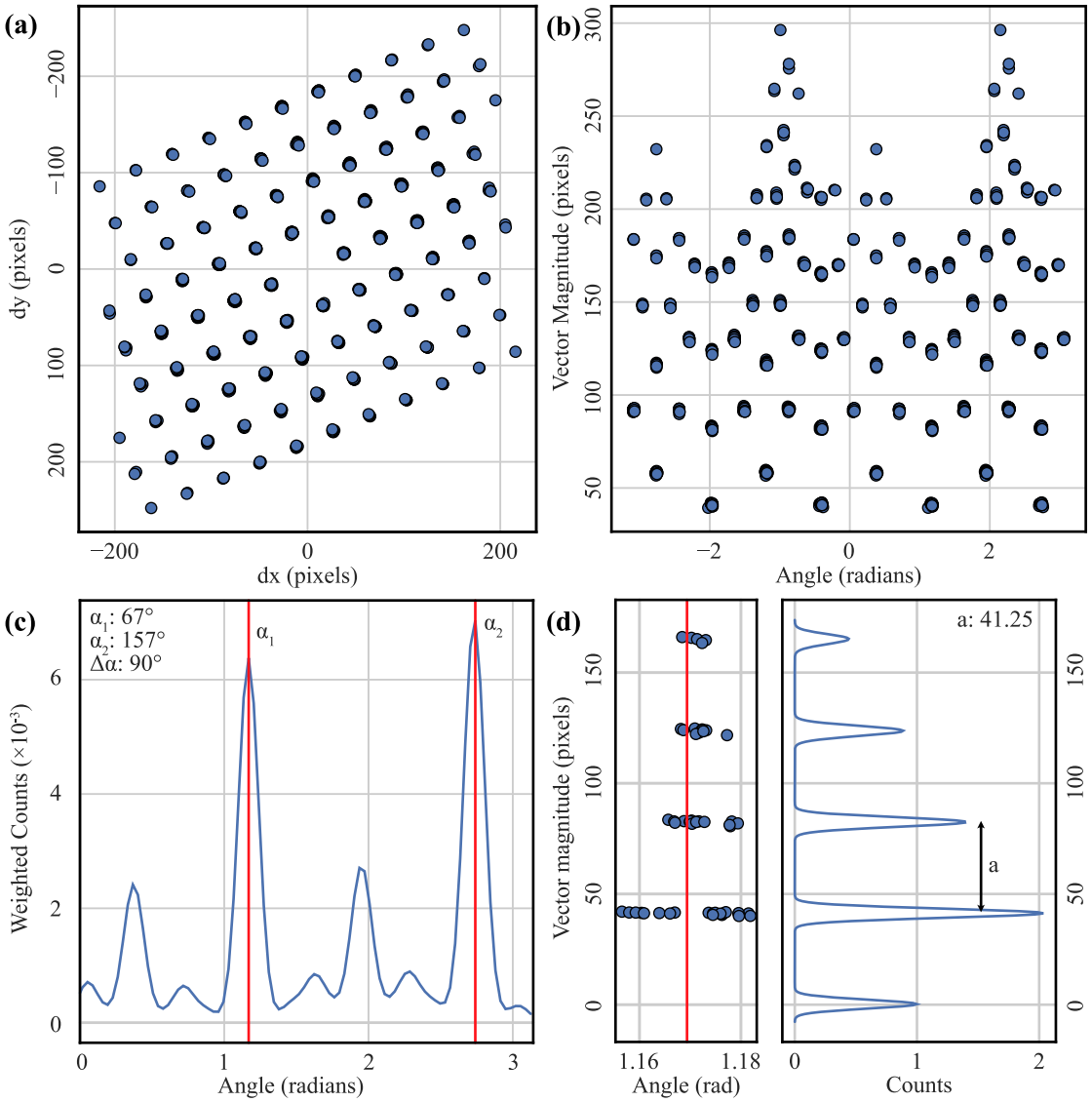

Figure 7.4: Basis vector estimation process. (a) Calculation of all combinations of vectors connecting peak positions calculated in the previous step. (b) Conversion of vector combinations into polar coordinates. (c) Histogram where vectors are binned by direction, identifying the two most common angles for the basis vectors. (d) Magnitudes of vectors which lie close to the first angle, α_1, found in (c) and the corresponding histogram of those points, with periodic peaks. The period corresponds to the magnitude of the first basis vector.

simple statistical approach is outlined which considers the lattice vectors which separate all the peaks, reducing the data to a description of the pattern by a pair of basis vectors which describe a primitive cell that maps the coordinates of all peaks. These neighbour-distances are visualised in Figure 7.4(a). Converting these vectors into polar coordinates – shown in Fig.7.4(b) – allows for direct inspection of the directions and magnitudes of all the calculated lattice vectors. To identify the basis vectors which give the best description of the lattice, a histogram is generated from the polar-space data, where vectors are binned according to polar angle, illustrated in Fig.7.4(c). A $1/r^2$ weighting of the points in the histogram increases the significance of nearest-neighbour relationships between peaks, reducing the influence larger separations which may be subject to image aberrations across the field-of-view. The two most significant peaks in the histogram are identified (marked by vertical red lines in the figure) and correspond to the angles of the two basis vectors. All vectors which lie within some margin of this angle are then selected to form a histogram binned by magnitude shown in Fig.7.4(d). This results in a histogram with peaks which are periodic in vector magnitude, where the period defines magnitude of the basis vector. This period can be determined using peak detection to identify positions, or by Fourier analysis, extracting the magnitudes of the vectors at these angles and completing the initial calculation of the basis vectors.

To check the quality of fit that the calculated basis vectors give to the diffraction pattern, they can be compared with the original peak position data, as shown in Figure 7.5. This comparison involves generating a set of peak coordinates from the calculated basis vectors for inspection alongside the individually located peak positions. At this point, peak positions which do not fit well with the lattice described by the basis vectors can optionally be considered as outliers to be excluded from further analysis. In the check for outliers in Fig.7.5(a), the original peak positions (solid blue circles) all align with the calculated lattice positions (open red circles) within some acceptable degree of error. The overall error between the two lattices is shown in the top-right of the plot, and can be reduced through least squares fitting of the peak positions to the lattice points to optimise the basis vectors. The results of the least-squares optimisation process are shown in Fig.7.5(b). Note that as a result of this refinement, there is a greater overlap between the two sets of points and that the overall fit error has reduced. The optimised fit parameters, which include the centre coordinates (c_y, c_x)[1], vector angles (α_1 and α_2) and vector magnitudes (a and b), are annotated on the plot.

[1]Note here the unusual order of the coordinates, which is chosen to be consistent with the way array coordinates are represented in Python

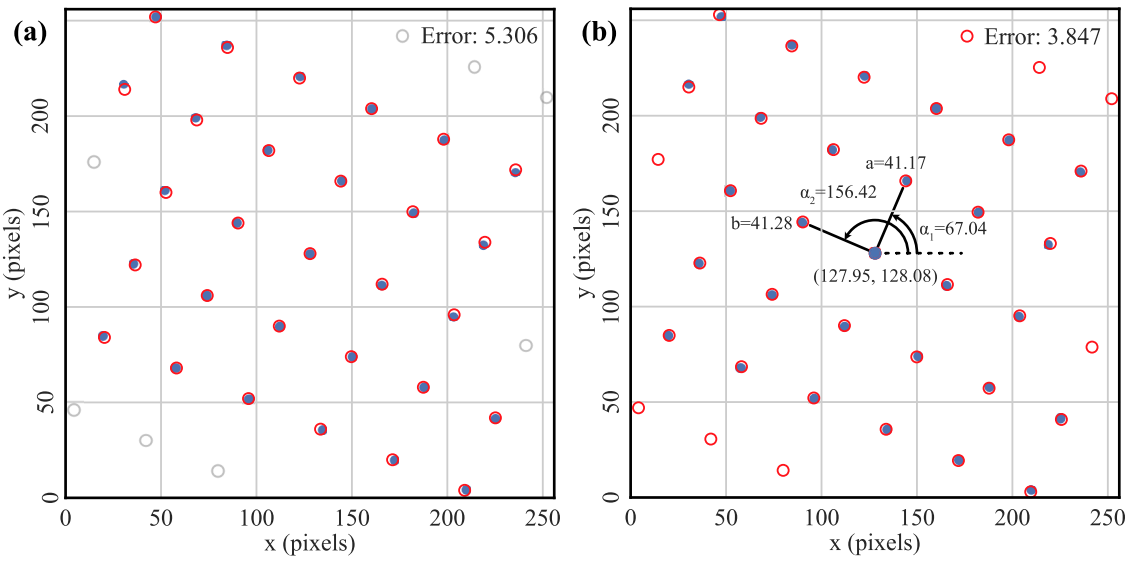

Figure 7.5: (a) Comparison of peak positions found in the peak identification step (solid circles) and lattice positions described by the calculated basis vectors (open circles). (b) Comparison of peak positions and basis-vector lattice after fitting to optimise vector parameters.

As a statistical approach, this method requires the recording of many peaks to be effective. Consequently this approach is best suited to patterns obtained on low-order zone axes, such as those presented throughout this chapter. Conversely, the method fails when patterns are recorded far from a zone axis and contain few ($<\sim$ 10) Bragg peaks. In these situations, other approaches can be adopted which require some prior knowledge of the materials involved. One such method is a template-matching approach where a bank diffraction patterns are calculated from a unit cell for a range of orientations and the best match between the experimental pattern and the bank is found [358]. If such an approach were required in future, it could be easily incorporated into the existing workflow, inserting the different method after the peak identification stage.

The stages of processing which have been outlined above often result in a single, common set of basis vectors per material. However, it is possible for different sets of basis vectors to be returned for different diffraction patterns within the same material, or for the primitive unit cell described by these vectors to be different from the unit cell we wish to study. Thus, as an additional step, the fit results can be conditioned to resolve basis vectors along specific, user-defined directions. This is achieved by choosing two angles the basis vectors should lie on, then lattice vectors from the fitted lattice are found which are close to the specified angles. The lowest magnitude vector found at each angle is then chosen for the new representation of the primitive cell. This conditioning can also be useful for comparing lattice parameters of different materials to assess strain in hetero-epitaxial systems.

7.1.4 Precision of lattice analysis

Figure 7.6 shows the accumulated results of analysing 1040 precession diffraction patterns obtained from MgO. The MgO material is FIB-sectioned single-crystal which was used as substrates for the TiNiSn thin films grown for this chapter. The diffraction patterns were recorded with a scan pixel spacing of 2.2 nm in a region ~30 nm from the substrate surface. During acquisition, the electron beam was precessed at an angle of 1.5° (~26 mrad), completing one precession during a 10 ms exposure. Operating the TEM in TEM-L mode, spot size 5 and a 20 µm condenser aperture, the convergence semi-angle was determined to be 1.1 mrad. The camera length throughout was 100 cm. A precession diffraction pattern typical of those acquired and analysed here is presented in Fig.7.6(a).

This SPED data is analysed using the methods described above, using edge-filtered cross-correlation and sub-pixel peak fitting followed by a statistical estimation of lattice vectors. The precision analysis presented below is for the full combination of processing steps only and a comprehensive break-down of the difference in quality of fit with and without the sub-pixel refinements is presented in full elsewhere [357]. The parameters which describe the resulting vectors are illustrated on the diffraction pattern in Fig.7.6(a). From the centre of the direct beam at coordinates (c_y, c_x), the lattice vectors are defined by their magnitudes, *a* and *b*,

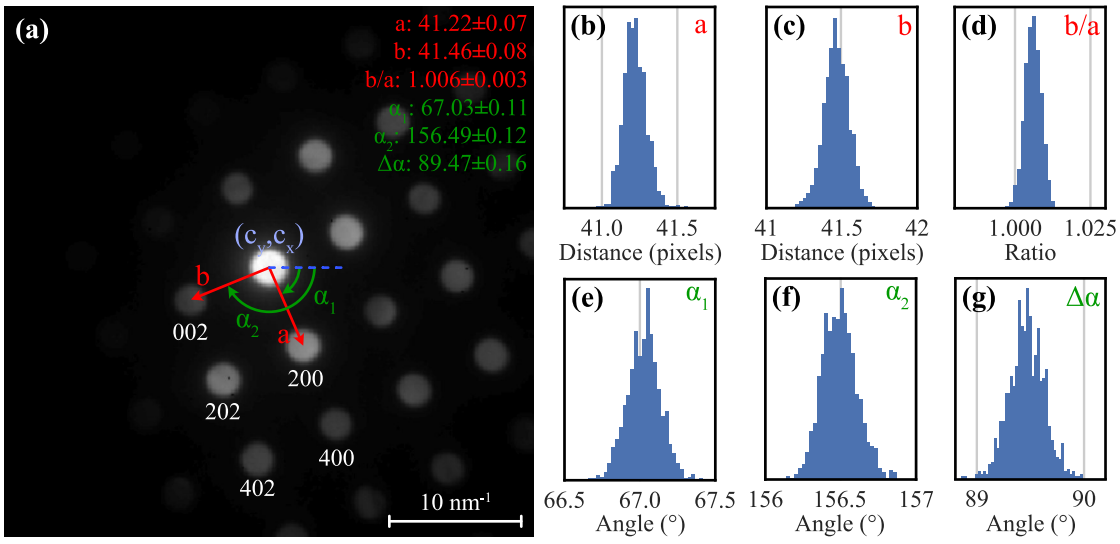

Figure 7.6: (a) Position-averaged precession electron diffraction pattern of MgO recorded with beam close to the |010| zone axis. The Miller indices of some peaks are shown based on the unit cell of MgO, while the scale bar is based on calibration with bulk MgO lattice parameters. The properties of the basis vectors which are calculated from the diffraction pattern are illustrated on the pattern centre. Histograms of the lattice vector properties based on analysis of 1040 MgO patterns are shown in figures (b-g), with the mean values and standard deviations for each parameter presented in the top-right of (a).

and by the angles α_1 and α_2. The parameters extracted from the data are shown in histograms in Fig.7.6(b-g), including the ratio of the lattice magnitudes, b/a, in Fig.7.6(d) and the angle between the basis vectors, $\Delta\alpha = \alpha_2 - \alpha_1$, in Fig.7.6(g). The lattice vector magnitudes calculated for all patterns are shown in Fig.7.6(b) and (c) corresponding to the $|200|$ and $|002|$ vectors, respectively. In raw, uncalibrated units, the means (standard deviations) of these values are $a = 41.22$ (0.07) pixels and $b = 41.46$ (0.08) pixels. These values along with the mean and standard deviations of other parameters explored in Fig.7.6, are summarised in Fig.7.6(a). Using knowledge of the bulk properties of the MgO lattice, these reciprocal lattice vectors should have a value of 4.756 nm^{-1} if unstrained, giving a detector calibration of 0.12 nm^{-1} $pixel^{-1}$ represented by the scale bar in Fig.7.6(a).

MgO, which has an unstrained cubic fcc crystal structure, should have |200| and |002| lattice vectors which are equal in magnitude and separated by 90° when the beam is aligned to the remaining orthogonal direction, as in this instance. In the SPED data examined here, the mean vector magnitude ratio (b/a, Fig.7.6(d)) is 1.006 pixels ±0.003 pixels (0.3 %) while the mean separation angle ($\Delta\alpha$, Fig.7.6(g)) is 89.47° ±0.16° (0.18 %). This indicates that the atomic lattice is marginally skewed and may be evidence of crystallographic strain. However, these effects are marginal and care in interpreting results is important to distinguish between genuine strain effects and the influence of image aberrations. For instance, small amounts of elliptical distortion in the image of the diffraction pattern can have a marked impact on strain measurements [184]. Characterisation of such elliptical distortion requires the recording of several, nominally identical diffraction patterns at various specimen rotations, making this an arduous approach to facilitating the correction of these image aberrations. Alternately, a simpler approach to handling image aberrations in lattice analysis is to use a diffraction pattern from a known material as a reference for an 'unstrained' lattice. Strain effects can then be calculated relative to this reference [369]. In many cases, the expediency of simply using a reference material for relative measurements is preferred [189, 370] and is an approach which is merited through its mathematical similarity to GPA [335].

Estimating the signal-to-noise ratio (SNR) from the lattice magnitudes calculated here, as well as their root-mean-square (rms) errors, the SNR value for these results is 55 dB. The corresponding fractional precision of the analysis is approximately 0.1 %. Greater precision using this approach has been demonstrated, with the same calculations on data presented in [357] resulting in a fractional precision of 0.03 % (an SNR of 70 dB). This demonstrates the ability of this procedure to approach the best precision values found in literature

of 0.02 % [189]. Notably, this parity in precision is achieved using exposures 100× smaller and with a superior sub-pixel precision when comparing the 256×256 pixels of the MediPix3 versus a 2k×2k CCD (64× fewer pixels). Greater precision in results could be achieved with different DEDs with larger numbers of pixels. For instance, the base 256×256 array of the MediPix3 detectors can be tiled effectively to increase the pixel count by multiples of 256 [371, 372] and detectors tiled in this way are already in use in electron microscopy [373]. Using a longer camera length – which would increase the distance between peaks – may also provide greater precision, using only Bragg peaks at smaller reciprocal lattice vector magnitudes for lattice analysis, and would be more pragmatic than a technological upgrade. The degree of precision found here, if measurements are calibrated to the bulk lattice constant of MgO, corresponds to an absolute precision of 3×10^{-3} Å, based on the fractional precision of 0.1 % for the data presented here. Compared to the expected lattice variations between full and half-Heusler phases of TiNiSn, which range in the order of 10^{-2}-10^{-1} Å, this level of precision is very good. It is worth noting that, as these protocols approach the best standards reported by others, the fractional precisions detailed here do not necessarily reflect the best possible precision achievable with this setup. A thorough investigation of the optimal approach to both data acquisition and processing is still yet to be carried out, and may yield far greater precisions than those here.

7.2 Nanoscale lattice variations in Heusler thin-film stacks

The data analysis procedures described in Section 7.1 were applied to SPED data from a specimen of a Heusler thin-film bilayer structure to extract the lattice information. An overview of this specimen is presented in Figure 7.7, which was fabricated by pulsed laser deposition as described in the methods in Chapter 2. Approximately 40 nm of full-Heusler (fH) $TiNi_2Sn$ was deposited on MgO, with a further ~65 nm of half-Heusler (hH) TiNiSn deposited atop the fH layer, before capping the specimen with platinum using a sputter coater. Conditions for PLD were the same for both layers, using a substrate temperature of 673 K and a pulse-burst approach as described in Chapter 5. RHEED was used throughout, monitoring the diffraction pattern to ensure epitaxial growth. This specimen provides a coherent interface between fH and hH to explore. As discussed at the start of the chapter, coherent interfaces are understood to play an important role in phonon scattering and reducing the lattice thermal conductivity of Heusler alloys. Chemical variations and strain fields associated with coherent interfaces

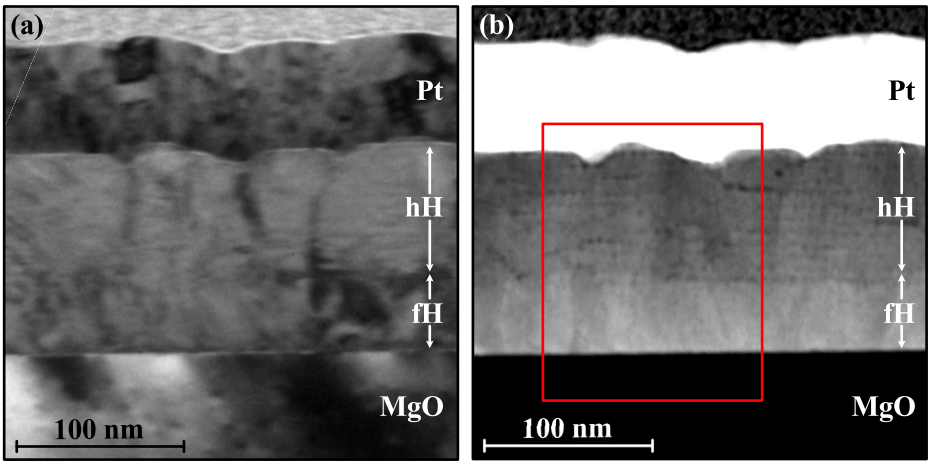

Figure 7.7: (a) Cross-sectional bright-field TEM image of $TiNi_2Sn$/TiNiSn Heusler bilayer specimen. (b) STEM-HAADF image covering the same area as (a). The contrast between the fH and hH layers is more apparent in STEM, as well as nanostructures in the hH layer that appear as dark spots. The region bounded by the red line in (b) indicates the region for which SPED data were collected.

will be related to the phonon scattering properties and thus their direct inspection in STEM is beneficial. The two Heusler layers in the specimen, annotated in a bright-field TEM image shown in Fig.7.7(a) can be difficult to distinguish, as the good epitaxial match and only small chemical difference lead to minimal contrast at the interface between the layers. Contrast between the layers is more evident in STEM, and a STEM-HAADF image covering the same area as the TEM image is presented in Fig.7.7(b). In the HAADF image, the higher concentration of Ni in the fH layer leads to a slightly higher level of brightness due to Z-contrast, allowing the layers to be identified by image intensity. Contrast variations from nanostructuring in the hH layer, identical to those observed in Chapter 5, can be more prominent than the inter-layer contrast variations and provide an easier way of distinguishing the hH from the fH, which does not show any evidence for nanostructuring.

SPED data for the bilayer was obtained for the region marked by the red outline in Fig.7.7(b). As in Section 7.1, a precession angle of 1.5° and a convergence semi-angle of 1.1 mrad (from a 20 µm condenser aperture) were used. The choice of convergence angle yields a theoretical probe size of ~1 nm, estimated from the full-width half-maximum (FWHM) of an Airy beam. However, the large precession angle increases the volume of the specimen which is probed at each position in the scan; a more conservative estimate of the probe size which takes into account this 'blurring' (approx 1 nm for the 1.5° precession angle here [374]) gives a probe size of approximately 2 nm. The spatial scan was set for inter-pixel distances of 2 nm to avoid over-sampling. However, in comparison of virtual

images generated from SPED data with TEM images, a pixel size of 2.2 nm was needed to match the TEM image calibration, suggesting a measurable inaccuracy in the DigiStar scan controls at these lengthscales and highlighting that care needs to be taken in ensuring the correct spatial calibration of SPED data.

An overview of the SPED data is presented in Figure 7.8. A virtual annular dark-field (VDF) image is calculated by integrating intensity inside an annular region from the diffraction patterns in the SPED data and is shown in Fig.7.8(a). The annular region used to generate this VDF image is illustrated on the diffraction patterns in Fig.7.8(b-e) by a yellow shaded ring. These patterns, in order from top-most to bottom-most layer, are typical of the platinum (Fig.7.8(b)), hH TiNiSn (Fig.7.8(c)), fH $TiNi_2Sn$ (Fig.7.8(d)) and the MgO substrate (Fig.7.8(e)). The annular mask for the VDF image has been chosen to provide the largest variance in intensity throughout the image, giving clear contrast between the layers. The MgO substrate and Pt capping layer, which have no Bragg peaks within the annular mask, appear dark while the hH and fH layers appear lighter owing to the six diffraction peaks incident on the virtual mask. The difference in intensity between the hH and fH layers in the VDF image arises from the different Ni occupations in the full and half-Heusler phases. As noted in Chapter 1, filling the vacant 4*d* sites changes the space group symmetry from the $F\bar{4}3m$ of the hH to $Fm\bar{3}m$ for the fH. The associated change in structure factors denotes an increase in the scattering on the Heusler $|004|$ lattice vectors relative to the $|002|$ lattice vectors. Thus the fH appears slightly darker in this VDF image. The difference in scattering factors can been seen directly in the PED patterns, where dynamical scattering effects are mostly suppressed to yield pseudo-kinematical diffracted intensities which can be related to the underlying structure factors. Comparing the intensity of the $|002|$ and $|004|$ peaks in Fig.7.8(c) and Fig.7.8(d) for the hH and fH, respectively, it is clear to see that the $|004|$ peak of the fH is much brighter than the $|002|$ peak, while the corresponding peaks in the hH pattern have similar intensity.

Lattice analysis of the SPED data was used to extract the lattice vectors which correspond to the primitive cell axes along the directions parallel and perpendicular to the MgO interface. The directions of these vectors are identified on the VDF image in Fig.7.8(a) as $a_{\parallel}$ (orange) and $a_{\perp}$ (light-blue). Further, the Bragg peaks which represent the corresponding reciprocal lattice vectors have been identified for each material and circled in the corresponding colours in Fig.7.8(c-e). As is evident from the disordered nature of the Pt diffraction pattern in Fig.7.8(b), the capping layer is not single-crystalline and thus no appropriate lattice vector could be identified. The in-plane lattice vector, $a_{\parallel}$ (orange circles), is coincident in all of the

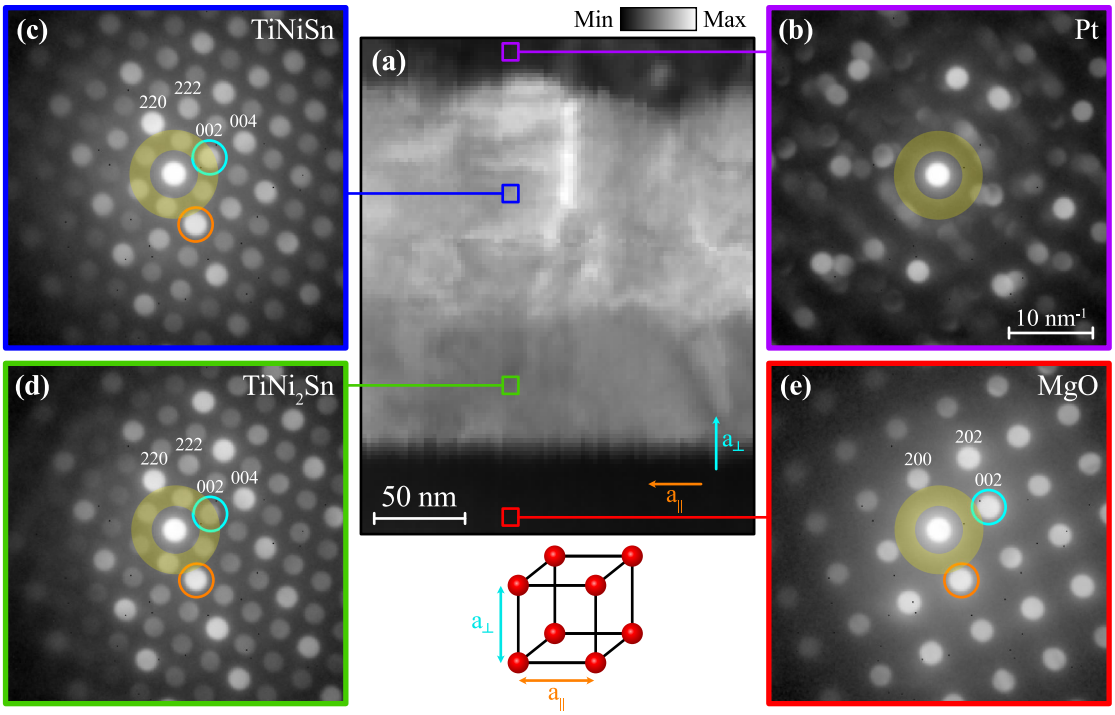

Figure 7.8: Overview of the SPED dataset. In the centre (a) a virtual annular dark-field (VDF) image shows the region of the specimen probed by SPED, with contrast generated by integrating intensity from the yellow-shaded region indicated in (b-e). Typical precession diffraction patterns from each layer are shown for (b) Pt, (c) TiNiSn, (d) $TiNi_2Sn$ and (e) MgO, with colour-matched boxes in (a) indicating the collection position. The in-plane and out-of-plane lattice spacings, $a_{\parallel}$ and $a_{\perp}$, are illustrated on a primitive cubic unit-cell below (a) and their directions relative to the dataset are illustrated in the VDF image. The Bragg peaks which represent the reciprocal lattice vectors corresponding to $a_{\parallel}$ and $a_{\perp}$ are circled in (c-e). The scale bar in (b) is representative of the calibration of all diffraction patterns.

MgO, fH and hH patterns, indicative of the epitaxial relationship between these layers. This coincidence involves matching of the $|200|$ lattice vector in MgO with the $|220|$ vector of the Heusler unit cell, as discussed in Chapter 5. The out-of-plane lattice spacing, $a_{\perp}$ (blue circles), is nominally for the same $|002|$ lattice vector in MgO, fH and hH. The magnitude of this vector is different by a factor of approximately $\sqrt{2}$ between the MgO and the Heuslers, which is evident from comparison of the diffraction patterns in Fig.7.8(c-e).

The results of the lattice analysis are presented in Figure 7.9(a-b), which contains images where contrast derives from the calculated in-plane and out-of-plane lattice spacings identified in Fig.7.8. Elemental analysis of STEM-EELS data is also shown in Fig.7.9, which will be discussed in detail in Section 7.3, below. A colour bar identifying the relationship between intensity in the image and calibrated lattice spacing is shown below each image along with a histogram of the distribution of lattice spacings within the dataset. Peaks in the histograms identify clusters of values which derive from different layers in the specimen. Addressing first the in-plane lattice spacings, which are shown in Fig.7.9(a), The fH and hH layers can

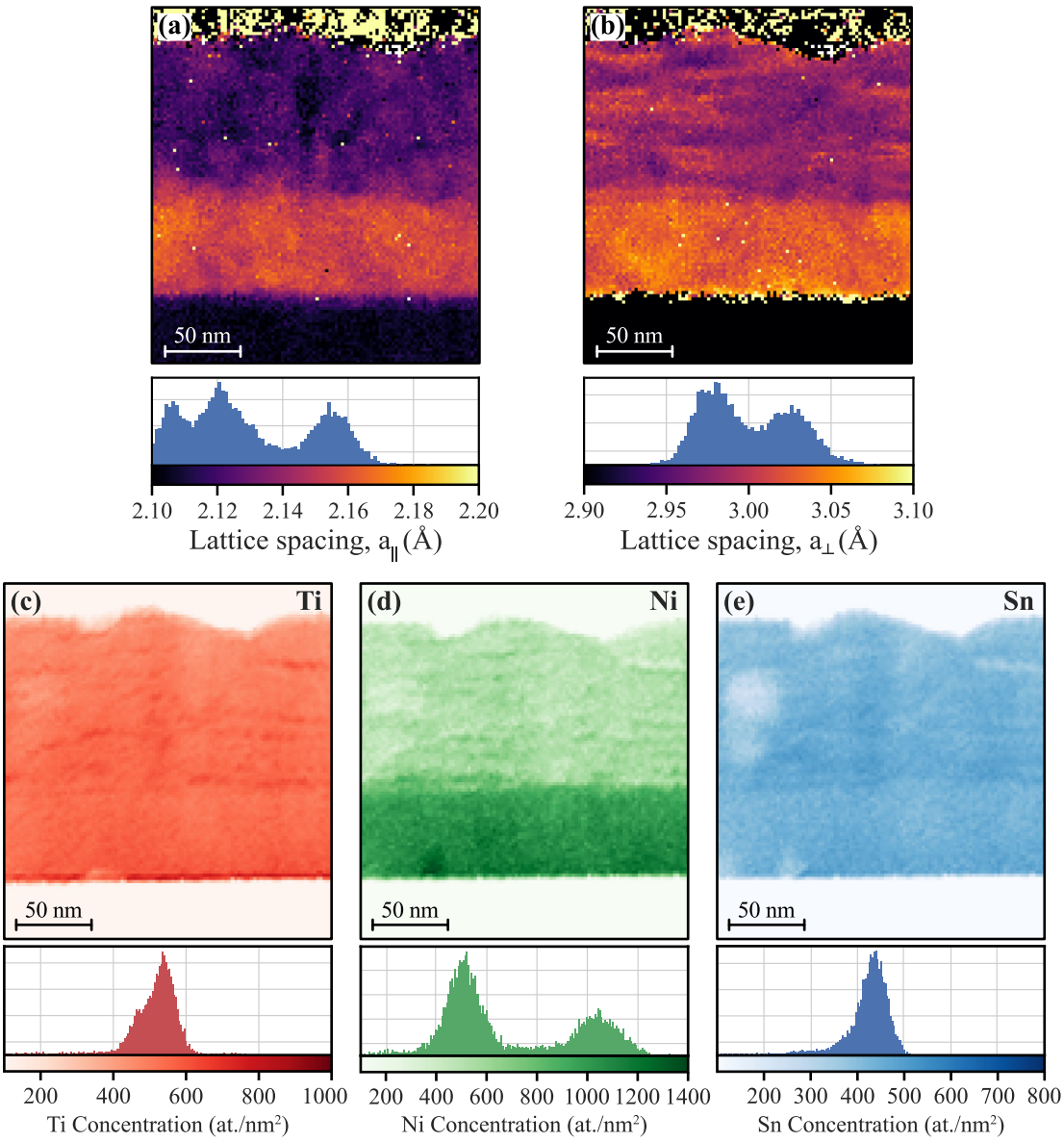

Figure 7.9: Results of lattice analysis (top row), presented as maps of (a) the in-plane lattice spacing ($a_{\parallel}$) and (b) the out-of-plane lattice spacing ($a_{\perp}$). In (b), the MgO out-of-plane lattice spacing (mean value 2.105 Å) is not represented in the range of values shown. Elemental maps (bottom row) of (c) Ti, (d) Ni and (e) Sn deriving from results of elemental quantification of STEM-EELS data in the same region. Greater intensity/darkness of colour in the elemental maps denote greater absolute concentrations of each element, as indicated by the colour-bars below each image. Histograms presented atop the colour scales show the overall distribution of results for each quantity.

now be very clearly identified, as the lattice of the hH is not fully strained to the fH which, in turn, is not fully strained to the MgO. The mean in-plane lattice spacings for each layer are calculated as 2.105 Å for MgO, 2.156 Å for the fH and 2.121 Å for the hH. Comparing the calculated magnitudes to the expected values for the corresponding lattice vector of the relaxed bulk lattice – 2.098 Å for the hH and 2.156 Å for the fH [282] – we conclude that the fH layer is fully relaxed, while the hH layer experiences a partial, tensile strain of 1.1 % in this direction.

For the out-of-plane lattice properties presented in Fig.7.9(b), the most noticeable difference from the in-plane lattice image in Fig.7.9(a) is the increased intensity in the hH layer. There are also streaked features in the hH layer that are strikingly similar to the character of the chemical variations which can be observed in STEM-HAADF images or in STEM-EELS elemental maps. Comparison with the STEM-HAADF image in Fig.7.7(b) suggests that the brighter (larger $a_{\perp}$) streaks in the lattice map are coincident with regions of greater brightness in the HAADF image of the specimen. As discussed in depth in Chapter 5, these variations in HAADF images are associated with Ni-enrichment of the hH to form near-fH nanoinclusions, while darker HAADF intensity in the hH layer is connected to the presence of TiO inclusions. Comparison of the lattice maps here with the elemental maps in Fig.7.9(c-e) indicates similar contrast variations consistent with out-of-plane lattice expansions for fH nanoinclusions and out-of-plane lattice contractions associated with oxide inclusions. These structure-chemistry links are explored further in Section 7.3. The connection between Ni enrichment and lattice expansion along the direction of growth indicates that, even for inclusions smaller than ~10 nm in size, the filling of the Heusler 4*d* sites is inevitably accommodated by expansion of the unit cell and the fH composition cannot be supported within the dimensions of the hH lattice. Thus, while strain from epitaxial clamping appears to match the in-plane lattice spacings of the fH nanoinclusions to the hH matrix, structural accommodations have to be made for the increase in Ni concentration through lattice expansion along the growth direction, $a_{\perp}$.

To further the interpretation of the lattice calculations, the lattice vectors can be used to analyse crystallographic strain variations throughout the image. Conventionally, this can be done with reference to a pattern which represented the unstrained material, similar to GPA protocols [335]. However, this approach to strain analysis assumes that lattice variations vary slowly and thus cannot reliably be applied to discontinuities like crystal interfaces or heterostructures [369]. For this reason, the MgO substrate cannot be used as a reference and there is no part of the Heusler thin film that could be interpreted as unstrained. In the absence of an appropriate strain-free region to use as a reference, a measure of strain can still be estimated through calculation of the *tetragonal distortion*. This characteristic assumes that the ideal lattice is naturally cubic – i.e. that $a_{\parallel} = a_{\perp}$ – when unstrained. The tetragonal distortion, T is then calculated from the reciprocal lattice vectors by

$$T = \frac{g_{\perp}}{g_{\parallel}} - 1 \ , \tag{7.1}$$

where $g_{\perp}$ and $g_{\parallel}$ are the reciprocal lattice vectors corresponding to $a_{\perp}$ and $a_{\parallel}$, respect-

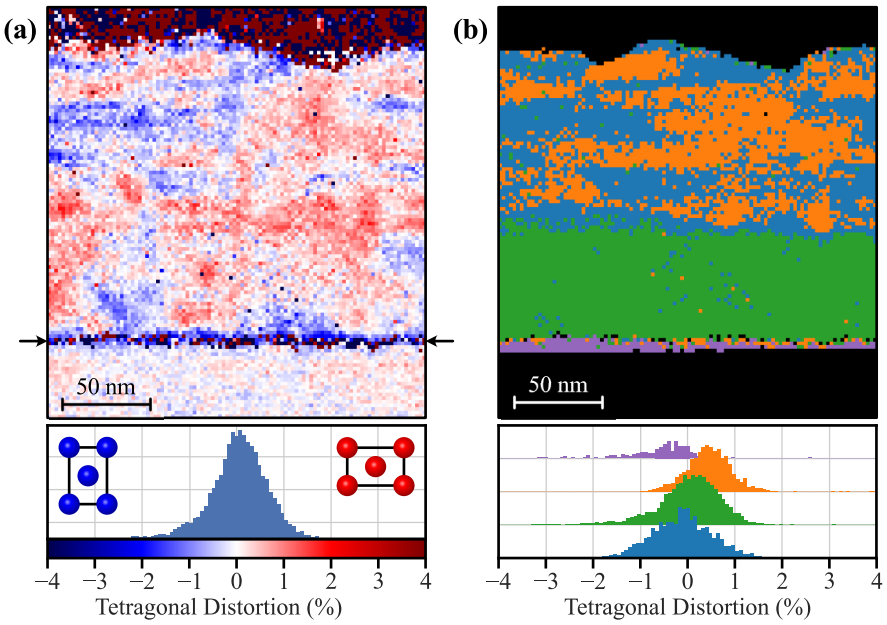

Figure 7.10: (a) Results of calculating tetragonal distortion presented as an image, spanning the same region shown in Fig.7.9, where contrast directly relates to the percentage distortion according to the colour bar. The histogram of all distortion values shows that the lattice is subject to small strains between 2 and -2 percent. The cartoons at either side of the histogram indicate how to interpret positive and negative distortions, with $a_{\parallel} > a_{\perp}$ for positive values, and negative values corresponding to $a_{\perp} > a_{\parallel}$. (b) False-colour map which shows phases identified by spectral clustering. In the histogram below, the distribution of tetragonal distortion values is shown again, but separated by clustered phase and offset vertically for clarity.

ively [184], such that negative values of T represent a relative out-of-plane elongation of the lattice. When using reciprocal lattice vectors of different lengths, as was done here for the Heusler, the magnitudes of the reciprocal lattice vectors are both normalised by the sum of the Miller indices of the vector, $M = \sqrt{h^2 + k^2 + l^2}$. This calculation can be used to identify the presence of uniaxial or planar strain, where the two observed crystallographic axes are differently affected. It should be noted, however, that this calculation will be insensitive to hydrostatic strain, where all crystallographic axes are deformed equally.

The results of calculating the tetragonal distortion are presented in Figure 7.10(a). From the image, which shows contrast based on the calculated distortion, and comparison with the Ni elemental map in Fig.7.9(d), it appears that the Ni-rich inclusions in the hH layer have negative tetragonal distortion; i.e. the inclusions have a larger magnitude lattice spacing out-of-plane than in-plane. This is represented by regions in the image that are shaded blue. Most of the remaining area of the hH layer are positively distorted, having a larger in-plane than out-of-plane lattice spacing, and are shaded red in the image. Considering the discussion above of the hH layer being epitaxially strained to the fH layer, the positive distortion of

the hH matrix calculated here is likely representative of a planar strain imposed by epitaxial clamping in the in-plane direction, while the lattice has greater freedom to relax in the out-of-plane direction. The positive distortion here is most prominent at the interface with the fH, supporting the hypothesis that it is indicative of the epitaxial tensile strain between the layers.

Variations in tetragonal distortion are also found to be present in the fH layer, most notably with a strong negative distortion at the interface with the MgO substrate, marked by arrows at the edges of Fig.7.10. The proximity of this strong strain field at the interface is clearly a manifestation of the coherency strain associated with epitaxy and the difference in lattice parameters between the MgO and the fH. Comparison of bulk values for these materials indicates a 2.4 % difference in lattice dimensions between $TiNi_2Sn$ and MgO [282, 290], which appears consistent with the contrast levels at the interface in the distortion image in Fig.7.10(a) which shows a significant compressive strain at the interface of around -2 to -3 %. Further into the fH layer, the relaxation of the initial epitaxial strain leads to organisation into regions of positive and negative distortions which could be interpreted as columnar variations in the formation of the layer. This interpretation is supported by the presence of slight columnar variations in contrast in both the BF-TEM and STEM-HAADF images which were shown in Figure 7.7 which could arise from subtle contributions from diffraction contrast.

To aid quantitative interpretation of lattice distortion results, spectral clustering – the use of which was previously introduced in Chapter 6 – has been used to automate identification of different phases from the lattice data and mask results. Four phases have been identified using the clustering algorithm on the in- and out-of-plane lattice spacing data, and a false-colour image of the specimen, where each colour is used to identify a single phase, is shown in Fig.7.10(b). The phases identified by clustering correspond to the fH layer (green), the hH matrix (orange), the inclusions plus some surrounding material in the hH layer(blue) and the strained fH at the interface with the MgO substrate (purple). The histogram below the false-colour image illustrates how these phases contribute to the overall distribution of distortion values which is shown in Fig.7.10(a). Determining the mean of each distribution, the typical distortion of each phase is found to be +0.1 % for the fH, which changes to -0.73 % at the MgO/fH interface. The main hH phase is found to have a mean distortion value of +0.47 %, while the inclusions – which are elongated out-of-plane – are described by a mean of -0.31 %.

The ‘inversion’ of the tetragonal distortion between the phases of the hH layer, where the

elongated axis changes from being the in-plane to the out-of-plane, is of particular interest. Strain effects in nanostructures have the potential for profound impact on their contribution to the thermal conductivity of a material. The lattice distortions found here, both the 0.47 % in-plane elongation and 0.31 % out-of-plane elongation, can be regarded as either planar or uniaxial strain. While the in-plane lattice vector that lies along the beam direction presumably has the same magnitude as the measured in-plane vector here, definitive distinction between uniaxial and planar strain would require additional measurement of the lattice parallel to the beam direction. This information is not typically captured in TEM/STEM as it requires analysis of diffraction features at large scattering angles in higher-order Laue zones [375]. Whether planar or uniaxial, strain can have a significant impact on the thermal conductivity of nanostructures, either reducing or increasing it by as much as a factor of 2 and potentially introducing anisotropy in the thermal conductivity [376]. Given the importance of thermal conductivity in thermoelectric materials, it is important to tune material properties to reduce, not increase, the thermal conductivity. Simulations demonstrate that strain fields do not have to be particularly large to generate significant change in the thermal properties, with strains of approximately 1 - 2 % sufficient to significantly increase phonon scattering in thermoelectrics [377]. This suggests that the difference in deformation values calculated here – 0.78 % – may be sufficiently large to cause a meaningful difference in the thermal conductivity. This would require significant theoretical investigation to corroborate and future studies could involve the calculation of phonon properties – either by DFT or another framework – of the strained states of both the half-Heusler and the full-Heusler phases to identify whether strain effects would have a positive or negative impact on the thermoelectric figure of merit in these materials. The success of such simulations would benefit from understanding the compositions behind the strain effects identified here. Correlation of the structural information discussed here with the underlying composition is outlined in the next section.

7.3 A correlative-STEM approach to investigating structure-chemistry relations

To realise a correlative SPED/STEM-EELS investigation here, the SPED measurements – which have already been presented in the previous section – were recorded first. The microscope was then reconfigured for STEM-EELS acquisition and comparison of STEM images with TEM images (as in Figure 7.7) was used to identify the region over which a spectrum

image (SI) should be recorded. The EELS-SI was initialised with a spatial scan step-size nominally identical to that of the SPED data (2 nm). The spectrometer dispersion was also measured in line with protocols from Chapter 3 and elemental quantification of spectra carried out using methods specified in Chapter 4. As the datasets were acquired sequentially, they first had to be spatially aligned prior to any comparative analysis. To achieve spatial registration of the datasets, the STEM-ADF image from the STEM-EELS data and a VDF image from the SPED data were taken and cross-correlation of the Sobel-edge-filtered versions of these images was used to determine the overlapping region. The processed results from each dataset were cropped to the overlap region rather than the raw data itself, to reduce computation time.

The companion STEM-EELS results for the SPED data from the previous section are presented in Figure 7.9(c-e), which shows the outcomes of elemental quantification for Ti, Ni and Sn within the area of the SI which is common to the SPED dataset. The fH and hH layers are easily distinguished from each other in the Ni map in Fig.7.9(d). Meanwhile the concentration of Ti and Sn is nominally the same in both Heusler phases, so there is minimal contrast between the two layers. Within the hH layer, chemical variations are observed which are identical to those discussed in Chapter 5. Namely, nanoscale inclusions are found distributed throughout the hH layer, which include those which are Ni-rich Heusler inclusions most easily observed in Fig.7.9(d), and TiO inclusions which are observed as enrichment of Ti in Fig.7.9(c) and slight decreases in the concentrations of Ni and Sn in Fig.7.9(d-e). A region of low Sn concentration in the hH layer identified at the left-hand edge of the map can be seen in Fig.7.9(e). Through mapping of the carbon *K* EELS edge (not shown), carbon contamination has been identified in this region of the specimen, which will be excluded from further analysis as it may be distorting results. Relative thickness (t/λ) calculations across the SI, in conjunction with the experimentally derived hH inelastic mean-free-path of 92.8 nm from Chapter 4, place the specimen thickness at ~40 nm.

To represent the joint chemical and structural phase-space which results from correlating STEM-EELS and SPED data, a two 2d histograms are presented in Figure 7.11 that reduce the many-dimensional phase-space to the percentage Ni composition and the in- and out-of-plane lattice vectors. The distributions in the histograms are dominated by inter-layer differences, resulting in two main populations corresponding to the full- and half-Heusler end-members with net compositions of $TiNi_{1.9}Sn_{0.8}$ and $TiNi_{1.02}Sn_{0.85}$, respectively. These compositions are notably deficient in Sn; more so than found previously in Chapter 5, where Sn levels

were typically ~90 % of the Ti concentration. The origin of the differences in composition between this and other thin films fabricated for this work is unclear and may require further investigation. Without any obvious issues in the EELS quantification, the increase in Sn deficiency in this film compared to previous films may indicate a change in the character of the PLD target material, where further ablation might drive Sn evaporation through surface melting. Alternately, this could be indicative of variations in the net composition, like the minor columnar variations discussed in Chapter 5, but on much greater lengthscales than explored previously.

The remainder of the distribution, which appears to form a path through the phase space connecting the two main populations, is indicated on the histogram in Fig.7.11(b). In essence, this band describes how the Heusler lattice parameters vary for intermediate compositions and highlights some interesting behaviour. The points in this band primarily derive from the interface region between the fH and hH layers, and thus demonstrates how strain relief occurs as the composition transitions from fH to hH. The point of interest here is that the relationship between the Ni concentration and the unit cell size - especially the in-plane lattice spacing in Fig.7.11(b) - is not linear; the Ni concentration decreases significantly from ~52 % to ~40 % before a decrease in the lattice parameters toward hH values is observed. The most likely explanation for this robustness of the fH lattice dimensions to significant change in Ni concentration lies in the epitaxial nature of the interface, with coherency-maintaining strain forcing the adoption of a larger unit cell for lower Ni concentrations. However, the results here draw to mind earlier discussion in Chapter 5 about a possible non-linear variation of lattice constant with Ni concentration arising from the transition from metallic to semiconducting electrical behaviour between the fH and hH phases [99]. Thus, these results could be highlighting an interesting departure from Veygard's law and be used to assess the rate of change of lattice parameters with Ni concentration. Potentially, in an appropriate Heusler specimen with significant variations in Ni occupation such as a fH/hH multilayer or superlattice system, SPED would be an ideal tool to explore the full nature of the relationship between composition and lattice constant, given the large surveys of structural properties which can be conducted in this technique.

Rigorous, quantitative correlations between structure and composition relating to the Ni-rich inclusions in the hH layer have proven difficult to achieve, both by manual inspection of the results and by application of machine learning techniques to automate phase identification. Two potential root causes have been identified. The first point of concern is the influence of

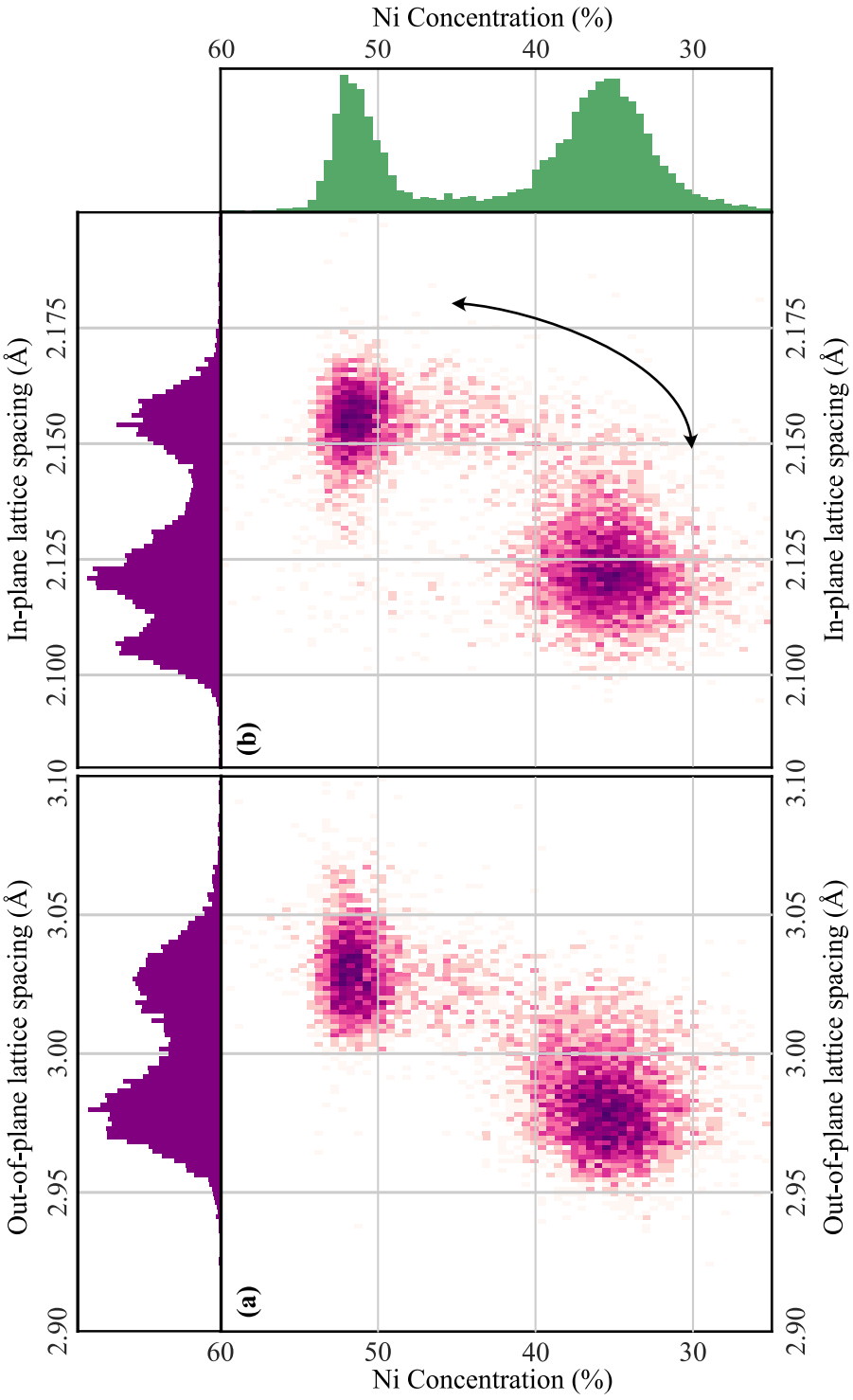

Figure 7.11: Histograms correlating nickel concentration determined by STEM-EELS with lattice properties determined by SPED. The out-of-plane ($a_{\perp}$) and in-plane ($a_{\parallel}$) lattice vectors are plotted in (a) and (b), respectively. Colour intensity in the 2-d histograms is logarithmically scaled to emphasise minor features in the distribution.

the surrounding matrix material on signal from the nanoinclusions. This was discussed in detail in Chapter 5, where the composition of nanoscale features could only be accurately determined after accounting for and subtracting the composition of the matrix from the nanoinclusions in the elemental maps. This approach to isolating features from EELS results works well because we can reasonably presume incoherent summation of intensity throughout the spectrum. However, the same assumptions cannot be made for the analysis of diffraction patterns, as coherent summation of scattering may occur in addition to incoherent summation of intensity and potentially suppress contributions from nanoinclusions in the diffraction pattern. The second possible cause may lie in a slight misalignment of the SPED and STEM-EELS results, preventing completely accurate registration of features across both datasets. Thus, while correlative analysis proves relatively straightforward over lengthscales of 10's of nanometres, analysis of features smaller than this becomes slightly less reliable. Given the discrepancy in the spatial calibration which was commented on earlier, problems in image registration preventing proper alignment of data likely originate from unresolved issues with the scan control during SPED acquisition and caution should be urged in interpretation of SPED data at ~1 nm lengthscales.

In spite of the technical limitations described above, the results presented here highlight interesting links between composition and lattice strain which merit further investigation. In the previous section, we remarked upon the in-plane lattice spacing of the fH, which had fully-relaxed to a value that agreed with the bulk lattice properties. However, the out-of-plane lattice spacing was calculated as 3.032 Å, which is slightly smaller than expected for the bulk fH |*002*| lattice spacing of 3.049 Å [282], i.e., 99.4 % of the bulk value. Given that, from STEM-EELS quantification, the composition of the fH layer is known as $TiNi_{1.9}Sn_{0.8}$, this suggests that leaving ~10 % of the Ni 4*d* sites vacant has a minimal effect on the fH lattice. Meanwhile, from Figure 7.11, the non-linear transition between hH and fH compositions and corresponding lattice parameters is marked by an initial, relatively rapid expansion of the lattice as the Ni concentration increases from hH levels. Though this effect is more challenging to fully characterise with the available data, it points to greater sensitivity of the lattice parameters to the filling of Ni vacancy sites in the hH. The contrasting behaviour of the lattice in the hH and fH phases may relate to the relative stability of these phases and, in particular, to the solubility limits of excess Ni in the hH phase, as discussed in Chapter 6.

Based on the difficulty in achieving accurate spatial registration of STEM techniques for correlation, a number of adjustments which may improve the quality of SPED measurements

are proposed. Specifically, there are a couple of adjustments which could improve upon the spatial resolution achieved with SPED. The first involves increasing the size of condenser aperture used. This would increase the convergence angle of the beam, which reduces the minimum diameter of the beam at the crossover point [156]. The downside to this is that increasing the convergence angle significantly will result in overlapping discs in the diffraction pattern, which become challenging to reliably identify separately using the current protocols. However, the use of patterned probes, which has been demonstrated very recently for improving the precision of strain measurements with NBED [378], may potentially provide a means of separately identifying discs with partial overlaps. Second, the precession angle used throughout this chapter causes significant 'blurring' of the STEM probe, effectively doubling the area probed at each position. As the number of Bragg reflections which have been excited in the precession diffraction pattern is much greater than needed for the lattice analysis protocol, the use of a smaller precession angle could significantly reduce the effective probe size without sacrificing precision of lattice analysis. Investigations into the optimisation of SPED probes have shown that reducing the precession angle by half could potentially reduce the blurring caused by precession by a factor of ten [374], at which point it would be inconsequential compared to the fundamental limit imposed by the probe convergence angle. A third point to investigate lies in further developing the lattice analysis in Section 7.1. As noted in Chapter 5, the presence of hH and fH phases can lead to incoherent summation in diffraction which leads to observation of asymmetric Bragg peaks. The current analysis protocol would be insensitive to this, but could be adapted to capture shape irregularities in detected peaks by taking advantage of the potential to be sensitive to ellipticity in the LoG feature detection algorithm [365]. This would help identify when detected peaks comprise of multiple, incoherently summed peaks and may facilitate estimation of the positions of the individual peaks in these circumstances.

7.4 Conclusions

In this chapter we have explored the use of scanning precession electron diffraction in a novel experimental set-up which integrates the use of a pixelated direct electron detector (DED), providing structural information that is complementary to STEM-EELS chemical analysis. Protocols detailed here for processing the 4 dimensional datasets produced by SPED measurements are highly successful for studying epitaxial systems and initial results demonstrate

the incredible sub-picometre precision (0.3 pm) which can be achieved in lattice analysis. That this degree of precision can be achieved without significant investment in optimisation of the experimental conditions is testament to the advantages both of the quality of lattice information available from SPED and the excellent fidelity of measurements made possible by pixelated DEDs. Taking further time and care to optimise experimental acquisition conditions and fine-tune data processing could potentially achieve measurements of lattice variations with much greater precision, below 0.1 pm. The combination of such analytical precision and a spatial resolution of approximately 2 nm makes for a highly promising approach to structural analysis of nanostructuring in thermoelectric materials. There is also a great deal more which could be achieved using SPED data, including the incorporation of crystal orientation analysis [358] and even structure refinement calculations [379].

Initial investigations, carried out on an epitaxial $TiNi_2Sn$/TiNiSn bi-layer already highlight some potentially interesting lattice strain properties. The anisotropic strains and lattice deformations found here, some of which are proposed to be linked to the presence of fH nanoinclusions in the hH matrix, may have implications for the macroscopic thermal conductivity which are functionally pertinent for thermoelectric materials and demonstrate the relevance of such investigations for these systems. These nanoscale variations would be hidden completely or lost in a continuum of other contributions in bulk techniques, as was found for XRD analysis in Chapter 5, highlighting the importance of accurate nanoanalysis. Of the observations made in this chapter, the difference in strain of ~0.8 % between regions of the hH layer, and the non-linear variation of lattice constant with Ni composition are identified as being of greatest potential interest and most warranting of further investigation. Further work would benefit from developing a theoretical understanding of the impact of strain on the thermal conductivity of Heusler materials, which could be achieved by computational studies of the changes in phonon properties when these materials are subject to different types of strain.

STEM-EELS spectrum imaging was also carried out to complement SPED data and provide a means for correlating nanoscale variations in both structure and chemistry. While correlative STEM analysis was broadly successful for the larger scales in the data, clearly identifying distinctiveness of the fH and hH layers, the approach highlighted discrepancies between the spatial resolution of the two different techniques which made in depth analysis of the nanoscale (sub-10 nm) features in the hH layer challenging. These issues are presumed to derive from the scan resolution of the SPED acquisition, given the observed discrepancies

in the automated data collection. More care to ensure that the spatial calibration of the SPED equipment is accurate would be beneficial, and other scan issues are believed to have been resolved by the system engineers since collection of the data presented here. More generally, to ensure that the spatial resolution can be improved by reducing the probe size, the size of the condenser aperture could be increased to reduce the theoretical minimum probe size, while reducing the precession angle would reduce the volume of material probed at each position.

Overall, though there is a great deal more which can still be done to advance this avenue of research, the results presented here demonstrate that use of the TEM in multiple modes can successfully yield correlative datasets where many aspects of material properties can be connected with each other at nanometre lengthscales. One future area for application is the study of bulk thermoelectric Heuslers. Previous investigations have highlighted the need for multi-lengthscale characterisation of these materials [28, 104] and the work presented throughout this thesis – in Chapter 5 especially – emphasise the importance of accurate nano-scale analysis in characterising features which can be virtually invisible in bulk analytical techniques. The combination of STEM-EELS and SPED presented here is well-placed to provide comprehensive information about the chemistry and structure of nanoscale features in thermoelectric materials and, indeed, in other materials with nanoscale disorder.

Au revoir. It's French. It means... ciao.

Jack O'Neill

8

Concluding Remarks

IN THIS THESIS, a number of studies relating to thermoelectric half-Heusler alloys were presented, with a focus on developing high-precision, quantitative chemical analysis in the transmission electron microscope to provide accurate characterisation of nanoscale features that can be overlooked in bulk characterisation techniques. These studies contribute to the understanding of the properties, formation and evolution of nanostructures in thermoelectric materials, which are essential to improving thermoelectric efficiencies and increasing the viability of thermoelectric power generation. Chapters 3 and 4 concerned the development of procedures for absolute elemental quantification from STEM-EELS spectra, which were used for compositional characterisation of Heusler thin films in Chapters 5, 6 & 7. Having the tools for studying nanostructural features at appropriate lengthscales is important for reaching an accurate understanding of the minority features that can have profound impact on the functionality of the material; bulk analytical techniques more commonly used to assess the properties of thermoelectrics often lack the necessary sensitivity and can completely miss the presence of nanostructures.

The main basis for high-precision quantitative analysis throughout the thesis is compositional characterisation by STEM-EELS. The protocols for EELS data analysis, which were presented in Chapter 4, needed to have sufficient precision to be sensitive to dopant-level quantities of an element. A specimen of copper-doped half-Heusler thermoelectric $TiNiCu_{0.1}Sn$, where accurate characterisation is key to understanding granular variations in dopant concentration, was studied to test the efficacy of the adopted quantification procedures and determine their ultimate precision. The minimum detectable fraction of copper in the studied data was found to be ~1 %. Further improvements on this level of precision were impeded by the specific nature of the Cu edge, in conjunction with fixed-pattern noise in the spectrum, which cannot be eliminated by long exposure times and must be tackled by other means. The composition of the grain found using the improved quantification – $TiNi_{1.19}Cu_{0.19}Sn_{0.95}$ – contains nearly twice the concentration of Cu as expected from the overall mean composition. Other grains from the same specimen – which are discussed elsewhere – were found to have differing Cu concentrations, including a complete absence of Cu dopants and copper segregation to grain boundaries was also observed [104]. Such microstructural variation, which is critical to the thermoelectric functionality of the material, was completely absent from the bulk XRD analysis used to verify the nominal composition, stressing the importance of accurate tools for characterising microscale variations.

The method for measuring and correcting non-uniformities of the energy dispersion of EELS spectra detailed in Chapter 3 is a critical step in the absolute elemental quantification described in Chapter 4. The developed dispersion correction improves the reliability of the energy calibration of spectra with an absolute precision better than 0.1 eV, an important criterion for the reliable use of reference materials for elemental quantification. However, the dispersion correction protocol has wider relevance for the electron microscopy community, providing routines to assess and compensate for dispersion errors that will be of interest to advanced microscope users and all who desire reliable interpretation of EELS results. The strength of the protocol lies in the elimination of prohibitive factors – namely standardised reference specimens – which would normally be used and deter users from routinely checking the dispersion calibration. The standard-less routine presented here is both easy to implement and fast, enabling users to accurately capture the nature of dispersion errors on a regular basis without concern for time-dependent variation in microscope conditions.

The developments in EELS quantification are immediately validated in Chapter 5, which presents the pulsed laser deposition of thin films of half-Heusler TiNiSn. In optimising the

deposition for high-quality, epitaxial thin films, the spontaneous formation of nanostructures was identified in these films through high-resolution STEM analysis. These nanostructures – whose presence would be entirely unexpected based on bulk analysis alone – are a result of phase segregation driven by proximity to titanium oxide phases, which arise from transfer of similar oxide content from bulk materials during pulsed laser deposition. Thin film growth was also used to investigate appropriate buffer layers for TiNiSn and vanadium was chosen for its dual ability to suppress chemical interactions with the Heusler and act as an electrical contact layer. This combination of properties is important for incorporation of TiNiSn into real thermoelectric devices, where the electrical resistance of the contact needs to be minimised while eliminating the possibility of volatile interfaces which could have a deleterious effect on device performance upon heating. Next stages of development for vanadium contact layers would begin with studies of adhesion and chemical stability when interfaced with bulk Heusler materials.

In Chapter 6, we moved from characterising the basic configuration of the as-deposited TiNiSn thin films to studying the dynamic behaviour of nanostructures and phase segregation in these films. Demonstrating how *in situ* electron microscopy can be combined with the high-precision STEM-EELS analysis of earlier chapters, nanoscale chemical diffusion was observed to lead to significant modification of the Heusler alloy, resulting in the formation of unexpected chemical phases, some of which would not normally be found in bulk materials. With care, elemental analysis can be used to determine diffusion rates, and then activation energies, of different thermally-activated processes, as was demonstrated for Ni mobility between Heusler phases. There is opportunity here to develop more sophisticated models for diffusion profiles than the one-dimensional approximations used here, and generalising models to 2 dimensions would be of particular interest as these would capture the essence of a greater number of situations which would arise in *in situ* TEM.

Transitioning from compositional to structural analysis, Chapter 7 introduced the use of scanning precession electron diffraction (SPED). The novel use of SPED in conjunction with the MediPix3 pixelated electron detector enables 4dSTEM imaging with incredible fidelity whereupon the lattice analysis protocols which were outlined at the start of the chapter achieved excellent precision of 0.3 pm without extensive optimisation of experimental conditions. SPED analysis was demonstrated for an epitaxial full-Heusler/half-Heusler layer stack to explore strain at coherent interfaces in thermoelectric Heuslers in more detail. Further to evidence for different degrees of epitaxial strain relief in the fH and hH layers, strain vari-

ations were observed in association with the different types of nanostructures present in the half-Heusler layer. While these observations could be of significant merit for thermoelectric improvement, the theoretical framework to compare these results is sparse and requires further development through calculation and simulation.

The ‘correlative-STEM’ aspect of this work, which proposes unifying structural and chemical analyses in STEM to gain greater insight into materials, has been demonstrated successfully. Although there is scope to do more to improve the spatial resolution of correlation, the results in Chapter 7 already highlight interesting lattice expansion effects that are incommensurate with the corresponding changes in Ni concentration. Many more possibilities arise from utilising the full extent of information present in precession electron diffraction patterns, much of which has been left untapped in this thesis. For instance, it would be interesting to implement a structure-factor analysis, taking advantage of the pseudo-kinematical intensities of SPED patterns to reconstruct and ‘solve’ the crystal structure. This would be analogous to Rietveld structure refinement used in X-ray diffraction, and would complement STEM-EELS data – from which the quantities of different elements can be extracted – with information about the ordering of atoms in the unit cell. Resolving the crystal structure with this level of detail could provide a route to study atomic-scale disorder in thermoelectric materials, which becomes important for scattering phonons in the high-frequency range. Correlative-STEM could be beneficial for other materials systems as well, but the approach as it is used here is limited by the relatively large electron dose resulting from the sequential application of analytical techniques, which will be prohibitive to more radiation-sensitive materials. One could envisage an approach where STEM-EDS is used for chemical analysis instead of STEM-EELS, as this would overcome the issue of mutually-exclusive detector geometries experienced with the MediPix3 DED and the post-column EELS spectrometer. For microscopes which already possess the necessary equipment, this would be a cost effective route to enabling simultaneous recording of diffraction and spectroscopic data for correlative-STEM. STEM-EDS, however, presents its own set of complexities which would need to be handled, not least of which is the poorer counting statistics when compared to EELS, which could significantly limit the precision of chemical analysis.

Looking to the future, continuing advances in STEM instrumentation are unlocking access to new information in the electron microscope. Refinements to the designs of electron monochromators and EELS spectrometers are greatly improving the energy resolution possible in STEM-EELS [205], with recently commissioned instruments achieving better than

5 meV energy resolution [380]. With this superior resolution, STEM-EELS is becoming a viable technique for vibrational spectroscopy, enabling experimental investigation of phonon properties in materials at the spatial resolution afforded by the scanning transmission electron microscope, where localised phonon modes can be identified at the nanometre [381] and even single-atom scale [177, 382]. Nanoscale vibrational studies would ideally complement the chemical and structural analyses of nanostructured thermoelectric materials presented throughout this thesis, providing experimental evidence from which to derive unambiguous links between nanostructures and their impact on phonon properties.

References

1. Lawrence-Livermore National Laboratory. *Estimated U.S. Energy Consumption in 2018* Accessed: 2019-05-21. https://flowcharts.llnl.gov/.
2. International Energy Agency. *World Energy Outlook* (2018). https://www.iea.org/weo2018/.
3. The Scottish Government. *Scottish Energy Strategy: The future of energy in Scotland* (2017). https://www.gov.scot/publications/scottish-energy-strategy-future-energy-scotland-9781788515276/.
4. UK Department for Energy and Climate Change. *UK Renewable Energy Roadmap: Update 2013* (2013). https://www.gov.uk/government/publications/uk-renewable-energy-roadmap-second-update.
5. European Commission. *Energy roadmap 2050* (2012). https://doi.org/10.2833/10759.
6. IRENA. *Global energy transformation: A roadmap to 2050* (2019). https://www.irena.org/publications/2019/Apr/Global-energy-transformation-A-roadmap-to-2050-2019Edition.
7. Le Quéré, C. *et al.* Global Carbon Budget 2018. *Earth System Science Data* **10,** 2141–2194. https://doi.org/10.5194/essd-10-2141-2018 (2018).
8. Viklund, S. B. & Johansson, M. T. Technologies for utilization of industrial excess heat: Potentials for energy recovery and CO2 emission reduction. *Energy Conversion and Management* **77,** 369–379. https://doi.org/10.1016/j.enconman.2013.09.052 (2014).
9. Yang, J. & Caillat, T. Thermoelectric Materials for Space and Automotive Power Generation. *MRS Bulletin* **31,** 224–229. https://doi.org/10.1557/mrs2006.49 (2006).

10. Yang, J. & Stabler, F. R. Automotive Applications of Thermoelectric Materials. *Journal of Electronic Materials* **38,** 1245–1251. https://doi.org/10.1007/s11664-009-0680-z (2009).
11. Ota, T., Fujita, K., Tokura, S. & Uematsu, K. *Development of thermoelectric power generation system for industrial furnaces* in *International Conference on Thermoelectrics, ICT, Proceedings* (IEEE, 2006), 354–357. http://doi.org/10.1109/ICT.2006.331253.
12. Meng, F., Chen, L., Sun, F. & Yang, B. Thermoelectric power generation driven by blast furnace slag flushing water. *Energy* **66,** 965–972. https://doi.org/10.1016/j.energy.2014.02.0182 (2014).
13. Wireless sensor node powered by aircraft specific thermoelectric energy harvesting. *Sensors and Actuators, A: Physical* **172,** 240–244. https://doi.org/10.1016/j.sna.2010.12.020 (2011).
14. Francioso, L., De Pascali, C., Farella, I., Martucci, C., Cretì, P., Siciliano, P. & Perrone, A. Flexible thermoelectric generator for ambient assisted living wearable biometric sensors. *Journal of Power Sources* **196,** 3239–3243. https://doi.org/10.1016/J.JPOWSOUR.2010.11.081 (2011).
15. Leonov, V., Torfs, T., Fiorini, P. & Van Hoof, C. Thermoelectric converters of human warmth for self-powered wireless sensor nodes. *IEEE Sensors Journal* **7,** 650–656. http://doi.org/10.1109/JSEN.2007.894917 (2007).
16. Kim, S. J., We, J. H. & Cho, B. J. A wearable thermoelectric generator fabricated on a glass fabric. *Energy & Environmental Science* **7,** 1959. http://doi.org/10.1039/c4ee00242c (2014).
17. Miorandi, D., Sicari, S., De Pellegrini, F. & Chlamtac, I. Internet of things: Vision, applications and research challenges. *Ad Hoc Networks* **10,** 1497–1516. https://doi.org/10.1016/J.ADHOC.2012.02.016 (2012).
18. European Chemical Society. *Elemental Scarcity - EuChemS Periodic Table* Accessed: 2019-05-21. https://www.euchems.eu/euchems-periodic-table/.
19. Johnsen, S., He, J., Androulakis, J., Dravid, V. P., Todorov, I., Chung, D. Y. & Kanatzidis, M. G. Nanostructures Boost the Thermoelectric Performance of PbS. *Journal of the American Chemical Society* **133,** 3460–3470. https://doi.org/10.1021/ja109138p (2011).
20. Pettes, M. T., Kim, J., Wu, W., Bustillo, K. C. & Shi, L. Thermoelectric transport in surface- and antimony-doped bismuth telluride nanoplates. *APL Materials* **4,** 104810. https://doi.org/10.1063/1.4955400 (2016).

21. Dughaish, Z. Lead telluride as a thermoelectric material for thermoelectric power generation. *Physica B: Condensed Matter* **322,** 205–223. https://doi.org/10.1016/S0921-4526(02)01187-0 (2002).
22. Hook, J. R. & Hall, H. E. *Solid State Physics, 2nd Edition* ISBN: 0471928054 (Wiley, 1995).
23. Rowe, D. M. *Handbook of Thermoelectrics* ISBN: 978-0-8493-0146-7 (CRC Press, Boca Raton, 1994).
24. Singleton, J. *Band Theory and Electronic Properties of Solids (Oxford Master Series in Physics)* ISBN: 0198506449 (Oxford University Press, 2001).
25. Toberer, E. S., Zevalkink, A., Snyder, G. J., Mei, Z. & Chen, L. D. Phonon engineering through crystal chemistry. *Journal of Materials Chemistry* **21,** 15843. https://doi.org/10.1039/c1jm11754h (2011).
26. Gelbstein, Y., Tal, N., Yarmek, A., Rosenberg, Y., Dariel, M. P., Ouardi, S., Balke, B., Felser, C. & Köhne, M. Thermoelectric properties of spark plasma sintered composites based on TiNiSn half-Heusler alloys. *Journal of Materials Research* **26,** 1919–1924. https://doi.org/10.1557/jmr.2011.107 (2011).
27. Ding, G., Gao, G. Y. & Yao, K. L. Examining the thermal conductivity of the half-Heusler alloy TiNiSn by first-principles calculations. *Journal of Physics D: Applied Physics* **48,** 235302. http://dx.doi.org/10.1088/0022-3727/48/23/235302 (2015).
28. Biswas, K., He, J., Blum, I. D., Wu, C. I., Hogan, T. P., Seidman, D. N., Dravid, V. P. & Kanatzidis, M. G. High-performance bulk thermoelectrics with all-scale hierarchical architectures. *Nature* **489,** 414–418. https://doi.org/10.1038/nature11439 (2012).
29. Bell, L. E. Cooling, heating, generating power, and recovering waste heat with thermoelectric systems. *Science (New York, N.Y.)* **321,** 1457–61. https://doi.org/10.1126/science.1158899 (2008).
30. DiSalvo, F. J. Thermoelectric cooling and power generation. *Science (New York, N.Y.)* **285,** 703–6. https://doi.org/10.1126/science.285.5428.703 (1999).
31. Seebeck, T. J. Ueber den magnetismus der galvenische kette, Abh. K. *Akad. Wiss., Berlin* **289,** 1821 (1821).
32. Ashcroft, N. W. & Mermin, N. D. *Solid State Physics* International. ISBN: 0-03-049346-3 (Holt, Rinehart and Winston, 1976).
33. Simon, S. H. *The Oxford Solid State Basics* ISBN: 978-0-19-968077-1 (Oxford University Press, 2013).

34. Cutler, M., Leavy, J. F. & Fitzpatrick, R. L. Electronic transport in semimetallic cerium sulfide. *Physical Review* **133,** A1143. https://doi.org/10.1103/PhysRev.133.A1143 (1964).
35. Snyder, G. J. & Toberer, E. S. Complex thermoelectric materials. *Nature Materials* **7,** 105–114. https://doi.org/10.1038/nmat2090 (2008).
36. Chen, Z. G., Hana, G., Yanga, L., Cheng, L. & Zou, J. Nanostructured thermoelectric materials: Current research and future challenge. *Progress in Natural Science: Materials International* **22,** 535–549. https://doi.org/10.1016/j.pnsc.2012.11.011 (2012).
37. Liu, W., Wang, H., Wang, L., Wang, X., Joshi, G., Chen, G. & Ren, Z. Understanding of the contact of nanostructured thermoelectric n-type Bi2Te2.7Se0.3 legs for power generation applications. *Journal of Materials Chemistry A* **1,** 13093–13100. https://doi.org/10.1039/c3ta13456c (2013).
38. Finn, C. B. P. *Thermal physics* 256. ISBN: 9780748743797 (CRC Press, 1993).
39. Liu, W., Yan, X., Chen, G. & Ren, Z. Recent advances in thermoelectric nanocomposites. *Nano Energy* **1,** 42–56. https://doi.org/10.1016/j.nanoen.2011.10.001 (2012).
40. Green, M. A. The path to 25% silicon solar cell efficiency: History of silicon cell evolution. *Progress in Photovoltaics: Research and Applications* **17,** 183–189. https://doi.org/10.1002/pip.892 (2009).
41. Green, M. A., Hishikawa, Y., Dunlop, E. D., Levi, D. H., Hohl-Ebinger, J. & Ho-Baillie, A. W. Solar cell efficiency tables (version 51). *Progress in Photovoltaics: Research and Applications* **26,** 3–12. https://doi.org/10.1002/pip.2978 (2018).
42. Pichanusakorn, P. & Bandaru, P. Nanostructured thermoelectrics. *Materials Science and Engineering R: Reports* **67,** 19–63. https://doi.org/10.1016/j.mser.2009.10.001 (2010).
43. Alam, H. & Ramakrishna, S. A review on the enhancement of figure of merit from bulk to nano-thermoelectric materials. *Nano Energy* **2,** 190–212. https://doi.org/10.1016/j.nanoen.2012.10.005 (2013).
44. Kuroki, T., Kabeya, K., Makino, K., Kajihara, T., Kaibe, H., Hachiuma, H., Matsuno, H. & Fujibayashi, A. Thermoelectric generation using waste heat in steel works. *Journal of Electronic Materials* **43,** 2405–2410. https://doi.org/10.1007/s11664-014-3094-5 (2014).

45. LeBlanc, S. Thermoelectric generators: Linking material properties and systems engineering for waste heat recovery applications. *Sustainable Materials and Technologies* **1,** 26–35. https://doi.org/10.1016/j.susmat.2014.11.002 (2014).

46. Liu, Y., Sahoo, P., Makongo, J. P., Zhou, X., Kim, S. J., Chi, H., Uher, C., Pan, X. & Poudeu, P. F. Large enhancements of thermopower and carrier mobility in quantum dot engineered bulk semiconductors. *Journal of the American Chemical Society* **135,** 7486–7495. https://doi.org/10.1021/ja311059m (2013).

47. Hicks, L. D. & Dresselhaus, M. S. Effect of quantum-well structures on the thermoelectric figure of merit. *Physical Review B* **47,** 12727–12731. https://doi.org/10.1103/PhysRevB.47.12727 (1993).

48. Hicks, L. D. & Dresselhaus, M. S. Thermoelectric figure of merit of a one-dimensional conductor. *Physical Review B* **47,** 16631–16634. https://doi.org/10.1103/PhysRevB.47.16631 (1993).

49. Dresselhaus, M. S., Chen, G., Tang, M. Y., Yang, R. G., Lee, H., Wang, D. Z., Ren, Z. F., Fleurial, J.-P. & Gogna, P. New Directions for Low-Dimensional Thermoelectric Materials. *Advanced Materials* **19,** 1043–1053. https://doi.org/10.1002/adma.200600527 (2007).

50. Slack, G. in *CRC Handbook of Thermoelectrics* (CRC Press, 1995). https://doi.org/10.1201/9781420049718.ch34.

51. Beekman, M., Morelli, D. T. & Nolas, G. S. Better thermoelectrics through glass-like crystals. *Nat Mater* **14,** 1182–1185. https://doi.org/10.1038/nmat4461 (2015).

52. Ward, A. & Broido, D. A. Intrinsic phonon relaxation times from first-principles studies of the thermal conductivities of Si and Ge. *Physical Review B - Condensed Matter and Materials Physics* **81,** 085205. https://doi.org/10.1103/PhysRevB.81.085205 (2010).

53. Klemens, P. G. Thermal resistance due to point defects at high temperatures. *Physical Review* **119,** 507–509. https://doi/org/10.1103/PhysRev.119.507 (1960).

54. Klemens, P. G. The Scattering of Low-Frequency Lattice Waves by Static Imperfections. *Proceedings of the Physical Society. Section A* **68,** 1113–1128. https://doi.org/10.1088/0370-1298/68/12/303 (1955).

55. Goldsmid, H. J. & Penn, A. W. Boundary scattering of phonons in solid solutions. *Physics Letters A* **27,** 523–524. https://doi.org/10.1016/0375-9601(68)90898-0 (1968).

56. Parrott, J. E. The thermal conductivity of sintered semiconductor alloys. *Journal of Physics C: Solid State Physics* **2,** 320. http://doi.org/10.1088/0022-3719/2/1/320 (1969).

57. Li, M., Ding, Z., Meng, Q., Zhou, J., Zhu, Y., Liu, H., Dresselhaus, M. S. & Chen, G. Nonperturbative Quantum Nature of the Dislocation–Phonon Interaction. *Nano Letters,* acs.nanolett.6b04756. https://doi.org/10.1021/acs.nanolett.6b04756 (2017).

58. Hess, K. Impurity and phonon scattering in layered structures. *Applied Physics Letters* **35,** 484–486. https://doi.org/10.1063/1.91205 (1979).

59. Okuyama, Y. & Tokuda, N. Electron-phonon interactions in modulation-doped AlxGa1-xAs/GaAs heterojunctions. *Physical Review B* **40,** 9744–9750. https://doi.org/10.1103/PhysRevB.40.9744 (1989).

60. Kanatzidis, M. G. *Nanostructured thermoelectrics: The new paradigm?* 2010. https://doi.org/10.1021/cm902195j.

61. Zebarjadi, M., Joshi, G., Zhu, G., Yu, B., Minnich, A., Lan, Y., Wang, X., Dresselhaus, M., Ren, Z. & Chen, G. Power factor enhancement by modulation doping in bulk nanocomposites. *Nano Letters* **11,** 2225–2230. https://doi.org/10.1021/nl201206d (2011).

62. Yu, B., Zebarjadi, M., Wang, H., Lukas, K., Wang, H., Wang, D., Opeil, C., Dresselhaus, M., Chen, G. & Ren, Z. Enhancement of thermoelectric properties by modulation-doping in silicon germanium alloy nanocomposites. *Nano Letters* **12,** 2077–2082. https://doi.org/10.1021/nl3003045 (2012).

63. Whitlow, L. W. & Hirano, T. Superlattice applications to thermoelectricity. *Journal of Applied Physics* **78,** 5460–5466. https://doi.org/10.1063/1.359661 (1995).

64. Peranio, N., Eibl, O. & Nurnus, J. Structural and thermoelectric properties of epitaxially grown Bi_2Te_3 thin films and superlattices. *Journal of Applied Physics* **100,** 114306. https://doi.org/10.1063/1.2375016 (2006).

65. Samarelli, A. *et al.* The thermoelectric properties of Ge/SiGe modulation doped superlattices. *Journal of Applied Physics* **113,** 233704. https://doi.org/10.1063/1.4811228 (2013).

66. Douglas, J. E., Birkel, C. S., Verma, N., Miller, V. M., Miao, M.-S., Stucky, G. D., Pollock, T. M. & Seshadri, R. Phase stability and property evolution of biphasic Ti-Ni-Sn alloys for use in thermoelectric applications. *Journal of Applied Physics* **115,** 43720. https://doi.org/10.1063/1.4862955 (2014).

67. Bos, J.-W. G. & Downie, R. A. Half-Heusler thermoelectrics: a complex class of materials. *Journal of Physics: Condensed Matter* **26,** 433201. https://doi.org/10.1088/0953-8984/26/43/433201 (2014).

68. Berry, T., Fu, C., Auffermann, G., Fecher, G. H., Schnelle, W., Serrano-Sanchez, F., Yue, Y., Liang, H. & Felser, C. Enhancing Thermoelectric Performance of TiNiSn Half-Heusler Compounds via Modulation Doping. *Chemistry of Materials* **29,** 7042–7048. https://doi.org/10.1021/acs.chemmater.7b02685 (2017).

69. Felser, C., Wollmann, L., Chadov, S., Fecher, G. H. & Parkin, S. S. Basics and prospective of magnetic Heusler compounds. *APL Materials* **3,** 041518. https://doi.org/10.1063/1.4917387 (2015).

70. Graf, T., Felser, C. & Parkin, S. S. P. Simple rules for the understanding of Heusler compounds. *Progress in Solid State Chemistry* **39,** 1–50. https://doi.org/10.1016/j.progsolidstchem.2011.02.001 (2011).

71. Acet, M., Duman, E., Wassermann, E. F., Mañosa, L. & Planes, A. Coexisting ferro- and antiferromagnetism in Ni_2MnAl Heusler alloys. *Journal of Applied Physics* **92,** 3867–3871. https://doi.org/10.1063/1.1504498 (2002).

72. Sanvito, S., Oses, C., Xue, J., Tiwari, A., Zic, M., Archer, T., Tozman, P., Venkatesan, M., Coey, M. & Curtarolo, S. Accelerated discovery of new magnets in the Heusler alloy family. *Science Advances* **3,** e1602241. https://doi.org/10.1126/sciadv.1602241 (2017).

73. Galanakis, I., Mavropoulos, P. & Dederichs, P. H. Electronic structure and Slater–Pauling behaviour in half-metallic Heusler alloys calculated from first principles. *Journal of Physics D: Applied Physics* **39,** 765–775. https://doi.org/10.1088/0022-3727/39/5/S01 (2006).

74. Kandpal, H. C., Fecher, G. H. & Felser, C. Calculated electronic and magnetic properties of the half-metallic, transition metal based Heusler compounds. *Journal of Physics D: Applied Physics* **40,** 1507–1523. https://doi.org/10.1088/0022-3727/40/6/S01 (2007).

75. Wernick, J. H., Hull, G. W., Geballe, T. H., Bernardini, J. E. & Waszczak, J. V. Superconductivity in ternary Heusler intermetallic compounds. *Materials Letters* **2,** 90–92. https://doi.org/10.1016/0167-577X(83)90043-5 (1983).

76. Sprungmann, D., Westerholt, K., Zabel, H., Weides, M. & Kohlstedt, H. Evidence for triplet superconductivity in Josephson junctions with barriers of the ferromagnetic Heusler alloy Cu_2MnAl. *Physical Review B - Condensed Matter and Materials Physics* **82,** 060505. https://doi.org/10.1103/PhysRevB.82.060505 (2010).

77. Al-Sawai, W., Lin, H., Markiewicz, R. S., Wray, L. A., Xia, Y., Xu, S. Y., Hasan, M. Z. & Bansil, A. Topological electronic structure in half-Heusler topological insulators. *Physical Review B - Condensed Matter and Materials Physics* **82,** 125208. https://doi.org/10.1103/PhysRevB.82.125208 (2010).

78. Xiao, D., Yao, Y., Feng, W., Wen, J., Zhu, W., Chen, X. Q., Stocks, G. M. & Zhang, Z. Half-Heusler compounds as a new class of three-dimensional topological insulators. *Physical Review Letters* **105,** 096404. https://doi.org/10.1103/PhysRevLett.105.096404 (2010).

79. Suzuki, S., Takagi, T. & Tani, J. Structural and magnetic phase transitions in shape-memory alloys $Ni_{2+x}Mn_{1-x}Ga$. *Physical Review B - Condensed Matter and Materials Physics* **59,** 1113–1120. https://doi.org/10.1103/PhysRevB.59.1113 (1999).

80. Liu, Z. H., Zhang, M., Cui, Y. T., Zhou, Y. Q., Wang, W. H., Wu, G. H., Zhang, X. X. & Xiao, G. Martensitic transformation and shape memory effect in ferromagnetic Heusler alloy Ni_2FeGa. *Applied Physics Letters* **82,** 424–426. https://doi.org/10.1063/1.1534612 (2003).

81. Fu, C., Bai, S., Liu, Y., Tang, Y., Chen, L., Zhao, X. & Zhu, T. Realizing high figure of merit in heavy-band p-type half-Heusler thermoelectric materials. *Nature Communications* **6,** 1–7. https://doi.org/10.1038/ncomms9144 (2015).

82. Zhu, T., Fu, C., Xie, H., Liu, Y. & Zhao, X. High Efficiency Half-Heusler Thermoelectric Materials for Energy Harvesting. *Advanced Energy Materials* **5.** https://doi.org/10.1002/aenm.201500588 (2015).

83. Zeier, W. G., Schmitt, J., Hautier, G., Aydemir, U., Gibbs, Z. M., Felser, C. & Snyder, G. J. Engineering half-Heusler thermoelectric materials using Zintl chemistry. *Nature Reviews Materials* **1,** 16032. https://doi.org/10.1038/natrevmats.2016.32 (2016).

84. Downie, R. A., Smith, R. I., MacLaren, D. A. & Bos, J.-W. G. Metal Distributions, Efficient n-Type Doping, and Evidence for in-Gap States in $TiNiM_ySn$ (M = Co, Ni, Cu) half-Heusler Nanocomposites. *Chemistry of Materials* **27,** 2449–2459. https://doi.org/10.1021/cm5045682 (2015).

85. Barczak, S., Buckman, J., Smith, R., Baker, A., Don, E., Forbes, I. & Bos, J.-W. Impact of Interstitial Ni on the Thermoelectric Properties of the Half-Heusler TiNiSn. *Materials* **11,** 536. https://doi.org/10.3390/ma11040536 (2018).

86. Douglas, J. E., Birkel, C. S., Miao, M.-S., Torbet, C. J., Stucky, G. D., Pollock, T. M. & Seshadri, R. Enhanced thermoelectric properties of bulk TiNiSn via formation of a

$TiNi_2Sn$ second phase. *Applied Physics Letters* **101,** 183902. https://doi.org/10.1063/1.4765358 (2012).

87. Sootsman, J. R., Chung, D. Y. & Kanatzidis, M. G. New and old concepts in thermoelectric materials. *Angewandte Chemie - International Edition* **48,** 8616–8639. https://doi.org/10.1002/anie.200900598 (2009).
88. Wu, T., Jiang, W., Li, X., Zhou, Y. & Chen, L. Thermoelectric properties of p -type Fe-doped TiCoSb half-Heusler compounds. *Journal of Applied Physics* **102,** 103705. https://doi.org/10.1063/1.2809377 (2007).
89. Muta, H., Kanemitsu, T., Kurosaki, K. & Yamanaka, S. High-temperature thermoelectric properties of Nb-doped MNiSn (M = Ti, Zr) half-Heusler compound. *Journal of Alloys and Compounds* **469,** 50–55. https://doi.org/10.1016/j.jallcom.2008.02.041 (2009).
90. Kimura, Y., Ueno, H. & Mishima, Y. *Thermoelectric properties of directionally solidified half-heusler ($M_{0.5a}$,$M_{0.5b}$)NiSn (M_a, M_b = Hf, Zr, Ti) alloys* in *Journal of Electronic Materials* **38** (Springer, 2009), 934–939. https://doi.org/10.1007/s11664-009-0710-x.
91. Xie, W., Weidenkaff, A., Tang, X., Zhang, Q., Poon, J. & Tritt, T. Recent Advances in Nanostructured Thermoelectric Half-Heusler Compounds. *Nanomaterials* **2,** 379–412. https://doi.org/10.3390/nano2040379 (2012).
92. Chen, S. & Ren, Z. Recent progress of half-Heusler for moderate temperature thermoelectric applications. *Materials Today* **16,** 387–395. https://doi.org/10.1016/j.mattod.2013.09.015 (2013).
93. Xie, H., Wang, H., Pei, Y., Fu, C., Liu, X., Snyder, G. J., Zhao, X. & Zhu, T. Beneficial contribution of alloy disorder to electron and phonon transport in half-heusler thermoelectric materials. *Advanced Functional Materials* **23,** 5123–5130. https://doi.org/10.1002/adfm.201300663 (2013).
94. Xie, W. J., Yan, Y. G., Zhu, S., Zhou, M., Populoh, S., Gałązka, K., Poon, S. J., Weidenkaff, A., He, J., Tang, X. F. & Tritt, T. M. Significant ZT enhancement in p-type Ti(Co,Fe)Sb-InSb nanocomposites via a synergistic high-mobility electron injection, energy-filtering and boundary-scattering approach. *Acta Materialia* **61,** 2087–2094. https://doi.org/10.1016/j.actamat.2012.12.028 (2013).
95. Katsuyama, S. & Kobayashi, T. Effect of mechanical milling on thermoelectric properties of half-Heusler $ZrNiSn_{0.98}Sb_{0.02}$ intermetallic compound. *Materials Science and Engineering B: Solid-State Materials for Advanced Technology* **166,** 99–103. https://doi.org/10.1016/j.mseb.2009.10.021 (2010).

96. Huang, L., Zhang, Q., Yuan, B., Lai, X., Yan, X. & Ren, Z. Recent progress in half-Heusler thermoelectric materials. *Materials Research Bulletin* **76,** 107–112. https://doi.org/10.1016/j.materresbull.2015.11.032 (2016).

97. Dove, M. T. *Structure and dynamics : an atomic view of materials* ISBN: 978-0-19-850678-2 (Oxford University Press, 2003).

98. Shiga, T., Hori, T. & Shiomi, J. Influence of mass contrast in alloy phonon scattering. *Japanese Journal of Applied Physics* **53,** 021802. https://doi.org/10.7567/JJAP.53.021802 (2014).

99. Romaka, V. V., Rogl, P., Romaka, L., Stadnyk, Y., Melnychenko, N., Grytsiv, A., Falmbigl, M. & Skryabina, N. Phase equilibria, formation, crystal and electronic structure of ternary compounds in Ti–Ni–Sn and Ti–Ni–Sb ternary systems. *Journal of Solid State Chemistry* **197,** 103–112. https://doi.org/10.1016/J.JSSC.2012.08.023 (2013).

100. Sauerschnig, P., Grytsiv, A., Vrestal, J., Romaka, V. V., Smetana, B., Giester, G., Bauer, E. & Rogl, P. On the constitution and thermodynamic modelling of the system Zr-Ni-Sn. *Journal of Alloys and Compounds* **742,** 1058–1082. https://doi.org/10.1016/j.jallcom.2017.12.012 (2018).

101. Page, A., Uher, C., Poudeu, P. F. & Van Der Ven, A. Phase separation of full-Heusler nanostructures in half-Heusler thermoelectrics and vibrational properties from first-principles calculations. *Physical Review B - Condensed Matter and Materials Physics* **92,** 174102. https://doi.org/10.1103/PhysRevB.92.174102 (2015).

102. Page, A., Van Der Ven, A., Poudeu, P. F. & Uher, C. Origins of phase separation in thermoelectric (Ti, Zr, Hf)NiSn half-Heusler alloys from first principles. *Journal of Materials Chemistry A* **4,** 13949–13956. https://doi.org/10.1039/c6ta04957e (2016).

103. Schwall, M. & Balke, B. Phase separation as a key to a thermoelectric high efficiency. *Physical Chemistry Chemical Physics* **15,** 1868–1872. https://doi.org/10.1039/c2cp43946h (2013).

104. Barczak, S. A., Halpin, J. E., Buckman, J., Decourt, R., Pollet, M., Smith, R. I., MacLaren, D. A. & Bos, J.-W. G. Grain-by-grain compositional variations and interstitial metals—a new route toward achieving high performance in half-Heusler thermoelectrics. *ACS Applied Materials & Interfaces* **10,** 4786–4793. https://doi.org/10.1021/acsami.7b14525 (Feb. 2018).

105. Makongo, J. P., Misra, D. K., Zhou, X., Pant, A., Shabetai, M. R., Su, X., Uher, C., Stokes, K. L. & Poudeu, P. F. Simultaneous large enhancements in thermopower and

electrical conductivity of bulk nanostructured half-Heusler alloys. *Journal of the American Chemical Society* **133,** 18843–18852. https://doi.org/10.1021/ja206491j (2011).

106. Gürth, M., Grytsiv, A., Vrestal, J., Romaka, V. V., Giester, G., Bauer, E. & Rogl, P. On the constitution and thermodynamic modelling of the system Ti-Ni-Sn. *RSC Advances* **5,** 92270–92291. https://doi.org/10.1039/c5ra16074j (2015).
107. Mena, J. M., Rausch, E., Ouardi, S., Gruhn, T., Fecher, G. H., Schoberth, H. G., Emmerich, H. & Felser, C. Miscibility Gap in the Phase Diagrams of Thermoelectric Half-Heusler Materials $CoTi_{1-x}Y_xSb$ (Y = Sc, V, Mn, Fe). *Journal of Electronic Materials* **45,** 1382–1388. https://doi.org/10.1007/s11664-015-4041-9 (2016).
108. Kirievsky, K., Gelbstein, Y. & Fuks, D. Phase separation and antisite defects in the thermoelectric TiNiSn half-Heusler alloys. *Journal of Solid State Chemistry* **203,** 247–254. https://doi.org/10.1016/j.jssc.2013.04.032 (2013).
109. Chai, Y. W. & Kimura, Y. Microstructure evolution of nanoprecipitates in half-Heusler TiNiSn alloys. *Acta Materialia* **61,** 6684–6697. https://doi.org/10.1016/j.actamat.2013.07.030 (2013).
110. Feynman, R. P. There's Plenty of Room at the Bottom. *Engineering and Science* **23,** 22–36. http://resolver.caltech.edu/CaltechES:23.5.1960Bottom (1960).
111. Egerton, R. F. *Electron Energy-Loss Spectroscopy in the Electron Microscope* 3rd ed. ISBN: 978-1-4419-9582-7. http://link.springer.com/10.1007/978-1-4419-9583-4 (Springer US, Boston, MA, 2011).
112. Dijkkamp, D., Venkatesan, T., Wu, X. D., Shaheen, S. A., Jisrawi, N., Min-Lee, Y. H., McLean, W. L. & Croft, M. Preparation of Y-Ba-Cu oxide superconductor thin films using pulsed laser evaporation from high Tc bulk material. *Applied Physics Letters* **51,** 619–621. https://doi.org/10.1063/1.98366 (1987).
113. Baibich, M. N., Broto, J. M., Fert, A., Van Dau, F. N., Petroff, F., Etienne, P., Creuzet, G., Friederich, A. & Chazelas, J. Giant Magnetoresistance of (001)Fe/(001)Cr Magnetic Superlattices. *Physical Review Letters* **61,** 2472–2475. https://doi.org/10.1103/PhysRevLett.61.2472 (1988).
114. Faist, J., Capasso, F., Sivco, D. L., Sirtori, C., Hutchinson, A. L. & Cho, A. Y. Quantum cascade laser. *Science (New York, N.Y.)* **264,** 553–6. https://doi.org/10.1126/science.264.5158.553 (1994).
115. Alferov, Z. I. Nobel Lecture: The double heterostructure concept and its applications in physics, electronics, and technology. *Reviews of Modern Physics* **73,** 767–782. https://doi.org/10.1103/RevModPhys.73.767 (2001).

116. Ptak, A. J. Principles of Molecular Beam Epitaxy. *Handbook of Crystal Growth,* 161–192. https://doi.org/10.1016/B978-0-444-63304-0.00004-4 (2015).

117. Eason, R. *Pulsed Laser Deposition of Thin Films: Applications-Led Growth of Functional Materials* ISBN: 978-0-47-144709-2. https://doi.org/10.1002/9780470052129 (2006).

118. Krebs, H.-U. in Eason, R. *Pulsed Laser Deposition of Thin Films: Applications-Led Growth of Functional Materials* chap. Pulsed Laser Deposition of Metals (2006). ISBN: 978-0-47-144709-2. https://doi.org/10.1002/9780470052129.

119. Cherief, N., Givord, D., Liénard, A., Mackay, K., McGrath, O., Rebouillat, J., Robaut, F. & Souche, Y. Laser ablation deposition and magnetic characterization of metallic thin films based on rare earth and transition metals. *Journal of Magnetism and Magnetic Materials* **121,** 94–101. https://doi.org/10.1016/0304-8853(93)91157-3 (1993).

120. Ohtomo, A., Kawasaki, M., Sakurai, Y., Yoshida, Y., Koinuma, H., Yu, P., Tang, Z., Wong, G. & Segawa, Y. Room temperature ultraviolet laser emission from ZnO nanocrystal thin films grown by laser MBE. *Materials Science and Engineering: B* **54,** 24–28. https://doi.org/10.1016/S0921-5107(98)00120-2 (1998).

121. Willmott, P. Deposition of complex multielemental thin films. *Progress in Surface Science* **76,** 163–217. https://doi.org/10.1016/j.progsurf.2004.06.001 (2004).

122. Jagannadham, K., Sharma, A. K., Wei, Q., Kalyanraman, R. & Narayan, J. Structural characteristics of AlN films deposited by pulsed laser deposition and reactive magnetron sputtering: A comparative study. *Journal of Vacuum Science & Technology A: Vacuum, Surfaces, and Films* **16,** 2804–2815. https://doi.org/10.1116/1.581425 (1998).

123. Rengan, A., Biunno, N., Narayan, J. & Moyer, P. Laser Assisted Techniques for Diamond and Diamondlike Thin Films. *MRS Proceedings* **162,** 185. https://doi.org/10.1557/PROC-162-185 (1989).

124. Doll, G. L., Sell, J. A., Taylor, C. A. & Clarke, R. Growth and characterization of epitaxial cubic boron nitride films on silicon. *Physical Review B* **43,** 6816–6819. https://doi.org/10.1103/PhysRevB.43.6816 (1991).

125. Cheung, J. T. & Sankur, H. Growth of thin films by laser-induced evaporation. *Critical Reviews in Solid State and Materials Sciences* **15,** 63–109. https://doi.org/10.1080/10408438808244625 (1988).

126. Willmott, P. R. & Huber, J. R. Pulsed laser vaporization and deposition. *Reviews of Modern Physics* **72,** 315–328. https://doi.org/10.1103/revmodphys.72.315 (2000).

127. Kools, J. C. S. in Chrisey, D. B. & Hubler, G. K. *Pulsed Laser Deposition of Thin Films* chap. Pulsed Laser Deposition of Metals (John Wiley & Sons, 1994). ISBN: 0-471-59218-8.

128. Barr, W. P. The production of low scattering dielectric mirrors using rotating vane particle filtration. *Journal of Physics E: Scientific Instruments* **2,** 432. https://doi.org/10.1088/0022-3735/2/12/432 (1969).

129. Kelly, R. & Miotello, A. in Chrisey, D. B. & Hubler, G. K. *Pulsed Laser Deposition of Thin Films* chap. Mechanisms of Pulsed Laser Sputtering (John Wiley & Sons, 1994). ISBN: 0-471-59218-8.

130. Hopwood, J. Ionized physical vapor deposition of integrated circuit interconnects. *Physics of Plasmas* **5,** 1624–1631. https://doir.org/10.1063/1.8728299 (1998).

131. Rossnagel, S. M. Sputter deposition for semiconductor manufacturing. *IBM Journal of Research and Development* **43,** 163–179. https://doi.org/10.1147/rd.431.0163 (1999).

132. Helmersson, U., Lattemann, M., Bohlmark, J., Ehiasarian, A. P. & Gudmundsson, J. T. Ionized physical vapor deposition (IPVD): A review of technology and applications. *Thin Solid Films* **513,** 1–24. https://doi.org/10.1016/J.TSF.2006.03.033 (2006).

133. Neave, J. H., Joyce, B. A., Dobson, P. J. & Norton, N. Dynamics of film growth of GaAs by MBE from Rheed observations. *Applied Physics A Solids and Surfaces* **31,** 1–8. https://doi.org/10.1007/BF00617180 (1983).

134. Reflection high-energy electron diffraction and atomic force microscopy studies on homoepitaxial growth of SrTiO3(001). *Physica C: Superconductivity* **305,** 233–250. https://doi.org/10.1016/S0921-4534(98)00338-4 (1998).

135. *k-Space Associates inc.* https://www.k-space.com/ (2019).

136. Blank, D. H., Rijnders, G. J., Koster, G. & Rogalla, H. In-situ monitoring by reflective high energy electron diffraction during pulsed laser deposition. *Applied Surface Science* **138-139,** 17–23. https://doi.org/10.1016/S0169-4332(98)00470-X (1999).

137. Rijnders, G. J. H. M., Koster, G., Blank, D. H. A. & Rogalla, H. *In situ* monitoring during pulsed laser deposition of complex oxides using reflection high energy elec-

tron diffraction under high oxygen pressure. *Applied Physics Letters* **70,** 1888–1890. https://doi.org/10.1063/1.118687 (1997).

138. Ichimiya, A. & Cohen, P. I. *Reflection high-energy electron diffraction* 353. ISBN: 978-0-52-145373-8 (Cambridge University Press, 2004).
139. Iakoubovskii, K., Mitsuishi, K., Nakayama, Y. & Furuya, K. Mean free path of inelastic electron scattering in elemental solids and oxides using transmission electron microscopy: Atomic number dependent oscillatory behavior. *Physical Review B - Condensed Matter and Materials Physics*. https://doi.org/10.1103/PhysRevB.77.104102 (2008).
140. Overwijk, M. H. F., van den Heuvel, F. C. & Bulle-Lieuwma, C. W. T. Novel scheme for the preparation of transmission electron microscopy specimens with a focused ion beam. *Journal of Vacuum Science & Technology B: Microelectronics and Nanometer Structures* **11,** 2021. https://doi.org/10.1116/1.586537 (1993).
141. Giannuzzi, L. A., Drown, J. L., Brown, S. R., Irwin, R. B. & Stevie, F. A. Applications of the FIB lift-out technique for TEM specimen preparation. *Microscopy Research and Technique* **41,** 285–290. https://doi.org/10.1002/(SICI)1097-0029(19980515)41:4%3C285::AID-JEMT1%3E3.0.CO;2-Q (1998).
142. Giannuzzi, L. & Stevie, F. A review of focused ion beam milling techniques for TEM specimen preparation. *Micron* **30,** 197–204. https://doi.org/10.1016/S0968-4328(99)00005-0 (1999).
143. Wirth, R. Focused Ion Beam (FIB) combined with SEM and TEM: Advanced analytical tools for studies of chemical composition, microstructure and crystal structure in geomaterials on a nanometre scale. *Chemical Geology* **261,** 217–229. https://doi.org/10.1016/J.CHEMGEO.2008.05.019 (2009).
144. Schaffer, M., Schaffer, B. & Ramasse, Q. Sample preparation for atomic-resolution STEM at low voltages by FIB. *Ultramicroscopy* **114,** 62–71. https://doi.org/10.1016/J.ULTRAMIC.2012.01.005 (2012).
145. *DENSsolution B.V.* https://denssolutions.com/products/wildfire/ (2019).
146. Almeida, T. P., McGrouther, D., Pivak, Y., Perez Garza, H. H., Temple, R., Massey, J., Marrows, C. H. & McVitie, S. Preparation of high-quality planar FeRh thin films for in situ TEM investigations. *Journal of Physics: Conference Series* **903,** 012022. https://doi.org/10.1088/1742-6596/903/1/012022 (2017).
147. Miller, M. K. & Forbes, R. G. *Atom-Probe Tomography* ISBN: 978-1-4899-7429-7. https://doi.org/10.1007/978-1-4899-7430-3 (Springer US, Boston, MA, 2014).

148. Thompson, K., Lawrence, D., Larson, D., Olson, J., Kelly, T. & Gorman, B. In situ site-specific specimen preparation for atom probe tomography. *Ultramicroscopy* **107,** 131–139. https://doi.org/10.1016/J.ULTRAMIC.2006.06.008 (2007).

149. Halpin, J. E., Webster, R. W., Gardner, H., Moody, M. P., Bagot, P. A. & MacLaren, D. A. An in-situ approach for preparing atom probe tomography specimens by xenon plasma-focussed ion beam. *Ultramicroscopy* **202,** 121–127. https://doi.org/10.1016/j.ultramic.2019.04.005 (2019).

150. Halliday, D., Resnick, R. & Walker, J. *Fundamentals of Physics Extended 9th Edition* ISBN: 978-0-47-046908-8 (John Wiley & Sons, Inc., 2010).

151. Richards, D. Near-field microscopy: throwing light on the nanoworld. *Philosophical Transactions of the Royal Society of London. Series A: Mathematical, Physical and Engineering Sciences* **361** (ed Thompson, J. M. T.) 2843–2857. https://doi.org/10.1098/rsta.2003.1282 (2003).

152. Ishizuka, K. Contrast transfer of crystal images in TEM. *Ultramicroscopy* **5,** 55–65. https://doi.org/10.1016/0304-3991(80)90011-X (1980).

153. Otten, M. T. & Coene, W. M. High-resolution imaging on a field emission TEM. *Ultramicroscopy* **48,** 77–91. https://doi.org/10.1016/0304-3991(93)90173-U (1993).

154. Batson, P. E., Dellby, N. & Krivanek, O. L. Sub-ångstrom resolution using aberration corrected electron optics. *Nature* **418,** 617–620. https://doi.org/10.1038/nature00972 (2002).

155. Hammond, C. *The Basics of Crystallography and Diffraction* ISBN: 978-0-19-873867-1 (Oxford University Press, 2015).

156. Williams, D. B. & Carter, C. B. *Transmission Electron Microscopy* ISBN: 978-0-387-76500-6. https://doi.org/10.1007/978-0-387-76501-3 (Springer US, Boston, MA, 2009).

157. Egerton, R., Li, P. & Malac, M. Radiation damage in the TEM and SEM. *Micron* **35,** 399–409. https://doi.org/10.1016/J.MICRON.2004.02.003 (2004).

158. Williams, D. B. & Carter, C. B. in. *Transmission Electron Microscopy* chap. 4. Inelastic Scattering and Beam Damage (Springer US, Boston, MA, 2009). ISBN: 978-0-387-76500-6. https://doi.org/10.1007/978-0-387-76501-3.

159. Zhang, H. R., Egerton, R. & Malac, M. Electron irradiation damage and color centers of MgO nanocube. *Nuclear Instruments and Methods in Physics Research, Section B: Beam Interactions with Materials and Atoms* **316,** 137–143. https://doi.org/10.1016/j.nimb.2013.08.042 (2013).

160. Ricolleau, C., Nelayah, J., Oikawa, T., Kohno, Y., Braidy, N., Wang, G., Hue, F., Florea, L., Pierron Bohnes, V. & Alloyeau, D. Performances of an 80–200 kV microscope employing a cold-FEG and an aberration-corrected objective lens. *Microscopy* **62,** 283–293. https://doi.org/10.1093/jmicro/dfs072 (2013).

161. Honda, T., Tomita, T., Kaneyama, T. & Ishida, Y. Field emission ultrahigh-resolution analytical electron microscope. *Ultramicroscopy* **54,** 132–144. https://doi.org/10.1016/0304-3991(94)90112-0 (1994).

162. Williams, D. B. & Carter, C. B. in. *Transmission Electron Microscopy* chap. 9. The Instrument (Springer US, Boston, MA, 2009). ISBN: 978-0-387-76500-6. https://doi.org/10.1007/978-0-387-76501-3.

163. Benner, G. & Probst, W. Köhler illumination in the TEM: Fundamentals and advantages. *Journal of Microscopy* **174,** 133–142. https://doi.org/10.1111/j.1365-2818.1994.tb03461.x (1994).

164. *CEOS Gmbh* https://http://www.ceos-gmbh.de/en/products/cscorrector (2019).

165. Gubbens, A., Barfels, M., Trevor, C., Twesten, R., Mooney, P., Thomas, P., Menon, N., Kraus, B., Mao, C. & McGinn, B. The GIF Quantum, a next generation post-column imaging energy filter. *Ultramicroscopy* **110,** 962–970. https://doi.org/10.1016/J.ULTRAMIC.2010.01.009 (2010).

166. McGrouther, D., Krajnak, M., MacLaren, I., Maneuski, D., O'Shea, V. & Nellist, P. D. Use of a hybrid silicon pixel (Medipix) detector as a STEM detector. *Microscopy and Microanalysis* **21,** 1595–1596. https://doi.org/10.1017/s1431927615008752 (2015).

167. Haider, M., Müller, H., Uhlemann, S., Zach, J., Loebau, U. & Hoeschen, R. Prerequisites for a Cc/Cs-corrected ultrahigh-resolution TEM. *Ultramicroscopy* **108,** 167–178. https://doi.org/10.1016/j.ultramic.2007.07.007 (2008).

168. Williams, D. B. & Carter, C. B. in. *Transmission Electron Microscopy* chap. 6. Lenses, Apertures and Resolution (Springer US, Boston, MA, 2009). ISBN: 978-0-387-76500-6. https://doi.org/10.1007/978-0-387-76501-3.

169. Rose, H. Prospects for aberration-free electron microscopy. *Ultramicroscopy* **103,** 1–6. https://doi.org/10.1016/J.ULTRAMIC.2004.11.017 (2005).

170. Müller, H., Uhlemann, S., Hartel, P. & Haider, M. Advancing the Hexapole C s -Corrector for the Scanning Transmission Electron Microscope. *Microscopy and Microanalysis* **12,** 442–455. https://doi.org/10.1017/S1431927606060600 (2006).

171. Chang, L., Kirkland, A. & Titchmarsh, J. On the importance of fifth-order spherical aberration for a fully corrected electron microscope. *Ultramicroscopy* **106,** 301–306. https://doi.org/10.1016/J.ULTRAMIC.2005.09.004 (2006).

172. Yamazaki, T., Kotaka, Y., Kikuchi, Y. & Watanabe, K. Precise measurement of third-order spherical aberration using low-order zone-axis Ronchigrams. *Ultramicroscopy* **106,** 153–163. https://doi.org/10.1016/J.ULTRAMIC.2005.07.001 (2006).

173. Browning, R., Li, T. Z., Chui, B., Ye, J., Pease, R. F. W., Czyżewski, Z. & Joy, D. C. Empirical forms for the electron/atom elastic scattering cross sections from 0.1 to 30 keV. *Journal of Applied Physics* **76,** 2016–2022. https://doi.org/10.1063/1.357669 (1994).

174. Williams, D. B. & Carter, C. B. in. *Transmission Electron Microscopy* chap. 22. Amplitude Contrast (Springer US, Boston, MA, 2009). ISBN: 978-0-387-76500-6. https://doi.org/10.1007/978-0-387-76501-3.

175. Williams, D. B. & Carter, C. B. in. *Transmission Electron Microscopy* chap. 23. Phase-Contrast Images (Springer US, Boston, MA, 2009). ISBN: 978-0-387-76500-6. https://doi.org/10.1007/978-0-387-76501-3.

176. Forbes, B. D., Martin, A. V., Findlay, S. D., D'Alfonso, A. J. & Allen, L. J. Quantum mechanical model for phonon excitation in electron diffraction and imaging using a Born-Oppenheimer approximation. *Physical Review B* **82,** 104103. https://doi.org/10.1103/PhysRevB.82.104103 (2010).

177. Hage, F. S., Kepaptsoglou, D. M., Ramasse, Q. M. & Allen, L. J. Phonon Spectroscopy at Atomic Resolution. *Physical Review Letters* **122,** 016103. https://doi.org/10.1103/PhysRevLett.122.016103 (2019).

178. *Quantum Detectors Ltd.* https://quantumdetectors.com/n/products/merlinem/ (2019).

179. Ophus, C. Four-Dimensional Scanning Transmission Electron Microscopy (4D-STEM): From Scanning Nanodiffraction to Ptychography and Beyond. *Microscopy and Microanalysis* **25,** 563–582. https://doi.org/10.1017/S1431927619000497 (2019).

180. Rauch, E. F. & Véron, M. Virtual dark-field images reconstructed from electron diffraction patterns. *The European Physical Journal Applied Physics* **66,** 10701. https://doi.org/10.1051/epjap/2014130556 (2014).

181. Nellist, P. D. & Rodenburg, J. M. Electron Ptychography. I. Experimental Demonstration Beyond the Conventional Resolution Limits. *Acta Crystallographica Section*

A: Foundations of Crystallography **54,** 49–60. https://doi.org/10.1107/S0108767397010490 (1998).

182. Pennycook, T. J., Lupini, A. R., Yang, H., Murfitt, M. F., Jones, L. & Nellist, P. D. Efficient phase contrast imaging in STEM using a pixelated detector. Part 1: Experimental demonstration at atomic resolution. *Ultramicroscopy* **151,** 160–167. https://doi.org/10.1016/J.ULTRAMIC.2014.09.013 (2015).

183. Krajnak, M., McGrouther, D., Maneuski, D., Shea, V. O. & McVitie, S. Pixelated detectors and improved efficiency for magnetic imaging in STEM differential phase contrast. *Ultramicroscopy* **165,** 42–50. https://doi.org/10.1016/J.ULTRAMIC.2016.03.006 (2016).

184. Mahr, C., Müller-Caspary, K., Ritz, R., Simson, M., Grieb, T., Schowalter, M., Krause, F. F., Lackmann, A., Soltau, H., Wittstock, A. & Rosenauer, A. Influence of distortions of recorded diffraction patterns on strain analysis by nano-beam electron diffraction. *Ultramicroscopy* **196,** 74–82. https://doi.org/10.1016/j.ultramic.2018.09.010 (2019).

185. Mir, J. *et al.* Characterisation of the Medipix3 detector for 60 and 80 keV electrons. *Ultramicroscopy* **182,** 44–53. https://doi.org/10.1016/J.ULTRAMIC.2017.06.010 (2017).

186. Williams, D. B. & Carter, C. B. in. *Transmission Electron Microscopy* chap. 18. Obtaining and Indexing Parallel-Beam Diffraction Patterns (Springer US, Boston, MA, 2009). ISBN: 978-0-387-76500-6. https://doi.org/10.1007/978-0-387-76501-3.

187. Eggeman, A. S. & Midgley, P. A. Precession Electron Diffraction. *Advances in Imaging and Electron Physics* **170,** 1–63. https://doi.org/10.1016/B978-0-12-394396-5.00001-4 (2012).

188. White, T. A., Eggeman, A. S. & Midgley, P. A. Is precession electron diffraction kinematical? Part I: "Phase-scrambling" multislice simulations. *Ultramicroscopy* **110,** 763–770. https://doi.org/10.1016/j.ultramic.2009.10.013 (2010).

189. Rouviere, J.-L., Béché, A., Martin, Y., Denneulin, T. & Cooper, D. Improved strain precision with high spatial resolution using nanobeam precession electron diffraction. *Applied Physics Letters* **103,** 241913. https://doi.org/10.1063/1.4829154 (2013).

190. Eggeman, A. S., Krakow, R. & Midgley, P. A. Scanning precession electron tomography for three-dimensional nanoscale orientation imaging and crystallographic ana-

lysis. *Nature Communications* **6,** 7267. https://doi.org/10.1038/ncomms8267 (2015).

191. Jeanguillaume, C. & Colliex, C. Spectrum-image: The next step in EELS digital acquisition and processing. *Ultramicroscopy* **28,** 252–257. https://doi.org/10.1016/0304-3991(89)90304-5 (1989).
192. Krivanek, O. L., Gubbens, A. J. & Dellby, N. Developments in EELS instrumentation for spectroscopy and imaging. *Microscopy Microanalysis Microstructures* **2,** 315–332. https://doi.org/10.1051/mmm:0199100202-3031500 (1991).
193. Hunt, J. & Williams, D. Electron energy-loss spectrum-imaging. *Ultramicroscopy* **38,** 47–73. https://doi.org/10.1016/0304-3991(91)90108-I (1991).
194. Schaffer, B., Kothleitner, G. & Grogger, W. EFTEM spectrum imaging at high-energy resolution. *Ultramicroscopy* **106,** 1129–1138. https://doi.org/10.1016/j.ultramic.2006.04.028 (2006).
195. Craven, A. J., Wilson, J. A. & Nicholson, W. A. A fast beam switch for controlling the intensity in electron energy loss spectrometry. *Ultramicroscopy* **92,** 165–180. https://doi.org/10.1016/S0304-3991(02)00130-4 (2002).
196. Scott, J., Thomas, P., MacKenzie, M., McFadzean, S., Wilbrink, J., Craven, A. & Nicholson, W. Near-simultaneous dual energy range EELS spectrum imaging. *Ultramicroscopy* **108,** 1586–1594. https://doi.org/10.1016/j.ultramic.2008.05.006 (2008).
197. Thomas, P., Trevor, C., Strohbehn, E., Wilbrink, J., Twesten, R. & Gubbens, A. High-Speed, Hardware-Synchronized STEM EELS Spectrum-Imaging Using a Next Generation Post-Column Imaging Filter. *Microscopy and Microanalysis* **16,** 126–127. https://doi.org/10.1017/S1431927610058551 (2010).
198. Binnig, G., Rohrer, H., Gerber, C. & Weibel, E. Surface Studies by Scanning Tunneling Microscopy. *Physical Review Letters* **49,** 57–61. https://doi.org/10.1103/PhysRevLett.49.57 (1982).
199. Binnig, G., Quate, C. F. & Gerber, C. Atomic Force Microscope. *Physical Review Letters* **56,** 930–933. https://doi.org/10.1103/PhysRevLett.56.930 (1986).
200. Paulo, Á. S. & García, R. Unifying theory of tapping-mode atomic-force microscopy. *Physical Review B* **66,** 041406. https://doi.org/10.1103/PhysRevB.66.041406 (2002).
201. Meyer, G. & Amer, N. M. Novel optical approach to atomic force microscopy. *Applied Physics Letters* **53,** 1045–1047. https://doi.org/10.1063/1.100061 (1988).
202. *Bruker Nano Inc.* https://www.brukerafmprobes.com/ (2019).

203. Egerton, R. F. Electron energy-loss spectroscopy in the TEM. *Reports on Progress in Physics* **72,** 016502. https://doi.org/10.1088/0034-4885/72/1/016502 (2009).

204. Nicoletti, O., de la Peña, F., Leary, R. K., Holland, D. J., Ducati, C. & Midgley, P. A. Three-dimensional imaging of localized surface plasmon resonances of metal nanoparticles. *Nature* **502,** 80–84. https://doi.org/10.1038/nature12469 (2013).

205. Krivanek, O. L., Lovejoy, T. C., Dellby, N., Aoki, T., Carpenter, R. W., Rez, P., Soignard, E., Zhu, J., Batson, P. E., Lagos, M. J., Egerton, R. F. & Crozier, P. A. Vibrational spectroscopy in the electron microscope. *Nature* **514,** 209–212. https://doi.org/10.1038/nature13870 (2014).

206. Oikawa, T., Shibata, N., Nakanishi, K., Kobuko, Y. & Bando, Y. An EELS Spectrometer with a Double Dispersion Lens for a Medium Voltage TEM. *Journal of Electron Microscopy* **35,** 353–358. https://doi.org/10.1093/oxfordjournals.jmicro.a050588 (1986).

207. Batson, P., Pennycook, S. & Jones, L. A new technique for the scanning and absolute calibration of electron energy loss spectra. *Ultramicroscopy* **6,** 287–289. https://doi.org/10.1016/S0304-3991(81)80210-0 (1981).

208. Mitchell, D. & Schaffer, B. Scripting-customised microscopy tools for Digital Micrograph™. *Ultramicroscopy* **103,** 319–332. https://doi.org/10.1016/J.ULTRAMIC.2005.02.003 (2005).

209. Bosman, M. & Keast, V. J. Optimizing EELS acquisition. *Ultramicroscopy* **108,** 837–846. https://doi.org/10.1016/J.ULTRAMIC.2008.02.003 (2008).

210. Daulton, T. L. & Little, B. J. Determination of chromium valence over the range Cr(0)–Cr(VI) by electron energy loss spectroscopy. *Ultramicroscopy* **106,** 561–573. https://doi.org/10.1016/J.ULTRAMIC.2006.02.005 (2006).

211. Tan, H., Verbeeck, J., Abakumov, A. & Van Tendeloo, G. Oxidation state and chemical shift investigation in transition metal oxides by EELS. *Ultramicroscopy* **116,** 24–33. https://doi.org/10.1016/J.ULTRAMIC.2012.03.002 (2012).

212. Schmid, H. & Mader, W. Oxidation states of Mn and Fe in various compound oxide systems. *Micron* **37,** 426–432. https://doi.org/10.1016/J.MICRON.2005.12.004 (2006).

213. Potapov, P. & Schryvers, D. Measuring the absolute position of EELS ionisation edges in a TEM. *Ultramicroscopy* **99,** 73–85. https://doi.org/10.1016/S0304-3991(03)00185-2 (2004).

214. Sasano, Y. & Muto, S. Energy-drift correction of electron energy-loss spectra from prolonged data accumulation of low SNR signals. *Journal of Electron Microscopy* **57,** 149–158. https://doi.org/10.1093/jmicro/dfn014 (2008).

215. Kimoto, K. & Matsui, Y. Software techniques for EELS to realize about 0.3 eV energy resolution using 300 kV FEG-TEM. *Journal of Microscopy* **208,** 224–228. https://doi.org/10.1046/j.1365-2818.2002.01083.x (2002).

216. Webster, R. W. H., Craven, A. J., Schaffer, B., McFadzean, S., MacLaren, I. & MacLaren, D. A. *Ultramicroscopy* **217.** https://doi.org/10.1016/j.ultramic.2020.113069 (2020).

217. Penner, S. Calculations of properties of magnetic deflection systems. *Review of Scientific Instruments* **32,** 150–160. https://doi.org/10.1063/1.1717300 (1961).

218. Brown, K. L., Belbeoch, R. & Bounin, P. First- and second-order magnetic optics matrix equations for the midplane of uniform-field wedge magnets. *Review of Scientific Instruments* **35,** 481–485. https://doi.org/10.1063/1.1718851 (1964).

219. Brown, K. L. *SLAC 75: A First-and Second-Order Matrix Theory for the Design of Beam Transport Systems and Charged Particle Spectrometers* tech. rep. (1967). https://cds.cern.ch/record/283218?ln=en.

220. Matsuda, H. & Wollnik, H. Third order transfer matrices of the fringing field of an inhomogeneous magnet. *Nuclear Instruments and Methods* **77,** 283–292. https://doi.org/10.1016/0029-554X(70)90097-2 (1970).

221. Tang, T. T. Correction of aberrations in a magnetic spectrometer by electric multipole lenses. *Ultramicroscopy* **7,** 305–309. https://doi.org/10.1016/0304-3991(82)90255-8 (1982).

222. Wang, Y., Huang, M. R. S., Salzberger, U., Hahn, K., Sigle, W. & van Aken, P. A. Towards atomically resolved EELS elemental and fine structure mapping via multi-frame and energy-offset correction spectroscopy. *Ultramicroscopy* **184,** 98–105. https://doi.org/10.1016/J.ULTRAMIC.2017.10.014 (2018).

223. Press, W. H., Teukolsky, S. A., Vetterling, W. T. & Flannery, B. P. *Numerical Recipes 3rd Edition: The Art of Scientific Computing* 3rd ed. ISBN: 0521880688, 9780521880688 (Cambridge University Press, New York, NY, USA, 2007).

224. Mooney, J. & Kambhampati, P. Get the Basics Right: Jacobian Conversion of Wavelength and Energy Scales for Quantitative Analysis of Emission Spectra. *The Journal of Physical Chemistry Letters* **4,** 3316–3318. https://doi.org/10.1021/jz401508t (2013).

225. Batson, P. *personal communication* 2019.

226. Gatan Inc. *private communication* 2019.

227. Leapman, R. D., Grunes, L. A. & Fejes, P. L. Study of the L23 edges in the 3d transition metals and their oxides by electron-energy-loss spectroscopy with comparisons to theory. *Physical Review B* **26,** 614–635. https://doi.org/10.1103/PhysRevB.26.614 (1982).

228. Fink, J., Müller-Heinzerling, T., Scheerer, B., Speier, W., Hillebrecht, F. U., Fuggle, J. C., Zaanen, J. & Sawatzky, G. A. 2p absorption spectra of the 3d elements. *Physical Review B* **32,** 4899–4904. https://doi.org/10.1103/PhysRevB.32.4899 (1985).

229. Fuggle, J. C. & Mårtensson, N. Core-level binding energies in metals. *Journal of Electron Spectroscopy and Related Phenomena* **21,** 275–281. https://doi.org/10.1016/0368-2048(80)85056-0 (1980).

230. Salter, P. S., Booth, M. J., Courvoisier, A., Moran, D. A. J. & MacLaren, D. A. High resolution structural characterisation of laser-induced defect clusters inside diamond. *Applied Physics Letters* **111,** 081103. https://doi.org/10.1063/1.4993118 (2017).

231. Coffman, F. L., Cao, R., Pianetta, P. A., Kapoor, S., Kelly, M. & Terminello, L. J. Near-edge x-ray absorption of carbon materials for determining bond hybridization in mixed sp2/sp3 bonded materials. *Applied Physics Letters* **69,** 568–570. https://doi.org/10.1063/1.117789 (1996).

232. Campbell, B. & Mainwood, A. Radiation damage of diamond by electron and gamma irradiation. *Physica Status Solidi (A) Applied Research* **181,** 99–107. https://doi.org/10.1002/1521-396X(200009)181:1%3C99::AID-PSSA99%3E3.0.CO;2-5 (2000).

233. Craven, A. J., Webster, R. W. H., Sala, B., MacLaren, D. A., McFadzean, S., Schaffer, B. & MacLaren, I. Splicing DualEELS Spectra: the effects of spectrometer dispersion non-uniformity and stray scattering. *To be published* (2020).

234. Bunker, G. *Introduction to XAFS* https://doi.org/10.1017/cbo9780511809194 (Cambridge University Press, 2010).

235. Vlachos, D., Craven, A. J. & McComb, D. W. *Specimen charging in X-ray absorption spectroscopy: Correction of total electron yield data from stabilized zirconia in the energy range 250-915 eV* in *Journal of Synchrotron Radiation* **12** (International Union of Crystallography, 2005), 224–233. https://doi.org/10.1107/S0909049504030146.

236. Deslattes, R. D., Kassler, E. G., Indelicato, P., De Billy, L., Lindroth, E. & Anton, J. X-ray transition energies: New approach to a comprehensive evaluation. *Reviews of*

Modern Physics **75,** 35–99. https://doi.org/10.1103/RevModPhys.75.35 (2003).

237. Chen, J. G., Kirn, C. M., Frühberger, B., DeVries, B. D. & Touvelle, M. S. A NEXAFS determination of the oxidation state of vanadium carbide on V(110): observation of charge transfer from vanadium to carbon. *Surface Science* **321,** 145–155. https://doi.org/10.1016/0039-6028(94)90035-3 (1994).

238. Bobynko, J., MacLaren, I. & Craven, A. J. Spectrum imaging of complex nanostructures using DualEELS: I. digital extraction replicas. *Ultramicroscopy* **149,** 9–20. https://doi.org/10.1016/j.ultramic.2014.10.014 (2015).

239. Craven, A. J., Bobynko, J., Sala, B. & MacLaren, I. Accurate measurement of absolute experimental inelastic mean free paths and EELS differential cross-sections. *Ultramicroscopy* **170,** 113–127. https://doi.org/10.1016/j.ultramic.2016.08.012 (2016).

240. Craven, A. J., Sala, B., Bobynko, J. & MacLaren, I. Spectrum imaging of complex nanostructures using DualEELS: II. Absolute quantification using standards. *Ultramicroscopy* **186,** 66–81. https://doi.org/10.1016/j.ultramic.2017.12.011 (2018).

241. Webster, R. W. H. *SQuEELS (Standard-based Quantification of Electron Energy-Loss Spectra)* Link confirmed as valid: 2020-04-01. https://gitlab.com/rwebster/SQuEELS.

242. Egerton, R. F. Inelastic scattering of 80 keV electrons in amorphous carbon. *Philosophical Magazine* **31,** 199–215. https://doi.org/10.1080/14786437508229296 (1975).

243. Verbeeck, J. & Van Aert, S. Model based quantification of EELS spectra. *Ultramicroscopy* **101,** 207–224. https://doi.org/10.1016/J.ULTRAMIC.2004.06.004 (2004).

244. De la Peña, F. *et al. HyperSpy* version 1.5.2. 2019. https://doi.org/10.5281/zenodo.3396791.

245. Misell, D. L. & Jones, A. F. The determination of the single-scattering line profile from the observed spectrum. *Journal of Physics A: General Physics* **2,** 540. https://doi/org/10.1088/0305-4470/2/5/007 (1969).

246. Johnson, D. W. & Spence, J. C. H. Determination of the single-scattering probability distribution from plural-scattering data. *Journal of Physics D: Applied Physics* **7,** 771–780. https://doi.org/10.1088/0022-3727/7/6/304 (1974).

247. Egerton, R. F., Williams, B. G. & Sparrow, T. G. Fourier deconvolution of electron energy-loss spectra. *Proceedings of the Royal Society of London. A. Mathematical and Physical Sciences* **398,** 395–404. https://doi.org/10.1098/rspa.1985.0041 (1985).

248. Wang, F., Egerton, R. & Malac, M. Fourier-ratio deconvolution techniques for electron energy-loss spectroscopy (EELS). *Ultramicroscopy* **109,** 1245–1249. https://doi.org/10.1016/j.ultramic.2009.05.011 (2009).

249. Robinett, R. W. *Quantum Mechanics: classical results, modern systems and visualised examples* ISBN: 978-0-19-853097-8 (Oxford University Press, Oxford, UK, 2006).

250. Malis, T., Cheng, S. C. & Egerton, R. F. EELS log-ratio technique for specimen-thickness measurement in the TEM. *Journal of Electron Microscopy Technique* **8,** 193–200. https://doi.org/10.1002/jemt.1060080206 (1988).

251. Egerton, R. F. Oscillator-strength parameterization of inner-shell cross sections. *Ultramicroscopy* **50,** 13–28. https://doi.org/10.1016/0304-3991(93)90087-E (1993).

252. Hébert, C. Practical aspects of running the WIEN2k code for electron spectroscopy. *Micron* **38,** 12–28. https://doi.org/10.1016/j.micron.2006.03.010 (2007).

253. Moreno, M. S., Jorissen, K. & Rehr, J. J. Practical aspects of electron energy-loss spectroscopy (EELS) calculations using FEFF8. *Micron* **38,** 1–11. https://doi.org/10.1016/j.micron.2006.03.011 (2007).

254. Potapov, P. L., Jorissen, K., Schryvers, D. & Lamoen, D. Effect of charge transfer on EELS integrated cross sections in Mn and Ti oxides. *Physical Review B - Condensed Matter and Materials Physics* **70,** 045106. https://doi.org/10.1103/PhysRevB.70.045106 (2004).

255. Mauchamp, V., Jaouen, M. & Schattschneider, P. Core-hole effect in the one-particle approximation revisited from density functional theory. *Physical Review B - Condensed Matter and Materials Physics* **79,** 235106. https://doi.org/10.1103/PhysRevB.79.235106 (2009).

256. Varambhia, A., Jones, L., London, A., Ozkaya, D., Nellist, P. D. & Lozano-Perez, S. Determining EDS and EELS partial cross-sections from multiple calibration standards to accurately quantify bi-metallic nanoparticles using STEM. *Micron* **113,** 69–82. https://doi.org/10.1016/j.micron.2018.06.015 (2018).

257. Oh-ishi, K. & Ohsuna, T. Inelastic mean free path measurement by STEM-EELS technique using needle-shaped specimen. *Ultramicroscopy* **212,** 112955. https://doi.org/10.1016/j.ultramic.2020.112955 (2020).

258. Mitchell, D. R. G. *Mean Free Path Estimator* Accessed: 2020-03-10. http://www.dmscripting.com/meanfreepathestimator.html.

259. Jain, A., Ong, S. P., Hautier, G., Chen, W., Richards, W. D., Dacek, S., Cholia, S., Gunter, D., Skinner, D., Ceder, G. & Persson, K. a. Commentary: The Materials Project: A materials genome approach to accelerating materials innovation. *APL Materials* **1,** 011002. https://doi.org/10.1063/1.4812323 (2013).

260. Kirievsky, K., Shlimovich, M., Fuks, D. & Gelbstein, Y. An ab initio study of the thermoelectric enhancement potential in nano-grained TiNiSn. *Physical Chemistry Chemical Physics* **16,** 20023–20029. https://doi.org/10.1039/c4cp02868f (2014).

261. Craven, A. J., Webster, R. W. H., Tencé, M., Schaffer, B. & MacLaren, I. Stray scattering in EELS spectroscopy. *To be published* (2020).

262. Verbeeck, J., Van Aert, S. & Bertoni, G. Model-based quantification of EELS spectra: Including the fine structure. *Ultramicroscopy* **106,** 976–980. https://doi.org/10.1016/j.ultramic.2006.05.006 (2006).

263. Van Der Walt, S., Colbert, S. C. & Varoquaux, G. The NumPy array: A structure for efficient numerical computation. *Computing in Science and Engineering* **13,** 22–30. https://doi.org/10.1109/MCSE.2011.37 (2011).

264. Stearns, C. W. *A generalized Hann window for apodization of filtered backprojection PET images* in *IEEE Nuclear Science Symposium Conference Record* **5** (2005), 2719–2721. ISBN: 0780392213. https://doi.org/10.1109/NSSMIC.2005.1596898.

265. Door, R. & Gängler, D. Multiple least-squares fitting for quantitative electron energy-loss spectroscopy - an experimental investigation using standard specimens. *Ultramicroscopy* **58,** 197–210. https://doi.org/10.1016/0304-3991(94)00198-V (1995).

266. Leapman, R. D. & Swyt, C. R. Separation of overlapping core edges in electron energy loss spectra by multiple-least-squares fitting. *Ultramicroscopy* **26,** 393–403. https://doi.org/10.1016/0304-3991(88)90239-2 (1988).

267. Schaffer, B. in *Transmission Electron Microscopy* 167–196 (Springer International Publishing, 2016). https://doi.org/10.1007/978-3-319-26651-0_6.

268. Levenberg, K. A method for the solution of certain non-linear problems in least squares. *Quarterly of Applied Mathematics* **2,** 164–168. https://doi.org/10.1137/0111030 (1944).

269. Marquardt, D. W. An Algorithm for Least-Squares Estimation of Nonlinear Parameters. *Journal of the Society for Industrial and Applied Mathematics* **11,** 431–441. https://doi.org/10.1137/0111030 (1963).

270. Virtanen, P. *et al.* SciPy 1.0: fundamental algorithms for scientific computing in Python. *Nature Methods* **17,** 261–272. https://doi.org/10.1038/s41592-019-0686-2 (2020).

271. Rose, A. Quantum limitations to vision at low light levels. *Image Technology* **12,** 13 (1970).

272. Rose, A. *Vision: Human and Electronic* ISBN: 9780306307324. https://archive.org/details/visionhumanelect01rose/ (Plenum Press, 1973).

273. Zhu, Y., Egerton, R. F. & Malac, M. Concentration limits for the measurement of boron by electron energy-loss spectroscopy and electron-spectroscopic imaging. *Ultramicroscopy* **87,** 135–145. https://doi.org/10.1016/S0304-3991(00)00094-2 (2001).

274. Riegler, K. & Kothleitner, G. EELS detection limits revisited: Ruby - a case study. *Ultramicroscopy* **110,** 1004–1013. https://doi.org/10.1016/j.ultramic.2010.02.010 (2010).

275. Wang, Y. Y., Ho, R., Shao, Z. & Somlyo, A. P. Optimization of quantitative electron energy loss spectroscopy in the low loss region: Phosphorus L-edge. *Ultramicroscopy* **41,** 11–31. https://doi.org/10.1016/0304-3991(92)90091-W (1992).

276. Shuman, H. & Somlyo, A. P. Electron energy loss analysis of near-trace-element concentrations of calcium. *Ultramicroscopy* **21,** 23–32. https://doi.org/10.1016/0304-3991(87)90004-0 (1987).

277. Leapman, R. D. & Newbury, D. E. Trace Elemental Analysis at Nanometer Spatial Resolution by Parallel-Detection Electron Energy Loss Spectroscopy. *Analytical Chemistry* **65,** 2409–2414. https://doi.org/10.1021/ac00066a003 (1993).

278. De Groot, R. A., Mueller, F. M., van Engen, P. G. & Buschow, K. H. J. New Class of Materials: Half-Metallic Ferromagnets. *Physical Review Letters* **50,** 2024–2027. https://doi.org/10.1103/PhysRevLett.50.2024 (1983).

279. Galanakis, I., Dederichs, P. H. & Papanikolaou, N. Slater-Pauling behavior and origin of the half-metallicity of the full-Heusler alloys. *Physical Review B* **66,** 174429. https://doi.org/10.1103/PhysRevB.66.174429 (2002).

280. *Heusler Alloys* (eds Felser, C. & Hirohata, A.) ISBN: 978-3-319-21448-1. https://doi.org/10.1007/978-3-319-21449-8 (Springer International Publishing, Cham, Switzerland, 2016).

281. Minnich, A. J. *et al.* Bulk nanostructured thermoelectric materials: current research and future prospects. *Energy & Environmental Science* **2,** 466. https://doi.org/10.1039/b822664b (2009).

282. Downie, R. A., MacLaren, D. A., Smith, R. I. & Bos, J. W. G. Enhanced thermoelectric performance in TiNiSn-based half-Heuslers. *Chemical Communications* **49,** 4184. https://doi.org/10.1039/c2cc37121a (2013).

283. Bartholomé, K., Balke, B., Zuckermann, D., Köhne, M., Müller, M., Tarantik, K. & König, J. Thermoelectric Modules Based on Half-Heusler Materials Produced in Large Quantities. *Journal of Electronic Materials* **43,** 1775–1781. https://doi.org/10.1007/s11664-013-2863-x (2014).

284. Callaway, J. Model for Lattice Thermal Conductivity at Low Temperatures. *Physical Review* **113,** 1046–1051. https://doi.org/10.1103/PhysRev.113.1046 (1959).

285. Katayama, T., Kim, S. W., Kimura, Y. & Mishima, Y. The effects of quaternary additions on thermoelectric properties of TiNiSn-based half-heusler alloys. *Journal of Electronic Materials* **32,** 1160–1165. https://doi.org/10.1007/s11664-003-0006-5 (2003).

286. Onoue, M., Ishii, F. & Oguchi, T. Electronic and Thermoelectric Properties of the Intermetallic Compounds M NiSn (M =Ti, Zr, and Hf). *Journal of the Physical Society of Japan* **77,** 054706. https://doi.org/10.1143/JPSJ.77.054706 (2008).

287. Hazama, H., Matsubara, M. & Asahi, R. Thermoelectric Properties of Off-Stoichiometric Ti-Ni-Sn Half-Heusler Systems. *Journal of Electronic Materials* **41,** 1730–1734. https://doi.org/10.1007/s11664-012-2048-z (2012).

288. Akram, R., Zhang, Q., Yang, D., Zheng, Y., Yan, Y., Su, X. & Tang, X. Enhanced Thermoelectric Properties of La-Doped ZrNiSn Half-Heusler Compound. *Journal of Electronic Materials* **44,** 3563–3570. https://doi.org/10.1007/s11664-015-3882-6 (2015).

289. Jaeger, T., Mix, C., Schwall, M., Kozina, X., Barth, J., Balke, B., Finsterbusch, M., Idzerda, Y. U., Felser, C. & Jakob, G. Epitaxial growth and thermoelectric properties of TiNiSn and $Zr_{0.5}Hf_{0.5}NiSn$ thin films. *Thin Solid Films* **520,** 1010–1014. https://doi.org/10.1016/J.TSF.2011.08.008 (2011).

290. Kawasaki, J. K., Neulinger, T., Timm, R., Hjort, M., Zakharov, A. a., Mikkelsen, A., Schultz, B. D. & Palmstrøm, C. J. Epitaxial growth and surface studies of the Half Heusler compound NiTiSn (001). *Journal of Vacuum Science & Technology B: Microelectronics and Nanometer Structures* **31,** 04D106. https://doi.org/10.1116/1.4807715 (2013).

291. Rice, A. D., Kawasaki, J. K., Verma, N., Pennachio, D. J., Schultz, B. D. & Palmstrøm, C. J. Structural and electronic properties of molecular beam epitaxially grown

$Ni_{1+x}TiSn$ films. *Journal of Crystal Growth* **467,** 71–76. https://doi.org/10.1016/J.JCRYSGRO.2017.03.015 (2017).

292. Chrisey, D. B. & Hubler, G. K. *Pulsed Laser Deposition of Thin Films* ISBN: 0-471-59218-8 (John Wiley & Sons, 1994).
293. Matsubara, M., Azuma, H. & Asahi, R. Fabrication of Nanocomposite Thermoelectric Materials by a Pulsed Laser Deposition Method. *Journal of Electronic Materials* **40,** 1176–1180. https://doi.org/10.1007/s11664-011-1575-3 (2011).
294. Webster, R. W. H., Halpin, J. E., Popuri, S. R., Bos, J.-W. G. & MacLaren, D. A. Spontaneous formation of nanostructures during pulsed laser deposition of epitaxial half-Heusler TiNiSn on MgO(001). *APL Materials* **7,** 013206. https://doi.org/10.1063/1.5052361 (2019).
295. Webster, R. W. H., Scott, M. T., Popuri, S. R., Bos, J. W. G. & MacLaren, D. A. Epitaxial vanadium nanolayers to suppress interfacial reactions during deposition of titanium-bearing Heusler alloys on MgO(001). *Applied Surface Science* **512,** 145649. https://doi.org/10.1016/j.apsusc.2020.145649 (2020).
296. Scharf, T. & Krebs, H. Influence of inert gas pressure on deposition rate during pulsed laser deposition. *Applied Physics A: Materials Science & Processing* **75,** 551–554. https://doi.org/10.1007/s00339-002-1442-4 (2002).
297. Ibach, H. *Physics of Surfaces and Interfaces* ISBN: 978-3-540-34709-5. https://doi.org/10.1007/3-540-34710-0 (Springer Berlin Heidelberg, 2006).
298. Leonard, J. P., Shin, B., McCamy, J. W. & Aziz, M. J. *Comparison of Growth Morphology in Ge (001) Homoepitaxy Using Pulsed Laser Deposition and MBE* in *Materials Research Society Symposium - Proceedings* **749** (Cambridge University Press, 2002), 291–296. https://doi.org/10.1557/proc-749-w16.11.
299. Gupta, P., Sokhey, K. J. S., Rai, S., Choudhary, R. J., Phase, D. M. & Lodha, G. S. Pulsed laser ablated off-stoichiometric thin films of the Heusler alloy Co2TiSn on Si (100) substrate. *Thin Solid Films* **517,** 3650–3655. https://doi.org/10.1016/j.tsf.2008.11.142 (2009).
300. Giapintzakis, J., Grigorescu, C., Klini, A., Manousaki, A., Zorba, V., Androulakis, J., Viskadourakis, Z. & Fotakis, C. Pulsed-laser deposition of NiMnSb thin films at moderate temperatures. *Applied Surface Science* **197,** 421–425. https://doi.org/10.1016/S0169-4332(02)00353-7 (2002).
301. Duriez, C., Chapon, C., Henry, C. R. & Rickard, J. M. Structural characterization of MgO(100) surfaces. *Surface Science* **230,** 123–136. https://doi.org/10.1016/0039-6028(90)90021-Y (1990).

302. Abriou, D., Creuzet, F. & Jupille, J. Characterization of cleaved MgO(100) surfaces. *Surface Science* **352,** 499–503. https://doi.org/10.1016/0039-6028(95)01187-0 (1996).

303. Robach, O., Renaud, G. & Barbier, A. Very-high-quality MgO(001) surfaces: roughness, rumpling and relaxation. *Surface Science* **401,** 227–235. https://doi.org/10.1016/S0039-6028(97)01082-0 (1998).

304. Arnold, C. & Aziz, M. Stoichiometry issues in pulsed-laser deposition of alloys grown from multicomponent targets. *Applied Physics A Materials Science & Processing* **69,** S23–S27. https://doi.org/10.1007/s003399900182 (1999).

305. Politi, P., Grenet, G., Marty, A., Ponchet, A. & Villain, J. Instabilities in crystal growth by atomic or molecular beams. *Physics Reports* **324,** 271–404. https://doi.org/10.1016/S0370-1573(99)00046-0 (2000).

306. Koster, G., Rijnders, G. J., Blank, D. H. & Rogalla, H. Imposed layer-by-layer growth by pulsed laser interval deposition. *Applied Physics Letters* **74,** 3729–3731. https://doi.org/10.1063/1.123235 (1999).

307. Rijnders, G., Koster, G., Leca, V., Blank, D. H. & Rogalla, H. Imposed layer-by-layer growth with pulsed laser interval deposition. *Applied Surface Science* **168,** 223–226. https://doi.org/10.1016/S0169-4332(00)00602-4 (2000).

308. Lüth, H. *Solid Surfaces, Interfaces and Thin Films* ISBN: 978-3-642-13591-0. https://doi.org/10.1007/978-3-642-13592-7 (Springer Berlin Heidelberg, Berlin, Heidelberg, 2010).

309. Patterson, A. L. The Scherrer formula for X-ray particle size determination. *Physical Review* **56,** 978–982. https://doi.org/10.1103/PhysRev.56.978 (1939).

310. Goldstein, J. I., Newbury, D. E., Echlin, P., Joy, D. C., Lyman, C. E., Lifshin, E., Sawyer, L. & Michael, J. R. *Scanning Electron Microscopy and X-ray Microanalysis* ISBN: 978-1-4613-4969-3. https://doi.org/10.1007/978-1-4615-0215-9 (Springer US, Boston, MA, 2003).

311. Stoyanov, E., Langenhorst, F. & Steinle-Neumann, G. The effect of valence state and site geometry on Ti L3,2 and O K electron energy-loss spectra of TixOy phases. *American Mineralogist* **92,** 577–586. https://doi.org/10.2138/am.2007.2344 (2007).

312. Berry, M. W., Browne, M., Langville, A. N., Pauca, V. P. & Plemmons, R. J. Algorithms and applications for approximate nonnegative matrix factorization. *Computational Statistics and Data Analysis* **52,** 155–173. https://doi.org/10.1016/j.csda.2006.11.006 (2007).

313. Gražulis, S., Chateigner, D., Downs, R. T., Yokochi, A. F. T., Quirós, M., Lutterotti, L., Manakova, E., Butkus, J., Moeck, P. & Le Bail, A. Crystallography Open Database – an open-access collection of crystal structures. *Journal of Applied Crystallography* **42,** 726–729. https://doi.org/10.1107/S0021889809016690 (2009).

314. *Crystal structrure of Ni_3Sn_4 (COD Entry 2106093)* http://www.crystallography.net/cod/2106093.html.

315. Berche, A. & Jund, P. Oxidation of half-Heusler NiTiSn materials: Implications for thermoelectric applications. *Intermetallics* **92,** 62–71. https://doi.org/10.1016/J.INTERMET.2017.09.014 (2018).

316. Zhang, C., Hao, F., Gao, G., Liu, X., Ma, C., Lin, Y., Yin, Y. & Li, X. Enhanced superconductivity in TiO epitaxial thin films. *NPJ Quantum Materials* **2,** 2. https://doi.org/10.1038/s41535-016-0006-3 (2017).

317. Valeeva, A. A., Rempel, A. A. & Gusev, A. I. Ordering of Cubic Titanium Monoxide into Monoclinic Ti5O5. *Inorganic Materials* **37,** 603–612. https://doi.org/10.1023/A:1017568301183 (2001).

318. Gusev, A. I. Family of Ti5O5 superstructures. *Journal of Experimental and Theoretical Physics* **120,** 851–859. https://doi.org/10.1134/S1063776115040044 (2015).

319. Kubo, T. & Nozoye, H. Morphology and structure of Mg–Ti–O spinel(100) epitaxially grown on MgO(100): effect of solid state reactions. *Thin Solid Films* **394,** 150–157. https://doi.org/10.1016/S0040-6090(01)01011-2 (2001).

320. Fork, D. K., Ponce, F. A., Tramontana, J. C. & Geballe, T. H. Epitaxial MgO on Si(001) for Y-Ba-Cu-O thin-film growth by pulsed laser deposition. *Applied Physics Letters* **58,** 2294–2296. https://doi.org/10.1063/1.104903 (1991).

321. Narayan, J., Tiwari, P., Jagannadham, K. & Holland, O. W. Formation of epitaxial and textured platinum films on ceramics-(100) MgO single crystals by pulsed laser deposition. *Applied Physics Letters* **64,** 2093–2095. https://doi.org/10.1063/1.111693 (1994).

322. Huttel, Y., Navarro, E. & Cebollada, A. Epitaxy and lattice distortion of V in MgO / V / MgO(001) heterostructures. *Journal of Crystal Growth* **273,** 474–480. https://doi.org/10.1016/J.JCRYSGRO.2004.09.051 (2005).

323. Rajanikanth, A., Hauet, T., Montaigne, F., Mangin, S. & Andrieu, S. Magnetic anisotropy modified by electric field in V/Fe/MgO(001)/Fe epitaxial magnetic tunnel junction. *Applied Physics Letters* **103,** 062402. https://doi.org/10.1063/1.4817268 (2013).

324. Jaeger, T. *Thermoelectric properties of TiNiSn and $Zr_{0.5}$ $Hf_{0.5}$ NiSn thin films and superlattices with reduced thermal conductivities* PhD thesis (Johannes Gutenberg Universitat Mainz, 2013), 178. https://publications.ub.uni-mainz.de/theses/volltexte/2014/3614/pdf/3614.pdf.

325. Gutsche, M., Kraus, H., Jochum, J., Kemmather, B. & Gutekunst, G. Growth and characterization of epitaxial vanadium films. *Thin Solid Films* **248,** 18–27. https://doi.org/10.1016/0040-6090(94)90204-6 (1994).

326. Bencok, P., Andrieu, S., Arcade, P., Richter, C., Ilakovac, V., Heckmann, O., Vesely, M. & Hricovini, K. Growth of vanadium ultrathin films on Fe(100) studied by RHEED. *Surface Science* **402,** 327–331. https://doi.org/10.1016/S0039-6028(98)00009-0 (1998).

327. Rau, C., Liu, C., Schmalzbauer, A. & Xing, G. Ferromagnetic order at (100) p(1×1) surfaces of bulk paramagnetic vanadium. *Physical Review Letters* **57,** 2311–2313. https://doi.org/10.1103/PhysRevLett.57.2311 (Nov. 1986).

328. Parkin, S. S. P. Systematic variation of the strength and oscillation period of indirect magnetic exchange coupling through the 3d, 4d, and 5d transition metals. *Physical Review Letters* **67,** 3598–3601. https://doi.org/10.1103/PhysRevLett.67.3598 (1991).

329. Harp, G. R., Parkin, S. S. P., Obrien, W. L. & Tonner, B. P. X-ray magnetic-circular-dichroism study of Fe/V multilayers. *Physical Review B* **51,** 3293–3296. https://doi.org/10.1103/PhysRevB.51.3293 (1995).

330. Yuen, H., Princen, J., Illingworth, J. & Kittler, J. Comparative study of Hough Transform methods for circle finding. *Image and Vision Computing* **8,** 71–77. https://doi.org/10.1016/0262-8856(90)90059-E (1990).

331. Klinger, M., Němec, M., Polívka, L., Gärtnerová, V. & Jäger, A. Automated CBED processing: Sample thickness estimation based on analysis of zone-axis CBED pattern. *Ultramicroscopy* **150,** 88–95. https://doi.org/10.1016/j.ultramic.2014.12.006 (2015).

332. Klinger, M. More features, more tools, more CrysTBox. *Journal of Applied Crystallography* **50,** 1226–1234. https://doi.org/10.1107/S1600576717006793 (2017).

333. Gotoh, T., Murakami, S., Kinosita, K. & Murata, Y. Surface Rumpling of MgO(001) Deduced from Changes in RHEED Kikuchi Pattern. I. Experimental. *Journal of the Physical Society of Japan* **50,** 2063–2068. https://doi.org/10.1143/JPSJ.50.2063 (1981).

334. Krivanek, O. L. & Paterson, J. H. ELNES of 3d transition-metal oxides: I. Variations across the periodic table. *Ultramicroscopy* **32,** 313–318. https://doi.org/10.1016/0304-3991(90)90077-Y (1990).

335. Hÿtch, M., Snoeck, E. & Kilaas, R. Quantitative measurement of displacement and strain fields from HREM micrographs. *Ultramicroscopy* **74,** 131–146. https://doi.org/10.1016/S0304-3991(98)00035-7 (1998).

336. Peters, J. *Strain++* 2017. https://jjppeters.github.io/Strainpp/.

337. Naden, A. B., O'Shea, K. J. & MacLaren, D. A. Evaluation of crystallographic strain, rotation and defects in functional oxides by the moiré effect in scanning transmission electron microscopy. *Nanotechnology* **29,** 165704. https://doi.org/10.1088/1361-6528/aaae50 (2018).

338. Barczak, S. A., da Silva, I. & Bos, J. W. G. In situ neutron diffraction monitoring of $TiNi_{1+y}Sn$ (y = 0, 0.075 and 0.25) half-Heusler formation. *Unpublished* (2019).

339. Birkel, C. S. *et al.* Rapid microwave preparation of thermoelectric TiNiSn and TiCoSb half-Heusler compounds. *Chemistry of Materials* **24,** 2558–2565. https://doi.org/10.1021/cm3011343 (2012).

340. Verma, N., Douglas, J. E., Krämer, S., Pollock, T. M., Seshadri, R. & Levi, C. G. Microstructure Evolution of Biphasic $TiNi_{1+x}Sn$ Thermoelectric Materials. *Metallurgical and Materials Transactions A: Physical Metallurgy and Materials Science* **47,** 4116–4127. https://doi.org/10.1007/s11661-016-3549-9 (2016).

341. Von Luxburg, U. A tutorial on spectral clustering. *Statistics and Computing* **17,** 395–416. https://doi.org/10.1007/s11222-007-9033-z (2007).

342. Pedregosa, F. *et al.* Scikit-learn: Machine Learning in Python. *Journal of Machine Learning Research* **12,** 2825–2830. http://jmlr.org/papers/v12/pedregosa11a.htm (2011).

343. Yu, S. X. & Shi, J. *Multiclass spectral clustering* in *Proceedings of the IEEE International Conference on Computer Vision* **1** (2003), 313–319. https://doi.org/10.1109/iccv.2003.1238361.

344. Szkudlarek, A., Rodrigues Vaz, A., Zhang, Y., Rudkowski, A., Kapusta, C., Erni, R., Moshkalev, S. & Utke, I. Formation of pure Cu nanocrystals upon post-growth annealing of Cu–C material obtained from focused electron beam induced deposition: comparison of different methods. *Beilstein Journal of Nanotechnology* **6,** 1508–1517. https://doi.org/10.3762/bjnano.6.156 (2015).

345. Puydinger Dos Santos, M. V., Velo, M. F., Domingos, R. D., Zhang, Y., Maeder, X., Guerra-Nuñez, C., Best, J. P., Béron, F., Pirota, K. R., Moshkalev, S., Diniz, J. A.

& Utke, I. Annealing-Based Electrical Tuning of Cobalt-Carbon Deposits Grown by Focused-Electron-Beam-Induced Deposition. *ACS Applied Materials and Interfaces* **8,** 32496–32503. https://doi.org/10.1021/acsami.6b12192 (2016).

346. Do, D. T., Mahanti, S. D. & Pulikkoti, J. J. Electronic structure of Zr–Ni–Sn systems: role of clustering and nanostructures in half-Heusler and Heusler limits. *Journal of Physics: Condensed Matter* **26,** 275501. https://doi.org/10.1088/0953-8984/26/27/275501 (2014).
347. Paul, A., Laurila, T., Vuorinen, V. & Divinski, S. V. in. *Thermodynamics, diffusion and the Kirkendall effect in solids* chap. Fick's Laws of Diffusion (Springer International Publishing, 2014). ISBN: 9783319074610. https://doi.org/10.1007/978-3-319-07461-0.
348. Mita, M., Kajihara, M., Kurokawa, N. & Sakamoto, K. Growth behavior of Ni_3Sn_4 layer during reactive diffusion between Ni and Sn at solid-state temperatures. *Materials Science and Engineering A* **403,** 269–275. https://doi.org/10.1016/j.msea.2005.05.012 (2005).
349. Douglas, J. E., Chater, P. A., Brown, C. M., Pollock, T. M. & Seshadri, R. Nanoscale structural heterogeneity in Ni-rich half-Heusler TiNiSn. *Journal of Applied Physics* **116,** 163514. https://doi.org/10.1063/1.4900497 (2014).
350. Askeland, D. R. in. *The Science and Engineering of Materials* chap. Atom Movement in Materials (Springer US, 1996). https://doi.org/10.1007/978-1-4899-2895-5.
351. Hazama, H., Matsubara, M., Asahi, R. & Takeuchi, T. Improvement of thermoelectric properties for half-Heusler TiNiSn by interstitial Ni defects. *Journal of Applied Physics* **110,** 063710. https://doi.org/10.1063/1.3633518 (2011).
352. Delpierre, P. A history of hybrid pixel detectors, from high energy physics to medical imaging. *Journal of Instrumentation* **9.** https://doi.org/10.1088/1748-0221/9/05/C05059 (2014).
353. Ballabriga, R., Alozy, J., Blaj, G., Campbell, M., Fiederle, M., Frojdh, E., Heijne, E. H. M., Llopart, X., Pichotka, M., Procz, S., Tlustos, L. & Wong, W. The Medipix3RX: a high resolution, zero dead-time pixel detector readout chip allowing spectroscopic imaging. *Journal of Instrumentation* **8,** C02016–C02016. https://doi.org/10.1088/1748-0221/8/02/C02016 (2013).
354. *NanoMEGAS* https://nanomegas.com/digistar-3/ (2020).
355. *FPD: Fast pixelated detector data storage, analysis and visualisation* https://gitlab.com/fpdpy/fpd. Accessed 2019-05-29.

356. Nord, M., Webster, R. W. H., Paton, K. A., McVitie, S., McGrouther, D., MacLaren, I. & Paterson, G. W. Fast Pixelated Detectors in Scanning Transmission Electron Microscopy. Part I: Data Acquisition, Live Processing and Storage. arXiv: 1911.11560. https://arxiv.org/abs/1911.11560 (2019).

357. Paterson, G. W., Webster, R. W. H., Ross, A., Paton, K. A., Macgregor, T. A., McGrouther, D., MacLaren, I. & Nord, M. Fast Pixelated Detectors in Scanning Transmission Electron Microscopy. Part II: Post Acquisition Data Processing, Visualisation, and Structural Characterisation. arXiv: 2004.02777. https://arxiv.org/abs/2004.02777 (2020).

358. Rauch, E. F., Portillo, J., Nicolopoulos, S., Bultreys, D., Rouvimov, S. & Moeck, P. Automated nanocrystal orientation and phase mapping in the transmission electron microscope on the basis of precession electron diffraction. *Zeitschrift für Kristallographie* **225,** 103–109. https://doi.org/10.1524/zkri.2010.1205 (2010).

359. Ding, L. & Goshtasby, A. On the canny edge detector. *Pattern Recognition* **34,** 721–725. https://doi.org/10.1016/S0031-3203(00)00023-6 (2001).

360. Illingworth, J. & Kittler, J. The Adaptive Hough Transform. *IEEE Transactions on Pattern Analysis and Machine Intelligence* **PAMI-9,** 690–698. https://doi.org/10.1109/TPAMI.1987.4767964 (1987).

361. Gouillart, E., Nunez-Iglesias, J. & van der Walt, S. Analyzing microtomography data with Python and the scikit-image library. *Advanced Structural and Chemical Imaging* **2,** 18. https://doi.org/10.1186/s40679-016-0031-0 (2016).

362. Van Der Walt, S., Schönberger, J. L., Nunez-Iglesias, J., Boulogne, F., Warner, J. D., Yager, N., Gouillart, E. & Yu, T. Scikit-image: Image processing in python. *PeerJ* **2014,** e453. https://doi.org/10.7717/peerj.453 (2014).

363. Schaffer, B., Grogger, W. & Kothleitner, G. Automated spatial drift correction for EFTEM image series. *Ultramicroscopy* **102,** 27–36. https://doi.org/10.1016/j.ultramic.2004.08.003 (2004).

364. Pekin, T. C., Gammer, C., Ciston, J., Minor, A. M. & Ophus, C. Optimizing disk registration algorithms for nanobeam electron diffraction strain mapping. *Ultramicroscopy* **176,** 170–176. https://doi.org/10.1016/j.ultramic.2016.12.021 (2017).

365. Kong, H., Akakin, H. C. & Sarma, S. E. A generalized laplacian of gaussian filter for blob detection and its applications. *IEEE Transactions on Cybernetics* **43,** 1719–1733. https://doi.org/10.1109/TSMCB.2012.2228639 (2013).

366. Shortis, M. R., Clarke, T. A. & Short, T. *Comparison of some techniques for the sub-pixel location of discrete target images* in *Videometrics III* (ed El-Hakim, S. F.) **2350** (SPIE, 1994), 239–250. http://doi.org/10.1117/12.189136.

367. Anthony, S. M. & Granick, S. Image analysis with rapid and accurate two-dimensional Gaussian fitting. *Langmuir* **25,** 8152–8160. https://doi.org/10.1021/la900393v (2009).

368. Miyake, S. & Uyeda, R. Friedel's law in the dynamical theory of diffraction. *Acta Crystallographica* **8,** 335–342. https://doi.org/10.1107/s0365110x55001023 (1955).

369. Rouvière, J. L. & Sarigiannidou, E. Theoretical discussions on the geometrical phase analysis. *Ultramicroscopy* **106,** 1–17. https://doi.org/10.1016/j.ultramic.2005.06.001 (2005).

370. Béché, A., Rouvìre, J. L., Cĺment, L. & Hartmann, J. M. Improved precision in strain measurement using nanobeam electron diffraction. *Applied Physics Letters* **95,** 123114. https://doi.org/10.1063/1.3224886 (2009).

371. Tick, T. & Campbell, M. TSV processing of Medipix3 wafers by CEA-LETI: a progress report. *Journal of Instrumentation* **6,** C11018–C11018. https://doi.org/10.1088/1748-0221/6/11/C11018 (2011).

372. Ponchut, C., Collet, E., Hervé, C., Caer, T. L., Cerrai, J., Siron, L., Dabin, Y. & Ribois, J. F. SMARTPIX, a photon-counting pixel detector for synchrotron applications based on Medipix3RX readout chip and active edge pixel sensors. *Journal of Instrumentation* **10.** https://doi.org/10.1088/1748-0221/10/01/C01019 (2015).

373. Bücker, R., Hogan-Lamarre, P., Mehrabi, P., Schulz, E. C., Bultema, L. A., Gevorkov, Y., Brehm, W., Yefanov, O., Oberthür, D., Kassier, G. H. & Dwayne Miller, R. J. Serial protein crystallography in an electron microscope. *Nature Communications* **11,** 1–8. https://doi.org/10.1038/s41467-020-14793-0 (2020).

374. Barnard, J. S., Johnstone, D. N. & Midgley, P. A. High-resolution scanning precession electron diffraction: Alignment and spatial resolution. *Ultramicroscopy* **174,** 79–88. https://doi.org/10.1016/j.ultramic.2016.12.018 (2017).

375. Nord, M., Ross, A., McGrouther, D., Barthel, J., Moreau, M., Hallsteinsen, I., Tybell, T. & MacLaren, I. Three-dimensional subnanoscale imaging of unit cell doubling due to octahedral tilting and cation modulation in strained perovskite thin films. *Physical Review Materials* **3,** 063605. https://doi.org/10.1103/PhysRevMaterials.3.063605 (2019).

376. Picu, R. C., Borca-Tasciuc, T. & Pavel, M. C. Strain and size effects on heat transport in nanostructures. *Journal of Applied Physics* **93,** 3535–3539. https://doi.org/10.1063/1.1555256 (2003).

377. Ortiz, B. R., Peng, H., Lopez, A., Parilla, P. A., Lany, S. & Toberer, E. S. Effect of extended strain fields on point defect phonon scattering in thermoelectric materials. *Physical Chemistry Chemical Physics* **17,** 19410–19423. https://doi.org/10.1039/c5cp02174j (2015).

378. Zeltmann, S. E., Müller, A., Bustillo, K. C., Savitzky, B., Hughes, L., Minor, A. M. & Ophus, C. Patterned probes for high precision 4D-STEM Bragg measurements. *Ultramicroscopy* **209,** 112890. https://doi.org/10.1016/j.ultramic.2019.112890 (2020).

379. Palatinus, L., Jacob, D., Cuvillier, P., Klementová, M., Sinkler, W., Marks, L. D. & IUCr. Structure refinement from precession electron diffraction data. *Acta Crystallographica Section A Foundations of Crystallography* **69,** 171–188. https://doi.org/10.1107/S010876731204946X (2013).

380. STEM@LPS Orsay (@STEM_LPS). *Chromatem delivers on-site sub-5 meV @ 30 keV* 2018. https://twitter.com/STEM_LPS/status/979011634415984640?s=20.

381. Collins, S. M., Kepaptsoglou, D. M., Hou, J., Ashling, C. W., Radtke, G., Bennett, T. D., Midgley, P. A. & Ramasse, Q. M. Functional Group Mapping by Electron Beam Vibrational Spectroscopy from Nanoscale Volumes. *Nano Letters* **20,** 1272–1279. https://doi.org/10.1021/acs.nanolett.9b04732 (2020).

382. Hage, F. S., Radtke, G., Kepaptsoglou, D. M., Lazzeri, M. & Ramasse, Q. M. Single-atom vibrational spectroscopy in the scanning transmission electron microscope. *Science* **367,** 1124–1127. https://doi.org/10.1126/science.aba1136 (2020).